Self-assembly of colloidal spheres and rods in external fields

Front and back cover: details of ‘192 Farben’ by Gerhard Richter
Oil on canvas, 1966
200 × 150.5 × 4.5 cm^3

Foto: Elke Walford

PhD thesis, Utrecht University, The Netherlands, 2014
ISBN 978-90-393-6248-8
A digital version of this thesis is available at http://www.colloid.nl

Self-assembly of colloidal spheres and rods in external fields

---

Zelforganisatie van colloïdale bollen en staven in externe velden

(met een samenvatting in het Nederlands)

Proefschrift

ter verkrijging van de graad van doctor aan de Universiteit Utrecht op gezag van de rector magnificus, prof. dr. G.J. van der Zwaan, ingevolge het besluit van het college voor promoties in het openbaar te verdedigen op

maandag 24 november 2014 des middags te 2.30 uur

door

Thijs Herman Besseling

geboren op 26 maart 1984 te Fiesole, Italië

Promotor: Prof. dr. A. van Blaaderen

Copromotor: Dr. A. Imhof

This work was carried out under project number M62.7.08SDMP25 in the framework of the Industrial Partnership Program on Size Dependent Material Properties of the Materials innovation institute (M2i) and the Foundation of Fundamental Research on Matter (FOM), which is part of the Netherlands Organisation for Scientific Research (NWO).

Contents

1

Introduction

Abstract

In this chapter, we give a general introduction to the work described in this thesis. We first briefly introduce colloids, followed by a description of their use as a hard-sphere and hard-rod model system. We then describe recent research on the self-assembly of both colloidal spheres and rod-like particles in external fields. This is followed by a discussion of the model systems that we used in this thesis and the type of analysis that we applied. At the end of this chapter, we give an outline of the topics that are presented in each chapter of this thesis.

1.1. Colloids

When Thomas Graham was studying diffusion through membranes in 1861, he found that a sticky substance remained on the membrane for certain types of aqueous solutions [1]. He called these substances ‘colloids’, after the Greek word for glue: $\kappa o \lambda \lambda \alpha$. Although the term ‘colloid’ might be unfamiliar to many, we are actually surrounded by colloids every day. Colloids can be found in for example foods, cosmetics, living creatures, the atmosphere and in electronic devices such as e-readers. What colloids have in common is that they exist of an insoluble substance, roughly between 10 nanometer and several micrometer, dispersed throughout another substance. These two components are referred to as the dispersed phase and a continuous phase. Both components can be either gas, liquid or solid, giving rise to a wealth of classifications of colloids. In a foam (such as shaving cream or the head of a glass of beer), the dispersed phase is a gas and the continuous phase is a liquid. If both phases are liquid, the colloid is called an emulsion. Many food products are oil-in-water emulsions: milk, mayonnaise, vinaigrette, and so on. The colloids that are described in this thesis are classified as sols: they consist of solid particles dispersed in a liquid. Many types of sols are used in industry, such as paint, ink and drilling mud. Although the term ‘colloid’ is often used to refer to the dispersed phase only, the term ‘colloidal suspension’ refers to the two component system.

Because a colloidal suspension is a state of matter somewhere between that of a fluid and a solid, it has the intricate property that the viscosity is dependent on the stress (or shear rate) that is applied to the suspension. These suspensions are therefore also called non-Newtonian fluids or complex fluids. For certain types of suspensions, the viscosity decreases as a function of shear rate, called shear thinning (this is what happens when ketchup is squeezed out of its bottle). There are also suspensions of which the viscosity increases as a function of shear rate, known as shear thickening (which can be experienced when stirring through a mixture of cornstarch and water). Finally, there are many examples of complex fluids that show, for increasing shear rate, both shear thinning and shear thickening behaviour [2].

Another characteristic of a colloidal suspensions is that the particles perform erratic motion due to collisions with atoms or molecules in the suspending liquid. This motion is known as ‘Brownian motion’, after its discoverer Robert Brown. In 1827, the botanist Robert Brown was studying pollens of the plant *Clarkia pulchella* suspended in water [3]. When he viewed the rapid and erratic motion of tiny objects through an optical microscope, he first believed that these were small living organisms. He however soon found out that also finely ground lifeless substances such as sand and clay also showed the same type of spontaneous movement when suspended in water. A comprehensive quantitative theory of the phenomenon, however, was only formulated many decades later by Albert Einstein [4]. In his 1905 *annis mirabilis*, he derived an expression for the mean squared displacement of the random motion of spherical particles suspended in a liquid and showed that the diffusion constant of a spherical particle is given by

$$D_t = \frac{k_B T}{6\pi\eta R}, \tag{1.1}$$

with k_B the Boltzmann constant, T the temperature, η the solvent viscosity and R the radius of the sphere. The same diffusion equation was independently derived in 1904 by the Australian physicist Sutherland in 1904, and hence equation (1.1) is known as the Stokes-Einstein-Sutherland equation, although the last name is often omitted (or forgotton) due to historical reasons. The derivation of equation (1.1) can be considered quite revolutionary as this was done in a time when the existence of molecules and the kinetic theory of fluids was still disputed. The dispute was finally put to rest by Jean Perrin, who applied equation (1.1) to his experimental measurements on colloidal particles to determine Avogadro's number [5, 6]. He used mastic spheres of approximately 1 μm in diameter which were made monodisperse by laborious centrifugation steps. By viewing the suspended particles through an optical microscope, he could record their translational trajectories over time, from which he then calculated their mean squared displacements. This was however only one out of the five methods he used to determine Avogadro's number. He also exploited the *rotational* Brownian motion of spherical colloids, together with the expression for the rotational diffusion coefficient of spherical colloids. This expression was also derived by Einstein and is given by

$$D_r = \frac{k_B T}{8\pi\eta R^3}. \tag{1.2}$$

Perrin realized that colloidal spheres with a diameter of 1 μm dispersed in water would rotate much to fast to be recorded by hand ($\sim 8^\circ/\,0.01\,\mathrm{s}$). He therefore used much larger spheres of 13 μm in diameter, which only rotated $15^\circ/\,\mathrm{min}$. To avoid sedimentation of these large particles to the bottom of the sample (which slows down the particle dynamics), he density matched the particles by a solvent mixture of 27% urea in water, which was the only solvent he could find that did not induce aggregation of his suspensions. Using small vacuoles or air pockets that some of the particles contained, he could record the slow (projected) rotational motion, from which he then computed the mean-squared-angular displacement. Almost exactly a century after the discovery of Brownian motion, Jean Perrin received the Nobel Prize in Physics in 1926, for his experimental work on colloids (or 'discontinuous structure of matter').

1.2. MODEL SYSTEMS OF COLLOIDAL SPHERES AND RODS

From the time of Perrin onwards, the field of colloid science has matured into a wide and diverse research field. The type of colloid research described in this thesis is focussed on the use of colloids as a model system to study fundamental questions in (soft) condensed matter physics regarding crystallization, flow-induced behaviour and the glass transition. In this field of study, many of the experimental challenges that Perrin faced in the beginning of the 20th century, we still face in the lab today: decreasing the particles polydispersity; finding the right solvent (composition) to avoid sedimentation;

avoiding particle aggregation; handling the fast (rotational) motion of particles and extracting 3D information from 2D projected rotational trajectories. Fortunately, we have much more sophisticated tools today to handle these problems. One of the reasons that colloids are so well suited as a model system has not changed however: colloids are large enough to be observed with an optical microscope in real-space. Furthermore, compared to atoms or simple molecules, they also move very slowly: it takes a spherical particle of 1 μm approximately 0.5 s to diffuse over its own diameter, when suspended in an aqueous solution. The possibility to study colloidal particles in real-space and in real-time thus allows for detailed investigations of both structure and dynamics on the single particle level.

Monodisperse colloidal spheres with a hard interaction potential (hard spheres in short) have served over the last decades as the 'fruit fly' of the colloid scientist. The theoretical hard-sphere system consists of particles that have an infinite repulsion at contact but otherwise do not have any interaction. As a result, the internal energy of the system is always zero and the phase behaviour is completely driven by entropy. The phase diagram of hard-spheres is therefore dictated by a single parameter: the density (or volume fraction) of the spheres. Furthermore, the equilibrium phase diagram consists of only a fluid and a crystal phase [7,8]. Systems that behave like hard spheres can also be fabricated in the laboratory: spherical particles are often made of a polymer such as poly(methyl methacrylate) (PMMA) [9] or from inorganic material such as silica [10].

There are however a few important differences between the theoretical hard-sphere model and the colloidal particles used in the experimental systems [11]. Three important differences are that in reality, colloids have a charged surface, there is always a distribution of sizes present and finally, the particles are affected by gravity. By addition of an as large as possible amount of salt to the suspension, electric charges are screened over distances much smaller than the diameter of the particle. Combined with an additional steric stabilizer (in case of the polymer particles), these particles behave approximately as hard-spheres [9,12]. Due to subtle charge effects and possible swelling of the particles, they do not have an infinite repulsion upon contact, but nevertheless, their phase behaviour can be mapped effectively onto the hard-sphere phase diagram by introduction of an effective diameter (and effective volume fraction) [11, 13–15]. Furthermore, the particles have a size polydispersity (standard deviation over the mean) of at least 3 - 5%, which has an effect on the fluid-solid coexisting volume fractions. Finally, the particles are affected by gravity. If the particles are around 1 μm in diameter, they will eventually sediment (in the direction of gravity) or cream (against the direction of gravity). This effect can be counteracted by carefully matching the mass density of the solvent to that of the particles, however, this is not always possible or easy to achieve. Despite these (minor) deviations from the ideal hard-sphere system, hard-sphere colloids can crystallize in face-centered cubic (fcc) or hexagonal close-packed (hcp) crystals, similar to simple atomic systems. Furthermore, the screening length can also be used as a parameter to tune the interactions between the particles: by changing the salt concentration, the interactions can be tuned from strongly screened (hard) to a long-range repulsive electrostatic potential (soft) [12]. Both computer simulations and experiments on soft colloidal spheres showed that they can crystallize into a body-centered cubic (bcc) phase [12, 16, 17].

Compared to spherical particles, colloidal *rod-like* particles display a wealth of novel phase behaviour. Rod-like colloids are known since the 1920s, when needle-like vanadium pentoxide particles were found to form a nematic phase [18]. In this phase, the particles are orientationally ordered but positionally disordered (or liquid-like). Later, also smectic phases were reported in suspensions of the tobacco mosaic virus (TMV) [19]. In a smectic phase, the particles are not only orientationally ordered but also positionally ordered into layers. Several types of smectic phases are distinguished, based on the order within the smectic layers, ranging from smectic-A to smectic-L [20]. Currently, progress in synthesis methods has enabled the fabrication of many well-defined rod-shaped colloids of a large variety of materials, including PMMA, polystyrene, silica or iron hydroxides [21–25]. Also bio-organic materials such as the *fd*-virus can serve as well-defined model system of colloidal rods [26, 27]. Just as the hard-sphere particles, these rod-like particles have a typical screening length (which is usually small compared to diameter of the particle), they also have a certain size-distribution (in both length and diameter) and they are affected by gravity. Nevertheless, it was recently shown that a system of rod-like silica particles could be mapped with reasonable agreement onto the hard spherocylinder phase diagram (obtained with computer simulations), by introducing an effective diameter and effective length of the rods [28]. Also systems of *fd*-viruses or iron hydroxide rods have shown to form nematic and smectic phases in equilibrium [21, 26, 29]. Most of the colloidal liquid-crystal systems are lyotropic: their phase behaviour is driven by concentration (or volume fraction). This is in contrast with most molecular liquid crystals, which are thermotropic: their phase behaviour is determined by temperature. However, because the lyotropic colloidal liquid crystals form the same equilibrium phases as many thermotropic molecular liquid crystals, they still serve as a valuable model system.

1.3. Colloidal self-assembly in external fields

Because many of the phenomena studied in this thesis involve both structural and dynamical components and both in- and out-of-equilibrium phases, we refer to these phenomena using the overall term *self-assembly.* Due to their size, colloidal particles easily couple to external fields such as shear-flow or electric fields. The self-assembly process can thus be guided or enhanced by such external fields, which is commonly referred to as *directed* self-assembly. Studies on the self-assembly of colloidal spheres in external fields are numerous. When, for example, the particles are heavier than the solvent, *gravity* acts as a constant external field on the particles. The gravitational force that pulls the particles down will eventually be balanced by an osmotic pressure gradient pushing the particles up, resulting in a density gradient (or sedimentation profile) along the direction of gravity. For large enough sediments, the sedimentation profile will contain all the possible phases of the system. For dilute, non-interacting particles, this will result in a barometric height distribution. Another example of a commonly encountered external field that acts on a colloidal suspension is *shear*. Shear is known to have a large effect on the ordering of colloidal spheres [30], and can even induce crystallization in suspensions that are in a fluid phase in equilibrium [31,32]. The third and final external field that we consider is an *electric field*. When the colloidal particles have a different dielectric constant than the suspending medium, they will acquire a dipole moment when an electric-field is applied to the suspension. High frequency AC electric fields can be used to prevent polarization of the double layer of the particles, but still resulting in additional dipole-dipole interactions between the particles. If these interactions are strong enough, they can induce string-formation in a suspension of spheres and, at higher densities, a body-centered tetragonal (bct) phase [12, 17].

When rod-like colloids are subjected to external fields, unlike spheres, their orientational degrees of freedom can couple to the field direction. For example, theory predicts a change in the nematic ordering of long rigid rods in a gravitational field, which broadens the region of phase separation, for large enough centrifugal acceleration [33]. Furthermore, it is well known that dense systems of liquid crystals can exhibit rich phase behaviour when shear flow is applied [34, 35]. Depending on the initial state of the system and the applied shear rate, the average alignment in the system (or director), displays complex time-periodic motion such as 'tumbling', 'wagging' and 'flow-aligning'. Using colloidal suspensions of *fd*-viruses, these three states were experimentally found [36, 37] and confirmed by Brownian Dynamics computer simulations [38, 39]. Recently, the enhanced rotational diffusion of single dumbbell particles under oscillatory shear was also determined [40]. Finally, electric fields can be used to align rod-like particles over large distances. Again, a high frequency AC electric field will prevent polarization of the electric double layers, however, such a field will still exert a torque on the particles, resulting in alignment in the field direction [41,42]. For higher field strengths, dielectric rod-like particles will line up in strings, due to the dipole-dipole interactions, and for higher concentrations new crystal structures are formed [41, 43, 44], similar to the behaviour of spherical particles in an AC electric field.

1.4. REAL-SPACE ANALYSIS OF COLLOIDAL SELF-ASSEMBLY

One of the advantages of using colloidal particles as model systems is that they can be made fluorescent, combined with the fact that often the refractive index of the solvent can be matched to that of the particles. This combination allows for imaging deep into the sample with the use of a confocal laser scanning microscope (CLSM). Because the use of confocal microscopy combined with subsequent image analysis is the central technique used in this thesis, we will give a brief introduction to both subjects.

The two key features of such a microscope are point-by-point illumination of the sample and rejection of out-of-focus light. The first feature is achieved by a pinhole in front of the laser light source and the second is achieved by a pinhole in front of the detector. This results in improved resolution, compared to conventional bright field microscopy. By scanning several 2D images while moving the microscope stage in the vertical direction, a 3D image of the sample can be obtained. The colloidal particles under investigation can therefore be studied in-situ and in three dimensions. Furthermore, the positions of the particles can be determined from the confocal microscopy data using image processing techniques. Usually, spherical particles are located using a local brightness maxima criterion and the positions are refined by calculating the brightness-weighted centroid of a cluster of pixels [45]. This was originally done in 2D but later extended to 3D [46–48]. The positions of particles can also be linked together between different time-frames to form trajectories, known as particle tracking [45]. Since the 90s, there have been numerous improvements to locate or track spherical particles [49–55]. Due to this progress, studies based on particle tracking of spherical colloids combined with fast confocal microscopy has led to many new insights in phenomena such as crystallization [12,47,56], gelation [48], defect dynamics [57], the glass transition [58,59] and flow-induced behaviour [52, 60–63].

Compared to the advancement of studies of spherical particles, few researchers have performed real-space studies on rod-like colloids. In contrast to the systems of e.g. ellipsoidal or dumbbell particles, we use in this thesis a model system of fluorescent rod-like silica particles, briefly described in the previous section, that forms both nematic and smectic phases in equilibrium [25, 28]. Quantitative measurements on the dense liquid-crystalline phases that this system forms have thus far only been performed in reciprocal space using small angle X-ray scattering (SAXS). The reason for this is that the individual particles are on the order of the resolution of the confocal microscope, resulting in strongly overlapping signals in the confocal microscopy images. Subsequent image analysis is therefore not accurate enough to determine all coordinates of the system. To circumvent this problem we developed a new image processing algorithm to extract the positions and orientations of the fluorescent rod-like particles from three dimensional confocal microscopy data stacks. The algorithm is tailored to work even when the fluorescent signals of the particles overlap considerably and a threshold method and subsequent clusters analysis alone do not suffice. If the resolution of the images was not good enough for accurate tracking, we also used image deconvolution. Finally, for particles which could not be identified individually, even after deconvolution, we used an alternative image processing approach, which still enabled calculation of the 2D (projected) orientation distribution of the particles.

1.5. OUTLINE OF THIS THESIS

This thesis is organized in two parts. In the first part, consisting of Chapters 2 - 4, we describe the methodology to analyse the structure of colloidal suspensions using confocal microscopy. In **Chapter 2**, we describe the general properties of the colloidal suspensions and the imaging techniques used to investigate their self-assembly. In **Chapter 3**, we present methods to calibrate and scale axial distances as a function of refractive index mismatch, often encountered while imaging colloidal suspensions. Finally, in **Chapter 4**, we present a new algorithm to accurately identify the positions and orientations of rod-like particles from 2D and 3D microscopy data.

The second part of this thesis, consisting of Chapters 5 - 9, contains investigations on the self-assembly of spherical and rod-like particles in external fields. In **Chapter 5** we investigate the oscillatory shear-induced order in hard-sphere colloidal suspensions that are fluid in equilibrium. In **Chapter 6**, we study the liquid-crystalline phase behaviour of (nearly) hard rods subjected to gravity. We compare our real-space results to predictions from theory and simulation on hard spherocylinders. In **Chapter 7**, we apply shear flow to suspensions of rods and investigate the shear-induced order in the suspensions. We also measure the rheological response of the suspensions during confocal microscopy imaging. In the last two chapters of this thesis, we change the interaction potential of the silica rods from hard to long-range repulsive by tuning the salt concentration. In **Chapter 8** we analyse the structure and dynamics of the plastic crystals that these long-range repulsive rods from. Finally, in **Chapter 9**, we show that at higher volume fractions, the long-range repulsive rods fail to crystallize and form a ‘plastic glass’. We use a high frequency AC electric field to switch both the plastic crystals and the plastic glasses to completely crystalline phases.

Part 1

Methods to Analyse Colloidal Particles in Real-Space

2

Suspension Characterisation and General Techniques

Abstract

In this chapter, we describe the general properties of the colloidal suspensions used in the experiments and we describe the imaging techniques that were applied to investigate their self-assembly. We used colloidal spheres, consisting of poly(methyl methacrylate) (PMMA) dispersed in a mixture of *cis*-decahydronaphthalene (*cis*-decalin) in cyclohexyl bromide (CHB) saturated with the salt tetrabutylammonium bromide (TBAB). We also used rod-like silica particle which were dispersed in either a mixture of glycerol and water, a mixture of dimethylsulfoxide (DMSO) and water or in pure (de-ionized) cyclohexyl chloride (CHC). We discuss the methods used to manipulate the electric screening length of the particles in these different mixtures, which we tuned from ~ 20 nm to ~ 10 μm. We then describe the basics of confocal microscopy imaging and the effect of the point spread function (PSF) on the imaging of rod-like particles. We also discuss the deconvolution method that we applied to suppress the effect of the PSF as much as possible. We end this chapter with preliminary results on stimulated emission depletion (STED) imaging of rods which were coated with a thin (~ 30 nm) fluorescein isothiocyanate (FITC) shell.

2.1. INTRODUCTION

In this thesis, we present results on the self-assembly process of both colloidal spheres and rods. The colloidal spheres consisted of poly(methyl methacrylate) (PMMA) dispersed in a mixture of *cis*-decahydronaphthalene (*cis*-decalin) in cyclohexyl bromide (CHB) saturated with the salt tetrabutylammonium bromide (TBAB). The rod-like particles consisted of silica and were dispersed in either polar or low-polar solvents. The polar solvents consisted of mixtures of glycerol and water or dimethylsulfoxide (DMSO) and water. The low-polar solvent that we used was cyclohexyl chloride (CHC). Because the uncoated particles were not stable in low-polar solvents, they were first coated with octadecyltrimethoxysilane (OTMOS). Both the spheres and rods were fluorescently labelled and (nearly) index matched, to allow for observation with a confocal microscope. This enabled us to acquire images in 3D, up to approximately 100 micrometer into the sample. We performed image analysis on the confocal microscopy images to investigate the self-assembly process in-situ and on the (single) particle level. Furthermore, we manipulated and directed the self-assembly process by application of external fields such as gravity, shear, and electric fields.

In this chapter we describe the main properties of the suspensions and the general methods that were used in the work presented in this thesis. We first describe the properties of the solvents. We then briefly describe the particle synthesis and the general particle properties. Next, we describe the basic principles of confocal laser scanning microscopy and image formation. This is followed by explanation of image deconvolution. Finally, we also briefly explain the principles of stimulated emission depletion (STED) microscopy and show preliminary STED images of fluorescent silica rods.

2.2. SOLVENT PROPERTIES

2.2.1. Low-polar Solvents

The spherical poly(methyl methacrylate) (PMMA) particles used in this work were always dispersed in a low-polar solvent mixture of approximately 27 wt% cis-decalin in CHB, see Table 2.1. This mixture not only matches the refractive index of the PMMA particles ($n_D^{25} = 1.492$), it also nearly matches their mass-density ($\rho = 1.19$ g/ml), making it an ideal model system. The silica particles are not directly stable in low-polar solvents. However, they can be made stable by coating them with e.g. 3-(trimethoxysilyl)propyl methacrylate (TPM) and a steric stabilizer or with octodecyltrimethoxysilane (OTMOS), which is described in more detail in Chapter 8. We used cyclohexylchloride (CHC) as dispersing solvent for these particles, as the refractive index is close to that of the silica particles ($n_D^{25} = 1.45$).

2.2.2. Polar Solvents

Silica rods without a surface modification were dispersed in mixtures of glycerol and water or dimethylsulfoxide (DMSO) and water. General properties of these polar solvents are listed in Table 2.2. Values from the literature are indicated in the table,

	ρ (g/ml)	n_D	η (cP)	ϵ_r (25°C)
CHB	1.3215 (25 °C) [64]	1.49345 (25°C) [64]	2.00 (25°C) [64]	7.92 [64]
cis-decalin	0.8968 (25 °C) [65]	1.4793 (25°C) [66]	3.355 (20°C) [65]	2.2102 [67]
27 wt% cis-decalin/CHB	1.1702 (21°C) [68]	1.4876 (25°C) [66]	2.726 (21°C) [68]	5.6205 [66]
CHC	0.993 (25°C) [69]	1.46265 (20°C) [70]	1.5675 (25°C) [69]	7.6 [71]

TABLE 2.1. Properties of the low-polar solvents used in this thesis. Here, ρ is the density, n_D the refractive index, η the absolute viscosity and ϵ_r the relative permittivity. All values were obtained from the literature.

measured values of the viscosity were obtained with a SV10 viscometer (A&D Company) and measured values of the refractive index were obtained with a refractometer (Atago 3T). The compositions of the DMSO/water and glycerol/water mixtures were chosen to (nearly) index-match the silica rods, which have a refractive index of $n_D^{25} = 1.45$ [72]. This enabled imaging deep into the sample and also minimized Van der Waals attractions between the particles. The glycerol/water mixture was used for its high viscosity, which slows down the dynamics of the particles enough to measure with 3D confocal microscopy e.g. dynamical properties of the rods (see Chapter 4) or the complete sedimentation profile of the rods (see Chapter 6).

	ρ (g/ml) (25°C)	n_D	η (cP)	ϵ_r
DMSO	1.096 [73]	1.477 (25°C) [73]	1.99 (25°C) [73]	48.4 (25°C) [74]
glycerol	1.258 [75]	1.474 (20°C) [75]	1410 (20°C) [75]	41.1 (20°C) [76]
93 wt% DMSO/water	1.096 * [73]	1.472 (20°C)	2.6 (22°C)	50.9 * (25°C) [74]
85 wt% glycerol/water	1.219 [75]	1.452 (20°C)	92 (22°C)	54.7 * (20°C) [76]

TABLE 2.2. Properties of the polar solvent (mixtures) used in this thesis, with ρ the density, n_D the refractive index, η the absolute viscosity and ϵ_r the relative permittivity. References are shown for values obtained from the literature. Values marked with an asterisk (*) are obtained from linear interpolation of literature values.

2.2.3. Electric conductivity & the Debye screening length

When the silica rods are dispersed in polar solvents, they acquire a negative surface charge due to dissociation of terminal silanol groups. In Chapter 8 we demonstrate that the OTMOS coated silica rods, dispersed in de-ionized CHC, also have a negative surface charge. On the other hand, the PMMA spheres are known to acquire a positive charge when they are dispersed in CHB/decalin. However, at sufficiently high concentration of added tetrabutylammonium bromide (TBAB) salt, the charge reverses from positive to negative, probably due to specific adsorption of ions [66, 77]. The length scale over which these surface charges on the particles are screened is known as the Debye screening length κ^{-1} and sets the typical interaction length-scale in the system. For monovalent ions, the Debye screening length is given by

$$\kappa^{-1} = \sqrt{\frac{\epsilon_r\, \epsilon_0\, k_B T}{2\, N_A\, c\, e^2}}, \tag{2.1}$$

with ϵ_r the dielectric constant of the solvent, ϵ_0 the permittivity of vacuum, N_A the Avogadro constant, c the concentration of ions in the suspension and e the elementary charge. The Debye screening length is thus directly related to the ionic strength of the suspension. The ionic strength can originate from trace ions in the solvents, however, it can also be controlled by adding a known amount of salt to the solvent. In the latter case, the degree of dissociation must be known to directly calculate the Debye screening length. Fortunately, the ionic strength (and the amount of salt dissociation) can be estimated from conductivity measurements of the solvent mixture. The concentration of dissociated ions c, is related to the conductivity via the equation:

$$c = \frac{\sigma}{\Lambda_0}. \tag{2.2}$$

Here, σ is the measured conductivity (in S/m) and Λ_0 the limiting molar conductance of the electrolyte at infinite dilution (in m^2 S/mol). The limiting molar conductances of ionic species are often only known for water and a few other solvents. Therefore, a useful empirical relationship is Walden's rule, which states that the product of the viscosity and the equivalent molar conductance at infinite dilution is a constant for the same species in different solvents [78]:

$$\Lambda_0^{\mathrm{A}}\, \eta_0^{\mathrm{A}} = \Lambda_0^{\mathrm{B}}\, \eta_0^{\mathrm{B}}. \tag{2.3}$$

The mixtures of cis-decalin/CHB (see Table 2.1) described in this thesis, were always saturated with the oil soluble salt TBAB to screen the charges on the PMMA spheres to a maximum extent, resulting in hard-sphere like behaviour [12]. The saturation concentration of this salt in cis-decalin/CHB is approximately 260 μM, with a degree of dissociation $< 2\%$, resulting in a screening length of $\kappa^{-1} \simeq 130$ nm [66, 68].

For the silica rods dispersed in CHC however, much larger screening lengths were desired. Therefore, the as received CHC (with conductivity $\sigma \gg 1000$ pS/cm) was deionized as follows. First, ~ 3 g of activated alumina was added to 50 ml of CHC and left overnight on a roller-bench. The alumina was then removed by centrifugation. Next, ~ 3 g of molecular sieves with pore size of 4 Å were added and left in contact with the solvent for at least 4 hours. The resulting conductivity of the solvent was as low as 10 pS/cm, as measured with a Scientifica model 627 conductivity meter. To estimate the screening length, we used literature values for the limiting equivalent conductance of HCl in ethanol, $\Lambda_0^{\mathrm{HCl}} = 84.3\ \mathrm{S\,cm^2/mol}$ [79], for the viscosity of ethanol $\eta_0^{\mathrm{EtOH}} = 1.08$ cP [79] and for the viscosity of CHC $\eta_0^{\mathrm{CHC}} = 1.57$ cP [69]. Using equations (2.1)-(2.3), this resulted in screening length $\kappa^{-1} \simeq 7$ μm.

Finally, we estimate the screening length for the silica rods dispersed in a mixture of 85 wt% glycerol/water and 93 wt% DMSO/water. In these polar solvent mixtures, the ionic strength was controlled by trace ions in the solvent. Although the identity of the trace ions is not known, we can make a rough estimate of the screening length by again using the limiting molar conductance of HCl in ethanol $\Lambda_0^{\mathrm{HCl}} = 84.3\ \mathrm{S\,cm^2/mol}$ [79], and the viscosity of ethanol $\eta_0^{\mathrm{EtOH}} = 1.08$ cP [79], together with the values of the viscosities and the dielectric constants of the two mixtures (see Table 2.2). We measured the conductivity of both mixtures with a CDM 230 conductivity meter (Radiometer Analytical). For the 85 wt% glycerol/water mixture we measured a conductivity $\sigma = 0.16\ \mu\mathrm{S/cm}$, resulting in a screening length $\kappa^{-1} \simeq 20$ nm. For the 93 wt% DMSO/water mixture these values were $\sigma = 0.71\ \mu\mathrm{S/cm}$ and $\kappa^{-1} \simeq 54$ nm.

2.3. Spherical particles

The poly(methyl methacrylate) (PMMA) spheres described in this thesis were synthesized using a dispersion polymerisation method reported by Bosma *et al.* [80]. The particles were sterically stabilized with poly(12-hydroxystearic acid) grafted onto a PMMA backbone which was chemically attached to the particles. Additionally, the particles were covalently labeled with fluorescent dye for imaging. Two types of fluorescent dye were used: rhodamine isothiocyanate-aminostyrene (RAS) and 4-methylaminoethylmethacrylate-7-nitrobenzo-2-oxa-1,3-diazol (NBD-MAEM), which are chemical derivatives of rhodamine isothiocyanate (RITC) and 4-chloro-7-nitrobenzo-2-oxa-1,3-diazol (NBD-Cl) respectively. This resulted in homogeneously fluorescent particles, as shown by the confocal microscopy images in Fig. 2.1. The size and polydispersity of the particles was determined by static light scattering (SLS). A list of PMMA particles used in the experiments presented in this thesis is given in Table 2.3.

As described in the previous section, the PMMA spheres were dispersed in a solvent mixture of cis-decalin/CHB saturated with TBAB. The high salt concentration screens the charges on the particles, making them behave approximately as hard spheres [12]. However, due to the non-zero screening length and due to the fact that the particles absorb some of the CHB, causing them to swell, their diameter determined from SLS (where the particles were dispersed in hexane) cannot be used to directly determine a hard-sphere volume fraction, which is the single parameter governing the phase behaviour of ideal hard-sphere particles [8]. However, many studies have shown that using an effective diameter, the phase behaviour of these particles can be successfully mapped onto the hard-sphere phase diagram, provided that κd is not too small [12,81].

2.4. Rod-like particles

2.4.1. Synthesis of particle cores

Fluorescent silica rods were prepared following the method of Kuijk *et al.* [25, 72]. Specific details of the synthesis (and adaptations to the procedure) can be found in Chapter 6. Here, we describe a general outline of the method. First, a water in pentanol emulsion (containing also ethanol) is produced using polyvinylpyrrolidone (PVP) and sodium citrate-dihydrate as stabilizers. Next, the silica precursor tetraethyl orthosilicate (TEOS) is added, together with ammonia, which acts as a catalyst. Hydrolysis and subsequent condensation of the TEOS takes place inside the water rich emulsion

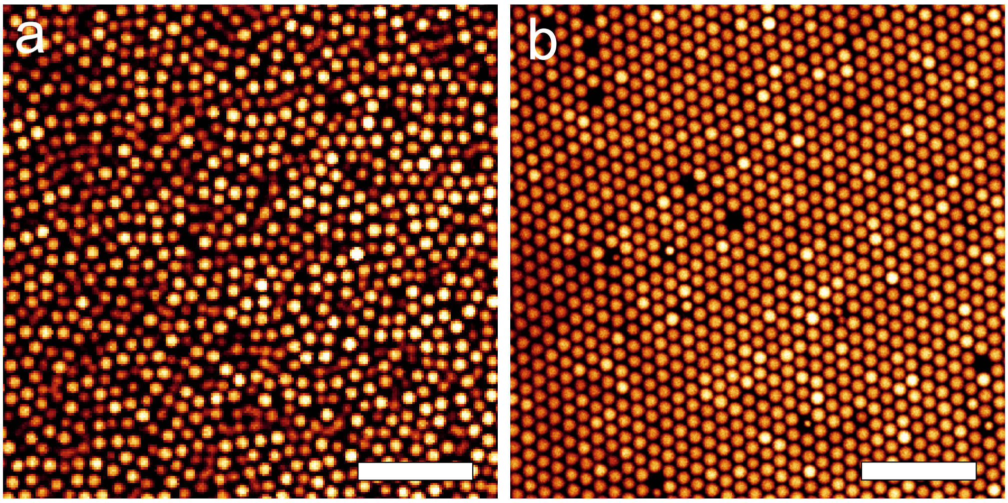

Figure 2.1. Confocal microscopy images of poly(methyl methacrylate) (PMMA) spheres with diameter $d = 2.07$ μm (JSPMR64), dispersed in 26 wt% cis-decalin in CHB. Depending on the (effective) volume fraction ϕ, particles were in (a) a fluid-like phase and (b) a close-packed crystalline phase. The scale bars are 15 μm.

	d (nm)	δ (%)	dye
JSPMR63	2100	3	RAS
JSPMR64	2070	3	RAS
JSPMR35	2640	2.5	RAS
JSPMN16	1040	3	NBD-MAEM

Table 2.3. Properties of the poly(methyl methacrylate) (PMMA) spheres used in this thesis. Here, d is the diameter of the particle and δ the polydispersity (standard deviation over the mean), determined from static light scattering (SLS) measurement. The particles were dispersed in an index and density matching mixture of cis-decalin/CHB, see Table 2.1.

droplets. The growing silica nucleus is positioned at, or close to, the droplet surface, resulting in an anisotropic supply of reactants (from inside the droplet). This in turn results in the growth of a rod-like particle with the droplet attached to one end of the particle, where subsequent growth takes place. The growth of the particle stops when all TEOS has reacted, which is typically after 24 hours. Afterwards, the particles are washed with water and ethanol by centrifugation.

The diameter of the particle is thus determined by the size of the droplet, which, given the right reagent concentrations, remains constant due to surface tension. This results in straight particles with a constant diameter, however, the particles are not completely up-down symmetric. The 'tail' of the particle (where the droplet was attached) is flat, whereas the 'head' is a hemispherical cap. Therefore, these particles are also referred to as silica bullets instead of silica rods. Nearly all reagent concentrations can influence the final geometry of the particles obtained, even resulting in spherical particles or curly rods. For a complete overview of the dependence of reagent concentrations on particle shape and dimensions, see the Supporting Information of Ref. 25.

The above described synthesis procedure typically results in rods with a broad size distribution. The size distribution can however be narrowed by repeated centrifugation and sedimentation steps, resulting in polydispersity values (standard deviation over the mean) for both diameter and length $\lesssim 10\%$.

2.4.2. Fluorescent labelling & shell coating

To fluorescently label the rods, we followed the procedures described in Ref. 72. We used two methods to label the rods: the first resulted in a gradient in fluorescent intensity along the main axis of the particle core, the second method resulted in a uniform fluorescent shell around the core. We either used fluorescein isothiocyanate (FITC) or rhodamine isothiocyanate (RITC), which have an excitation maximum around 488 nm and 543 nm respectively. Both dyes were covalently bonded to the silica surface with the silane coupling agent (3-aminopropyl)triethoxysilane (APS).

To obtain particles with a fluorescent gradient along their main axis, a dye-APS mixture was added during the rod synthesis, directly after addition of the TEOS. Because the availability of dye is higher during the beginning of the rod-growth, this method resulted in a gradient of dye molecules along the rod axis, see Figs. 2.2a-b. Fig. 2.2a shows particles with aspect ratio $l/d = 5.0$, dispersed in 93% DMSO in water and Fig. 2.2b shows particles with aspect ratio $l/d = 7.8$, dispersed in 85% glycerol in water.

To label the particles with a fluorescent shell, a silica shell was grown around the as prepared particle cores using a standard Stöber growth process [72]. Again, the dye-APS mixture was added directly after addition of TEOS. This procedure resulted in a homogeneous fluorescent shell of 30 - 60 nm thickness, see Figs. 2.2c-d. Fig. 2.2c shows silica rods with aspect ratio $l/d = 3.8$, dispersed in CHC whereas Fig. 2.2d shows silica rods with aspect ratio $l/d = 6.0$, dispersed in 85 wt% glycerol in water. The individual fluorescent shells of the particles in Fig. 2.2c are not visible due to the low magnification and the fact that the resolution of the microscope is on the order of the diameter of the non-fluorescent core. The (small) refractive index mismatch between the particles ($n_D^{25} = 1.45$) and the dispersing solvent (CHC, $n_D^{20} = 1.46$) further reduces the resolution (see Section 2.5.3). Fig. 2.2d shows a super-resolution image (see Section 2.5.6) of carefully index-matched particles close to the bottom of the sample, clearly showing the thin (~ 30 nm) fluorescent shell of the particles.

Because we wanted to resolve individual particles with confocal microscopy, even when the concentration was high, non-fluorescent silica shells were grown around the particles using the same procedure as described above but without the addition of dye. The thickness of the shell depended on the particle dimensions and TEOS concentration, but was usually between 30 - 60 nm. The shell growth step was repeated several times until the desired thickness was reached.

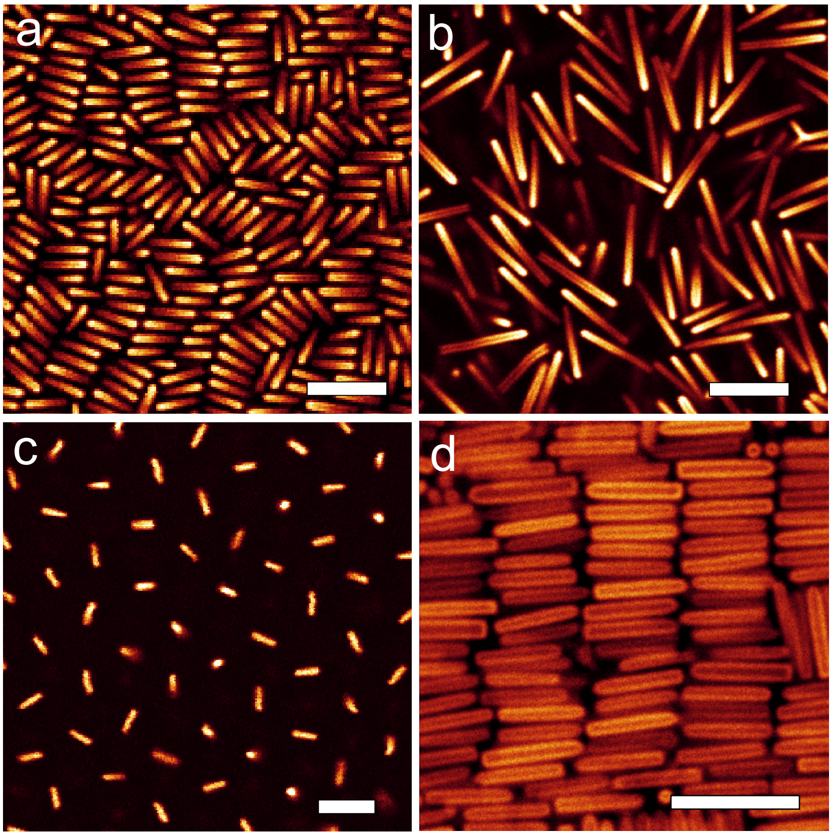

Figure 2.2. Confocal microscopy images of various fluorescently labelled silica rods. (a-b) Due to addition of dye during the rod-growth, particles had a gradient of fluorescence along their main axis. (c-d) Particles coated with a uniform fluorescent shell of $\sim$ 30 nm. (a) $l/d = 5.0$. (N51). Dispersed in DMSO/water. (b) $l/d = 7.8$ (THB5). Dispersed in glycerol/water. (c) $l/d = 3.8$ (R2). Dispersed in CHC. (d) $l/d = 6.0$. (B35) Dispersed in glycerol/water. Additional properties of the particle systems are listed in Table 2.4. All scale bars are 5 μm.

Table 2.4 lists the dimensions and fluorescent properties of the silica rods described in this thesis. Besides the dimensions of the particles, determined from transmission electron microscopy (TEM), Table 2.4 also lists the type and method of dye incorporation: ‘shell’ refers to a uniform fluorescent shell whereas ‘core’ refers to a gradient of fluorescence intensity along the core of the rod. The thickness of the non-fluorescent (NF) outer shell is indicated in the last column.

	l (μm)	δ_l (%)	d (μm)	δ_d (%)	l/d	dye	NF shell (nm)
R2	2.29	6	0.60	6.5	3.8	FITC shell	100
B31	2.4	10	0.64	8	3.8	FITC shell	190
B48	2.6	9	0.63	6	4.1	RITC core	175
N51	2.66	10	0.53	6	5.0	RITC core	150
CT1	3.4	12	0.63	7	5.4	FITC shell	137
B35	3.3	10	0.55	11	6.0	FITC shell	105
THB4	4.3	12	0.59	12	7.3	FITC core	76
THB5	5.2	11	0.67	8	7.8	FITC core	145
TH6	10.0	7	0.49	10	20.4	none	none

Table 2.4. Properties of the silica rods used in this thesis. Here, l is the end-to-end length, d is the diameter, δ_i the polydispersities and l/d the end-to-end aspect ratio, determined from transmission electron microscopy (TEM). Also listed is the type and method of dye incorporation: 'shell' refers to a uniform fluorescent shell whereas 'core' refers to a gradient of fluorescence intensity along the core of the rod. The last column lists the thickness of the outer non-fluorescent (NF) shell.

2.5. Microscopy Imaging

2.5.1. Colloids and microscopy

Systems of colloidal particles are widely used as model systems to study diverse fundamental problems in condensed matter physics regarding for instance crystallization, flow-induced behaviour and the glass transition [12, 47, 48, 56, 58–60, 82]. A key element of these systems is that the individual particles are large enough to be resolved with a microscope yet small enough to still perform significant Brownian motion. This allows for real-space and real-time investigation of structures that have a well defined thermodynamic equilibrium ground state. Using index-matched and fluorescently labelled particles, samples can even be imaged deep in the bulk of the sample (avoiding confinement or wall effects) and in three dimensions, using confocal laser scanning microscopy.

In this section we first describe some basic principles of microscopy imaging in general, followed by the principles of confocal microscopy and image formation. We end this section with an example of super-resolution imaging of a colloidal suspension.

2.5.2. The Point Spread Function

The intensity distribution of an ideal point source imaged with a light microscope is spread out in all three spatial dimensions, known as the point spread function (PSF). An object that is imaged with a microscope is therefore always a convolution of the object function $f_0(x, y, z)$ and the point spread function $PSF(x, y, z)$, together with added noise ξ:

$$f(x, y, z) = f_0(x, y, z) \circledast PSF(x, y, z) + \xi. \tag{2.4}$$

Here, $\circledast$ denotes a convolution. In the lateral direction, the PSF is described by the Airy function [83]

$$I_{xy} = I_0 \left(\frac{2J_1(k)}{k} \right)^2, \tag{2.5}$$

with J_1 a Bessel function of the first kind, $k = 2\pi r\,\mathrm{NA}/\lambda$, with r the distance from the center point, NA the numerical aperture of the objective and λ the wavelength of the light, see also Figs. 2.3a-b. The area within its first minimum is known as the Airy disk, with its radius given by

$$r_{\mathrm{Airy}} = 0.61\,\frac{\lambda}{\mathrm{NA}}. \tag{2.6}$$

The Rayleigh criterion states that to resolve two points, their intensity maxima should be separated by at least the radius of their Airy disks. Equation (2.6) is therefore a direct measure of the (diffraction limited) resolution of a microscope. Substituting in equation (2.6) for a wavelength $\lambda = 488$ nm and numerical aperture $\mathrm{NA} = 1.4$, we obtain $r_{\mathrm{airy}} = 213$ nm.

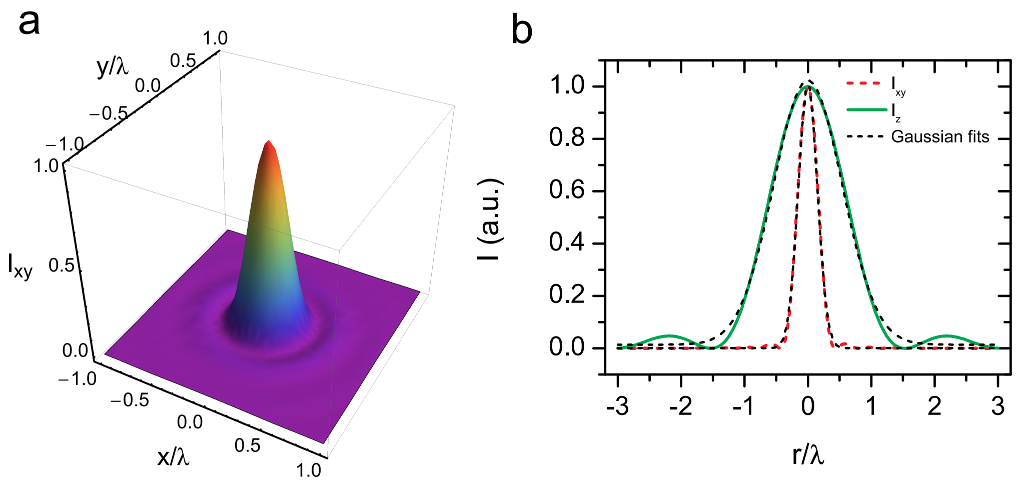

Figure 2.3. The microscope response function or point spread function (PSF). (a) The lateral intensity distribution I_{xy} of an idealized point source, is given by the Airy function. (b) Intensity distribution in the lateral direction (I_{xy}, red), and in the axial direction (I_z, green) as a function of distance from the center r/λ. Here, λ denotes the wavelength of the light. The black dashed lines are Gaussian fits.

In the *axial* direction, the intensity distribution of an ideal PSF can be modelled by the following response function [83]

$$I_z = \left(\frac{\sin(u/4)}{(u/4)} \right)^2 . \tag{2.7}$$

With, $u = 2\pi \, \mathrm{NA}^2 \, z/(\lambda \, n)$, z the distance along the optical axis and n the refractive index of the sample, see Fig. 2.3b. The distance to the first minimum is in this case given by

$$z = 2 \, \lambda \, n/\mathrm{NA}^2 . \tag{2.8}$$

Substituting for $\lambda = 488$ nm, numerical aperture $\mathrm{NA} = 1.4$, and refractive index $n = 1.5$, gives an axial resolution of 747 nm, which is 3.5 times larger than in the lateral direction.

The dashed lines in Fig. 2.3b indicate that the PSF can be well approximated with Gaussian functions with the full width at half maximum (FWHM) approximately 3 times larger in the axial (I_z) than in the lateral direction (I_{xy}). Because Gaussian functions are computationally much less expensive to use compared to equations (2.5) and (2.7), we will use them to approximate the PSF when generating confocal-like test data, as explained in Section 2.5.4.

2.5.3. Confocal laser scanning microscopy

Confocal laser scanning microscopy (CLSM) is a technique that is widely used in scientific fields such as soft condensed matter physics, material science, and cell biology. The two key features of a scanning confocal microscope are the point-by-point illumination of the sample and rejection of out of focus light [84]. Confocal microscopy originates from the patent by Marvin Minksy in 1957 [85] and was further developed in the 1980s in several European laboratories with the introduction of a laser as light source combined with a stage-scanner [84, 86, 87]. A schematic overview of a modern confocal laser scanning microscope is shown in Fig. 2.4a.

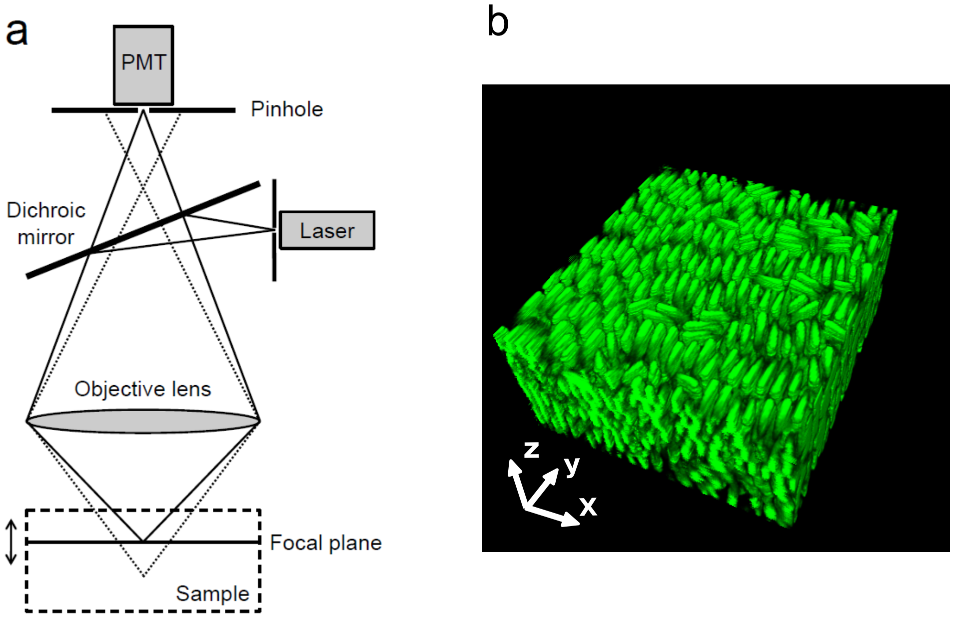

Figure 2.4. Microscopy imaging using a confocal microscope. (a) Schematic of a confocal laser scanning microscope. (b) 3D image stack ($32 \times 32 \times 9$ μm^3) of fluorescent rod-like particles (N51).

Point illumination is achieved by a pinhole that is placed in front of the laser excitation source, combined with the use of a high aperture objective lens, which serves as both the objective and condenser lens. When the fluorescent sample is excited, emitted light passes the dichroic mirror and reaches the detector, which can be a charge-coupled device (CCD), a photomultiplier tube (PMT), a photodiode or a combination of these [84]. Out-of-focus emission light is rejected by a pinhole placed in the *con*jugate *focal* plane of the sample, hence the name confocal. Point-by-point illumination is achieved by scanning a 2D plane e.g. with rotating mirrors placed in the beam path or by moving the sample. The point illumination combined with rejection of out-of-focus light results in a higher resolution as compared to conventional light microscopy. Due to the presence of two apertures, the PSF of a confocal microscope is a convolution of the illumination PSF and the detection PSF [88]

$$PSF_{\mathrm{conf}}(x, y, z) = PSF_{\mathrm{ill}}(x, y, z) \circledast PSF_{\mathrm{det}}(x, y, z), \tag{2.9}$$

which results in a focus spot-size that in theory is reduced by a factor $\sim \sqrt{2}$ compared to conventional light microscopy [84]. For an excitation wavelength $\lambda = 488$ nm and an oil-immersion objective with numerical aperture NA $= 1.4$, this results in a lateral resolution of 150 nm and axial resolution of 532 nm. However, the improvement by a factor of $\sqrt{2}$ is in practice hampered due to the finite detector (pinhole) size, resulting in a typical confocal resolution in the lateral direction of $\sim$ 200 nm [83, 88, 89]. The high axial resolution, however, allows for acquisition of thin 2D optical sections of the sample. A collection of 2D sections can be acquired at varying depth in the sample, by either moving the objective or by moving the sample in the vertical direction, resulting in a 3D image stack of the sample. Fig. 2.4b shows an example of a 3D image stack of fluorescent silica rods, with dimensions $32 \times 32 \times 9$ μm^3 and voxel-size 128 nm in xy and 103 nm in z, acquired with a Leica SP2 confocal microscope using a 488 nm laser and 100×/1.4 oil-immersion objective. In Chapter 4 we describe in detail a new algorithm to identify the positions and orientations of the rods in such a 3D confocal microscopy image stack of densely packed particles.

Although simple geometrical formulae exist for the expression of the resolution of a (confocal) microscope, a much more accurate method is via calculation of the PSF taking into account the vectorial properties of light and electromagnetic diffraction theory [88, 90]. This method allows for taking important microscopic parameters into account such as the finite size of the detector pinhole, the use of high aperture objectives and the often encountered refractive index mismatch between sample and immersion fluid. The later phenomenon is known to have a detrimental effect on the performance of the imaging system [88]. A refractive-index mismatch present between sample and immersion fluid deteriorates the PSF, which becomes progressively worse as a function of axial distance from the coverslip, and it also introduces an intensity fall-off with height and distorts axial distances [88]. Hell *et al.* showed that for a sample with refractive index $n_D = 1.47$ (which is close to the silica suspensions used in this thesis), excited with wavelength around 500 nm and observed with an oil-immersion objective with NA = 1.3, the axial resolution decreases by a factor of 1.2 per 10 μm, the intensity decreases by 30% per 10 μm and the axial distances are elongated by 4% [88]. The axial resolution 50 μm deep in a sample with refractive index $n_D = 1.47$ is therefore 2.5 times larger ($\sim$ 1250 nm) compared to an index-matched system. Fortunately, glycerol-objectives, optimized for samples with refractive index $n_D \sim 1.45$ do not suffer from such strong distortions and, additionally often have a longer working distance than an oil-immersion objective [91].

In Chapter 3 we will demonstrate the experimental measurement of the PSF of a point-scanning confocal microscope (Leica SP8) using an index matched sample, for λ = 488 nm and a 100×/1.4 oil immersion objective, resulting in resolutions of 190 nm in the lateral and 490 nm in the axial direction. We also present detailed measurements of the dependence of the refractive index mismatch on the scaling of axial distances.

2.5.4. The effect of the PSF on particle imaging

The rod-like particles studied in this thesis have a fluorescent diameter of typically 200 - 300 nm, which is *smaller* than the resolution of a confocal microscope in the axial direction (see Section 2.5.3). Because the PSF is anisotropic, this can result in a (strongly) distorted particle shape. To investigate the effect of the PSF on particle imaging, we created computer-generated confocal-like images with a theoretically approximated PSF and noise. These images can be compared to existing confocal microscopy images obtained from experiment or they can be used as test data for real-space particle tracking.

We now briefly explain the generation of test-images, for a more detailed description see Chapter 4. First, 3D coordinate sets of a specific configuration of rods were generated, with a line segment parallel to the main axis of the rod representing the particle. Next, all points closer than half the diameter of the line segment are given an intensity value of 0.95 (with the range of intensities between 0 and 1). The effect of the PSF was approximated by convolving these objects with a Gaussian kernel with a standard deviation $\sigma_x/d = \sigma_y/d = 0.1 - 0.3$ and $\sigma_z/d = 0.3 - 0.9$ with d the diameter of the particle. Besides a theoretical approximation of the PSF, we also added artificial noise to the images. Although noise from modern detectors is essentially photon-limited, suggesting a Poisson distribution [92], we added noise to each pixel in our images with a simple Gaussian distribution with standard deviation $\sigma_n = 0.10 - 0.30$. Finally, we converted all our data with intensity values between 0 and 1 to 8-bit grayscale tiff images.

Fig. 2.5 shows a comparison between computer-generated data and real experimental data. This figure shows three orthogonal views of an experimental (Fig. 2.5a-c) and a

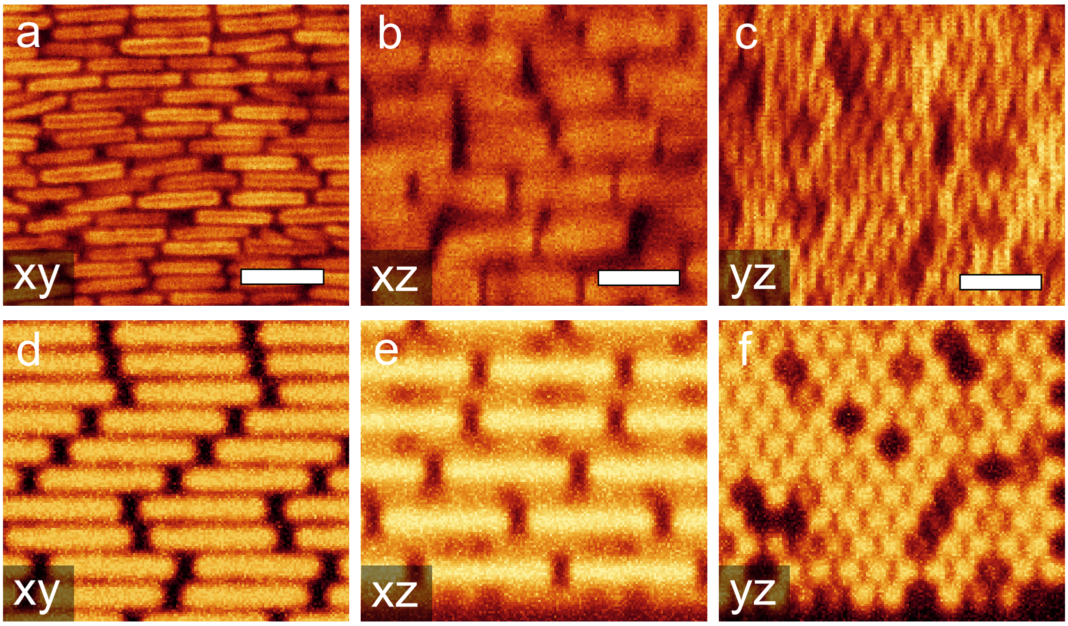

FIGURE 2.5. Effect of a point spread function (PSF) on rod-like particle imaging. (a-c) Confocal microscopy images of rods with length $l = 3.3$ μm, diameter $d = 550$ nm and aspect ratio $l/d = 6.0$ (B35). The rods were ordered into a hexagonal columnar phase. All scale bars are 3 μm. (d-f) Computer generated data of a columnar phase of rods. See text for details on how the data were created. Due to the lower resolution in the z-direction, rods appear larger in the z-direction than in the x- and y-direction. The apparent difference in rod diameter between figures (b) and (c) is because of the hexagonal columnar symmetry only.

computer-generated (Figs. 2.5d-f) hexagonal columnar phase of rod-like particles. The computer-generated images were constructed using a PSF with $\sigma_x/d = \sigma_y/d = 0.15$ and $\sigma_z/d = 0.3$. Gaussian noise was added with $\sigma_n = 0.1$. The effect of the anisotropy of the point spread function in the z-direction compared to the xy-direction is clearly visible (Figs. 2.5b,e), where the diameter of the rods in the xz plane appears broader than in the xy plane (Figs. 2.5a,d). The difference in apparent diameter between Fig. 2.5b and Fig. 2.5c is because of the hexagonal columnar symmetry only, resulting in different inter-particle spacing for different cuts through the sample.

2.5.5. Image Deconvolution

Since the shape of the PSF is known to a large extent *a priori*, it can be used to reverse the convolution process, which is a process known as deconvolution. However, due to the addition of noise (and possibly other image distortions), the effect of the PSF cannot be completely reversed but rather suppressed. Nevertheless, if both the signal-to-noise ratio is high and the sampling frequency is sufficient, deconvolution is capable of not only increasing resolution (especially in the axial direction), but also suppressing noise and enhancing contrast [84]. For a point-scanning fluorescent confocal microscopy setup using a 488 nm laser and an oil-immersion objective ($n_D = 1.515$) with numerical aperture NA $= 1.4$, the ideal Nyquist sampling rate is approximately 43 nm in the lateral (xy) direction and 130 nm in the axial (z) direction [93, 94], i.e. roughly 1/4 of the resolution of the microscope (see Section 2.5.3). Because the noise from modern detectors can be well modelled with a Poisson distribution [92], we use the definition SNR $= \sqrt{n_p}$ with n_p the number of detected photons in the brightest part of the image [95]. Using certain detectors, e.g. an avalanche photodiode (APD), n_p can be directly measured. Using a photo-multiplier tube (PMT), n_p can be estimated by comparing (empty) background parts of the image with a bright (signal) part. See Refs. 96 and 50 for further details and alternative methods. Using the definition SNR $= \sqrt{n_p}$, high quality confocal microscopy images have a SNR $\gtrsim 15$ [96]. All deconvolutions presented in this thesis were performed using commercially available software (Huygens Professional 4.4, Scientific Volume Imaging) using the classic maximum likelihood estimation restoration method [90]. When there was a refractive index-mismatch between immersion fluid and sample, we used a depth dependent theoretical PSF [90]. In other cases, we used a measured PSF, obtained using fluorescent polystyrene spheres as approximate point-sources, which is described in detail in Chapter 3. In Chapter 6 we demonstrate the effect of deconvolution of 3D confocal microscopy image stacks of dense sediments of fluorescent silica rods.

2.5.6. Stimulated Emission Depletion

A well known expression for the diffraction limited resolution of a light microscope was pioneered by Ernst Abbe and is given by the full width at half maximum of the focal spot:

$$\Delta x \approx \frac{\lambda}{2\,n\,\sin\alpha}, \tag{2.10}$$

with λ the wavelength, n the refractive index and α the semi-aperture angle of the objective lens, such that the numerical aperture $\mathrm{NA} = n \sin\alpha$. This expression is similar but slightly different from the later defined criterion by Lord Rayleigh (see equation (2.6)). The last several decades, many techniques have been developed to resolve features that are smaller than the diffraction limit, often referred to as super-resolution techniques. For an extensive overview of super-resolution imaging techniques we refer the reader to Ref. 97. One particular technique that we discus here is known as stimulated emission depletion (STED) [89,98]. A 2D version of this technique works as follows (see also Fig. 2.6). Using an excitation laser (green), a fluorescent sample is excited within a diffraction limited spot. With a second laser (red), that has a higher wavelength than the excitation laser, a helical-vortex phase filter is used to create a doughnut-shaped overlay. This doughnut drives all the fluorophores at the periphery of the focus spot to the ground state via stimulated emission of a lower energy photon. Due to the doughnut shape, the central spot alone is unaffected, which can decay spontaneously.

The resolution (in the lateral direction) of the resulting central focus spot can be expressed as an extension of Abbe's equation [89,98]

$$\Delta x \approx \frac{\lambda}{2\,n\,\sin\alpha\sqrt{1 + I/I_{sat}}}, \tag{2.11}$$

with I the peak intensity of the depletion beam and I_{sat} the intensity required to induce stimulated emission. This results (for biological samples) to typical values for the lateral resolution between 20 and 80 nm. Since the resolution of the axial direction is essentially unaffected to remain $\sim$ 500 nm, this results in a 'cigar-shaped' PSF. However, using an overlay that also extends in the z-direction, known as 3D-STED, axial resolutions down to $\sim$ 100 nm can be achieved [99–101].

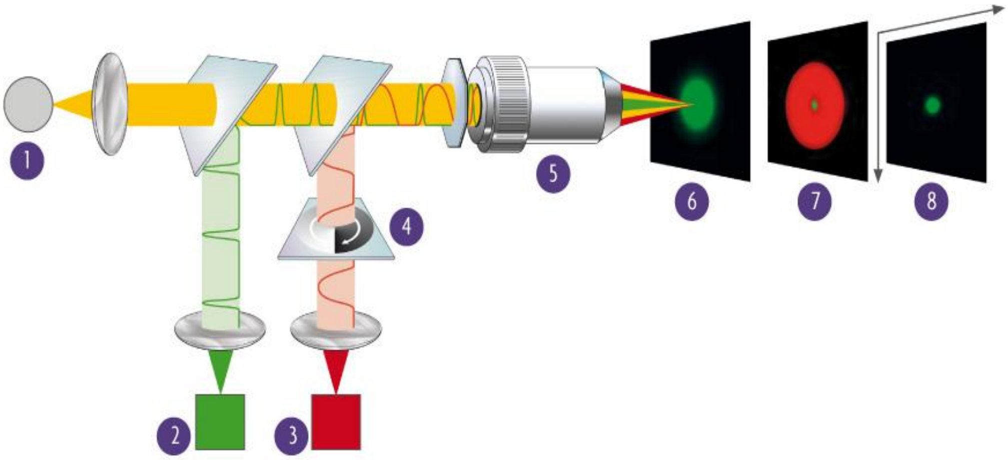

FIGURE 2.6. Schematic of a 2D-STED microscope. (1) Detector. (2) Excitation laser. (3) Depletion laser. (4) Phase filter. (5) STED objective (6) Focused excitation spot. (7) Doughnut overlay. (8) Resulting fluorescence spot. Image courtesy of Leica Microsystems, Germany.

In this thesis, however, we used 2D-STED techniques only. Fig 2.7 shows a comparision between conventional confocal microscopy and STED imaging. STED confocal microscopy images were taken with a Leica TCS SP5 and SP8, equipped with continuous wave (CW)-gated STED [100]. STED was performed in CW-STED mode, using a CW depletion laser at 592 nm wavelength and a pulsed excitation at 488 nm from a white light continuum laser.

Fig. 2.7a shows a 2D slice out of a 3D data set that was taken of a sample of silica rods (B35), dispersed in an index matching DMSO/water mixture after sedimentation, at a packing fraction above 50%. Fig. 2.7b clearly shows the increased resolution when the same particles were imaged in CW-STED mode. As a result of the improved resolution, the fact that the FITC is localized in a very thin (30 nm) shell is much better visible, especially for rods oriented perpendicularly to the imaging plane. The resolution could be even further increased by 3D STED deconvolution (Huygens Professional STED module, Scientific Volume Imaging), see Fig. 2.7c, thereby also significantly reducing background noise and increasing contrast.

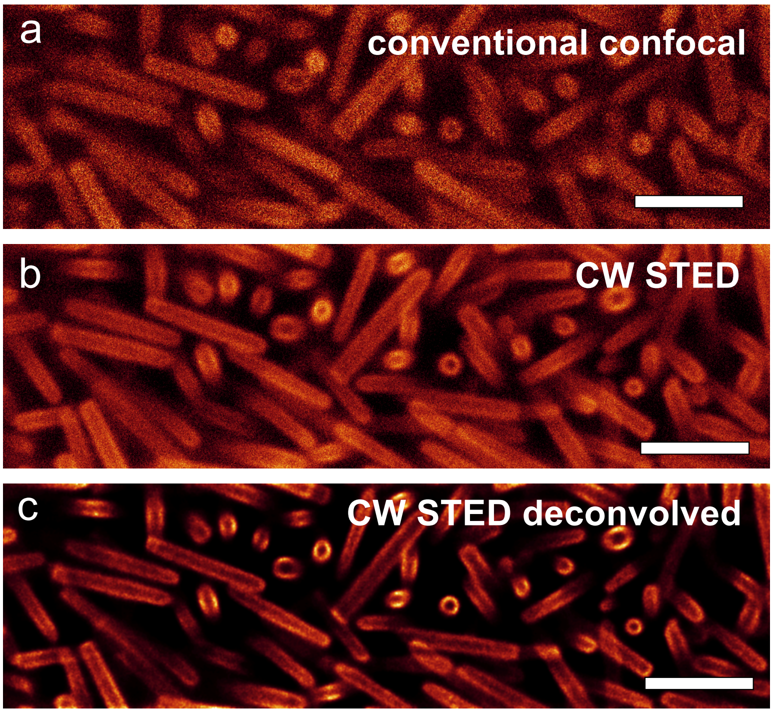

Figure 2.7. Difference between (a) conventional confocal microscopy, and (b) STED confocal microscopy. In (b), the location of the dye in the outer shell is much better visible due to the increased resolution. (c) Further improvement of the resolution by 3D STED deconvolution. Scale bars indicate 3 μm.

2.6. Acknowledgements

We thank Johan Stiefelhagen for synthesis of the PMMA particles and critical reading of this chapter. We also thank Anke Kuijk and Chris Kennedy for synthesis of several of the silica rod systems.

3

Calibration and Scaling of Axial Distances in Confocal Microscopy as a Function of Refractive Index

Abstract

Accurate distance measurement in 3D confocal microscopy is important for quantitative analysis, volume visualization and image restoration. However, axial distances can be distorted by both the point spread function and by a refractive-index mismatch between the sample and immersion liquid, which are difficult to separate. Additionally, accurate calibration of the axial distances in confocal microscopy remains cumbersome, although several high-end methods exist. In this chapter we present two methods to calibrate axial distances in 3D confocal microscopy that are both accurate and easily implemented. With these methods, we measured axial scaling factors as a function of refractive-index mismatch for high-aperture confocal microscopy imaging. We found that our scaling factors are almost completely linearly dependent on refractive index and that they were in good agreement with theoretical predictions that take the full vectorial properties of light into account. There was however a strong deviation from the theoretical predictions using (high-angle) geometrical optics, which predict much lower scaling factors. As an illustration, we measured the point-spread-function of a correctly calibrated point-scanning confocal microscope and showed that a nearly index-matched, micron-sized spherical object is still significantly elongated due to this PSF, which signifies that care has to be taken when determining axial calibration or axial scaling using such particles.

3.1. Introduction

Confocal microscopy is a powerful tool for 3D in-situ measurements of both structure and dynamics for a wide range of scientific disciplines, such as cell-biology, pharmaceutics and materials science [84, 102–104]. However, care has to be taken with 3D measurements because not all three dimensions are effected in the same way by both optics and data acquisition software. The inevitable difference in lateral and axial resolution affects the apparent shape of any (sub)micron-sized feature in a 3D measurement [50]. Furthermore, there is often a refractive index (RI) mismatch between immersion fluid and sample. Not only does the RI-mismatch deteriorate the point spread function (PSF) with increasing focus depth, and therefore the resolution, it also introduces a decrease in intensity and a shift of the objective focus [88, 105–114]. When the refractive index of the sample is smaller than the immersion liquid used for imaging, axial distances appear more elongated due to the refractive effects on the focus position. A clear distinction can be made between studies that analyse these focal shifts with geometrical optics and studies that take the vectorial properties of light into account. On the basis of geometrical optics, axial elongation up to a factor of three times the actual distance has been predicted for high-aperture oil-immersion imaging in aqueous samples [105, 106]. It seems likely however that in the mechanism of the axial shift, paraxial rays dominate over the high-angle rays that are used in the geometrical optics approach [108]. Studies that take the vectorial properties of light into account therefore predict significantly smaller axial elongations [88, 109, 115].

There are however still significant differences between the precise values of the axial scaling factors for different vector-based theories [88, 109, 110, 115] and the amount of experimental studies remains limited [88, 113, 116]. Also, in most experimental studies on axial distance scaling, little attention is devoted to the axial-distance *calibration*, which is indispensable for precise measurements. Calibration of the lateral distances is both straightforward and accurate, e.g. by using a calibration grid. However, accurate calibration of the axial distances in confocal microscopy remains cumbersome, although several high-precision methods exist [117–119].

In this chapter we demonstrate two methods to calibrate axial distances in confocal microscopy that are both accurate and practical to employ. In the first method we use light interference to accurately measure the height of an empty calibration cell. We filled the cell with four different solvents mixed with fluorescent dye, which enabled the determination of the axial scaling factors as a function of refractive index for high-aperture 3D confocal-microscopy imaging with an oil-immersion objective. We also demonstrate a second method to accurately calibrate the confocal microscope, which is with large (~ 50 μm) spherical particles that only have a thin fluorescent shell (compared to their size). Finally, we show with a correctly z-calibrated confocal microscope that spherical objects of a micrometer or smaller are still significantly elongated due to the PSF and possibly also due to a small refractive index mismatch between particle and solvent.

3.2. METHODS

3.2.1. Calibration cell construction and FTIR measurement

To calibrate the axial distances in a point-scanning confocal microscope, we built a custom sample cell with standard glass coverslips (Menzel Gläzer). The glass coverslips had a refractive index ($n_D^{23} = 1.523$) close to the refractive index of the oil-immersion liquid (Type F, Leica, $n_D^{23} = 1.515$) used for imaging. We avoided using glass capillaries (Vitrocom), often used in confocal studies on colloidal systems, since they provide lower quality imaging which is partially due to their manufacturing process and also due to the refractive index ($n_D^{23} = 1.47$). We used a standard No. 1.0 coverslide, which has a thickness between 130 - 160 μm, as specified by the manufacturer (Menzel Gläzer). Although standard confocal microscopy objectives are optimized for a coverslip thickness of 170 μm [84] and therefore a No. 1.5 coverslip (thickness 160 - 190 μm) would have been more accurate, we could not however completely image our cell (with a height $\sim$ 80 μm), due to the limited working distance of the high numerical aperture objectives that we used. As spacers, we used No. 00 coverslips (thickness 55 - 80 μm) and the individual components of the cell were permanently fixed onto a standard microscopy slide (Menzel Gläzer) with UV glue (Norland 68 Optical Adhesive), see Fig. 3.1a. The resulting height of the cell H was measured with a Fourier Transform Infrared (FTIR) spectrometer, with a selected diameter aperture of 0.25 mm (Vertex 70, Bruker). To avoid additional interference effects from the top coverslip itself, a drop of immersion oil was carefully placed on top of the cell before the measurement. The thickness and irregularities of the much thicker microscopy slide ($\sim$ 1 mm) made it not necessary to correct for its interference effects.

3.2.2. 50 μm PMMA spheres

We used large poly(methyl methacrylate) (PMMA) spheres as a second method for calibration. The spheres had an average diameter $\sigma = 50$ μm and large polydispersity ($> 10\%$, Altuglas, BS150N). To fluorescently dye the particles, we first prepared (rhodamine isothiocyanate)-aminostyrene (RAS) dye following the method described by Bosma *et al.* [80]. Then, we saturated a quantity of acetone (99%, Merck) with RAS and subsequently centrifuged the saturated acetone at high speed to sediment undissolved dye. The acetone was then added to dodecane (99%, Sigma-Aldrich) to give a 10 wt% solution of acetone. In this mixture, 50 wt% undyed PMMA particles and 0.35 wt% azo-bis-isobutyronitrile (98%, Acros) were suspended in a glass vial. The reaction mixture was heated up to 83°C and left to react for approximately 1 day. During this reaction, RAS molecules become chemically bonded with unreacted PMMA-ends at the surface of the particle. The vial was left open, so acetone could evaporate. The dyed particles were washed with hexane and dried under vacuum. Afterwards, the particles were suspended in a 24 wt% mixture of cis-decahydronaphthalene (cis-decalin, 99%, Sigma-Aldrich) in cyclohexylbromide (CHB, 98%, Sigma-Aldrich). The refractive index of this mixture was $n_D^{21} = 1.490$, as measured with a refractometer (Atago 3T). This solvent mixture closely matched the refractive index of the particles, based on the fact that the refractive index is close to that of the bulk material ($n_D^{20} = 1.491$ [120]) and that the particles hardly scattered when viewed under bright-field illumination. As a measure of shape uniformity, we determined the ellipticity of a small ensemble of particles suspended in 24 wt% cis-decalin in CHB. To this end, we fitted an ellipse to a binarized confocal microscopy image of the particles' equator using ImageJ software [121]. We measured the aspect ratio $AR = b/a$, with b the major and a the minor axis of the ellipse. For a total of 18 particles we found $AR = 1.016 \pm 0.002$.

3.2.3. Confocal microscopy measurements

The confocal microscopy measurements were all performed with a Leica SP2 or Leica SP8. All distance measurements were performed on 3D image stacks obtained in *xyz*-scanmode. Although a (single) vertical scan obtained in *xzy*-mode is a fast method to view vertical slices through the sample, the obtained distances are in general not accurate and were avoided for any quantitative measurement. Imaging of the empty calibration cell was performed with a 20x/0.7 air-objective (Leica), all other measurements were performed with a 100x/1.4 oil-immersion confocal objective (Leica). The largest measurement error is introduced by the top coverslip being under a small angle with respect to the microscopy glass slide (see Fig. 3.1a), despite careful application of the UV glue. Because we cannot place the sample in exactly the same position after its first measurement, we measured the height gradient in the x- and y-direction and found that the largest slope was 1.9 μm/mm. Assuming that it is possible to place the sample in its original position within 0.3 mm accuracy, a rough estimate of the error on the confocal height measurements is ~ 0.6 μm. We therefore chose our pixel-size in the axial direction to roughly half of this value. For the axial-scaling measurements, we used solvents of increasing RI: immersion oil (Type F, Leica, $n_D^{20} = 1.516$), cyclohexylchloride (CHC, >98%, Merck, $n_D^{20} = 1.463$), dodecane (>99%, Sigma-Aldrich, $n_D^{20} = 1.421$) and de-ionized water (Millipore system, $n_D^{20} = 1.333$). The first three (apolar) solvents were saturated with pyrromethene-567 dye (excitation maximum $\lambda_{max} = 518$ nm, Excition) whereas the water was saturated with fluorescein isothiocyanate (FITC, isomer I, 90%, Sigma-Aldrich). Undissolved dye was removed by centrifugation. Also, a small amount of sterically stabilized PMMA tracer particles [80] (diameter $\sigma = 2.07$ μm, polydispersity 3%), that often stick to untreated glass, was added to the apolar solvents to accurately determine the top and bottom of the cell. Because the volume fraction of the PMMA tracer particles is $\ll 1$ %, their contribution to the effective refractive index of the sample can be neglected. Solvents were removed from the sample cell with nitrogen flow and the cell was flushed three times with the new solvent before the sample was carefully placed on the marked area under the confocal microscope to record a new image-stack. The image-stacks of the calibration cell were all recorded on a Leica SP2 with a 488 nm laser and a scan speed of 1000 Hz. The voxel-size of the image stacks was 293 × 293 × 311 nm^3. The typical total volume of the images stacks was 38 × 38 × 115 μm^3. Images of the large PMMA spheres ($\sigma = 50$ μm) were recorded on a Leica SP8 with a 543 nm laser line, voxel-size 51 × 51 × 168 nm^3 and total volume 52.8 × 52.8 × 54.1 μm^3.

3.2.4. PSF measurement & deconvolution

To suppress the effect of the point-spread-function (PSF), we deconvolved the 3D confocal microscopy data-stacks of the spherical particles. All deconvolutions were performed using commercially available software (Huygens Professional 4.4, Scientific Volume Imaging) using the classic maximum likelihood estimation restoration method [90]. For the deconvolution of the image-stack of the large PMMA sphere ($\sigma = 50$ μm), we used a depth dependent theoretical PSF that takes into account the (small) RI-mismatch between sample and immersion fluid [90]. For the deconvolution of the 200 nm and 1040 nm particles, we used a measured PSF, obtained using fluorescent polystyrene spheres with diameter $\sigma = 200$ nm, polydispersity 5% and excitation maximum $\lambda = 441$ nm (YG Fluoresbrite Microparticles, Polysciences). The polystyrene particles (bulk material $n_D^{20} = 1.592$ [120]) were dried on a cover glass (Menzel Gläzer, No. 1.5) and subsequently a drop of immersion oil (Type F, Leica, $n_D^{20} = 1.516$) was placed on the glass slide to (nearly) index-match the particles. The sample was then placed on a microscopy slide with glass spacers and sealed with UV glue (Norland Optical Adhesive). Images of the beads were recorded with an inverted confocal microscope (Leica SP8) with a 100x/1.4 oil immersion objective (Leica) in combination with a Hybrid detector. To gain enough statistics, confocal image-stacks of 8 different spheres were recorded with (sub)Nyquist sampling rate ($18.2 \times 18.2 \times 83.9$ nm^3). Because these particles are only approximate point-sources, the PSF was obtained by iterative deconvolution with a 200 nm bead object [90]. Additionally, we imaged poly(methyl methacrylate) (PMMA) spheres with diameter $\sigma = 1040$ nm and a polydispersity δ = 3%, as determined with static light scattering (SLS). The particles were sterically stabilized with poly(12-hydroxystearic acid) (PHS) grafted onto the PMMA backbone which was chemically attached to the core of the particles and covalently labelled with fluorescent 4-methylaminoethylmethacrylate-7-nitrobenzo-2-oxa-1,3-diazol (NBD-MAEM) dye for imaging [80]. With the measured PSF, we deconvolved image-stacks of both the fluorescent polystyrene spheres ($\sigma = 200$ nm) and of the larger PMMA spheres ($\sigma = 1040$ nm) that were dried on a glass coverslip (Menzel Glazer, No. 1.5) and subsequently immersed in immersion oil (Type F, Leica). The particles were imaged within one hour of sample preparation. We acquired images stacks with voxel-size $5.4 \times 5.4 \times 41.96$ nm^3 and $18.75 \times 18.75 \times 83.9$ nm^3 respectively, using a 100x/1.4 oil objective and a 488 nm laser-line selected from a white light laser.

3.3. RESULTS

3.3.1. Calibration cell & distance measurements

The sample cell used for calibration is shown in Fig. 3.1a. When placed in a spectrometer, light reflecting from the front and back of the inside of the sample cell resulted in oscillations in the transmission spectrum, known as Fabry Perrot (FP) fringes, and shown in Fig. 3.1b. We determined the height of the cell from the spacing

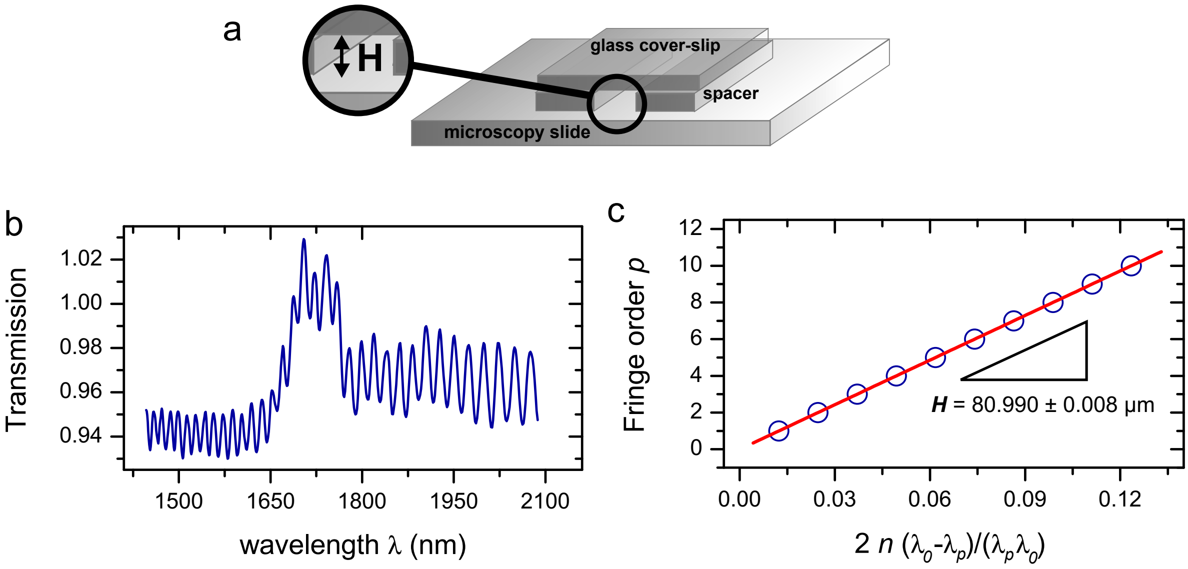

Figure 3.1. Construction and measurement of a calibration cell. (a) A sample cell with height H was built with glass coverslips and a standard microscopy slide, glued together with UV-glue. (b) When the (empty) cell was placed in a Fourier Transform Infrared (FTIR) spectrometer, Fabry Perrot (FP) fringes were visible in the transmission spectrum. (c) The height of the cavity ($H = 80.990 \pm 0.008$ μm) was determined from the spacing between the FP fringes [122]. The error-bars on individual points are smaller than the symbol size.

between the maxima of the FP fringes with the formula [122]

$$H = p\frac{\lambda_p \lambda_0}{2n(\lambda_0 - \lambda_p)}, \tag{3.1}$$

with λ_0 the longest wavelength, p the fringe order of subsequent maxima at wavelength λ_p and n the refractive index of the medium (air). In Fig. 3.1c the fringe order p is plotted as a function of $2n(\lambda_0 - \lambda_p)/\lambda_p\lambda_0$. The slope of the linear fit directly gives the height of the cell $H = 80.990 \pm 0.008$ μm.

In Fig. 3.2a we show a confocal micrograph of the empty calibration cell, imaged in reflection mode with a 20x/0.7 air objective and 488 nm laser. The image clearly shows the reflections at the glass-air interfaces, which we assumed to be positioned at the highest pixel-intensity. We measured the height at the same position as was done with the spectrometer (for four different times), which resulted in a mean value of H $=$ 80.8 ± 0.3 μm. This value is in good agreement with the spectrometer measurement ($H = 80.990 \pm 0.008$ μm) and thus confirms proper calibration of the microscope in the axial direction.

Fig. 3.2b shows the same cell, this time filled with solvents of decreasing refractive index, as indicated in the figure. The tracer particles were used to measure the height of the sample. When the cell was filled with immersion oil (Fig. 3.2b, left) a single value of H $=$ 80.30 μm was obtained. After removal of the oil, the empty cell was measured again with an air objective which resulted in a value of H $=$ 80.92 μm. From these measurements we can conclude that the confocal was accurately calibrated and that filling the cell with solvent did not alter the height significantly.

We also measured the effect of refractive index (RI) on the axial distances, indicated by the intensity profiles shown in Fig. 3.2c. Not only does the (apparent) axial distance change as a function of RI, also the intensity becomes non-linearly dependent on the axial distance, which is described in detail elsewhere [88]. We compared the data obtained from Fig. 3.2c with a theoretical model for the scaling factor of axial distances $h(n, NA)$, based on geometrical optics, given by [105, 106]

$$h(n, NA) = \sqrt{\frac{n^2 - NA^2}{n_{oil}^2 - NA^2}}, \tag{3.2}$$

with n the refractive index of the suspension, $n_{oil} = 1.516$ the refractive index of the oil immersion liquid and NA the numerical aperture of the objective. For low NA-objectives, equation (3.2) simplifies to an expression of the focal shift in the paraxial limit

$$k(n) = \frac{n}{n_{oil}}. \tag{3.3}$$

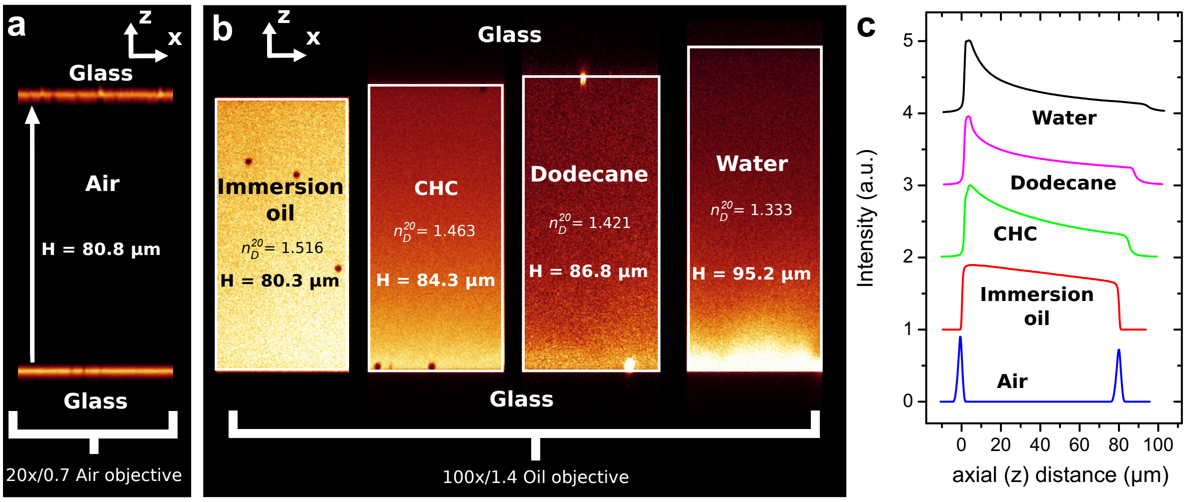

FIGURE 3.2. Axial distances measured with confocal microscopy. (a) The empty calibration cell with $H = 80.990 \pm 0.008$ μm was measured in confocal reflection mode (Leica SP2) with a 20x/0.7 air-objective (Leica), which resulted in $H = 80.8 \pm 0.3$ μm. (b) The cell filled with immersion oil, pyrromethene dye and poly(methyl methacrylate) (PMMA) tracer particles (left). The sample was imaged with an 100x/1.4 oil objective (Leica) and a similar height was measured ($H = 80.3$ μm). However, when the cell was re-filled with solvents that had a refractive index-mismatch with the oil-objective, deviating axial-distances were found, as indicated in the figure. (c) Intensity profiles along the axial (z) direction show the increase in (apparent) axial distance as well as decrease of intensity deeper in the sample. The profiles where normalized and shifted for better visualization.

We also compared our measurement to two theoretical studies that take the full vectorial properties of light into account [88, 109]. A summary of these scaling factors is shown in Fig. 3.3. The (black) circles are our measurement points, which are connected with a linear fit (dashed black line). The (green) continuous and (green) dashed-dotted lines are from the theoretical prediction of equation (3.2), for NA = 0.7 and NA = 1.4 respectively. The (pink) square is based on a theoretical study by Sheppard *et al.* [109] for NA = 1.4 and the (blue) diamonds show calculations based on a study by Hell *et al.* for NA = 1.3 [88], both at a wavelength around 500 nm. The reason for choosing a lower NA in the latter study is that due to total internal reflection at the glass/water interface, a numerical aperture of 1.4 becomes effectively 1.3 [88].
The calculations by Hell *et al.* seem to agree best with our measurements (black circles). It is also clear from Fig. 3.3 that the formula based on geometrical optics (equation 3.2) is highly dependent on NA and that our measurements do not correspond at all with the theoretical predictions for NA = 1.4. This is a confirmation that indeed the paraxial rays dominate the mechanism of axial shift instead of the high-angle rays used in geometrical optics. Interestingly though, if we assume an 'effective NA' of 0.7 (continuous green line), equation (3.2) fits our data remarkably well.

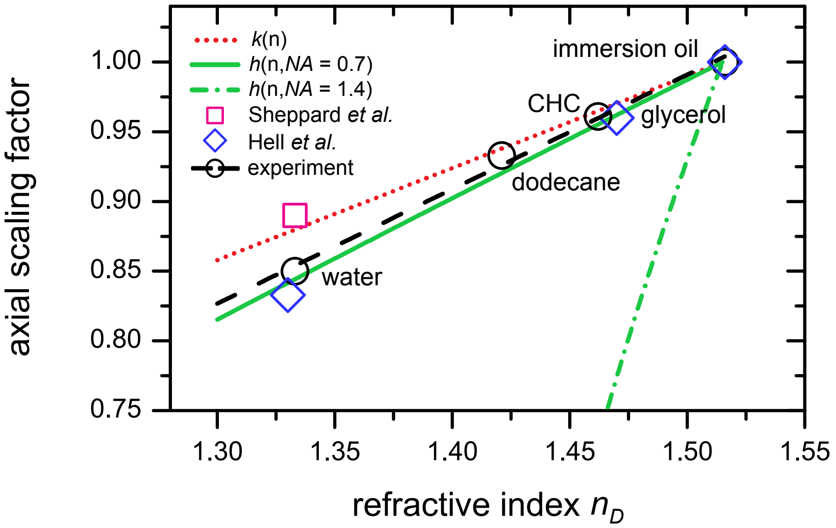

Figure 3.3. Axial scaling factors as a function of the sample refractive index n_D. Our measurements are indicated with black open circles, which were fitted with the dashed (black) line. The (green) continuous and (green) dashed-dotted lines are from the high-angle geometrical prediction of equation (3.2), for NA = 0.7 and NA = 1.4 respectively, and the (red) dotted line is from the paraxial limit of equation (3.3). The (pink) square is based on a theoretical study by Sheppard *et al.* [109] for NA = 1.4 and the (blue) diamonds show calculations based on a study by Hell *et al.* for NA = 1.3 [88], both at a wavelength around 500 nm.

We also measured the axial shift when the calibration cell was filled with CHC and imaged with a 100x oil-immersion objective with variable NA between 0.7 and 1.4 (not shown here). This resulted in an increase in axial distance of 2% from NA = 0.7 to

NA = 1.4, whereas equation (3.2) predicts an increase of 31%. This result is however again in good agreement with the theoretical prediction and experimental measurement reported by Hell *et al.* [88].

From a linear fit to our measurement points, we obtained the empirical formula

$$f(n_D) = 0.82\, n_D - 0.24, \tag{3.4}$$

with the coefficient of correlation $R^2 = 0.993$ indicating a strong linear correlation. This empirical formula could be used to predict (or estimate) the axial scaling factor for 3D images acquired with an oil-immersion objective (NA = 1.4) for any RI between 1.3-1.5.

3.3.2. Calibration with a 50 μm PMMA sphere

As a second method to calibrate the axial distance in a confocal microscope, we exploited the well-defined 3D geometry of large spherical PMMA particles (average diameter $\sigma = 50$ μm and polydispersity larger than 10%), dyed with a thin fluorescent shell ($\sim$ 500 nm). We used these particles to determine the z-calibration of a point-scanning confocal microscope (Leica SP8). We first confirmed correct calibration of the xy-distances of the microscope by imaging a calibration grid (Ted Pella, grid spacing 0.01 mm) in reflection mode using a 100x/1.4 oil immersion objective (Leica). Then we imaged a single particle in 3D using the same objective. Fig. 3.4a shows a 3D image-stack of a particle dispersed in an RI-matching mixture of 24 wt% cis-decalin/CHB. In Fig. 3.4b, a single xy-image shows that the diameter of the particle in the x- and y-direction is equal. However, a reconstructed xz-view of the particle (Fig. 3.4c) shows that there is an elongation in the z-direction. From the intensity profiles, shown in Fig. 3.4d, we determined the diameter of the particle in the x-, y- and z-direction, and found an elongation of 5.8% in the z-direction. We also deconvolved the 3D image stack with a theoretical depth-dependent PSF. The resulting intensity profile in the z-direction is indicated with the (blue) dashed line in Fig. 3.4d. The deconvolution resulted in a decrease of the width of both peaks, however, there was no significant change in the distance between them. Additionally, we acquired images for different scan-speeds and different image-sizes and found similar results. Due to the (small) refractive index mismatch between the suspension ($n_D^{21} = 1.490$) and the immersion oil ($n_D^{20} = 1.516$) we expected, based on equation (3.4), an axial scaling factor in the z-direction of only $f(1.49) = 0.98$. We therefore conclude that there is a small but significant elongation in the z-direction of 3.7%, which is most likely due to an incorrect calibration of the microscope. To confirm this statement, we measured the height of our calibration cell when it was filled with immersion-oil (Fig. 3.2b) with the same microscope and objective as used for the image-stack in Fig. 3.4, and found a distance of $H = 83.4$ μm. This indicated a similar deviation of 3.0% in the axial direction.

Because the calibration of the xy-distances in confocal microscopy is simple and straightforward (e.g. with a calibration grid), the fluorescent PMMA spherical particles described above can be used to measure absolute axial-distance deviations within $\sim$ 2%.

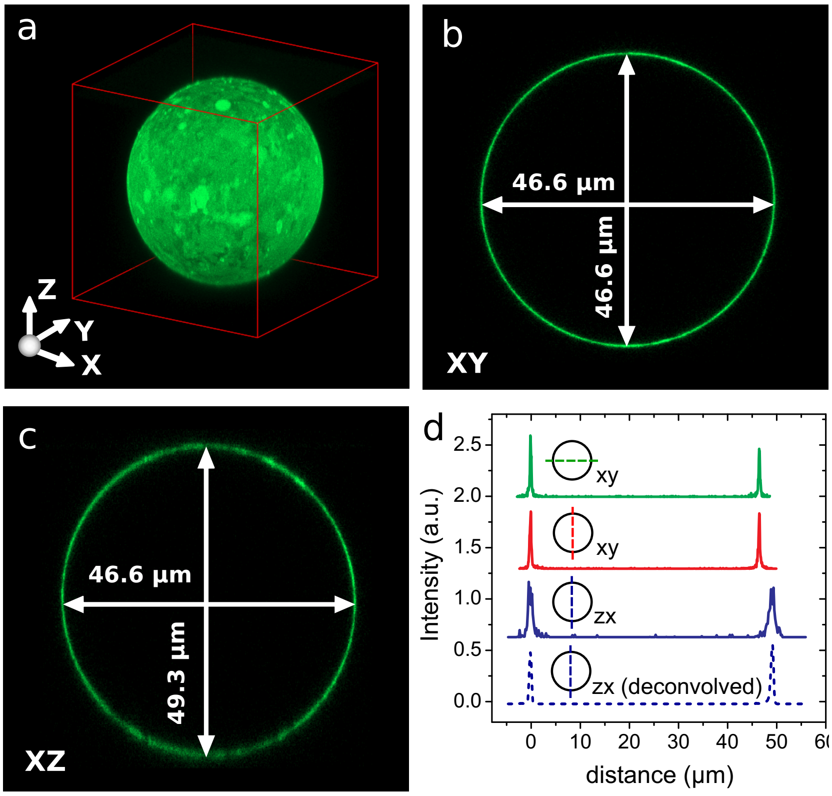

Figure 3.4. A fluorescent PMMA sphere dispersed in an index matching mixture of 24 wt% cis-decalin in CHB, recorded with a confocal microscope (Leica SP8). (a) 3D view constructed from a XYZ image stack. (b) A single XY image shows that x and y distances are equal. (c) The reconstructed XZ view of the image shows that there is a small (6%) elongation in the z-direction. Due to the refractive index mismatch between the suspension (n_D = 1.49) and the oil immersion ($n_D = 1.52$) an elongation in the z-direction of 2% was expected. (d) Intensity profiles along different lines trough the sphere, as indicated in the figure. The profiles were normalized and shifted for better visualization.

An additional benefit is that these particles hardly display thermal motion, even when dispersed in a solvent with viscosity ~ 1 cP, which is due to their large size.

3.3.3. PSF measurement & imaging of single fluorescent beads

In Fig. 3.5 we show examples of an experimental measurement of the PSF and its effect on confocal microscopy measurements of fluorescent particles. In Figs. 3.5a-c we show images of the PSF of an accurately calibrated point-scanning confocal microscope (Leica SP8) equipped with a 100x/1.4 oil-immersion objective (Leica). The intensity profiles of the PSF in the x, y and z-direction could be well fitted with Gaussian functions (Fig. 3.5d). From the FWHM of these Gaussian fits, we obtained a measure of the resolution of the microscope. The values that we obtained are 190 nm in the lateral and 490 nm in the axial direction, which is close to the maximum resolution possible for a conventional point-scanning confocal microscope, which is around 178 nm in the lateral and 459 nm in the axial direction for this setup [123, 124]. Also, the symmetry of the PSF in all three directions is high, indicating little optical aberration. In Figs. 3.5e-l we demonstrate the effect of the PSF on the geometry of two (nearly) index-matched spherical particles. In Figs. 3.5e-h, orthogonal views are shown of a polystyrene bead with a diameter of 200 nm that was immersed in immersion oil (Type

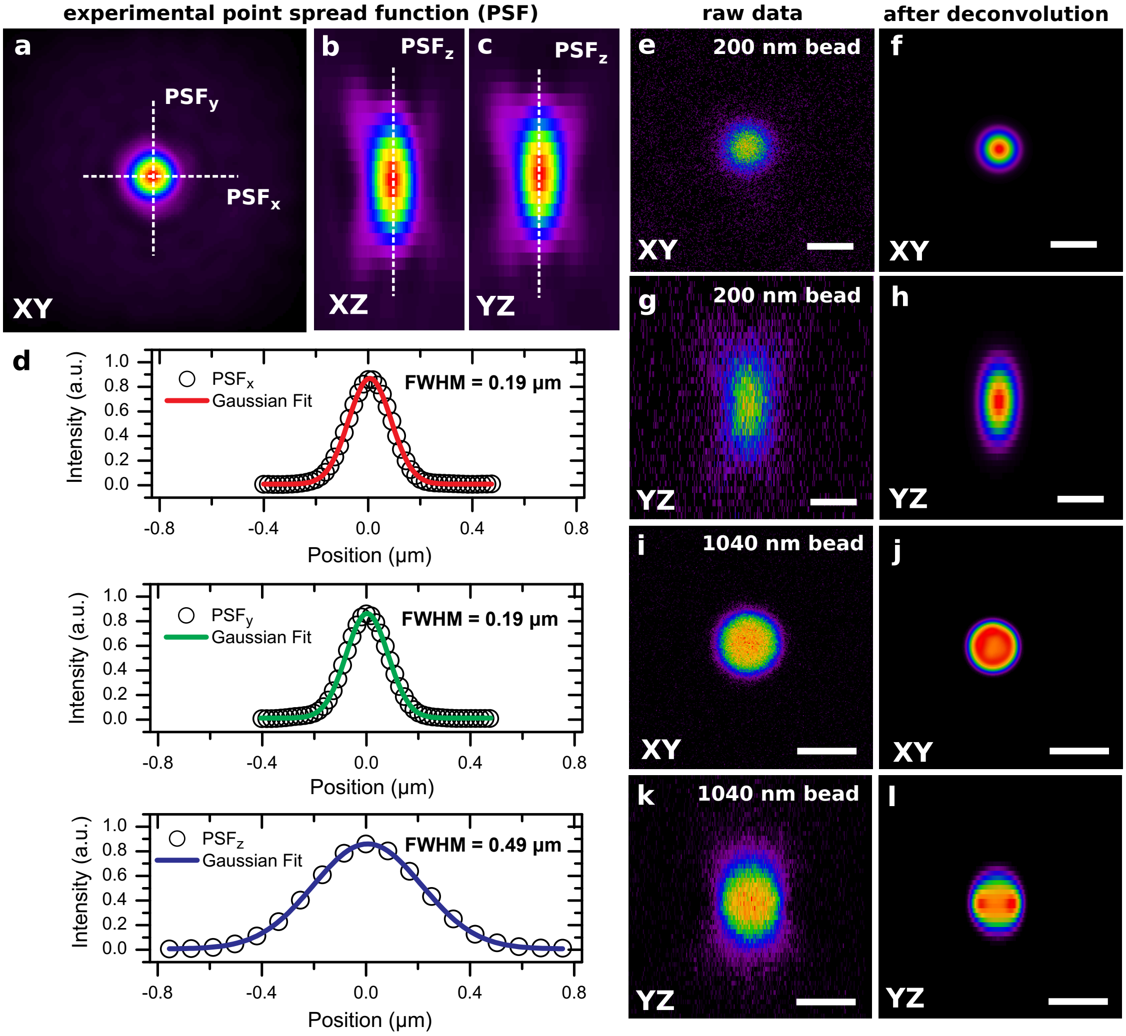

FIGURE 3.5. Experimental measurement of the point spread function (PSF) and imaging of single fluorescent beads. Images were recorded with a 100x/1.4 oil immersion objective. (a) The PSF in the XY plane. Intensity profiles were recorded along the indicated cross-sections. (b-c) The PSF in the z-direction clearly shows the expected elongation, due to the more limited resolution in the axial direction. (d) Recorded intensity profiles from the images in (a) and (b). The FWHMs that we obtained were 190 nm in the lateral and 490 nm in the axial direction. (e-h) Orthogonal views of a polystyrene bead with a diameter of 200 nm, before and after deconvolution. The scale bar is 300 nm. (i-l) Orthogonal views of a PMMA sphere with diameter 1040 nm, again before and after deconvolution. The scale bar is 1 μm.

F, Leica) before and after deconvolution. It is clear from Fig. 3.5g that its dimensions in the axial direction were stretched. Deconvolution (Figs. 3.5f,h) reduced the apparent size of the particle, however, anisotropy in the particle shape still remained. In Figs. 3.5i-l, orthogonal views are shown of a PMMA sphere (diameter 1040 nm), before and after deconvolution. Despite its larger size, the particle still seems elongated in the axial direction (Fig. 3.5k), however, deconvolution almost recovered the spherical shape of the particle (Fig. 3.5l).

These measurements demonstrate that even a micron-sized spherical object that was nearly RI-matched, seemed elongated in the axial direction due to the anisotropy of the PSF (and possibly to a lesser extent due to a subtle difference in RI between particle and solvent). This demonstrates that care has to be taken when using single, micron-sized features to determine if the microscope is correctly calibrated in the axial direction, even when the sample is almost RI-matched.

3.4. Discussion

With the calibration cell described in this chapter, we measured the scaling of axial distances as a function of refractive index (RI) mismatch. We found for an aqueous sample dyed with FITC (excitation wavelength 488 nm) imaged with an oil-immersion objective with NA = 1.4, an axial scaling factor of 0.85. This value is in good agreement with the theoretical calculations of Hell *et al.* [88], who found an value of 0.83 and to reasonable extent to the value of 0.89 calculated by Sheppard *et al.* [109]. The linear slope fitted to our data was however much smaller than the slope predicted from the high-angle geometrical optics equation (3.2), which predicts a scaling factor of 0.36 for NA = 1.3, and is slightly higher than the slope for the paraxial limit n/n_{oil}. Our experimental values are however in good agreement with other experimental measurements that use a fluorescent ‘sea’ between two coverslips [88, 116]. Theoretical expressions that take the vectorial properties of light into account found almost linear scaling in axial shift as a function of axial distance, and also found no strong dependence on excitation wavelength (around 500 nm) [88, 109, 115], which extends the applicability of these results.

Our measurements deviate considerably however from experimental studies on micron-sized particles that are immersed in a solvent with a RI-mismatch, where scaling factors of 0.4-0.7 are reported for aqueous samples [105, 106, 116]. In the case of a RI-mismatch between the sample and the immersion liquid, both the width of the PSF increases [88, 114], as well as the apparent axial distance (due to the focal shift). These two effects are hard to separate for micron-sized particles and has led to overestimation of axial distance scaling in previous studies, as described further in Ref. 110. The overestimated axial scaling obtained by measuring particles of a few micron in diameter corresponds however approximately to the incorrect axial scaling distances predicted by the geometrical optics model (equation 3.2).

This does not mean that micron-sized spheres are not useful for calibration samples. On the contrary, regular 3D colloidal crystals of fluorescent micro-spheres can act as an ideal calibration sample, because of the well defined (periodic) 3D distances of the crystal lattice. The particles can be immobilized by post-treatment of the sample and the lattice distances can be measured with complementary methods such as light scattering or X-ray diffraction [125]. Such 3D colloidal crystals are especially worth exploring because a complete theory exists on how to correct for refraction index differences between the micro-spheres and the surrounding medium. Presently we are using such samples to test effective medium theories that are used to arrive at approximate effective refractive indices for the combined particle-solvent system. Furthermore, if the particles have e.g. a small gold core, the sample can at the same time be used to measure the PSF (in reflection mode).

3.5. Conclusion

We demonstrated two methods to calibrate axial distances in confocal microscopy that are both accurate and practical to employ. The first method consists of a sample cell built from ordinary glass cover-slips. From the Fabry-Perrot fringes in the transmission spectrum of the empty cell, we could accurately measure its height. We filled the cell with four different solvents mixed with fluorescent dye, which enabled the determination of the axial scaling factors as a function of refractive index for high-aperture confocal-microscopy imaging. We found that our scaling factors are almost completely linearly dependent on the refractive index (RI) and therefore we determined an empirical formula that provides the axial scaling factor for confocal microscopy images acquired with an oil-immersion objective (NA = 1.4) for any RI between 1.3-1.5. Our results are in good agreement with theories that take the full vectorial properties of light into account, and consequently, there was a strong deviation with the high-angle theoretical prediction of geometrical optics, which predicts much lower scaling factors. The prediction in the paraxial limit (considered only valid for low NA) resulted in only slightly higher scaling factors compared to our measurements, which is in agreement with the assertion that paraxial rays dominate in the mechanism of axial shift. Using a straightforward calibration of the lateral distances of a confocal microscope with a calibration grid, we showed that large ($\sim 50\ \mu$m) spherical particles that only have a fluorescent shell, can conveniently be used to measure axial-distance deviations $\sim 2\%$. As an illustration, we demonstrated with a correctly calibrated confocal microscope that spherical objects of only a micrometer or smaller were still significantly elongated due to the PSF, and possibly due to a small RI-mismatch, which signifies that care has to be taken when determining axial calibration or axial scaling using such particles.

3.6. Acknowledgements

We thank Hans van der Voort, Hans Gerritsen and Job Thijssen for useful discussion. We thank Jissy Jose for the granular PMMA particles and Johan Stiefelhagen for the colloidal PMMA particles. We also thank Johan Stiefelhagen, Jissy Jose and Chris Kennedy for critical reading of this chapter.

4

Determination of the Positions and Orientations of Concentrated Rod-like Colloids from Microscopy Data

ABSTRACT

We developed a new particle-fitting algorithm that can extract the positions and orientations of fluorescent rod-like particles from three dimensional confocal microscopy data stacks. The algorithm is tailored to work even when the fluorescent signals of the particles overlap considerably and a threshold method and subsequent clusters analysis alone do not suffice. We demonstrate that our algorithm correctly identifies all five coordinates of uniaxial particles in both a concentrated disordered phase and a liquid-crystalline smectic-B phase. The algorithm also works on confocal microscopy images of other uni-axial symmetric particles such as dumbbells and on 3D electron tomography reconstructions of gold nanorods. We also give examples of position and orientation fitting from 2D images of concentrated 3D samples of silica rods and PMMA dumbbells and show that the projected 2D nematic order parameter gives a good estimate of the true 3D nematic order in the system. Lastly, we determined the accuracy of the algorithm using both simulated and experimental confocal microscopy data-stacks of diffusing silica rods in a dilute suspension. This novel particle-fitting algorithm allows for the study of structure and dynamics in both dilute and dense liquid-crystalline phases (such as nematic, smectic and crystalline phases) as well as the study of the glass transition of rod-like particles in three dimensions on the single particle level.

4.1. Introduction

The accurate determination of particle positions by means of microscopy has been important in scientific studies for at least a hundred years. For instance, research trying to quantify via microscopy what is now known as Brownian motion of colloidal particles goes back several centuries [126]. This type of quantitative study on Brownian motion culminated in essential contributions to proving the existence of atoms and molecules and led to a Nobel Prize in 1926 [6]. One year earlier, the Nobel Prize had been awarded for the development of the ultra-microscope by Zsigmondy. This type of microscopy made it possible to follow individual gold nanoparticles that are much smaller than the wavelength of visible light [127]. The ultra-microscope imaged the light scattered by such metallic nanoparticles using methodology that is now referred to as dark-field microscopy [128]. More recent developments have taken light microscopy to the imaging of single molecules [129] and with resolutions clearly so far below 100 nm that the correct term is starting to become: light nanoscopy [89, 97]. However, the focus of this chapter and the brief literature review in this introduction is on two particular classes of microscopy that enable quantitative 3D imaging of all individual colloidal particles present even in concentrated systems: fluorescence confocal microscopy and electron microscopy tomography. This is not to say that there are no exciting developments taking place in quantitative 3D imaging using other techniques. For instance, in the field of digital holography multiple particle trajectories can now be tracked with nm precision (also for z-coordinates) [130]. However, this technique can be used to disentangle the signals of only a few particles [131], but not (yet) of truly concentrated systems.

If all the particles in concentrated systems need to be followed in 3D, the approaches that have been successful until now try to limit the interaction of the incident photons or particles with the photons being detected as much as possible. This is also an important reason for the use of fluorescence, because with fluorescence there is almost no possibility of interference of the exciting light with the light that is detected. In addition, chemical attachment of dye in specific places inside the particles can help in resolving particles in concentrated systems significantly [132, 133]. By matching the refractive index of the particles and the medium one can minimize the interaction of the imaging light with the particles and image samples that consist of more than just a few layers of particles [46, 134]. In addition, having an as optically homogeneous medium as possible limits the degradation of the microscope response function, i.e. the point spread function (PSF) [88].

The first demonstration of the ability to quantitatively image individual particles in more concentrated systems was done by studying particles only a few layers away from the container wall [135, 136] or essentially 2D systems using (digital) video microscopy, which started to become important in the 1980s [137]. The group of Grier and his co-workers gave an important impetus to this field by publishing the methodology and making available the software they developed to track all particles quantitatively in 2D [45, 138]. After filtering steps to remove noise, coordinates were obtained with sub-pixel accuracy using a centroiding algorithm. Centroiding algorithms essentially determine the arithmetic mean of the pixels associated with a particle. Sub-pixel accuracy can be achieved with this approach if the noise is below a certain level and if the signals of the individual particles are well separated. In addition, Grier *et al.* also implemented a method to identify the same particles in consecutive video-frames after they have moved, known as particle tracking, which is based on the minimization of the mean squared displacement of the particles [45, 138]. This method is an example of a combinatorial optimization problem and is independent of the process of locating the particles.

Many other groups studying similar 2D model systems started using the methodology optimized by the Grier group. Often the systems studied were composed of charged polystyrene particles (refractive index $n_D = 1.6$) with a size of several hundred nm or larger in water ($n_D = 1.3$). Refractive index matching was considered not to be too important because there were no particles blocking each other's signal. For these kinds of 2D systems however, the significant index of refraction difference and the consequently strong interaction of the light with the particles can lead to an overlap of neighbouring particle signals. More recently it has come to light that if this overlap is not properly dealt with, it can lead to small systematic shifts in the determination of particle positions [139, 140]. The resulting systematic errors are small (order of tens of nm) compared to the particle size, but enough to lead to an incorrect interpretation of the interaction potential between such particles and the appearance of attractions at relatively large distances where there are really none [139, 140].

In the early 90s it was demonstrated that quantitative imaging of thousands of particles even in concentrated 3D systems is possible by using confocal microscopy in combination with fluorescent core-shell particles [46]. As mentioned in Ref. 46, particle coordinates were obtained with sub-pixel (or actually its 3D equivalent: a voxel) accuracy by fitting the full 3D data sets with the confocal microscope response function averaged and measured from a 2D collection of the particles stuck on a microscopy slide. It was soon found, however, that it was as accurate, but hundreds of times faster, to use a slice-by-slice approach. In this approach, first the x,y positions of all particles in each of the xy-slices out a 3D data stack were fitted, using a similar methodology as that of Grier *et al.* [45]. Subsequently, the coordinates in the different xy-slices belonging to the same particle were identified and finally a Gaussian function was fitted to this limited number of points (generally < 10) to also obtain the z-coordinate. This method makes use of the fact that the point spread function (PSF), can be approximated quite well by a Gaussian function in the x,y (lateral) direction and by another Gaussian in the z (axial) direction with a full-width-at-half-maximum that is approximately three times larger [102, 141]. The main reason that this methodology (further outlined in Ref. 47) is so much faster than direct 3D centroiding is that not the entire 3D data set needs to be loaded into memory at any time but only single 2D slices. Combined with the fact that the image filtering is only needed in 2D, and 2D image filtering has been highly optimized, this results in a significant decrease in execution time. Fast algorithms based on this method allowed for real-time tracking [49]. It is good to point out, however, that the speed gain was much more important 20 years ago than it is now.

Modern computers can easily contain an entire stack in their memory and fitting speed is no longer a limiting factor, which is why most recent studies locate particles using the full 3D image [48]. In connection to this it was recently pointed out in Ref. 142 that a shortcut implemented by Grier and others to gain speed in the earlier algorithms in a noise suppression step leads to unwanted artefacts in coordinate determination.

Around the turn of the millennium, 3D particle tracking of colloids combined with fast confocal microscopy became well established and enabled the investigation of phenomena such as crystallization, gelation, the glass transition and flow induced behaviour on the single-particle level [12, 47, 48, 52, 56–63]. Since then, there have been many examples of algorithms that locate spherical particles with increased accuracy or performance [49–51, 55]. For example, Jenkins and Egelhaaf demonstrated that for spherical colloids, improvements in both the position refinement and error estimation can be done by fitting with the 'sphere spread function' (SSF), the convolution of the PSF and the (fluorescent part of) the particle, which works particularly well for concentrated systems [50]. Improvements were also made for colloids under flow, where cross-correlation techniques have been used to track particles in a co-moving frame, known as 'correlated image tracking' [52, 53, 60]. Finally, we want to mention that via the dynamics of the tracked particles, additional (static) information can be acquired such as the accuracy of the particle location algorithm [45] and for dense suspensions of spheres interacting through a hard-sphere-like potential, an estimate of the individual particle radii [54].

Not only are there significant advances in our ability to track ever smaller particles with higher accuracy [143], also the range of fields for which this ability is important has expanded significantly. For instance, particle tracking is used to measure forces and other dynamical properties such as viscosity in cell-biology, materials science and food research, known as particle-tracking micro-rheology [144–148]. It is also used in the study of non-Brownian particles, for instance that of granular materials [149, 150], in fields where colloidal or larger particles are driven by external fields, such as particle tracking velocimetry [151, 152], or in the emergent field of 'active colloids', i.e. (self) propelled particles and bacteria [153–155].

Besides fluorescence confocal microscopy, the second method that we focus on in this chapter is electron microscopy. The relatively weak interaction of the electron beam in electron microscopy imaging, enables imaging of thousands of nanoparticles quantitatively in 3D [156–158]. However, there is an extreme difference in the numerical aperture of imaging with electrons as opposed to photons, which results in a focal depth that is enormous compared to the wavelength of the electrons. Therefore, the quantitative determination of particle coordinates can be achieved using scanning transmission electron tomography, in which transmission data are taken from an as large as possible range of projection angles [156, 159]. Although even the quantitative determination of ternary structures with electron tomography has been demonstrated [156–158] and the methodology in general is already well established [156, 159], the use of this technique for obtaining accurate coordinates of colloidal or nanoparticle systems is presently much less well developed and the same applies to the methodology of image processing of the data sets obtained. However, recent advances in electron microscopy are pushing ‘particle’ tracking as far as the atomic level. Huang *et al.* studied rearrangements of individual atoms in a two-dimensional glass, using a combination of high-resolution transmission electron microscopy, Gaussian fitting and the Crocker and Grier algorithm [160].

All studies described so far are based on the quantitative determination of particle positions and translational motion. It is, however, much less known to researchers in the field that Perrin, next to his determination of Avogadro’s number by measurement of the translational diffusion coefficient of spherical colloidal particles, also obtained their rotational diffusion coefficient [6]. Using larger (and therefore slower) particles, he focused on small inclusions inside these particles, making it possible to track their (projected) rotational motion [6]. It has long been known that by, for instance, bleaching part of a fluorescent particle a similar mark could be made in fluorescence confocal microscopy as well. However, until quite recently, such a procedure has not been implemented to measure rotational dynamics [161]. Thanks to recent progress in particle synthesis however, well-defined (shape) anisotropic colloids are becoming widely available, see e.g. Refs. 25, 28, 162–165. These particles can often be observed directly with a (confocal) microscope and therefore enable quantitative measurement of not only their positional but also their rotational degrees of freedom. Therefore, a rapid increase in the number of algorithms that extract coordinates of anisotropic particles from microscopy images has taken place, which will be briefly reviewed in the following.

If the anisotropic particle consists of a cluster of fused spheres, the centroid-algorithm of Crocker and Grier can still be applied [43, 164]. Hunter *et al.* described a method to track the rotational motion of these clusters [166], which was used to study the decoupling of rotational and translational motion upon approaching the glass transition in a tracer-host system [167]. Recently, this method was extended to the computation of the hydrodynamic friction tensor of clusters of (differently sized) spheres [168]. Anthony *et al.* used semi-fluorescent Janus-spheres to simultaneously measure the 2D position and 3D orientation from 2D images [169]. This method was extended to determine the orientation of single rod-like particles (consisting of jointed Janus-spheres), including the rotation around the rod axis [170]. Bright-field imaging and customized particle tracking of (quasi-)2D systems has also been applied to study Brownian motion of ellipsoids [171–173], boomerang particles [174, 175], the glass transition of ellipsoids [176–178] and the phase behaviour of Brownian squares [179] and triangles [180].

Mohraz and Solomon, however, were one of the first to determine the 3D position and orientation of uniaxial ellipsoidal particles, i.e. all five coordinates, using confocal microscopy and a novel anisotropic feature-finding algorithm [162]. Their algorithm identifies the points that are located on the central axis (or backbone) of a rod. These points are then grouped together by cluster analysis as individual rod-backbones, from which the centroid location and orientation are determined. This algorithm enabled the quantitative determination of the 3D translational and rotational motion of a dilute suspension of ellipsoids [181]. A different approach was used by Cohen *et al.* who first detected the centres and orientation angles of all two-dimensional confocal slices through ellipsoidal particles, which were then connected to analyse the 3D positional structure of a colloidal fluid of ellipsoids [182, 183].

Recent developments in anisotropic particle-tracking studies include the measurement of the coupling of diffusive motion of particles to external fields, such as shear-induced rotational motion [40]. A second direction is the quantitative study of anisotropic patchy particles, e.g. by the determination of all six degrees of freedom of Janus-spheroids [184]. A third is the study of liquid-crystalline phase behaviour on the single particle level. Progress has been made for suspensions of ellipsoids, where nematic order was found using a centrifugal field [185] and local crystalline order with an external electric field [44]. Additionally, large-scale crystalline order was found for soft dumbbells under an electric field [43]. When silica rods are made long-ranged repulsive, it was found by several of us that they can form 3D plastic crystals, that can be switched to a complete crystal with an electric field [186]. However, to the best of our knowledge, equilibrium nematic, smectic or crystalline phases of uniaxial particles have, thus far, not been quantified in 3D on the single particle level.

In this chapter we demonstrate a novel 3D image processing algorithm that is capable of extracting the positions and orientations of a recently developed system of fluorescent silica rods that forms both equilibrium nematic and smectic phases [25,28]. In brief, the algorithm detects the backbone of a particle by fitting a line to local bright pixels and grouping them together. Then the centroid is computed, the orientation is fitted and finally the length is fitted. This step is iterated and results in a refined estimate of the 3D positions and orientations of the rods. The algorithm still works for dense smectic-like phases where the fluorescent signals of the particles overlapped considerably. The algorithm also works for other uniaxial particles such as ellipsoids or dumbbells and on electron tomography data of gold nanorods.

This chapter is organized as follows. First, we describe the basics of particle-locating algorithms. Second, we describe our algorithm in detail. Third, we demonstrate the performance of the algorithm with 3D image stacks of concentrated fluorescent silica rods. Then, we illustrate that our algorithm can be applied to 3D electron tomography data of gold nanorods as well. We also give examples of position and orientation fitting from 2D images of concentrated 3D samples of silica rods and PMMA dumbbells. Next, we evaluate the accuracy of the algorithm by measuring the translational and rotational motion of non-overlapping rod-like particles. Finally, we compare our results with recent progress in the field and give an outlook on further studies that the algorithm enables.

4.2. Methods

4.2.1. Locating particles in confocal microscopy data sets

The aim is to identify and locate (rod-shaped) particles in a set of real-space images (or snapshots) and to obtain the full configuration of the system. A specific configuration of a system of particles is given by a set of parameters, one for each degree of freedom of every particle. In the case of rods, these degrees of freedom for particle i are centre position $\mathbf{r}_i$, orientation $\hat{\mathbf{u}}_i$ and possibly length l_i, diameter d_i and brightness b_i. If the length and diameter are known in advance they can be fixed, but if the particles vary in size they can also be left as free parameters. If the particles vary in brightness this can be added as an additional degree of freedom. Variations in brightness can be caused by the synthesis method, scattering or shading in the sample, but also by photo bleaching. In the case of fully symmetric, homogeneously dyed rods it is not possible to distinguish between the two ends of the rods. However, we also synthesised rods with a gradient in brightness, with one bright and one much darker end [72], of which the orientation could be fully determined. To keep the notation short we introduce $\mathbf{p}_i = \{\hat{\mathbf{u}}_i, l_i, d_i, b_i\}$ which contains all the degrees of freedom except the position.

To obtain the configuration ($\mathbf{r}_i$ and $\mathbf{p}_i$) we need to elaborate on what is measured. In case of fluorescent confocal laser scanning microscopy we can assume that the imaging system is linear so that we can add intensities. Furthermore, l_i and d_i refer to the fluorescent part of the particle length and diameter respectively. The measured image intensity $M(\mathbf{r})$ at position $\mathbf{r}$ can be written as the sum of the ideal (noiseless or averaged) images of the single particles,

$$M(\mathbf{r}) = \sum_{i=1}^{N} \mathrm{RSP}(\mathbf{r} - \mathbf{r}_i, \mathbf{p}_i), \tag{4.1}$$

and $\mathrm{RSP}(\mathbf{r}, \mathbf{p}_i)$ is the image of a single particle placed in the origin, or rod spread function (RSP). The image of a single particle at the origin depends on all the internal degrees of freedom of the particle such as orientation, length, diameter and brightness, but also on the point spread function (PSF) of the imaging system. It is given by

$$\begin{aligned} \mathrm{RSP}(\mathbf{r}, \mathbf{p}_i) &= \int \mathrm{d}\mathbf{r}' \rho_{\mathrm{dye}}(\mathbf{r}', \mathbf{p}_i) \mathrm{PSF}(\mathbf{r} - \mathbf{r}') \\ &= (\rho_{\mathrm{dye}}(\mathbf{p}_i) * \mathrm{PSF})(\mathbf{r}), \end{aligned} \tag{4.2}$$

which is a convolution ($*$) of the dye distribution $\rho_{\mathrm{dye}}(\mathbf{r}, \mathbf{p}_i)$ of particle i placed in the origin and the PSF. In a dilute sample this $\mathrm{RSP}(\mathbf{r}, \mathbf{p}_i)$ can be measured directly but it can also be calculated when the dye distribution is simple and the parameters of the optical systems are known.

Different approaches to obtain the particle coordinates are possible. If all the parameters such as the PSF and RSP are known, the locating problem becomes in principle a deconvolution. However, the RSP and the PSF can be time consuming to determine accurately, and deconvolutions are sensitive to small changes in the kernel function [187]. This is unfortunate since e.g. polydispersity will introduce changes in the RSP which would make the deconvolution difficult. If the RSP is not known, there exist several other possible options. The first option is to assume that the overlap between the RSPs is not too severe and to determine centre-of-mass and orientation with methods that are insensitive to the details of the optical system. This is the method used by centroiding algorithms and is also the method used in this chapter.

Another option is to use a Bayesian method [188]. This method searches for the configuration that has the largest probability of having resulted in the observed image.

This method has proven to work well for two-dimensional data sets [189]. It is, however, slow and complex and therefore not practical for large three-dimensional data sets.

4.2.2. Generation of test images

To test our algorithm we generated confocal-like images from sets of computer-generated particle trajectories. The images were first generated with intensity values between 0 and 1, which were later converted to an 8-bit grayscale. Using the centres-of-mass $\mathbf{r}_i$ and particle orientations $\hat{\mathbf{u}}_i$, we generated 3D stacks of xy-images of spherocylinders with aspect ratio $l/d = 5$, where l is the end-to-end length of the particle and d the diameter. This was done by calculating the closest distances D to a line segment, representing the backbone of a particle. The distance from a point in the origin to a line segment from $\mathbf{x}_1$ to $\mathbf{x}_2$ with length $l = |\mathbf{x}_1 - \mathbf{x}_2|$ is given by

$$D(\mathbf{x}_1, \mathbf{x}_2) = \begin{array}{rll} |\mathbf{x}_1| & \text{if} & \alpha < 0, \\ \sqrt{|\mathbf{x}_1|^2 - \alpha^2} & \text{if} & 0 < \alpha < l, \\ |\mathbf{x}_2| & \text{if} & \alpha > l, \end{array} \tag{4.3}$$

where $\alpha = (\hat{\mathbf{u}} \cdot \mathbf{x}_1)$ and $\hat{\mathbf{u}} = (\mathbf{x}_1 - \mathbf{x}_2)/l$ the unit vector along the length of the line segment. If this distance was less than half the diameter of the particle, the pixel was given a value of 0.95. This was then repeated for all particles. We approximated the effect of the PSF in our test images by convolving them with a Gaussian kernel with fixed standard deviation $\sigma_x/d = \sigma_y/d = 0.3$ and $\sigma_z/d = 0.3, 0.6$ and 0.9 with d the diameter of the particle. The full-width-at-half-maximum (FWHM) of the Gaussian function, given by $2\sqrt{2\ln 2}\,\sigma_i$, is a direct measure of the resolution of the images. Besides variation of resolution, we also varied the amount of noise in the images. Although noise from modern detectors is essentially photon-limited, suggesting a Poisson distribution [92], we added noise to each pixel in our images with a simple Gaussian distribution with standard deviation $\sigma_n = 0.10 - 0.30$. Because the amount of noise is known a priori, it is still straightforward to calculate the signal to noise ratio (SNR), which we define as $\mathrm{SNR} = (\sigma_g^2/\sigma_n^2 - 1)^{1/2}$, with σ_g^2 the variance of the constructed image and σ_n^2 the variance of the noise [50]. Finally, we converted all our data, with pixel-values between 0 and 1, to 8-bit grayscale tiff images.

4.2.3. Our algorithm

To demonstrate the three-dimensional rod tracking algorithm we will first illustrate all steps of the algorithm with an artificially created set of images of a single rod, shown in Fig. 4.1. This will allow us to demonstrate clearly what is going on on a single pixel/voxel level. Later we will demonstrate how the algorithm fares with real colloidal suspensions. The following description is for three dimensions but most of the steps are straightforward to modify for two dimensions.

Reading. In Figs. 4.1a-c we show three orthogonal slices through a generated 3D image that acts as the source image. The particle shown in the image has a diameter $d = 13.0$ pixels, and is blurred with a Gaussian kernel $\sigma_x/d = \sigma_y/d = 0.3$ and $\sigma_z/d = 0.9$.

Gaussian pixel noise of $\sigma_n = 0.1$ was added to the image. The first step is to read in these source images. To avoid accumulating rounding errors and to allow the use of images of arbitrary bit depth we perform all image manipulations on floating point numbers between zero and one. Next, the image is rescaled to make sure the voxels are cubic, which is often not the case for confocal microscopy image stacks. The rescaling avoids having to account for different x, y and z scales in all following routines. To make sure no information is lost, this is done by enlarging the image using a bicubic interpolation. Care should be taken not to use overexposed images since this will result in a loss of information and an increase of positional error. See Ref. 50 for a more detailed description and the optimal shape of the intensity histogram. We generally choose the magnification such that the particles are approximately 10 pixels in diameter. Larger magnification results in a large file size without any additional benefit.

Filter. The aim of the first filter step is to reduce image noise. We apply a Gaussian blur to the image, i.e. a convolution with a Gaussian kernel, that acts as a low pass filter. The optimal width of the function depends on the noise level in the images; a value between 1.5 and 3 pixels was found to give the best results for the images obtained in the present chapter. A value that is too large will result in the loss of resolution and in missing particles, a value that is too small will result in additional, incorrectly identified, particles. To ensure a black background for the particles, a background value is subtracted from every pixel. This background value is assumed to be mostly the result of photon noise, but it can also originate from other sources such as fluorescence from the solvent or immersion fluid. Pixels that have a negative value after the background value has been subtracted, are set to zero. In most cases a background value between 0.01 and 0.1 is used. This value should be chosen such that approximately half the empty pixels (not containing a particle) of the image are zero. We also save a copy of the image that has not been filtered. This allows us to perform the final fitting step on the original image. An example of a computer-generated image that has been filtered is shown in Fig. 4.1d.

Well separated particles. When the intensity distributions of the individual particles do not overlap significantly we apply what we call a threshold method. This threshold method works as follows. A typical value for the threshold is between 0.4 and 0.7 and can be determined by plotting a histogram or by a quick test on a single image in a program like Photoshop, Gimp or ImageJ. The next step is to group all connected pixels above the threshold value into sets, as described in the next section. This method works when these sets of pixels belong each to a single particle and each particle only corresponds to a single set of pixels. In Fig. 4.1e an example is shown of the threshold method applied to a single particle. All pixels above the threshold are marked in yellow. The particle coordinates can be obtained by applying a fit to these sets of pixels, as described later in this section. When this threshold method works, it is preferred over more complex methods since it is both robust and accurate.

General case. When a threshold does not successfully separate the image into regions belonging to single particles another method has to be used. The first step of this method is similar to the Crocker and Grier algorithm and is aimed at providing the final fitting steps with a good initial starting point. In this step, we roughly locate the

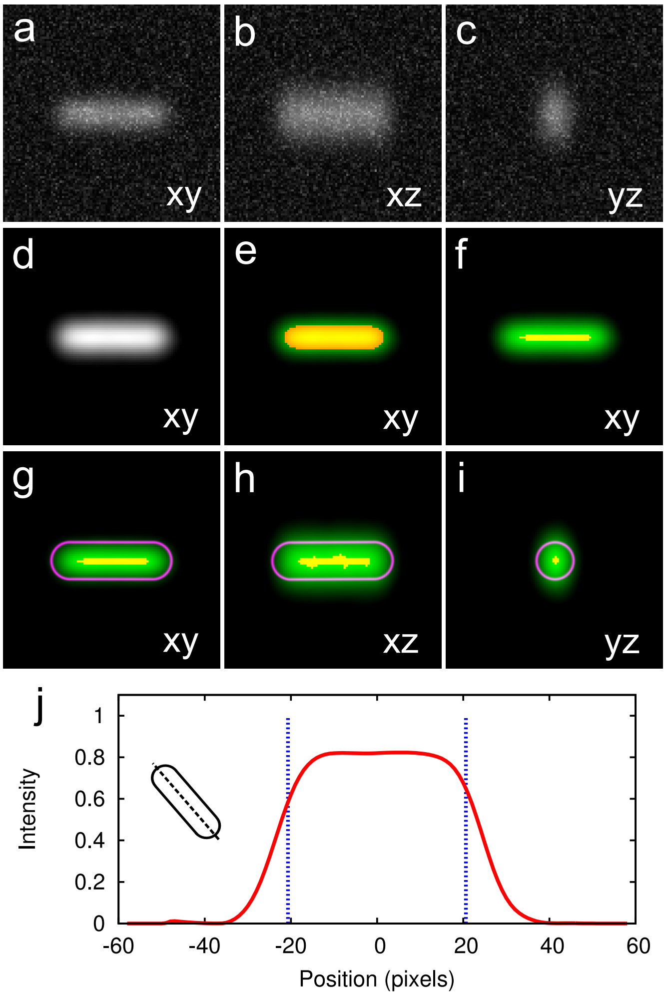

FIGURE 4.1. The different stages of identification of the position and orientation of a single rod-shaped particle. (a,b,c) Orthogonal slices through a computer generated 3D image stack. The particle has a diameter of 13.0 pixels and is blurred with a Gaussian kernel with width $\sigma_x/d = \sigma_y/d = 0.3$, and $\sigma_z/d = 0.9$. Pixel noise has been added by adding Gaussian noise with $\sigma_n = 0.1$. (d) The same image after the filter-step. (e) After a threshold step, the pixels above the threshold are marked in yellow. (f) After a backbone step, the pixels identified as backbone pixels are marked in yellow. (g,h,i) The rod as it is located, viewed from the xy, yz and xz plane. (j) The histogram of the average intensity along the rod length after smoothing and background removal. The dashed vertical lines mark the fitted end-points of the rod.

line segment starting from one end of the rod and ending at the other end, called the backbone of the particle. To locate the backbone, we look at all voxels brighter than a predetermined cut-off value. A good value for this is in general between 0.1 and 0.5 depending on the intensity fluctuations between the rods. For these bright pixels we then check whether they are part of a backbone. To do this we first note that all local maxima should be part of the backbone. To check if the brightness of the pixel is a local maximum we compare its intensity to that of all pixels within a distance r_{bb}. If none of these pixels are brighter the pixel is a local maximum. To find the parts of the backbone that are not on a local maximum, we look at the distribution of brighter pixels around the pixel in question. If the pixel is part of the backbone they should be on a ridge. Backbone pixels can have brighter pixels to one side or two sides but all these brighter pixels should be more or less on a line through the pixel in question. So to check if the pixel is part of a backbone we need to check if the pixels brighter than the pixel in question are on a straight line. To do this we fit a line to these bright pixels and sum the squared residuals χ, the squared distance between the brighter pixels and the line. If these bright pixels are part of the backbone of a rod this number will be low since the pixels will form an almost perfect line while on other places they will not form a line and the residuals will be much higher. We found that $r_{\mathrm{bb}} = 3$ pixels and a maximum value $\chi_{\max} = 80$ work well for all our data. This step depends on the initial filtering and on the thickness of the rod in pixels. Fig. 4.1f shows the pixels that have been identified as backbone pixels in yellow.

After having identified the backbone pixels, we group them into connected clusters. Due to noise there can be small gaps between the backbone pixels of a rod, so we use the same search range r_{bb} as before to identify neighbouring pixels. This should work as long as the diameter of a rod is larger than r_{bb}.

We now have groups of pixels most likely belonging to a single rod. To continue, we fit (least square) a straight line to these pixels using a singular value decomposition [190, 191]. The coordinates resulting from this fit are accurate, but still have a strong pixel bias since they only fit to a few backbone pixels. To eliminate this bias and to obtain more accurate results, we use these coordinates, lengths and orientations as a starting point to fit the real image again.

Fitting. The fitting steps work best when applied to the unfiltered image. The Gaussian blur filter will result in an additional overlap of the RSPs which can result in a decreased accuracy. The fitting is done in three steps; first the centre of mass of each group of pixels is computed, then the orientation is fitted and finally the length is fitted. The position is taken from the centre of mass, weighted with the pixel intensity, of the pixels within half a diameter from the previous fit. The orientation is obtained by fitting a straight line to these pixels where the fit is weighted with the intensity of the pixels using the same least square fitting algorithm as for the backbones. The length is obtained by calculating the average intensity of pixels along the rod length, see Fig. 4.1j. The histogram that is obtained from this is smoothed with a Gaussian kernel to avoid noise.

The end points are then obtained by determining where the histogram value drops below $I_{\text{end}} I_{\max}$, where $I_{\max}$ is the maximum intensity value in the smoothed histogram and I_{end} is a parameter that can be set manually. Usually a value of $I_{\text{end}} = 0.6$ - 0.8 was found to give good results, see the (blue) dashed lines in Fig. 4.1j. To obtain sub-pixel accuracy we fit a straight line to the 2 pixels above and 2 pixels below the point where the histogram crosses this value. To determine which pixels to take into account in the generation of the histogram and the other fits, we use the pixels within one radius of the central line segment of the previous fit. Therefore, the result of the fit might improve when the step is repeated. The fitting algorithm normally converges in one or two steps. If this is not the case there is something wrong with the data or one of the parameters. Figs. 4.1g-i show the same orthogonal sections as Figs. 4.1a-c with the backbone of the rod highlighted in yellow and the outline of the rod (resulting from the fit) highlighted in magenta.

Filtering. The final step is to filter out particles that are found more than once, particles that do not contain enough intensity or sometimes particles that are not long enough. Ideally not much filtering is required.

4.2.4. Generation of particle coordinates

We generated artificial particle trajectories to construct 3D test-image series. We used two different approaches to generate particle trajectories. The first is a single-particle approach where we independently drew random (orientational) displacements for a set of particles and not allowed particles to interact. The second is a Molecular Dynamics (MD) simulation where particles interact via a hard-core repulsion.

Using the single particle approach, we generated two sets of trajectories. For the first set of trajectories, we fixed 25 particles on a $5 \times 5 \times 1$ hexagonal lattice in 3D. For each particle a unit vector $\mathbf{u}_0$ was initialized, which represented the principal axis of the particle. The particles were not allowed to translate, however, they were able to rotate with a fixed diffusion coefficient D_r. The reduced rotational diffusion coefficient is given by $D_r^* = D_r\, t_s$ (in rad^2) with t_s the time-step. Particles were rotated by first randomly selecting rotation angles α, β and γ from a Gaussian distribution with $\sigma_i = \sqrt{2D_r^*}$. Then, the particles were rotated by applying the rotation matrices $\mathbf{u} = \mathbf{R}_x(\alpha)\mathbf{R}_y(\beta)\mathbf{R}_z(\gamma)\mathbf{u}_0$, as is described in detail in Ref. 166. For the second set of trajectories, we generated 36 trajectories of a single particle that could diffuse freely in all three dimensions. To this end, displacements $\Delta\mathbf{r}$ were drawn from a Gaussian distribution with standard deviation $\sigma_i = \sqrt{2D_t^*}$. Here, we define $D_t^* = D_t\, t_s/d^2$, with D_t the rotationally averaged translational diffusion coefficient, t_s the timestep and d the particle diameter. The centre-of-mass of the particle was displaced by $\mathbf{r} = \mathbf{r_0} + \Delta\mathbf{r}$. The particle was rotated as before with a fixed rotational diffusion coefficient D_r^*.

The final set of trajectories were from a more concentrated suspension of rods, which we obtained using a molecular dynamics (MD) simulation of hard spherocylinders in the

NVT ensemble [192]. The configuration consisted of 4000 spherocylinders with aspect ratio $l/d = 6$, with l the end-to-end length of the particle.

4.2.5. 3D particle tracking

To study particle dynamics, we applied our algorithm to time-series of 3D image-stacks. We first identified the positions and orientations of the rods in each 3D stack separately. Then, we obtained the particle trajectories using standard IDL-based routines [45]. To uniquely track the tip of the (up-down indistinguishable) rods, it is required that the angular displacements between successive frames $[\hat{\mathbf{u}}(t+1) - \hat{\mathbf{u}}(t)]^2 < 2$. Therefore, care was taken that displacements with $[\hat{\mathbf{u}}(t+1) - \hat{\mathbf{u}}(t)]^2 > 2$ were negligible. We then calculated the mean squared displacement (MSD) and the mean squared angular displacement (MSAD). We fitted the MSD to the expression

$$\langle \Delta \mathbf{r}^2(t) \rangle = 6\, D_t\, t + 6\, \epsilon_t^2, \tag{4.4}$$

with D_t the rotationally averaged translational diffusion coefficient and ϵ_t the error in measurement of each of the coordinates of the particle [193]. For the MSAD we used the expression [194, 195]

$$\langle \Delta \hat{\mathbf{u}}^2(t) \rangle = 2[1 - (1 - \epsilon_r^2) \exp(-2 D_r t)], \tag{4.5}$$

with D_r the average rotational diffusion coefficient and ϵ_r the measurement error in the determination of $\hat{\mathbf{u}}(t)$. For short times, equation (4.5) reduces to

$$\langle \Delta \hat{\mathbf{u}}^2(t) \rangle = 4 D_r t + 2 \epsilon_r^2\,. \tag{4.6}$$

To estimate the sedimentation velocity at infinite dilution, assuming complete decoupling of rotations, translations and sedimentation [196], we use the Svedberg equation [197]

$$v_{sed} = \frac{v_p\, D_t\, g\, (\rho_p - \rho_s)}{k_B\, T}, \tag{4.7}$$

with v_p the volume of the particle, g the gravitational acceleration, ρ_p the mass density of the particle and ρ_s the mass density of the solvent.

4.2.6. Calculation of the nematic order parameters

To quantify the 3D orientational order in our systems we calculated the 3D nematic order parameter defined by

$$S_{3D} = \frac{3}{2} \langle \cos^2 \theta \rangle - \frac{1}{2}, \tag{4.8}$$

with θ the angle between the main axis of the rod $\hat{\mathbf{u}}$ and the nematic director $\hat{\mathbf{n}}$. We find S_{3D} and $\hat{\mathbf{n}}$ by calculating the largest eigenvalue and corresponding eigenvector of the standard 3×3 nematic order parameter tensor

$$Q_{\alpha\beta}^{3D} = \frac{1}{N} \sum_{i=1}^{N} \left(\frac{3\, u_{i\alpha} u_{i\beta} - \delta_{\alpha\beta}}{2} \right), \tag{4.9}$$

with $u_{i\alpha}$ the α-component of the unit vector pointing along the main axis of particle i, and $\alpha, \beta = x, y, z$. $\delta_{\alpha\beta}$ is the Kronecker delta and N is the total number of particles in the system.

To quantify the (projected) 2D order in the system we calculated the corresponding 2D nematic order parameter, given by

$$S_{2D'} = 2\langle \cos^2 \psi \rangle - 1, \tag{4.10}$$

with ψ the angle between the projected main axis of the rod $\hat{\mathbf{u}}'$ and the projected nematic director $\hat{\mathbf{n}}'$, i.e. ψ is the in-plane projected angle that maximizes equation (4.10). Similarly, we calculated the 2 × 2 nematic order parameter tensor given by

$$Q^{2D}_{\alpha\beta} = \frac{1}{N} \sum_{i=1}^{N} \Big(2\, u'_{i\alpha} u'_{i\beta} - \delta_{\alpha\beta} \Big), \tag{4.11}$$

with $u'_{i\alpha}$ the α-component of the unit vector pointing along the projected main axis of particle i, $\delta_{\alpha\beta}$ the Kronecker delta and $\alpha = x, y$.

4.2.7. Expressions for the diffusion coefficients

To test the validity of our experimental measurements of the diffusion coefficients, we compared them to analytical expressions for hard cylinders at infinite dilution, as proposed by Tirado, Martinez and de la Torre [198],

$$D_\perp = \frac{k_B T}{4\pi\eta\, l}(\log p + \delta_\perp), \tag{4.12}$$

$$D_\parallel = \frac{k_B T}{2\pi\eta\, l}(\log p + \delta_\parallel), \tag{4.13}$$

$$D_t = \frac{2}{3} D_\perp + \frac{1}{3} D_\parallel, \tag{4.14}$$

$$D_r = \frac{3 k_B T}{\pi\eta\, l^3}(\log p + \delta_r), \tag{4.15}$$

with η the solvent viscosity, $p = l/d$ the aspect ratio of the particle and δ_i a correction term for the finite aspect ratio of the cylinders, given by [198]

$$\delta_\perp = 0.839 + 0.185/p + 0.233/p^2, \tag{4.16}$$

$$\delta_\parallel = -0.207 + 0.980/p - 0.133/p^2, \tag{4.17}$$

$$\delta_r = -0.662 + 0.917/p - 0.050/p^2. \tag{4.18}$$

4.2.8. Experimental methods

Dense sediments of silica rods. For the preparation of dense samples of silica rods, two different batches of particles were used. The first batch consisted of rods with length $l = 2.37$ μm ($\delta = 10\%$) and diameter $d = 640$ nm ($\delta = 7.5\%$), with δ the polydispersity (standard deviation over the mean) [25]. A transmission electron microscopy (TEM) image of these particles is shown in Fig. 4.2a. The particles contained a non-fluorescent core, a 30 nm fluorescein isothiocyanate (FITC) labelled shell, and a 190 nm non-fluorescent outer shell. For the second batch of silica rods, with length $l = 2.6$ μm (8.5%) and diameter $d = 630$ nm (6.3%), rhodamine isothiocyanate (RITC) dye was added during synthesis, which resulted in an intensity gradient of dye molecules along the major axis of the particle [72]. The particles were coated with a 175 nm non-fluorescent outer shell. Particle suspensions were prepared by dispersing the rods in an index-matching mixture ($n_D^{21} = 1.45$) of either dimethylsulfoxide (DMSO) and ultrapure water (Millipore system) or glycerol and ultrapure water. The particles were first dispersed in DMSO or glycerol, after which water was added until the suspension was index-matched by eye. This resulted in mixtures of 91 wt% DMSO in water and 85 wt% glycerol in water.

Next, sample cells were constructed with standard microscopy slides and No. 1.0-1.5 glass coverslips (Menzel-Gläzer). After the cells were filled with the suspension, they were sealed with UV-glue (Norland No. 68). The suspensions were imaged with a confocal microscope (Leica SP2 or Leica SP8) using a 63×/1.4 or 100×/1.4 oil-immersion confocal objective (Leica). We corrected the 3D images for distortion of the axial (z) distances due to the refractive index mismatch between sample ($n_D^{21} = 1.45$) and immersion oil ($n_D^{21} = 1.51$), which resulted in an increase of axial distances of 5% [141]. In Figs. 4.2c-e, three orthogonal slices through this 3D volume are shown. The larger width of the PSF in the axial (z) direction is clearly visible. Notice that the pixel size in x,y (50 nm) is smaller than in z (78 nm). Figs. 4.2f-h show the same rod after rescaling to cubic pixels, filtering and particle-fitting. In Fig. 4.2i, we show the intensity histograms of two rods that were oriented parallel to the xy image plane of the confocal microscope. The continuous (red) line shows the intensity histogram of a single uniformly dyed rod and the dashed (green) line that of a gradient-dyed rod [72].

Freely diffusing silica rods. For the experimental measurements on a dilute suspension of silica rods we used particles with length $l = 3.3$ μm ($\delta = 10\%$) and diameter $d = 550$ nm ($\delta = 11\%$), as measured with TEM. The particles were fluorescently labelled with a 30 nm (FITC) shell. The particles were dispersed in an index matching mixture of 85 wt% glycerol in water. The density of the solvent mixture was $\rho = 1.222$ g/ml [199] and the viscosity $\eta = 92$ cP (22°C), as measured with an SV10 viscometer (A&D Company). This mixture not only matches the refractive index of the particles ($n_D^{25} = 1.45$), the high viscosity slows down the particle dynamics enough to measure their short-time self-diffusion in 3D. Because the density of this mixture is significantly lower than the density of the particles $\rho = 1.9$ g/ml [72], sedimentation cannot be avoided. We assume, however, complete decoupling between translational motion, rotational motion and sedimentation [196]. A fused quartz capillary (Vitrocom) was filled with a dilute suspension (volume fraction $\phi < 1\%$) of the fluorescent silica rods. The suspension was imaged with a confocal microscope (Leica SP8) equipped with a fast 12 kHz resonant scanner and hybrid detector. Images with 8-bit pixel-depth were acquired using a white light laser with a selected wavelength of 488 nm. A confocal glycerol immersion objective 63×/1.3 (Leica) was used, which is optimized for refractive index $n_D = 1.45$. If we assume a Poisson distribution of the noise, we can easily estimate the signal to noise ratio (SNR) of a single image because of the photon counting mode of the hybrid detector. We use the definition SNR $= \sqrt{n_p}$ with n_p the number of detected photons in the brightest part of the image [95]. To avoid hydrodynamic interactions with the wall, particles were imaged 20 μm deep into the sample. We recorded 800 repeats of 3D

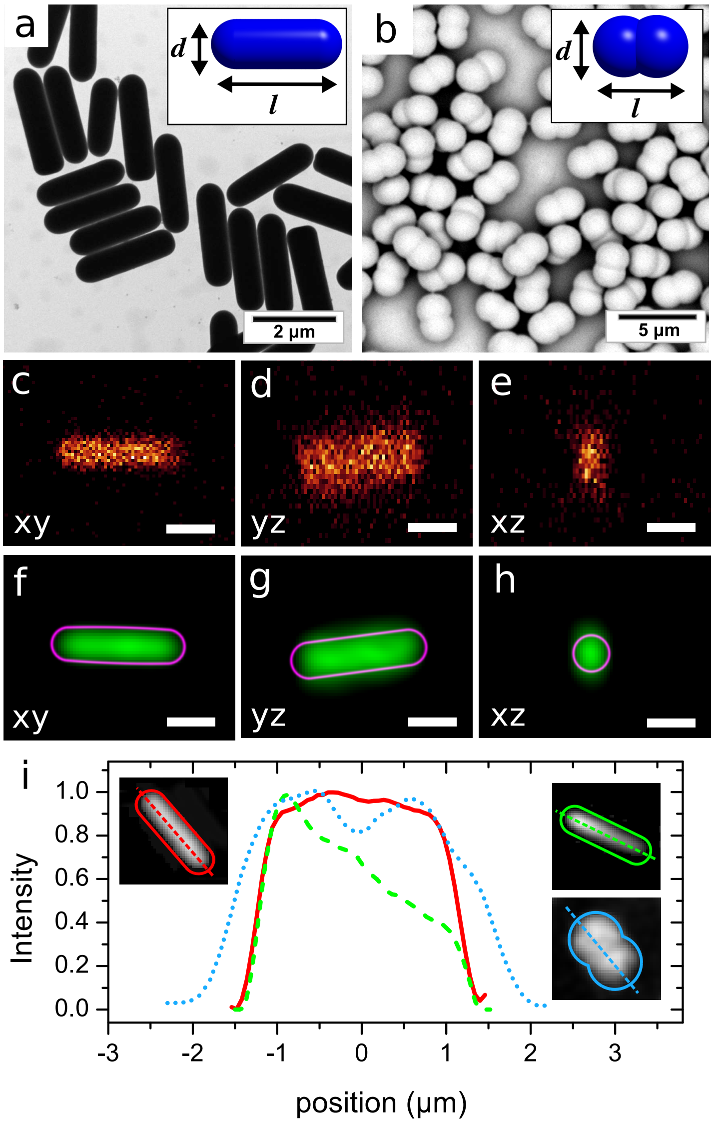

Figure 4.2. Particle fitting in 3D. (a) Transmission electron microscopy (TEM) micrograph of fluorescently labelled silica rods with length $l = 2.37$ μm ($\delta = 10\%$) and diameter $d = 640$ nm ($\delta = 7.5\%$). (b) Scanning electron microscopy (SEM) micrograph of poly(methyl methacrylate) (PMMA) dumbbells with length $l = 3.2$ μm ($\delta = 5\%$) and diameter $d = 2.1$ μm ($\delta = 8\%$). (c-e) Three orthogonal slices through a 3D confocal microscopy image of a fluorescent silica rod suspended in 85wt% glycerol/water. The scale bars are 800 nm. (f-h) The images after rescaling, filtering and fitting. The magenta outline indicates the final fit from which the position and orientation is computed. (i) The (normalized) intensity histograms along the major axis of particles that are oriented in the xy plane, obtained from confocal microscopy images. The (red) solid line is from a uniformly dyed silica rod. The (green) dashed line is from a silica rod with a gradient in dye distribution and the (blue) dotted line was obtained from a uniformly dyed PMMA dumbbell.

image stacks consisting of 512 × 261 × 66 pixels with voxel size 144 × 144 × 331 nm. The time to record a single 3D volume was $\tau = 1.80$ s. During this time, the particles are expected to translate on average $\sqrt{2\, D_t\, \tau} = 110$ nm in each direction and rotate only $\sqrt{4\, D_r\, \tau} = 0.1$ rad.

PMMA Dumbbells. Dumbbell-like poly(methyl methacrylate) PMMA particles were synthesized from spherical polymer particles [200] through an over-swelling method [165]. Scanning electron microscopy (SEM) was used to determine the length $l = 3.2$ μm ($\delta = 5\%$) and diameter $d = 2.1$ μm ($\delta = 8\%$) of the particles, see Fig. 4.2b. The particles were homogeneously fluorescently labelled by a post-dying treatment with (rhodamine B isothiocyanate)-aminostyrene (RAS) dye [165]. The particles were dispersed in decahydronaphthalene (decalin, mixture of cis/trans) and stabilized by a nonionic surfactant (span 85), which nearly matched the refractive index of the particles [165]. A glass capillary (VitroCom) was filled with the suspension and sealed with an epoxy glue (Bison kombi rapide). The samples were imaged with a confocal microscope (Nikon C1) using a laser wavelength of 543 nm and a 100×/1.4 oil immersion objective. The intensity distribution along the major axis of a dumbbell, as recorded with confocal microscopy, is indicated by the dotted (blue) line in Fig. 4.2i.

AuNRs@SiO$_2$ & 3D electron tomography. For the fabrication of a spherical cluster of nanorods, we first synthesized gold nanorods following the method described in Ref. 201. Next, the gold rods were coated with a layer of mesoporous silica (AuNRs@SiO$_2$) [202], which resulted in particles with length $l = 119$ nm and diameter $d = 68$ nm, as measured with TEM. Afterwards, clusters were fabricated via an emulsification process [158,203]. Brightfield TEM tilt series of an 11-particle NR-cluster were acquired by tilting the sample over a range of -65° to 65° and recording images every 2°. Images were taken on a Tecnai 20 (FEI) transmission electron microscope, operating at 200 kV with an LaB$_6$ electron source, in bright field mode. Tomographic reconstructions of the images were made with the iMOD software package using the simultaneous iterative reconstruction technique (SIRT) [204, 205]. After reconstruction, the data stack was filtered using a low frequency Fourier filter (iMOD) and inverted to ensure light particles on a dark background to enable individual particle identification.

4.3. Results

4.3.1. Determination of 3D particle positions & orientations in dense suspensions

To test our 3D particle-fitting algorithm we identified the fluorescent particles in a concentrated suspension of silica rods, as shown in Fig. 4.3. The particles were uniformly dyed, had a length $l = 2.37$ μm (10%), diameter $d = 640$ nm (7.5%) aspect ratio $l/d = 3.7$ and were dispersed in a 85 wt% glycerol in water mixture. Small regions of hexagonally stacked particles existed in the sample (Fig. 4.3c), however there was no long-ranged order in the sample and particles seemed jammed or arrested in different orientations. Fig. 4.3a shows that 5.2 μm deep in the sample, the fluorescent signals of the particles did not overlap significantly in xy, despite the high particle concentration. This is due to the 190 nm non-fluorescent outer shell of the particles which was deliberately grown around the particles during synthesis to resolve them individually, even when they were lying side-by-side. However, the orthogonal slices in Figs. 4.3b-c show that particle signals did overlap in the z-direction, even after noise filtering. Nevertheless, by visual inspection of the (magenta) particle outlines in Figs. 4.3d-f we conclude that the algorithm correctly identified the orientations and positions of the particles, despite the high particle concentration. Fig. 4.3g shows a computer generated reconstruction of the sample, with colours indicating the 3D orientation of the particles.

Fig. 4.4 shows a second example of the performance of our fitting-algorithm in a concentrated suspension. The rods in this sample had length $l = 2.6$ μm (8.5%), diameter $d = 630$ nm (6.3%) and were dispersed in an index-matching mixture of DMSO/water. After the particles had been left to sediment for several days, they ordered into smectic layers, more or less parallel to the xy-plane, as can be seen from Fig. 4.4a (12.5 μm deep in the sample). It can also be seen that the particles had an intensity gradient along their major axis and that there was significant overlap of the fluorescent signals in the xy-image (Fig. 4.4a). As expected, it was even more difficult to resolve individual particles in the z-direction (Figs. 4.4b-c), however, it is clear from the hexagonal pattern in Fig. 4.4b that the particles formed a smectic-B phase. The magenta outlines in Fig. 4.4d-f show the result of the particle fitting. By visual inspection of the outlines in the complete image-stack (containing 1699 particles), we conclude that $> 98\%$ of the particles had been correctly identified by the algorithm. In Fig. 4.4g we show a 3D reconstruction of a part of the image-stack, which clearly shows 3D orientational order, smectic layering, and transverse (red and blue) particles.

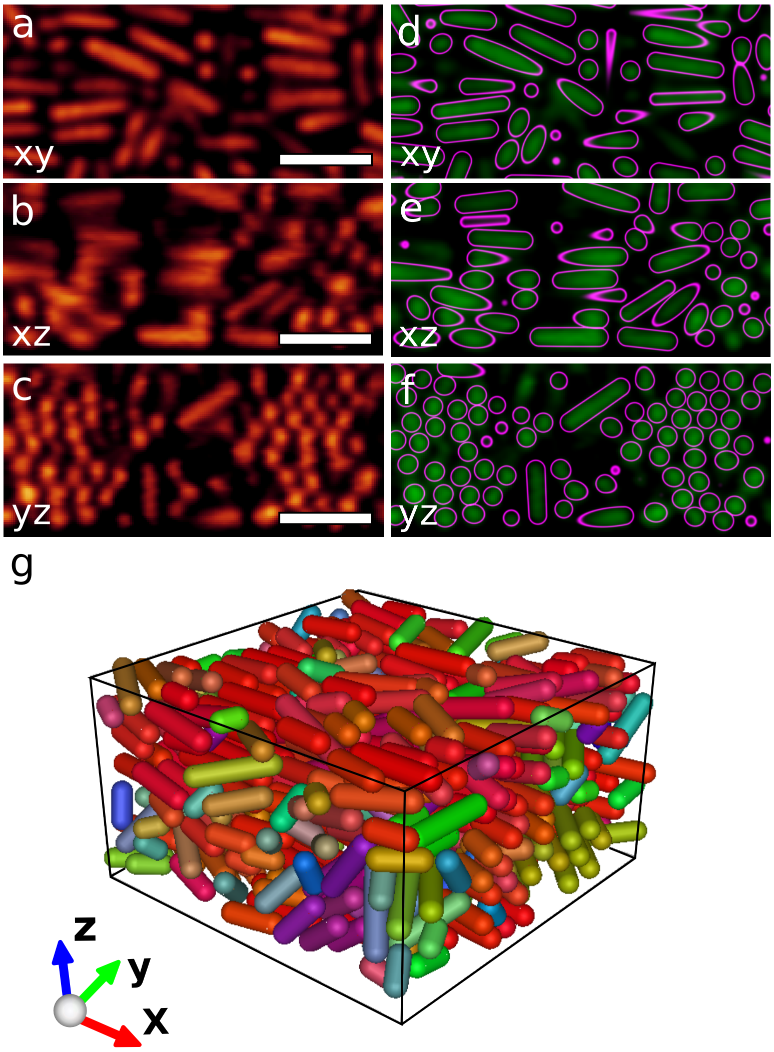

Figure 4.3. Local order in a dense sediment of rods with length $l = 2.37$ μm (10%), diameter $d = 640$ nm (7.5%) and aspect ratio $l/d = 3.7$, dispersed in a glycerol/water mixture. The particles had an outer non-fluorescent shell of 190 nm. The dimensions of the image volume were 512 × 201 × 79 pixels with voxel sizes 60 × 60 × 83 nm in x,y and z. The time to record the complete stack was 3.37 s. (a-c) Close-ups of orthogonal slices through the 3D image, after filtering and (d-f) after particle identification. The scale bars are 3 μm. (g) Computer rendered 3D reconstruction of the sample with the RGB value of the colour indicating the particle orientations.

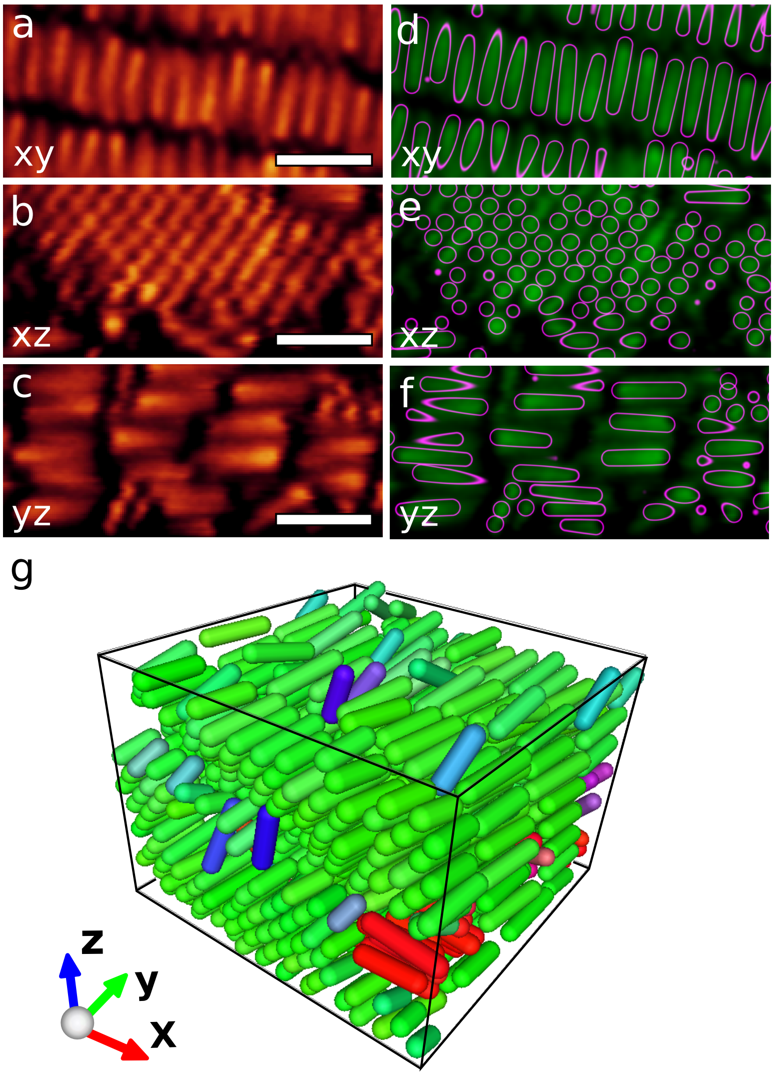

Figure 4.4. Smectic-B phase of rods with length $l = 2.6\ \mu$m (8.5%), diameter $d = 630$ nm (6.3%) and aspect ratio $l/d = 4.1$, dispersed in a DMSO/water mixture. The particles had an outer non-fluorescent shell of 175 nm. The dimensions of the image volume were 256 × 256 × 151 pixels with voxel size 58 × 58 × 104 nm in x,y and z. The time to record the image stack was 73.3 s. (a-c) Orthogonal sections after filtering. (a) 12.5 μm deep in the sample, particles were ordered in smectic-like layers. (d-f) Identified particles are outlined in magenta. All scale bars are 3 μm. (g) Computer rendered 3D reconstruction of the sample with the RGB value of the colour indicating the particle orientations.

4.3.2. Determination of 3D positions and orientations of gold nanorods

Although our algorithm was written for analysis of confocal microscopy images, it is also applicable to other 3D image-stacks of uniaxial symmetric particles. As an example, we show results of the identification of gold nanorods (AuNRs) from a 3D transmission electron microscopy (TEM) tomographic reconstruction in Fig. 4.5. The TEM micrograph in Fig. 4.5a shows the gold nanorods (in black), that were coated with a layer of mesoporous silica (dark grey). Figs. 4.5b-c show two orthogonal sections through the 3D reconstruction of the cluster. The images were inverted to enable particle identification with our algorithm. Figs. 4.5d-e show the same orthogonal sections after filtering, with identified particles outlined in red. Finally, Fig. 4.5f shows the 3D reconstruction, with color-coding of the 3D orientation of the rods. The algorithm had identified all 11 particles and the reconstruction clearly shows that there was some degree of orientational ordering inside the cluster.

We are aware that a substantial amount of information on the 3D structure of the nanoparticles can be measured directly (and manually) from the 3D tomogram itself. Our image-processing algorithm however can determine unambiguously the 3D positions

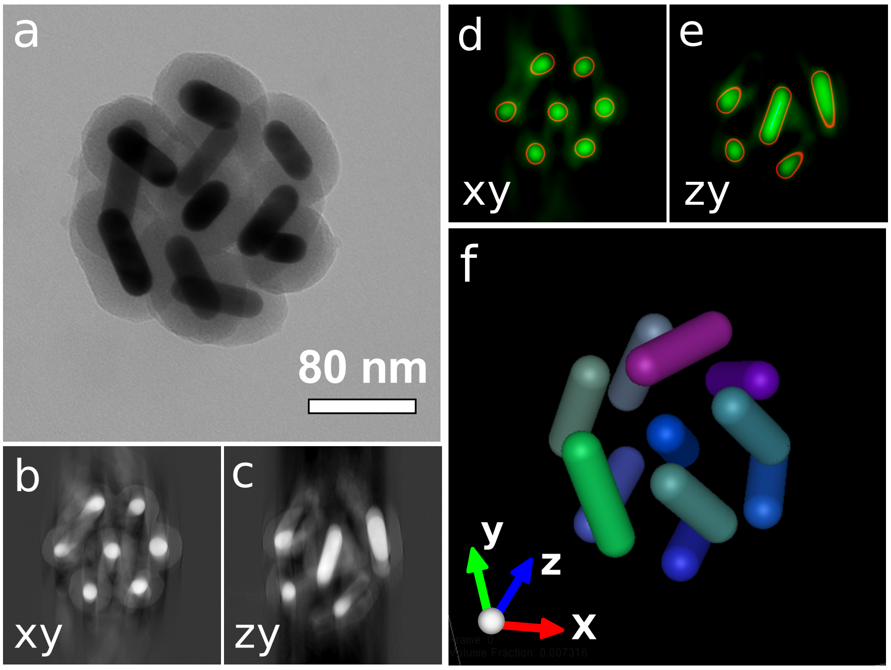

FIGURE 4.5. Identification of the positions and orientations of 11 gold nanorods coated with mesoporous silica (AuNRs@SiO$_2$), confined in a small spherical cluster. (a) A single TEM image that was part of the tilt-series used for the tomographic reconstruction. (b) An *xy*- and (c) *zy*-view of the 3D electron tomogram. The images were inverted for particle identification. (d) Corresponding *xy*- and (e) *zy*-views of the filtered images with the identified particles outlined in red. (f) 3D reconstruction of the nanorod cluster. Colours indicate their 3D orientations.

and orientations of the particles and can therefore be useful for the quantification of (larger) nanoparticle assemblies and should in principle also work on other types of samples, e.g. self-assembled clusters of nano-dumbbells [206].

4.3.3. 2D particle analysis

Our rod-like particle identification in 3D results in all 5 degrees of freedom of the particles and consequently enables unambiguous calculation of physical quantities such as translational motion and the orientation distribution function. However, fast 3D confocal imaging of particle suspensions is still limited to a time resolution of seconds, requires large data storage and subsequent image analysis is time consuming. Hence we now turn to some examples of anisotropic particle identification from 2D confocal images. For a 3D system, this will only result in *projected* angles and lengths of the particles. However, this information can still be useful to capture significant information on the physics of these systems. For example, Troppenz *et al.* derived a theoretical expression for the projected orientation distribution function of polarizable rod-like particles in an electric field and showed that these distributions were in good agreement with particle identification of 2D confocal microscopy images of 3D samples [207]. Another example is the extraction of the 3D rotational diffusion coefficient D_r and the perpendicular translational diffusion coefficient $D_\perp$ from 2D (projected) bright-field data [208].

In Fig. 4.6a, we show an example of a layer of fluorescent silica rods with length l = 2.37 μm (10%) and diameter d = 640 nm (7.5%) on the bottom glass slide of a 3D sample. The identified positions and orientations are indicated with a (green) line. Fig. 4.6b shows a 2D confocal slice through a 3D sample of fluorescent PMMA dumbbells with length l = 3.2 μm (5%) and diameter d = 2.1 μm (8%). The particles were ordered on a hexagonal lattice, however they were still free to rotate, i.e. they formed a plastic crystal [165]. A computer rendered reconstruction of the projected length and orientation of the rods and dumbbells is shown in Fig. 4.6c and Fig. 4.6d respectively. The colours indicate the orientation in the plane of observation. Note that particles that are oriented (almost) perpendicular to the plane of observation do not have a well defined projected orientation angle.

Using the projected angles obtained from 2D confocal microscopy images of 3D samples, we can calculate the projected 2D nematic order parameter $S_{2D'}(\psi)$, with ψ the in-plane projected angle, see equation 4.10. We investigated how well these values compare to the actual 3D nematic order in the system, using computer generated confocal-like test-images, shown in Fig. 4.7. In Fig. 4.7a, we show a 3D snapshot from a Molecular Dynamics (MD) simulation of 4000 spherocylinders with with aspect ratio l/d = 6 (with l the end-to-end length of the particle) and volume fraction ϕ = 0.3. The particles were initially perfectly aligned parallel to the planes that were later used to generate the test-images. Because the volume fraction $\phi = 0.3$ was below isotropic-nematic phase coexistence [209], the suspension gradually formed an isotropic phase upon equilibration, which resulted in the full range of perfect to almost absent nematic alignment in this system. For this set of 3D particle coordinates, we calculated the

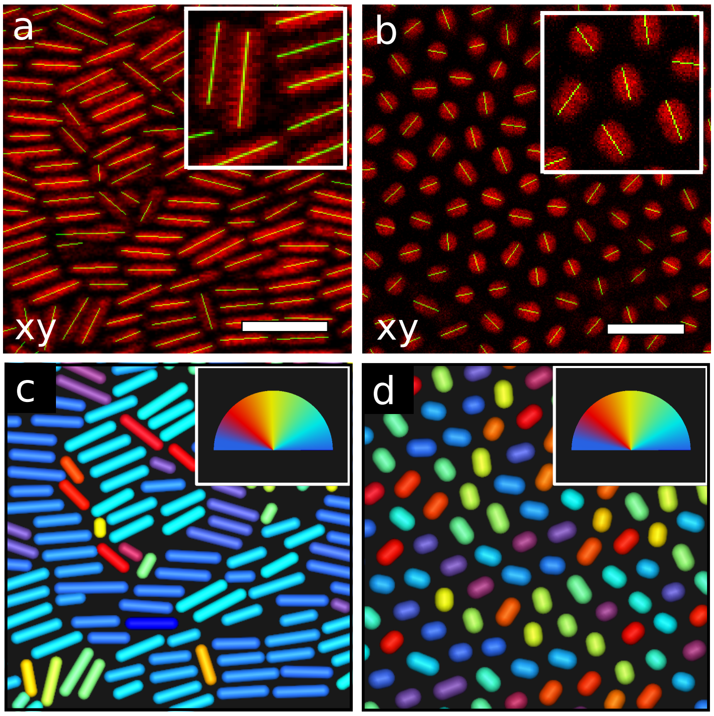

FIGURE 4.6. 2D particle identification. (a) Result of particle identification in a dense layer of silica rods with length $l = 2.37$ μm (10%), diameter $d = 640$ nm (7.5%) and aspect ratio $l/d = 3.7$, dispersed in a DMSO/water mixture. The identified particles are indicated by the green lines. The scale bar is 4 μm. (b) Identification of PMMA dumbbells with length $l = 3.2$ μm (5%), diameter $d = 2.1$ μm (8%) and aspect ratio $l/d = 1.5$ dispersed in decalin. The particles formed a (plastic) crystalline phase. The scale bar is 10 μm. (c-d) Computer generated reconstructions of the two samples in (a-b). Colours indicate the projected angle ψ.

3D nematic order in the system $S_{3D}(\theta)$, with θ the angle between the director and the main axis of the particle. Using the same set of 3D coordinates (obtained from simulation), we generated confocal-like 3D image-stacks (see Section 4.2.2). We first rescaled the simulation data so that the volume fraction was 0.1, the boxsize 256 × 256 × 256 voxels and the diameter of the rod 4.5 pixels. Then, the computer generated data were convolved with a 3D Gaussian approximation to the point spread function (PSF) ($\sigma_x/d = \sigma_y/d = 0.2$ and $\sigma_z/d = 0.4$). After the addition of some random Gaussian noise ($\sigma_n = 0.09$), a 2D slice of the sample resembled the real experimental data well, see Fig. 4.7b. In Fig. 4.7c we show the same image as in Fig. 4.7b, after 2D particle fitting, indicated by the green lines. Using the projected particle angles obtained from particle fitting, we obtained for the projected 2D nematic order parameter $S_{2D'}(\psi) = 0.54$, which is in strong agreement with the value for the 3D nematic order parameter $S_{3D}(\theta) = 0.53$. We then calculated the 3D nematic order parameter S_{3D} for the full set of coordinates obtained from simulation and compared them to the projected 2D order parameter $S_{2D'}$, shown in Fig. 4.7d. It is clear from Fig. 4.7d that the order parameter determined from 2D image slices gives a good indication of the actual 3D nematic order in the system, at least when the director lies approximately in the image plane of highest resolution. Analysis as a function of the orientation of the rods compared to the imaging plane is in progress.

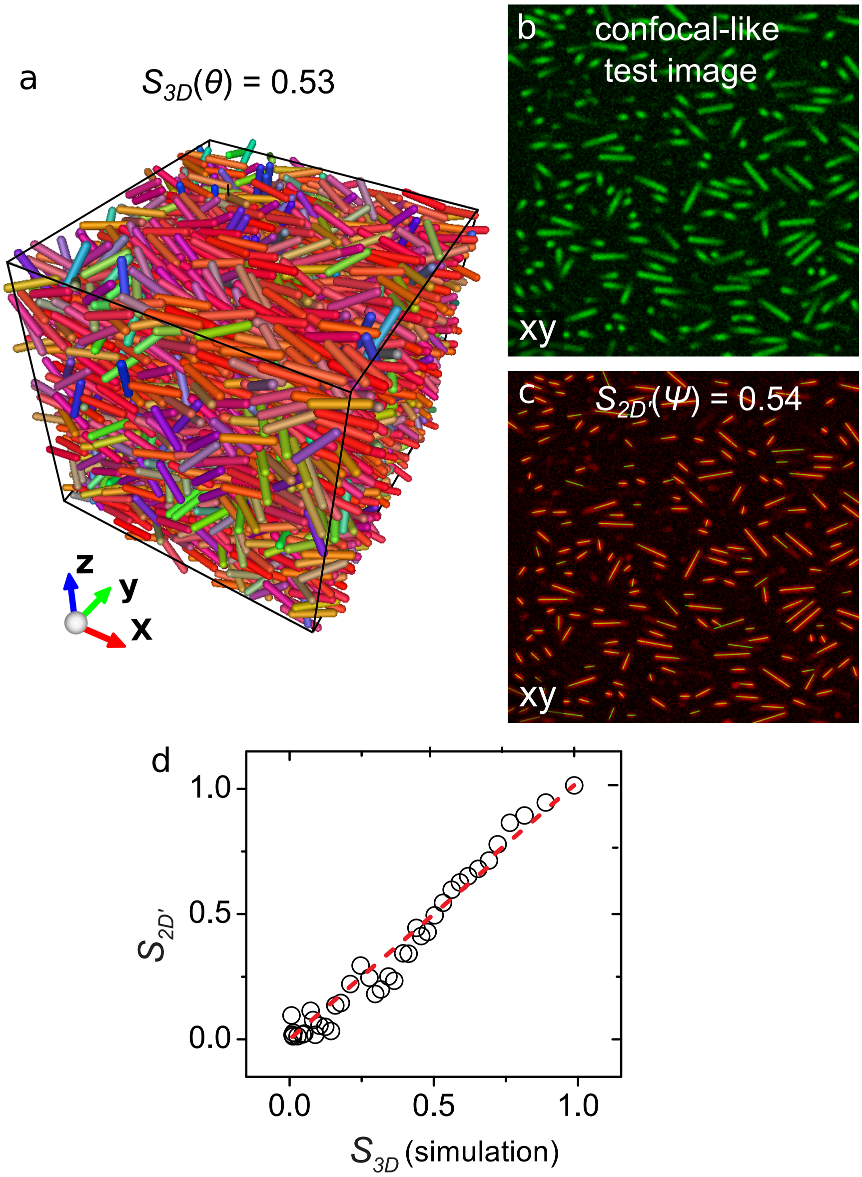

Figure 4.7. The nematic order parameter obtained from 2D slices compared to the actual 3D nematic order in the system. (a) Snapshot of a Molecular Dynamics (MD) simulation of 4000 spherocylinders with aspect ratio $l/d = 6$ and volume fraction $\phi = 0.3$. (b) Computer generated 2D confocal-like test-image, generated from the configuration shown in (a). (c) The same image as in (b) after 2D particle fitting. (d) The 3D nematic order parameter S_{3D} calculated from simulation compared to the projected 2D order parameter $S_{2D'}$ calculated after particle identification in 2D test-images.

4.3.4. Testing the accuracy of the algorithm for non-overlapping particle signals

In this section, we assess the accuracy of our algorithm in more detail. We focus on the fitting accuracy of the algorithm when applied to images containing particle signals that are well separated. Although this situation is much less demanding compared to partially overlapping signals, care has to be taken when fitting this type of data as well. The main reason is that the (fluorescent) diameter of typical rod-like particles used in our experiments ($d_{fl} \sim 300$ nm) is comparable to the resolution of a typical confocal microscope ($200-300$ nm in the lateral and $500-700$ nm in the axial direction [102, 141]). Additionally, the PSF itself is anisotropic, which can result in a (strongly) distorted particle shape. Things become progressively worse when there is a refractive-index mismatch between the sample and immersion fluid, which deteriorates the PSF, introduces an intensity fall-off with height and distorts axial distances [88, 141].

We therefore determined the accuracy of our algorithm using two approaches. In the first approach we investigated both the effect of the PSF and the effect of noise on particle tracking accuracy using computer generated data. The second approach consisted of an experimental measurement of the translational and rotational diffusion of a dilute suspension of silica rods.

The effect of the point spread function and noise on particle fitting accuracy. To test the effect of a theoretically approximated PSF and the effect of noise on particle tracking accuracy, we constructed time-series of 3D test-data using a single-particle approach (see Section 4.2.2 and 4.2.4). For the first set of particles (fixed on a hexagonal lattice) we used a rotational diffusion coefficient $D_r^* = 0.0025$ rad^2. We generated 3D image stacks of 200 × 163 × 37 pixels for every timestep (1000 timesteps in total). The particles that we generated had a length of $l = 25$ pixels and diameter $d = 7$ pixels in an xy-image. To approximate the effect of the PSF we used a fixed $\sigma_x/d = \sigma_y/d = 0.3$, representing a constant resolution in the xy direction, with σ_i the standard deviation of the Gaussian kernel and d the diameter of the particle. In the vertical direction we used $\sigma_z/d = 0.3$, 0.6 and 0.9. Figs. 4.8a-c show xz-views of this decrease in z-resolution. Typical rod-like particles used in our experiments have a length $l \sim 3$ μm and a fluorescent diameter $d_{fl} \sim 300$ nm. The FWHM of the Gaussian kernels in the z-direction therefore correspond to $2\sqrt{2\ln 2}\,\sigma_z = 212$ nm, 424 nm and 636 nm respectively. The resolution of our microscope, which we measured to be 190 nm in the lateral (xy) direction and 490 nm in the axial (z) direction (see Ref. 141 and Chapter 3), is within this range. In Figs. 4.8d-f we show increasing noise levels, obtained by adding Gaussian noise with standard deviation $\sigma_n = 0.09$, 0.18 and 0.27. These levels resulted in a signal-to-noise ratio (SNR) of 11.2, 3.8 and 1.7 respectively, which corresponds to typical SNR values of the confocal microscopy images that we used for particle tracking. Notice the strong similarity between Figs. 4.8d-f and Figs. 4.2d-e. In Fig. 4.8g, we show a test-image with $\sigma_z/d = 0.9$ and $\sigma_n = 0.27$, in Fig. 4.8h the same image after filtering

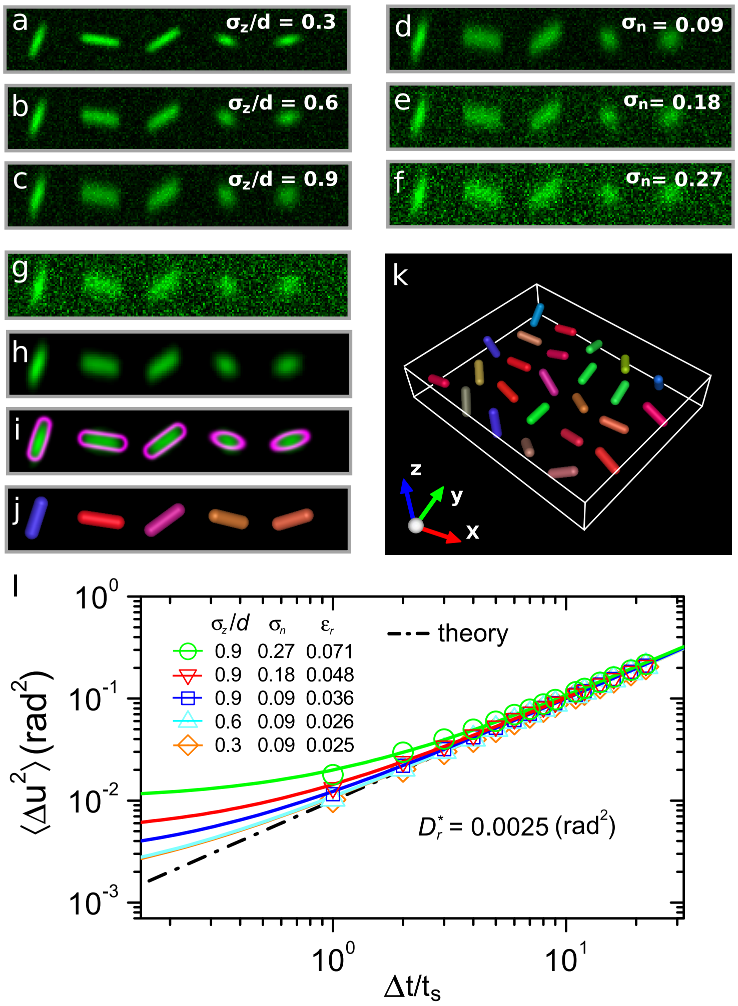

FIGURE 4.8. The effect of z-resolution (σ_z) and noise (σ_n) on the measurement of rotational motion. To study this effect, test-images were generated with 25 randomly rotating particles fixed on a lattice. (a-c) The effect of a decrease in z-resolution (increase in σ_z). (d-f) Increase in noise level σ_n. (g) Original test-image with $\sigma_z/d = 0.9$ and $\sigma_n = 0.27$. (h) The image after filtering and (i) after particle fitting. (j,k) Computer rendered particles with color coding based on their orientation. (l) Mean squared angular displacement (MSAD) for decreasing σ_z/d and σ_n. The measurement error ϵ_r decreases for decreasing σ_z/d and σ_n.

and in Fig. 4.8i the particle fitting as indicated by the magenta outline. Fig. 4.8j and Fig. 4.8k show the 3D reconstruction with RGB colours indicating particle orientation.

After identification of the orientations in each frame separately, we determined particle trajectories with existing IDL based routines [45]. Fig. 4.8l shows the calculated mean squared angular displacement (MSAD) for decreasing resolution and increasing noise levels. We obtained the correct D_r^* for all five test cases, as shown by the data-collapse with the theoretical result $4\,D_r\,t$ (black dashed dotted line) for $\Delta t/t_s > 10$. The (coloured) continuous lines are fits to equation (4.6). As expected, the error in the determination of the main axis of the rod (ϵ_r) increases with increasing noise level, as indicated in Fig. 4.8l. The results are summarized in Table 4.1, which shows that for our worst-case scenario of a z-resolution of 636 nm and signal to noise ratio of 1.7, we obtain for the error in the determination of the main-axis of the rod $\epsilon_r = 0.07$ rad, which corresponds to a small measurement error of 4.1°.

z-resolution		noise levels		error
σ_z/d	FWHM (nm)	σ_n	SNR	ϵ_r (rad)
0.3	212	0.09	13.5	0.025
0.6	424	0.09	11.4	0.026
0.9	636	0.09	11.2	0.036
0.9	636	0.18	3.8	0.048
0.9	636	0.27	1.7	0.071

TABLE 4.1. Static measurement error ϵ_r in the determination of the main axis of the rod, assuming $d = 300$ nm. The error increases with both σ_z and σ_n. For the worst case scenario of $\sigma_z/d = 0.9$ and $\sigma_n = 0.27$, the value for ϵ_r remains rather small.

To further test for any biases in our algorithm, we generated 3D test-images of single, freely diffusing particles with an imposed (rotationally averaged) translational diffusion coefficient $D_t^* = 0.01$ and rotational diffusion coefficient $D_r^* = 0.005$ rad^2. The particles were initially randomly oriented. We constructed 2000 time-frames of 3D image-stacks and convolved them with a Gaussian kernel with standard deviation $\sigma_x/d = \sigma_y/d = 0.3$ and $\sigma_z/d = 0.6$. We also added Gaussian noise with $\sigma_n = 0.09$ to the images. The particles had a length $l = 25$ pixels and a diameter $d = 7$ pixels. To test for a possible pixel-bias of the algorithm, we computed the fractional part of the determined positional coordinates as shown in Figs. 4.9a-c. Neither of the three coordinates shows a strong deviation from a flat distribution. We also computed the distributions of the absolute value of the three components of the orientation vector $\hat{\mathbf{u}}$, see Figs. 4.9d-f. The distributions are not completely flat, which is not surprising considering the limited number of pixels per particle and the effect of the (theoretically approximated) PSF. These deviations, however, did not hamper an accurate determination of the rotational motion of the particles. Fig. 4.9g shows the mean squared displacement (MSD) expected from theory and the corresponding result after particle tracking. The statistical errors for the individual measurement points are smaller than the symbol size. From the fit to equation (4.4), we obtain $D_t^* = (1.021 \pm 0.004) \times 10^{-2}$ and $\epsilon_t/d = (5.47 \pm 0.01) \times 10^{-2}$. In Fig. 4.9h, results are shown for the mean squared angular displacement (MSAD). Fitting to equation (4.5) results in $D_r^* = (5.06 \pm 0.06) \times 10^{-3}$ rad^2, which recovers the imposed theoretical value, and results in a small static orientation error of $\epsilon_r = (1.2 \pm 0.1) \times 10^{-2}$ rad.

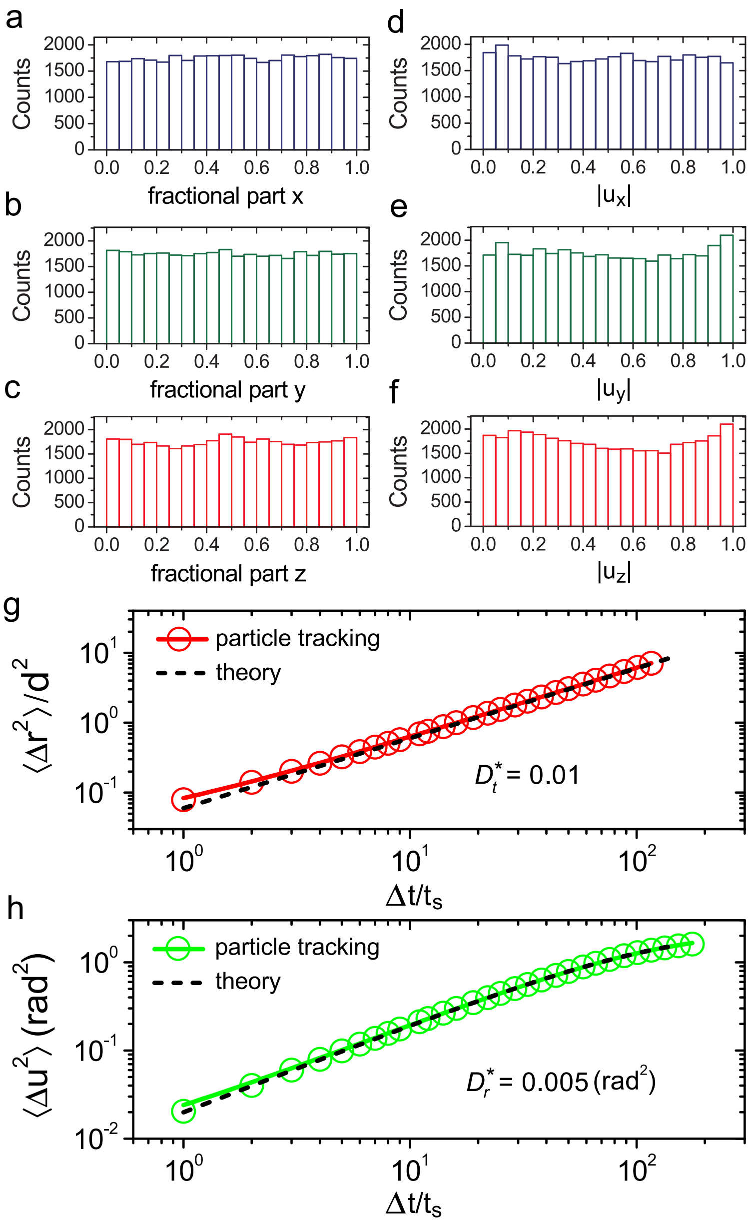

FIGURE 4.9. Tracking results from computer generated 3D test-images of single, freely diffusing particles. (a-c) The fractional parts of the positional coordinates do not show signs of significant pixel-bias. (d-f) The absolute value of the components of the orientation vector also do not indicate any strong orientational bias. (g) Mean squared displacement (MSD) of the centre-of-mass of the particles. (h) Mean squared angular displacements (MSAD). We retrieved the correct translational and rotational diffusion coefficients with small static errors ϵ_t and ϵ_r respectively. The statistical errors for the individual measurement points are smaller than the symbol size and the black dashed lines are expected from theory.

To summarize, we did not find any significant pixel-bias in either the position or the orientation. For the error in the positional measurement, we found $\epsilon_t/d \sim 0.05$, which indicates sub-pixel accuracy. Furthermore, the error in the measurement of the orientation also remained small ($\epsilon_r = (1.2 \pm 0.1) \times 10^{-2}$ rad).

Diffusive motion of rod-like particles. In this last section, we present experimental measurements of the diffusive motion of fluorescent silica rods in a dilute suspension, which provides a real-life test of the accuracy of our algorithm. The rods that were used had length $l = 3.3$ μm ($\delta = 10\%$), diameter $d = 550$ nm ($\delta = 11\%$) and aspect ratio $l/d = 6.0$. From the number of photons in the brightest part of the image, we estimated the signal to noise ratio to be SNR ≈ 3, which is in the range stated in Table 4.1. The tracking results, averaged over 8 particles, are shown in Fig. 4.10. A typical translational trajectory of 12 min is shown in Fig. 4.10a. From a fit to the average linear displacements (of all 8 particles) in the z-direction, we estimated the sedimentation speed to be $v_{sed} = 0.331 \pm 0.005$ μm/min. This value is slightly higher but comparable to the value of $v_{sed} = 0.28$ μm/min that we obtained from equation (4.7). For further analysis we subtracted the average linear displacements from the trajectories. Fig. 4.10b shows a rotational trajectory of 12 min for a single particle. In Fig. 4.10c we show the probability distribution of the norm of the displacement $|\Delta \mathbf{r}|$, for three different time-steps Δt. In Fig. 4.10d we show the same distribution for the norm of the displacements of the unit vector $|\Delta \hat{\mathbf{u}}|$. The solid black lines in Figs. 4.10c,d are fits proportional to $|\alpha|^2 \exp(-|\alpha|^2)$ with $\alpha = \Delta \mathbf{r}, \Delta \hat{\mathbf{u}}$ respectively. To extract the translational diffusion coefficient, we calculated the rotationally averaged mean squared displacement $\langle \Delta \mathbf{r}^2 \rangle$, as can be seen in Fig. 4.10e. For $\Delta t > 10$ s we found that $\langle \Delta \mathbf{r}^2 \rangle \sim t^{0.97}$ indicating diffusive behaviour. The statistical error in the individual measurement points is smaller than the symbol size. Fitting the data with equation (4.4), we obtain the short-time rotationally averaged translation diffusion coefficient $D_t = (3.06 \pm 0.01) \times 10^{-3}$ μm^2/s and static error $\epsilon_t = 45, 46$ and 59 nm in the x, y and z-direction respectively, which confirms that we can locate the particles with sub-pixel accuracy. The value for D_t is in strong agreement with the theoretical value obtained from equation (4.14) which is $D_t = 3.2 \times 10^{-3}$ μm^2/s. Finally, we calculated the mean squared angular displacement $\langle \Delta \hat{\mathbf{u}}^2 \rangle$, as shown in Fig. 4.10f. This time we obtained $\langle \Delta \hat{\mathbf{u}}^2 \rangle \sim t^{0.92}$ and for the short-time rotational diffusion coefficient $D_r = (1.32 \pm 0.02) \times 10^{-3}$ rad^2/s. This is in good agreement with the theoretical value $D_r = 1.5 \times 10^{-3}$ rad^2/s, obtained from equation (4.15). For the corresponding rotational relaxation time we found $\tau_r = 1/(2\, D_r) = 3.8 \times 10^2$ s, which confirms that we measured in the short-time diffusion regime. From the fit we also obtained $\epsilon_r = 0.07$ rad, which corresponds to a small angular uncertainty of $\sim 4°$.

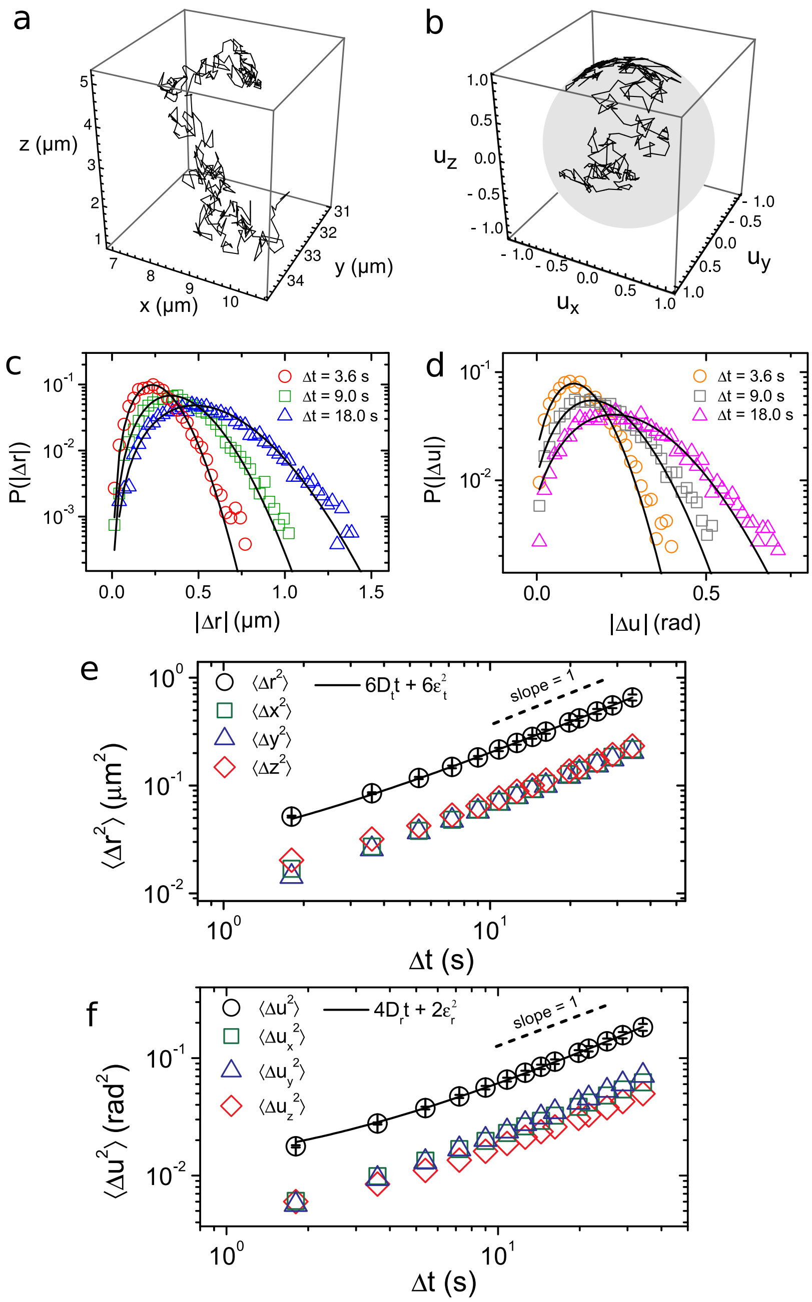

FIGURE 4.10. Experimental measurement on a dilute suspension of sedimenting silica rods with length $l = 3.3$ μm and diameter $l = 550$ nm suspended in a 85 wt% glycerol in water mixture. (a) Typical translational and (b) rotational trajectory of a single particle. (c) Distribution of the translational displacements $|\Delta\mathbf{r}|$ and (d) rotational displacements $|\Delta\hat{\mathbf{u}}|$ for three different time-steps Δt. The displacements are an average over 8 particles and the black lines are fits. (e) The average mean squared displacement (MSD). The estimate for the static error ($\epsilon_t = 45, 46$ and 59 nm in x, y and z respectively) confirms sub-pixel accuracy. (f) Mean squared angular displacement (MSAD). The static error in the determination of the unit vector $\epsilon_r = 0.07$ rad corresponds to an angular uncertainty of 4°.

4.4. DISCUSSION

In this chapter we demonstrated a new image-processing algorithm that is capable of extracting the positions and orientations of fluorescent rod-like particles in both dilute and concentrated suspensions. The algorithm was originally written for three dimensions, however, most steps are straightforward to modify for two dimensions. Mohraz and Solomon [162] were the first, as far as we know, to describe an algorithm that can detect the position and orientation of ellipsoidal particles in 3D confocal microscopy images and this work follows a similar approach. The algorithm of Mohraz and Solomon groups clusters of pixels together to form backbones but does not use additional fitting steps, which we found necessary to correctly identify particles when there is significant overlap of particle signals. The difference in particle geometry (ellipsoids versus rods) combined with the small (fluorescent) particle diameter in our study might be the reason why we find that using only a maximum threshold and cluster analysis is not sufficient to identify rods in concentrated suspensions, even when the rods have a large (> 150 nm) non-fluorescent shell and a considerable electric double layer (~ 50 nm) [25, 28]. The rod-like particles used in this study have a repulsive interaction potential and therefore form dense smectic-like phases, which we now can identify on the single-particle level in the bulk. The algorithm also enables the study of glassy phases of anisotropic particles in three dimensions, which is promising since all current real-space glass-transition studies of anisotropic particles so far are either 2D [176–178] or tracer-host [167]. Finally, we would like to mention that the algorithm is also applicable to study the dynamics of (concentrated) ‘active colloids’ (e.g. self-propelled particles and bacteria), a field that is rapidly emerging [210].

Since the typical fluorescent diameter of the rod-like particles is around 300 nm, deconvolution of the image-stacks before particle fitting can be useful when particles are difficult to resolve individually. The necessary higher (Nyquist) sampling rate, however, is not always practical or even not possible for faster moving particles. Additionally, deconvolutions are sensitive to small changes in the rod-spread-function (RSP), introduced by e.g. polydispersity. A clear improvement of the algorithm, therefore, is to fit the particles with the RSP, analogous to the fitting of the sphere-spread-function (SSF) reported by Jenkins *et al.* [50], which is work currently ongoing. With this type of extension of the current algorithm it should also be possible to accurately measure in-situ particle polydispersity, which is known to have a large effect on e.g. the liquid-crystalline phase behaviour [211].

We also demonstrated that analysis of 2D confocal microscopy image-slices through a 3D sample yields an accurate estimate of the 3D (nematic) orientational order in the sample, for the full range of nematic order. This is of course only true if the nematic director is (approximately) parallel to the plane of observation. This result will benefit many experimental studies where 3D imaging is difficult or not even possible, such as rod-like particles subjected to electric fields or under shear. A full analytical treatment of the projected orientation distributions (and corresponding nematic order parameter values) of single particles aligned by an electric field is currently in progress [207].

By measurement of freely diffusing rods, we acquired additional information on the accuracy of our algorithm. Although the motion is analysed in the lab-frame and therefore translational and rotational motion should be coupled [171], we did not observe such behaviour since the friction anisotropy in our 3D measurement is small $D_{\|}/D_{\perp}$ $= 1.3$ and because we averaged over an ensemble of particles and over many initial orientations. We found that the error in locating the rods ($\epsilon_t = 45, 46$ and 59 nm in the x, y and z-direction respectively) confirms sub-pixel accuracy and agrees roughly with the criterion for spherical particles that $\epsilon_t \sim M/N$, with M the pixel-size and N the diameter of the particle in pixels [45]. The value for the (short-time) rotational diffusion coefficient $D_r = (1.32 \pm 0.02) \times 10^{-3}$ rad^2/s, is one order of magnitude larger than previously accessible with 3D confocal microscopy [181] which is, however, due to the equipment rather than the image-processing. The error in the determination of the orientation of the rod ($\epsilon_r = 0.07$ rad) is in the range of the values obtained via simulated test-images, shown in Table 4.1. The rule-of-thumb that $\epsilon_r \sim 1/P_a$ with P_a the half-length of the rods in pixels [181] seems to hold quite well in our case, since $1/P_a = 0.08$ in our measurements.

4.5. CONCLUSION

We developed an algorithm that extracts the positions and orientations of rod-like particles from 2D and 3D confocal microscopy images. The algorithm is tailored to a system of fluorescently labelled silica rods and can identify these particles even in the bulk of 3D concentrated phases where the fluorescent signals of the particles overlap considerably. This allowed us to determine the 3D positions and orientations of particles in a concentrated disordered phase and in a liquid-crystalline smectic-B phase. The algorithm also works on confocal microscopy images of other uni-axial symmetric particles such as dumbbells and on tomography reconstructions of gold nanorods, which enables the 3D quantification of (large) nano-particle assemblies. By generating realistic 3D test-image stacks, we showed that it is possible to obtain an accurate estimate of the 3D nematic order in a system of rod-like particles from a single 2D confocal microscopy image-slice trough the sample. We determined the accuracy of the algorithm for varying z-resolution and noise levels from generated 3D test-images. Despite the (anisotropic) distortion of the theoretically approximated point spread function (PSF) and the low signal to noise ratio (SNR), the error in the determination of the orientation of the particles remained small. These results confirmed that we can accurately track rod-like particles with (fluorescent) diameters down to 300 nm. With our algorithm and a fast confocal microscope we determined the translational and rotational motion of a dilute suspension of sedimenting silica rods. We demonstrated that the measured diffusive motion was in good agreement with theory (neglecting sedimentation) and that we can track the particles with sub-pixel resolution.

This novel algorithm therefore allows for studies of structure and dynamics on the particle level of dense liquid-crystalline phase behaviour (such as nematic, smectic and crystalline phases), but also allows for studies of the glass transition of anisotropic rod-like particles in three dimensions. Of course, the algorithm will also be applicable to dilute suspensions or in cases where rod-like particles are used as tracers, such as in biophysical or micro-rheology studies.

4.6. ACKNOWLEDGEMENT

This work was done in collaboration with Michiel Hermes, Anke Kuijk, Bo Peng, Bart de Nijs, Tian-Song Deng and Marjolein Dijkstra. We thank Eric Weeks, Kenneth Desmond and Anjan Gantapara for useful discussion. We also thank Henriëtte Bakker, Chris Kennedy and Bing Liu for useful feedback on the algorithm and Hans Meeldijk for help with the electron microscopy data. We thank Teun Vissers for critical reading of this chapter.

Part 2

Self-assembly of Colloidal Spheres and Rods

5

Out-of-Equilibrium Crystallization in Hard-Sphere Colloidal Fluids Driven by Oscillatory Shear

ABSTRACT

In this chapter we investigated oscillatory shear-induced crystallization in hard-sphere colloidal fluids. We performed experiments on poly(methyl methacrylate) (PMMA) colloids and non-equilibrium Brownian Dynamics (NEBD) simulations, which allowed us to investigate the shear-induced order in real-space. All samples in both experiments and simulation were *below* the coexistence density of hard-sphere freezing, so the shear-induced crystals were out-of-equilibrium and melted after cessation of the shear. The physics is therefore fundamentally different from shear-induced crystallization in jammed or glassy systems. We investigated two distinct oscillatory shear-induced phases: an oscillatory twinned fcc phase and a sliding layer phase. For the twinned fcc phase, the crystallization seemed to proceed via a nucleation-and-growth type of mechanism. For the sliding layer phase, however, we found a much more continuous crystallization process. The simulation results (without hydrodynamic interactions and an enforced linear shear profile) were in strong agreement with the experiments, suggesting that hydrodynamic interactions do not strongly affect the shear-induced structures. We also present preliminary experimental results on the melting of these phases, which occurred immediately after cessation of the shear.

5.1. INTRODUCTION

It is well known that shear has a large effect on colloidal self-assembly [30]. A remarkable example is that a hard-sphere fluid can crystallize as the result of oscillatory shear and that the shear-induced crystal melts back upon cessation of the shear [31, 32]. These shear induced crystals are out-of-equilibrium and therefore the physics is fundamentally different from shear-induced crystallization in jammed or glassy systems [212, 213]. Out-of-equilibrium crystallization of particles can also occur in systems with other driving forces than shear-flow, such as charged particles in electric fields [214, 215], active colloidal particles [216] and shaken granular matter [217]. Crystallization induced by shear is the result of flow-induced rearrangements in the micro-structure of the fluid, caused by an interplay between hydrodynamics interactions, Brownian motion and inter-particle forces. Understanding such complex flow behavior is industrially important and the possibility to switch between different states by means of an external field is promising for many applications (e.g. in the case of electronic ink when the switching is between a state displaying color by interference effects and one with less order and no color).

When subjected to *steady* shear, hard-sphere suspensions that are fluid in equilibrium do not display pronounced three-dimensional (3D) ordering for shear rates ranging from $10^{-3} - 10^{2}\ s^{-1}$. However, when *oscillatory* shear is applied to these samples, shear-induced ordering is observed such as layering [62], string formation [218] and 3D crystal-like ordering [32]. The principal parameter governing the crystal-like ordering is the strain amplitude, which determines the distance of flow-induced interactions between the particles. For small strains, particles form hexagonal layers in the vorticity-velocity plane with one of the close-packed lines of particles perpendicular to the velocity direction. These layers slide from an ABC stacking at one extreme of the oscillation to ACB at the other, resulting in an oscillating twinned face-centered-cubic (fcc) crystal. For intermediate shear strain, the particles form hexagonal layers in the same plane as before, but now with one of the close-packed lines parallel to the velocity direction, and slide through the grooves of layers above and below. The oscillating twinned fcc phase and the sliding layer phase were observed with light scattering experiments on sheared hard-sphere suspensions [32] and on charged particles [219, 220]. The same structural rearrangements were observed in real space with suspensions that are *above* the bulk fluid coexistence density of hard spheres with optical and confocal microscopy [61, 221–223] and with light scattering experiments [32, 224]. Derks *et al.* showed for concentrated suspensions under steady shear, that the close-packed lines of particles of the hexagonal layers align with the velocity direction and that the hexagonal layers slide over each other in a zig-zag path, travelling from one triangular void of a neighboring layer to the other [225]. Non-equilibrium Molecular Dynamics (NEMD) simulations on oscillatory shear confirmed the formation of the twinned fcc and the sliding layer phase in samples that are fluid in equilibrium [226, 227].

For large strain amplitudes the hexagonal layers break up, resulting in strings of particles along the velocity direction, known as string formation. Weak string formation was observed in both steady and oscillatory shear experiments [32, 220]. Early NEMD simulation on hard-sphere fluids under *steady* shear showed that at very high shear rates particles form strings in the direction of the flow and that these strings arrange in a regular hexagonal pattern in the gradient-vorticity plane [228]. In some studies it was argued that this string phase is an artifact arising from the assumed linear velocity profile, founded on the fact that without such an assumption a shear thickening regime without strings was observed [229, 230], which is consistent with experiments on PMMA colloids under steady shear [231]. However, non-equilibrium Brownian Dynamics (NEBD) simulations on *oscillatory* shear revealed similar string like ordering [232], and the scattering diagram calculated from the string phase observed in simulations strongly resembles the experimental light scattering results [233]. NEMD simulations that do not make any assumption about the velocity profile revealed oscillatory shear-induced ordering in a Lennard-Jones fluid but do not report on ordering in all three dimensions [226]. More recently, real-space experiments identified *vorticity* aligned string-formation in oscillatory sheared hard-sphere fluids that are below the bulk freezing point [218]. However, this was mostly a confinement effect and the vorticity aligned strings disappeared when the volume fraction was increased towards the freezing point [218]. Real-space experiments by the same group, combined with rheological measurements and Stokesian dynamics, revealed that layering in hard-sphere fluids is not the driving force for shear thinning but is strongly correlated with a two-particle measure of the shear stress [234, 235]. The non-equilibrium phase behaviour of a bulk colloidal hard-sphere fluid under oscillatory shear was investigated by our group in 3D real-space, using both experiments on hard-sphere colloids and NEBD computer simulations, for volume fractions just below the freezing point ($\phi = 0.46 - 0.49$) [63, 236]. Depending on the amplitude and frequency of the oscillation, four regimes with different structures were identified: the oscillating twinned fcc phase, the sliding layer phase, a *velocity* aligned string phase and a phase that has not been reported previously in experiments, which consists of hexagonal layers of particles that are tilted with respect to the velocity-vorticity plane [63, 236].

In this chapter, we continue our real-space study of oscillatory shear-induced order in hard-sphere colloidal fluids using both experiments on poly(methyl methacrylate) (PMMA) colloids and non-equilibrium Brownian Dynamics (NEBD) simulations. First, the 3D real-space structure of an oscillating fcc phase and a sliding layer phase is presented and compared to existing light-scattering experiments. Then, we investigate the shear-induced crystallization kinetics of both phases on the single particle level and compare our experimental results to simulation. Finally, we present preliminary results on the melting of these phases, which occurs upon cessation of the shear.

5.2. Methods

5.2.1. Experimental methods

Particle characterization. The particles used in this study were poly(methyl methacrylate) (PMMA) spheres with a diameter $\sigma = 2.07$ μm and polydispersity of 3%, particles with diameter $\sigma = 2.10$ μm and polydispersity of 3%, and particles with diameter $\sigma = 2.64$ μm and polydispersity $\delta = 3\%$, as determined with Static Light Scattering (SLS). They were sterically stabilized with poly(12-hydroxystearic acid) (PHS) grafted onto a PMMA backbone which was chemically attached to the core of the particles and covalently labelled with fluorescent rhodamine isothiocyanate (RITC) dye for imaging [80]. Particles were dispersed in a 26 wt% mixture of *cis*-decahydronaphtalene (*cis*-decalin) in cyclohexyl bromide (CHB) saturated with the salt tetrabutylammonium bromide (TBAB). This mixture nearly matches the density of the particles ($\rho = 1.19$ g ml^{-1}) and also closely matches the index of refraction ($n_D^{25} = 1.492$). The viscosity of the solvent mixture was 2.2 mPa s [66]. The high salt concentration screens the charges on the particles, making them behave approximately as hard spheres [12].

The equilibrium phase behavior of the suspension was determined by filling five capillaries with different weight fraction of the sterically stabilized PMMA particles (0.388, 0.408, 0.419, 0.427 and 0.438). Because the particles were nearly density matched, these weighted values are approximately equal to the dry PMMA volume fraction ϕ_c. The capillaries were stored horizontally in a temperature controlled room at 21±1°C and after 22 hours the particle positions were determined over the complete height of the capillary with confocal microscopy. The fraction of particles that are part of a crystal was determined by 3D bond order parameter analysis, using the method of Ten Wolde *et al.* [237]. Because the particles were closely density matched, sedimentation did not have a significant effect during the 22 hours. With linear regression an average scaling factor $p = 1.23 \pm 0.01$ was determined that maps the values for ϕ_c onto the hard-sphere phase diagram [9], resulting in a freezing point $\phi_f = 0.40 \pm 0.01$ and melting point $\phi_m = 0.44 \pm 0.01$. The effective particle diameter was on average $1.23^{1/3} = 1.07$ times larger than determined with SLS. This is because the particles absorb some of the CHB, causing them to swell, combined with leftover charge effects [12]. The effective diameter was also measured by determining the distance of nearest approach from the first peak in the pair correlation function $g(r)$ of a crystalline domain in the coexistence region. Using the hard-sphere melting point ($\phi = 0.54$) as reference, this resulted in an effective particle diameter of 1.05σ, which is slightly smaller than obtained with the previous method.

Shear cell setup. A parallel plate shear cell mounted on top of an inverted confocal microscope was used to investigate the real-space behaviour of the particles under shear [238]. Fig. 5.1 shows a schematic of the shear cell and our choice of the coordinate system. The top and bottom plate are microscopy glass slides attached to translational cassettes that can be displaced with piezostepper motors. Alignment of the glass slides was performed using confocal microscopy in reflection mode using a 543 nm HeNe laser and an air objective (20x/0.7, Leica). The slides varied ~ 1 μm in the z-direction over

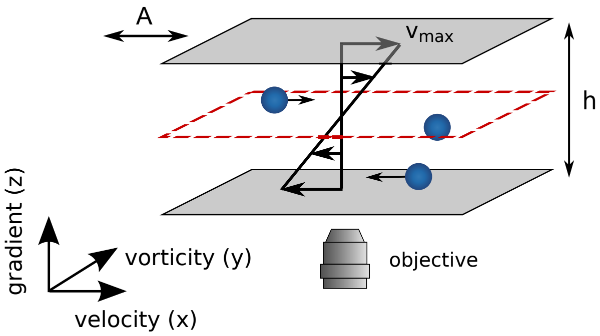

FIGURE 5.1. Parallel-plate shear cell mounted on top of an inverted confocal microscope [238]. The height between the two plates h, the amplitude A and the maximum speed v_{max} can be set during the experiment. Because both plates moved in opposite direction with equal speed, there was a plane of zero velocity in the middle of the cell, indicated by the dashed (red) line.

the full travel of 1 cm (0.01%) based on extensive testing of the setup [238]. The typical spacing between the slides h was 100 μm and an amount of $\sim$ 60 μL of suspension was placed between the slides to fill the cell. A metal vapor lock was used to prevent evaporation of the suspending liquid. The amplitude of the upper and lower slide A, the maximum velocity v_{max} and gap width h, which can be set prior to the experiment, determine the maximum strain amplitude $\gamma_{max} = 2A/h$ and the maximum shear rate $\dot{\gamma}_{max} = 2v_{max}/h$. We note that in the experimental literature on shear usually a 'peak to peak' distance for the strain amplitude is used, which is *twice* the value of the strain amplitude defined in rheology [30]. In this work the latter definition was chosen. For the results described in this chapter, we always applied oscillatory shear to our samples. This makes for a time dependent strain amplitude $\gamma(t)$ and shear rate $\dot{\gamma}(t)$, given by

$$\gamma(t) = \gamma_{max} \sin(2\pi f t) \tag{5.1}$$

$$\dot{\gamma}(t) = \dot{\gamma}_{max} \cos(2\pi f t), \tag{5.2}$$

with f the frequency of oscillation and $\dot{\gamma}_{max} = 2\pi f \gamma_{max}$. We define the Peclet number Pe as

$$Pe = \frac{\dot{\gamma}_{max}\, \eta\, a^3}{k_B T}, \tag{5.3}$$

with $a = \sigma/2$ the particle radius and η the viscosity of the medium.

Data acquisition. Digital images of the colloidal dispersion were obtained with a confocal microscope (Leica SP2) and a 100x/1.4 NA oil-immersion objective (Leica). The RITC labeled particles were excited with a 543 nm HeNe laser and a piezo focusing drive (Physik Instrumente) was used for scanning in the vertical direction. Measurements were performed in a temperature controlled room at 21 ± 1°C. Coordinates of the particles were obtained from 2D and 3D confocal microscopy images using an algorithm similar to the method described by Crocker and Grier [45], but extended to 3D as e.g. schematically described in Ref. 47.

5.2.2. Simulation method

Non-equilibrium Brownian Dynamics (NEBD) simulations were used to model colloidal particles of diameter σ under shear. The unit of time is the Brownian relaxation time $\tau_B = a^2/D_0$, with $a = \sigma/2$ the radius of the colloidal particles and $D_0 = k_B T/\xi$ the bare diffusion constant, k_B the Boltzmann constant, T the temperature and ξ the Stokes drag coefficient. We define $\xi = 6\pi\eta a$ as the unit of drag which fixes the viscosity η. For particles with diameter $\sigma = 2.07$ μm, the unit of time $\tau_B = 11.3$ s, the drag coefficient $\xi = 4.3 \times 10^{-8}$ Ns·m^{-1}, with the unit of energy $k_B T = 4.1 \times 10^{-21}$ J. The simulations were carried out in a simulation box with periodic boundary conditions in the x and y directions and two walls positioned at $z = 0$ and $z = h$. The number of particles varied between 1200 and 3456 and the shape of the box was chosen to be commensurate with the dimensions of the expected crystalline phases. To approximate hard-sphere like particles, an inverse power law was used for the pairwise interaction potential

$$U_{ij}(r) = \epsilon\left(\frac{\sigma}{r}\right)^{36}, \tag{5.4}$$

with ϵ the interaction energy, σ the particle diameter and $r \equiv |\mathbf{r}_i - \mathbf{r}_j|$ the center-of-mass distance between particles i and j. For efficiency reasons this potential was truncated at 1.02σ and shifted to make it continuous. The wall-particle interaction is taken to be

$$U_{wall} = \begin{cases} \epsilon_w(\frac{\sigma}{z})^6 & \text{for } z < \sigma/2 \\ \epsilon_w(\frac{\sigma}{h-z})^6 & \text{for } z > h - \sigma/2 \\ 0 & \text{otherwise} \end{cases} \tag{5.5}$$

with ϵ_w the wall-particle interaction energy and z the z-coordinate of a particle. We used the integration method of Ermak [239] with an additional term to account for the oscillating shear

$$\mathbf{r}_i(t + \delta t) = \mathbf{r}_i(t) + \delta t \frac{-\nabla U_i(t)}{\xi} + \delta \mathbf{r}_i^G + \delta t \dot{\gamma}(t) z_i(t) \hat{\mathbf{x}}, \tag{5.6}$$

with $-\nabla U_i$ the force acting on the particle as a result of the potential energy, $\delta \mathbf{r}_i^G$ a Gaussian random displacement with zero mean and variance $\langle(\delta r_{i\alpha}^G)^2\rangle = 2D_0\delta t$ where $\alpha \in \{x, y, z\}$. The term $\dot{\gamma}(t) z_i(t)\hat{\mathbf{x}}$ imposes a linear velocity profile on the system. Previous experimental work by Wu *et al.* has shown that the velocity profile of a partially crystallized (or sliding layer) suspension deviated from linearity and that the local shear rate is approximately 1.5 times higher in the layered region than in the fluid phase [240]. In the simulations we neglect these deviations from a linear profile because they do not strongly effect the shear-induced structures [63, 236]. The time step δt used to evaluate equation (5.6) was chosen to be much larger than the velocity relaxation time ($\sim m/\xi$), but much smaller than the Brownian relaxation time (a^2/D_0). It is important to note that hydrodynamic interactions, that are neglected in Brownian Dynamics simulations, become more important for larger shear rates and higher volume fractions [241] and that they also play an important role in determining the absolute time scales in the system.

5.2.3. Structure analysis

To quantify the symmetry of the 3D local structure surrounding a particle, the method of local bond orientational order parameters was followed [242]. Based on the spherical harmonics Y_{lm}, a set of numbers was computed for each particle

$$q_{lm}(i) = \frac{1}{n_c(i)} \sum_{j=1}^{n_c(i)} Y_{lm}(\hat{\mathbf{r}}_{ij}), \tag{5.7}$$

with l an integer parameter and m an integer running from $-l$ to l. The unit vector $\hat{\mathbf{r}}_{ij}$ connects particle i and one of its nearest neighbors j. To distinguish between particles that are in a liquid-like environment and particles that are in a crystal-like environment we used the method described by Ten Wolde *et al.* [237]. A normalized complex vector $\mathbf{q}_l(i)$ was constructed with $(2l+1)$ components $\tilde{q}_{lm}(i)$ that are proportional to the numbers $q_{lm}(i)$. Next, the correlation between the vector $\mathbf{q}_l(i)$ and the vector of its nearest neighbor $\mathbf{q}_l(j)$ was computed by defining the scalar product

$$S_{ij}^{3D} = \sum_{m=-l}^{l} \tilde{q}_{lm}(i)\, \tilde{q}_{lm}(j)^*. \tag{5.8}$$

If the local structures of particle i and j are similar, the value of the scalar product S_{ij}^{3D} is close to one and a crystal-like *bond* was assigned to the particles. Because thermal broadening results in a distribution of values it is necessary to define a threshold value S_c^{3D} for the scalar product. As we expect the crystal to have hexagonal order, we chose a symmetry index $l = 6$. We used a threshold value of $S_c^{3D} = 0.7$ and because some particles in the fluid phase exceed this threshold, a particle was called crystal-like only if in addition it had a minimum of 8 crystalline bonds.

When only 2D information of the system was available, we quantified the positional order by calculation of the hexagonal bond-orientational order parameter ψ_{6_k} given by

$$\psi_{6_k} = \frac{1}{n_c(k)} \sum_{j=1}^{n_c(k)} \exp(i6\theta(\mathbf{r}_{jk})), \tag{5.9}$$

with n_c the number of neighbors of particle k (which is taken to be the number of particles that are within a distance of $1.4\,\sigma$ of the particle), $\mathbf{r}_{jk}$ the vector connecting particle k and its neighbour j, $\theta(\mathbf{r}_{jk})$ the angle between $\mathbf{r}_{jk}$ and an arbitrary reference axis and i in the exponent the imaginary unit. In a perfect hexagonal layer, the angles $\theta(\mathbf{r}_{ij})$ are multiples of 60° and $|\psi_6(i)| = 1$.

To quantify the 2D *global* hexagonal order we used the global order parameter Ψ_6, given by

$$\Psi_6 = 1/N \left| \sum_{k=1}^{N} \psi_{6_k} \right|, \tag{5.10}$$

with N the number of particles in the plane. For a dense hard-sphere fluid, this order parameter vanishes in the limit of an infinitely large system size ($\lim_{N\to\infty} \Psi_6 = 0$).

In phases of hard spheres close to coexistence, $|\psi_{6_k}|$ alone is not sufficient to distinguish clearly between particles that are in a liquid-like environment and particles that are in a crystal-like environment. Therefore, we used a 2D analysis that is similar to the 3D bond orientational order method by Ten Wolde *et al.* described above. We quantified the correlation between the local structure of particle k and j by computing the normalized scalar product

$$S_{kj}^{2D} = \frac{\mathrm{Re}\,(\psi_{6_k}\psi_{6_j}^*)}{|\psi_{6_k}||\psi_{6_j}|}, \tag{5.11}$$

If the local structure of the two particles is similar (and hexagonal), S_{kj}^{2D} is close to 1. Therefore, a crystalline *bond* was assigned to the particle if $S_{kj}^{2D} > S_c$, with S_c a threshold value between 0 and 1. If the number of crystalline bonds $n_b \geq n_c$, with n_c the minimum number of bonds, the particle was classified as crystalline. We chose the values $S_c = 0.7$ and $n_c = 4$ for the analysis described in this chapter. We also determined the angle ϕ of a particle in a crystal-like (hexagonal) region, given by $\phi = \arg(\psi_{6_k})/6$.

To compare our real-space results with existing light-scattering literature, we calculated the structure factor $S(\mathbf{q})$ according to

$$S(\mathbf{q}) = \frac{1}{N}\left\langle \sum_{j,k}^{N} e^{i\mathbf{q}\cdot(\mathbf{r}_k - \mathbf{r}_j)} \right\rangle, \tag{5.12}$$

with N the number of particles in the sample and the angular brackets denoting an ensemble average. The vector $\mathbf{q}$ was chosen such that $q_\alpha = 2\pi\, n/L_\alpha$ with n an integer, $\alpha \in \{x, y, z\}$ and L_α the system size. A cosine window was used to avoid artefacts caused by the shape of the box.

5.3. Results

We studied oscillatory shear-induced ordering in fluid samples with volume fractions in the range $\phi = 0.46 - 0.49$, i.e. just below the freezing point. First, we describe two different ordered phases that were observed when the frequency and amplitude of the oscillatory shear were varied, both in the experiments and in the simulations. We discuss to what extent these phases agree with previous work, which was mainly done with light scattering techniques. We then show results of the crystallization kinetics during shear and show preliminary results on the melting of the shear-induced phases once the shear was stopped.

5.3.1. 3D structure of the shear-induced phases

Oscillatory twinned fcc. The structural changes that can be observed in the fluids under shear are rich and strongly dependent on the strain amplitude. In Fig. 5.2a, a suspension with volume fraction $\phi = 0.47 \pm 0.01$ is shown. Without shear, the sample remained in the fluid phase and for strain amplitudes $\gamma_{max} \leq 0.1$ no shear-induced order was observed for any frequency. Fig. 5.2b shows that for strain amplitude $\gamma_{max} = 0.36$ and frequency $f = 4.5\ \tau_B^{-1}$ ($Pe = 0.5$) the particles formed hexagonal layers in the velocity-vorticity plane with a close-packed direction (indicated by the lines of particles forming the 2D hexagonal arrangement) almost *perpendicular* to the velocity. Fig. 5.2c shows a snapshot of a simulation with volume fraction $\phi = 0.49$ and particles color coded according to their z-position, so they appear brighter the closer they are to the plane. After application of shear with $\gamma_{max} = 0.35$ and $f = 4.3\ \tau_B^{-1}$ (again $Pe = 0.5$), almost identical ordering compared to the experiments was observed (Fig. 5.2d). The insets show the increase in the values of the global hexagonal order parameter Ψ_6. Note that both in the experiments and simulations a slight deviation of the close-packed lines with respect to the vorticity direction was found. Similar small but systematic deviations were also found for the crystalline structures described below.

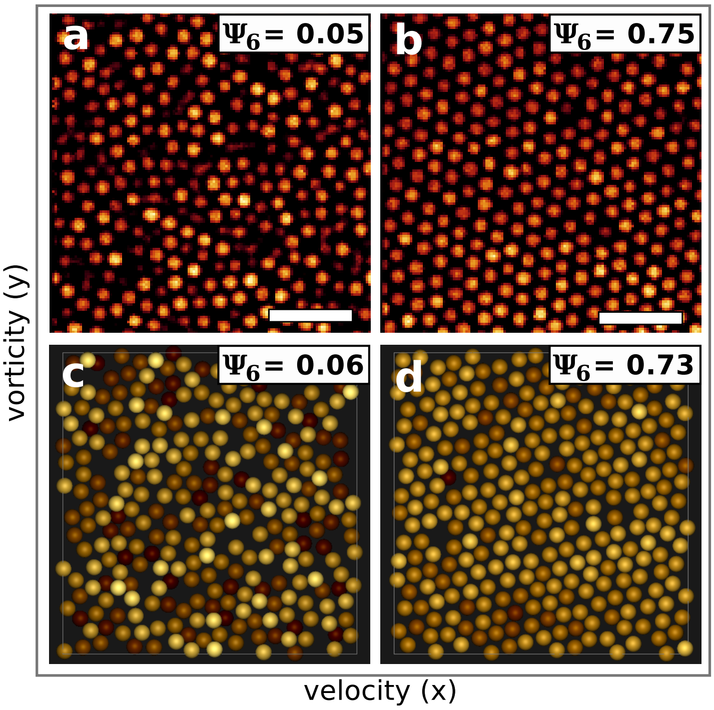

FIGURE 5.2. Shear-induced crystallization with perpendicular alignment, observed in the velocity-vorticity plane. Values of the global hexagonal order parameter Ψ_6 are indicated in the figures. (a,b) Experimental results for a sample with volume fraction $\phi = 0.47 \pm 0.01$. The scale bars are 10 μm. (a) The quiescent sample is fluid in equilibrium. (b) When subjected to shear with strain amplitude $\gamma_{max} = 0.36$ and frequency $f = 4.5\ \tau_B^{-1}$, particles form hexagonal layers with one of the close packed directions almost perpendicular to the velocity direction. (c,d) Simulation results for $\phi = 0.49$. The figures show a part of the simulation box with particles color coded according to their z-position. (d) For $\gamma_{max} = 0.35$ and $f = 4.3\ \tau_B^{-1}$, the ordering is almost identical compared to the experiment.

To determine the stacking of these hexagonal layers, confocal images of the gradient-velocity plane were taken directly after cessation of the shear and compared with simulations. Fig. 5.3 shows images taken at different moments of the oscillation cycle for $\gamma_{max} = 0.3$ and $f = 10.0\ \tau_B^{-1}$ (experiment) and $f = 50.0\ \tau_B^{-1}$ (simulation) after application of shear for 1200 oscillations. The higher frequency in the simulation was used for efficiency reasons. The crystal-like particles in the simulation snapshots are colored red and fluid-like particles are colored cyan. Both types of particles are reduced in diameter (0.5σ and 0.2σ respectively) to enhance visualization. In Fig. 5.3a, the oscillation is at maximum displacement and the layers are ABC stacked, indicating a face-centered-cubic (fcc) phase. At the equilibrium position of the oscillation (Fig. 5.3b), the layers are bridge-site stacked and a body-centered-tetragonal (bct) phase is temporarily formed. At the other maximum displacement (Fig. 5.3c), the particles are again fcc stacked, but with the other twin structure (ACB). The schematic drawing in Fig. 5.3d shows that this transition in stacking can be explained with a simple geometrical model where the particles oscillate between two neighbouring triangular voids, as proposed originally by Ackerson [32]. Probably, this movement enables the particles to minimize the stress caused by collisions with other particles during the shear.

From both experiments and simulations it is clear that for small strain amplitudes a twinned fcc-like phase is formed in an initial hard-sphere fluid. In both experiments and simulations we always observed the crystal together with a fluid phase. The strain amplitude that corresponds to the exact dimensions of an fcc crystal is given by $\gamma_{max} = \Delta x/\Delta z = 0.35$, with Δx the distance between two neighbouring voids and Δz the distance between two hexagonal layers. For lower volume fractions, the fcc phase can persist for significantly larger strain amplitudes because of the larger free volume. A simple geometrical calculation shows that for $\phi = 0.49$, the strain amplitude has to be larger than $\gamma_{max} = 0.69$ before particles in a perfect fcc crystal touch during the oscillatory motion.

To further demonstrate the twinning behaviour, particle coordinates were obtained from experiments with $\gamma_{max} = 0.3$, $f = 10.0\ \tau_B^{-1}$ and $\phi = 0.47 \pm 0.01$. In Fig. 5.4a the rendered particles are shown at the two extremes of the oscillation directly after cessation of the shear. Again, crystal-like particles are shown in red, fluid-like particles are shown in cyan and both are reduced in diameter to enhance visualization. Fig. 5.4b shows plots of the calculated 3D structure factor $S(\mathbf{q})$ in the q_x-q_y plane, confirming the twinning behavior. The light scattering experiments by Ackerson on hard-sphere fluids under oscillatory shear reveal the same position of the diffraction peaks as in Fig. 5.4b, however, the maxima are spread out around the inner ring instead of appearing as small spots [32]. This was also observed for soft spheres [219] and for samples above the bulk fluid coexistence density [221, 224], indicating a distribution of crystalline domains centred at the vorticity direction.

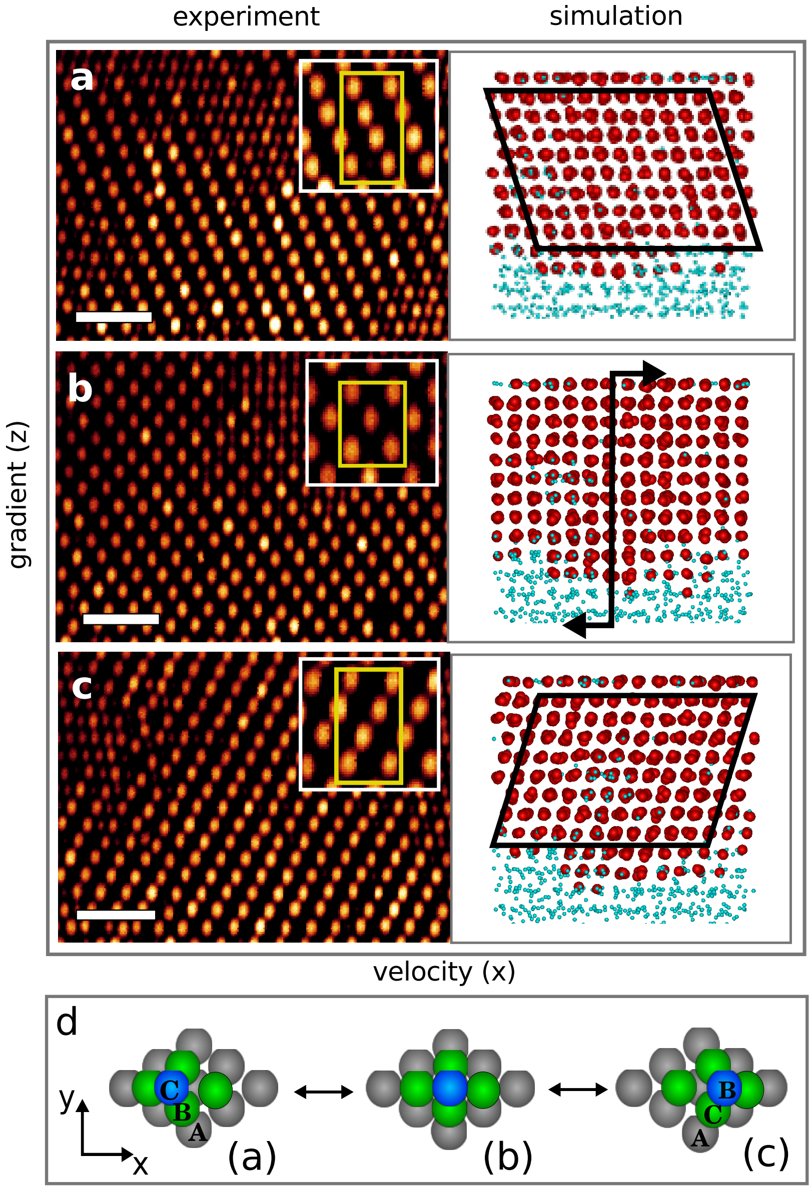

FIGURE 5.3. Oscillating fcc phase in the velocity-gradient plane. Experimental results (left) for $\phi = 0.46 \pm 0.01$, $\gamma_{max} = 0.3$ and $f = 10.0\ \tau_B^{-1}$ after 1200 oscillations. The scale bars indicate 12 μm. Simulation results (right) for $\phi = 0.49$, $\gamma_{max} = 0.3$ and $f = 50.0\ \tau_B^{-1}$, again after 1200 oscillations. Crystal particles are colored red and reduced to 0.5σ, fluid particles are colored cyan and reduced to 0.2σ to enhance visualization. (a) Particles are fcc stacked (ABC) at maximum displacement of the plates. (b) The hexagonal layers are bridge-site stacked, corresponding to a bct phase. (c) Particles are twin stacked at the other maximum displacement of the plates (ACB). (d) Schematic model of the relative movement of the layers during shear.

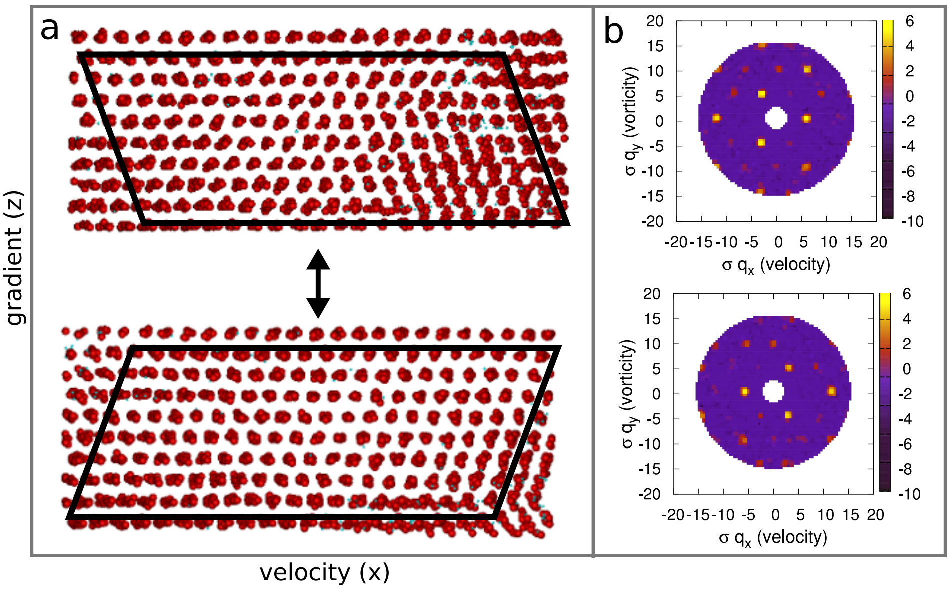

FIGURE 5.4. Experimental results on the twinned fcc phase. (a) Rendered particle positions at both extremes of the oscillation, after applying shear with $\gamma_{max} = 0.3$ and $f = 10.0\ \tau_B^{-1}$ to a suspension with volume fraction $\phi = 0.47 \pm 0.01$. Red indicates crystal-like particles and cyan indicates fluid order. Particles are reduced in diameter to enhance visualization. (b) The calculated 3D structure factor $S(\mathbf{q})$ at both extremes of the oscillation in the q_x-q_y plane demonstrates the twinning behavior.

Sliding layers. When the strain amplitude exceeds approximately 0.5, collisions between particles will prevent the formation of the twinned fcc phase and particles form hexagonal layers aligned *parallel* to the velocity direction. In Fig. 5.5 experimental results are shown for a quiescent sample (Fig. 5.5a) and after application of shear with strain amplitude $\gamma_{max} = 0.6$ and frequency $f = 2.5\ \tau_B^{-1}$ ($Pe = 0.5$, Fig. 5.5b) after approximately 100 oscillations. Simulation snapshots are shown before (Fig. 5.5c) and after shear with $\gamma_{max} = 0.8$ and $f = 3.7\ \tau_B^{-1}$ ($Pe = 0.5$, Fig. 5.5d) after 200 oscillations. The high values of the global order parameter Ψ_6 in Fig. 5.5b and Fig. 5.5d are a clear indication of the hexagonal ordering in the velocity-vorticity plane.

A comparison between the stacking of hexagonal layers observed in experiments and with simulations is shown in Fig. 5.6. Experimental results are from a suspension with volume fraction $\phi = 0.47 \pm 0.01$, $\gamma_{max} = 1.3$ and $f = 4.1\ \tau_B^{-1}$. The particle coordinates in Fig. 5.6a were obtained from a 3D data stack of confocal microscopy images taken directly after cessation of the shear and the structure factor $S(\mathbf{q})$ shown in Fig. 5.6c is calculated from these 3D coordinates. The view from the vorticity-gradient plane in Fig. 5.6a shows random stacking of layers, which is confirmed by the hexagonal pattern in Fig. 5.6c. The simulation snapshot in Fig. 5.6b is for $\phi = 0.49$, $\gamma_{max} = 1.2$ and $f = 9.0\ \tau_B^{-1}$ and shows that every third layer is positioned on top of the first, when viewed from the vorticity-gradient plane. The fourfold pattern of the corresponding structure factor (Fig. 5.6d) resembles the pattern observed by Ackerson with light scattering

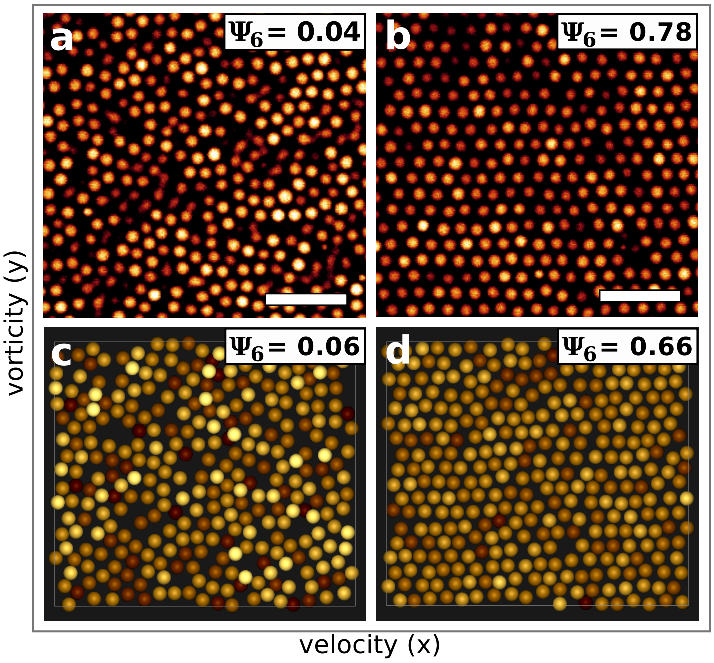

FIGURE 5.5. Formation of the sliding layer phase. (a,b) Experimental results for ordering in a sample with volume fraction $\phi = 0.47 \pm 0.01$ before and after application of shear with strain amplitude $\gamma_{max} = 0.6$ and frequency $f = 2.5$ τ_B^{-1}. The scale bars are 10 μm. (c,d) Simulation snapshots for $\phi = 0.49$, $\gamma_{max} = 0.8$ and frequency $f = 3.7$ τ_B^{-1}. Particles are color coded according to their z-position. Values of the global hexagonal order parameter Ψ_6 are indicated in the figure.

experiments [32, 220], who argued that if the volume fraction $\phi < 0.58$, the hexagonal layers can slide in straight lines through the grooves formed by a neighbouring layer, as indicated in Fig. 5.6e. The consequence of this movement is that the registry (in terms of the close packed stacking points ABC) between the layers vanishes and the resulting phase is called the freely sliding layer phase [32]. Fig. 5.6f shows that the view of the sliding layer phase in the vorticity-gradient plane is indeed very similar to what is found in the simulation (Fig. 5.6b). The six-fold pattern in Fig. 5.6c is expected for higher volume fractions $\phi > 0.58$ when there is still registry between the layers. This suggest that in the experiments, particles rearranged after cessation of the shear into the triangular voids of neighbouring layers during the time it takes to acquire the confocal images, which resulted in randomly stacked layers.

Transition point. The transition between the twinned fcc and the sliding layer phase occurred in the experiments at $\gamma_{max} \approx 0.5$, which is similar to the pioneering light scattering experiments by Ackerson *et al.* [32]. The transition strain value was independent of the applied frequency range of $f = 5$ - 15 τ_B^{-1}. In the experiments, the crystal-like phases were always observed together with a fluid phase. For both the oscillating fcc and the sliding layer phase, domains with deviating alignments were always present. In

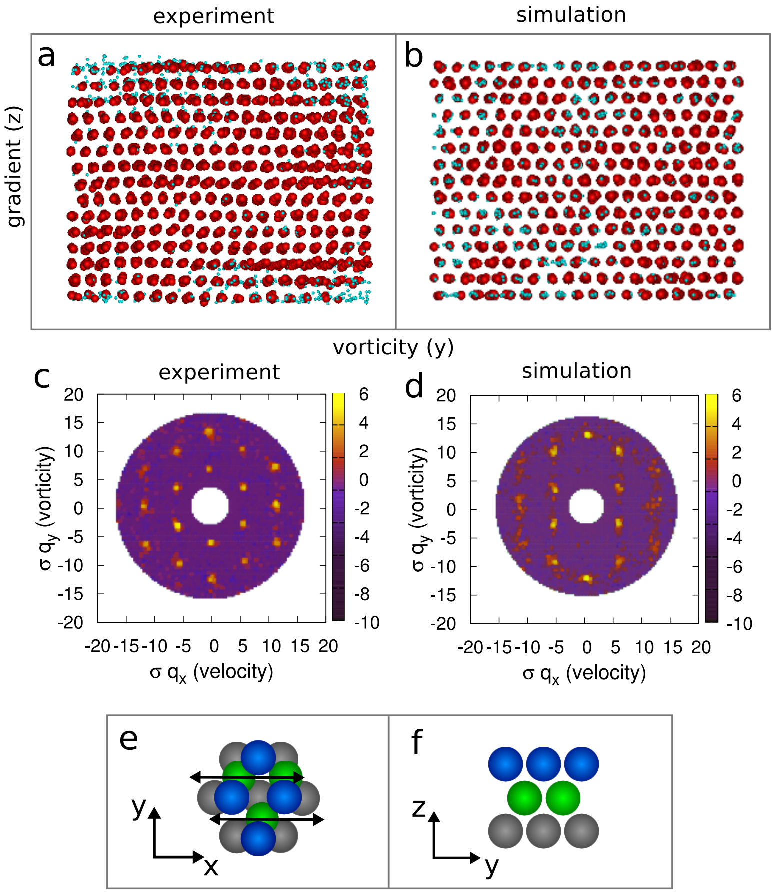

FIGURE 5.6. Structure of the sliding layer phase. Experimental results for $\gamma_{max} = 1.3$, $f = 4.1\ \tau_B^{-1}$ and $\phi = 0.47 \pm 0.01$ and simulation for $\gamma_{max} = 1.2$, $f = 10.0\ \tau_B^{-1}$ and $\phi = 0.49$. Crystal particles are shown in red and fluid particles in cyan. Both are reduced in diameter to enhance visualization. (a) After cessation of the shear, random stacked layers were found in the experiments. (b) Viewed from the vorticity-gradient plane, every third hexagonal layer is positioned on top of the first in the simulations. The structure factor $S(\mathbf{q})$, calculated from 3D coordinates, indicates (c) randomly stacked layers and (d) sliding layers. (e,f) Proposed movement of the layers during shear.

the simulations, the transition between the twinned fcc phase and sliding layer phase occurred at the same strain amplitude ($\gamma_{max} \approx 0.5$), and was also independent of frequency. The ordering in the simulations did persist for larger strain amplitudes compared to the experiments. It is highly likely that the absence of hydrodynamic interactions in the simulations promotes consistent layering of the sample even at strain amplitudes where in the experiments fluid order was found. For a detailed (frequency-strain amplitude) state diagram, which in addition also contains a velocity aligned string phase and a tilted layer phase, see Refs. 236 and 63.

5.3.2. Shear-induced crystallization kinetics

In this section, we investigate the shear-induced crystallization kinetics of the oscillating twinned fcc phase and the sliding layer phase using both experiments and simulation.

Fig. 5.7 shows experimental results on the shear-induced crystallization in a suspension with volume fraction $\phi = 0.49 \pm 0.02$ for equal Peclet number ($Pe = 0.5$) but different strain amplitude γ_{max}. Crystal-like particles were identified from confocal microscopy images obtained during shear. Because the images were acquired in the zero-velocity plane, the same particles were in the field-of-view for the complete duration of the experiment, see Movies 1-2 in Appendix B.1. Fig. 5.7a shows that for a maximum strain amplitude of $\gamma_{max} = 0.3$, multiple crystalline domains were formed oriented *around* the vorticity direction. Upon continuation of the shear, these domains slowly coarsened into larger ones, eventually forming an oscillatory twinned fcc phase, as shown in Fig. 5.3 and Fig. 5.4. The crystallization at this strain amplitude thus seems to proceed via a nucleation-and-growth type of mechanism. A significantly different scenario was observed for a larger strain amplitude of $\gamma_{max} = 0.6$ (Fig. 5.7b). Here, multiple crystal-like domains were formed that were all aligned with the velocity direction. These domains quickly grew into a large and uniform domain, forming the sliding layer phase shown in Fig. 5.6. This observation suggests a much more continuous crystallization process. To test for any history dependence, the sample was completely shear-melted by applying a high shear rate of $\dot{\gamma}_{max} = 10/s$. When the crystallization experiment was repeated at both strain amplitudes, we observed the same behaviour, indicating little or no history effects due to ordering of particles at the wall.

The time evolution of the 2D hexagonal order parameters are shown in Figs. 5.7c-d. Fig. 5.7c shows that there was a clear difference in the increase of the average local hexagonal order parameter $\langle|\psi_6|\rangle$ for both strain amplitudes. However, this difference is clearly more marked for the global hexagonal order parameter Ψ_6 shown in Figs. 5.7d. For a maximum strain amplitude of $\gamma_{max} = 0.6$, the global order increased fast and continuous, until it reached a plateau level of $\Psi_6 \sim 0.7$. On the other hand, for a strain amplitude of $\gamma_{max} = 0.3$, the increase was not only much slower (due to the slow coarsening of several domains), there were also significant fluctuations in the global order, corresponding to the formation and break-up of crystalline regions.

In Fig. 5.8, we analysed the orientation of the shear-induced crystalline domains in more detail. Figs. 5.8a,b show 2D reconstructions from confocal microscopy images of the zero-velocity plane, with colours indicating the in-plane orientation a particle and its nearest neighbours. Fig. 5.8a was obtained after applying shear with Peclet number $Pe = 0.5$ and strain amplitude $\gamma_{max} = 0.3$ for a duration of 63 τ_B. Individual crystalline domains are clearly visible, which were often found to have a small offset with the vorticity (y) direction. The distribution of orientations is shown in Fig. 5.8c. In Fig 5.8b, we show a single domain crystalline region, obtained after application of shear with Peclet number $Pe = 0.5$ and strain amplitude $\gamma_{max} = 0.6$ for a duration of

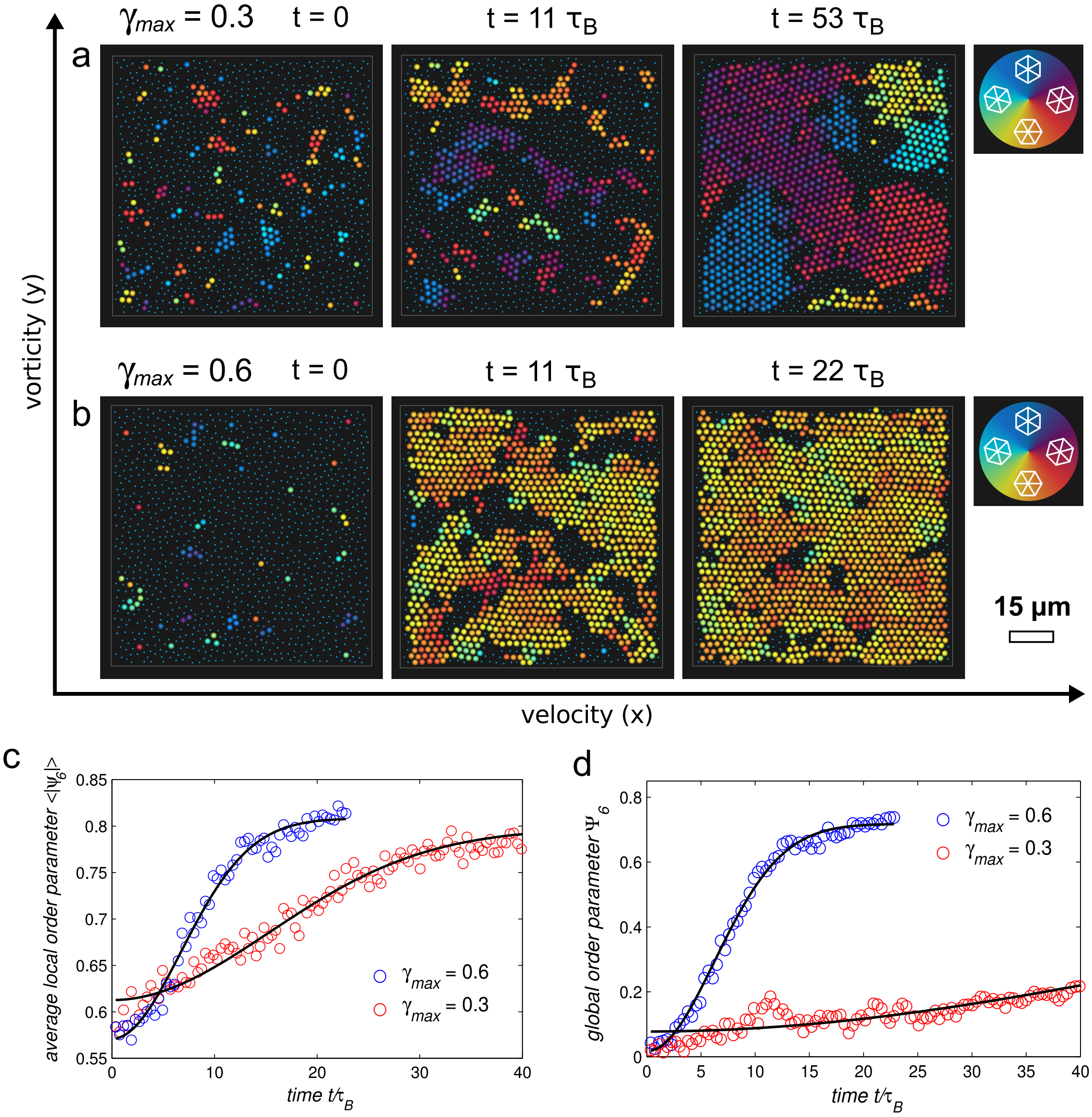

FIGURE 5.7. Experimental results on the shear-induced crystallization in a hard-sphere suspension. The volume fraction $\phi = 0.49 \pm 0.02$. Equal Peclet number ($Pe = 0.5$) were used but different strain amplitude γ_{max}. Crystal-like particles were identified from confocal microscopy images obtained during shear with colours indicating the orientation of the crystalline regions. Fluid-like particles were reduced in size to enable better visualization. (a) For small strain amplitude ($\gamma_{max} = 0.3$) multiple crystalline domains oriented *around* the vorticity direction were observed. (b) For larger strain amplitude ($\gamma_{max} = 0.6$) a single domain crystal was formed, aligned with the velocity direction. Notice the difference in time for the snapshots on the right. (c) Evolution of the average local hexagonal order parameter $\langle|\psi_6|\rangle$ and (d) the global hexagonal order parameter Ψ_6. Lines are drawn to guide the eye only.

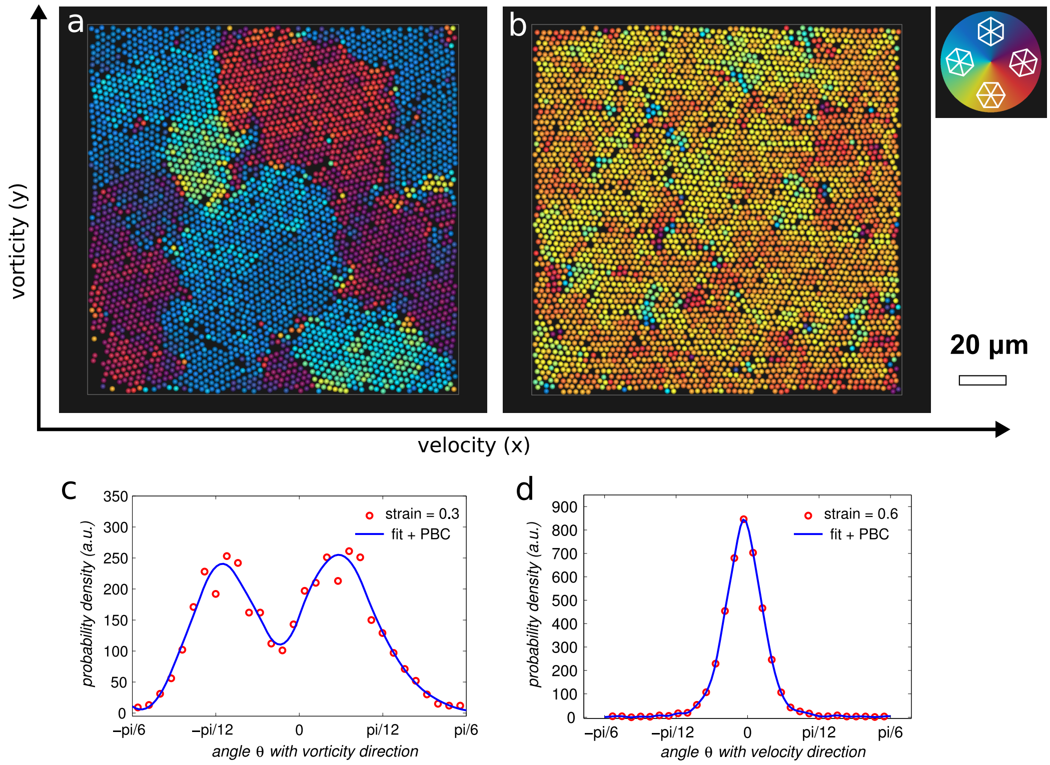

FIGURE 5.8. Distribution of the orientations of shear-induced crystalline domains. (a) A polycrystalline sample ($\gamma_{max} = 0.3$ and $Pe = 0.5$) and (b) a single domain crystal ($\gamma_{max} = 0.6$ and $Pe = 0.5$). (c) The distribution of the orientations of the image in (a) shows that the crystalline domains are centred, but not peaked, at the *vorticity* direction. (d) The distribution of the orientations of the image in (b) is narrow and centred at the *velocity* direction. The lines are spline fits with periodic boundary condition (PBC).

126 τ_B. The corresponding distribution of orientations in Fig. 5.8d shows that there was a narrow, single peaked distribution centred at the velocity direction.

Since the experimental measurements only allow for 2D analysis during shear (of particles in the zero-velocity plane), we also used simulations to investigate the shear-induced crystallization kinetics in 3D. However, because the simulations neglect hydrodynamic interactions, we cannot compare the time-scales for crystallization directly with the experiments. Fig. 5.9 shows the simulation counterpart of Fig. 5.7. Figs. 5.9a,b show the mid-plane of the simulation box (at $z = 7\sigma$), containing in total 6000 particles at a volume fraction $\phi = 0.49$. Again, colours indicate the orientation of the crystalline regions and fluid-like particles were reduced in diameter to enable better visualization. Oscillatory shear was applied with Peclet number $Pe = 4$ and strain amplitude $\gamma_{max} = 0.3$ (Fig. 5.9a) and $\gamma_{max} = 0.6$ (Fig. 5.9b). Despite the small system size, several distinct domains can be identified in Fig. 5.9a, which, upon continuation of the shear, coarsened into a single domain aligned with the vorticity direction. Even the characteristic small orientation offset with the vorticity direction was often found in the simulations, despite

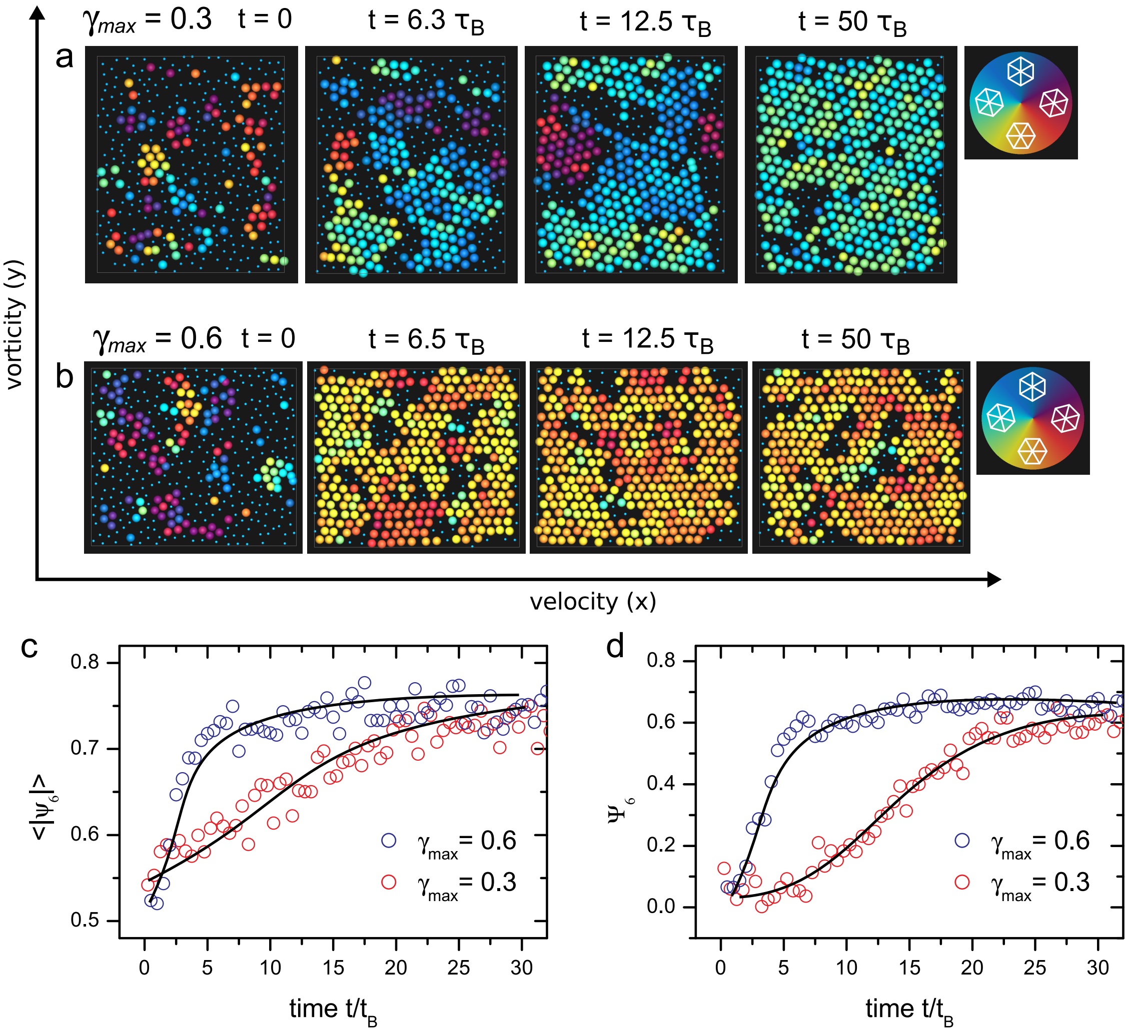

FIGURE 5.9. Simulation counterpart of Fig. 5.7. Results are shown for 6000 particles at $\phi = 0.49$ and Peclet number $Pe = 4.0$. The midplane of the simulation box at $z = 7\sigma$ was chosen for visualization. (a) For small strain amplitude ($\gamma_{max} = 0.3$), similar poly-crystalline domains as in the experiment were found. Upon continuation of the shear, the domains coarsened into a single domain. (b) For larger strain amplitude ($\gamma_{max} = 0.6$), a single-domain crystal was formed, aligned with the velocity direction. (c) The average local hexagonal order parameter $\langle|\psi_6|\rangle$ and (d) the global hexagonal order parameter Ψ_6, calculated for the midplane at $z = 7\sigma$, are in agreement with the experimental results. The lines are drawn to guide the eye only.

the fact that the boxsize was chosen to be commensurate with a perfectly vorticity-aligned fcc crystal. Fig. 5.9b shows that for strain amplitude $\gamma_{max} = 0.6$, one uniform domain was formed, again in good agreement with the experimental results. Also the values of the average local hexagonal order parameter $\langle|\psi_6|\rangle$ (Fig. 5.9c) and the global hexagonal order parameter Ψ_6 (Fig. 5.9d), calculated for the midplane at $z = 7\sigma$, are in good agreement with the experimental results (compare Figs. 5.7c,d with Figs. 5.9c,d).

For the two simulation results shown in Fig. 5.9, we also determined the density profiles $\rho(z)$, with z the gradient direction. Fig. 5.10a shows the results for strain amplitude $\gamma_{max} = 0.3$ and Fig. 5.10b for $\gamma_{max} = 0.6$. The density profiles are shifted for visualization and were obtained at times $t/\tau_B = 0$, 1.5, 2.5, 5 and 12.5 from bottom to top. It is clear from Fig. 5.10 that layering starts at the wall (even in the absence of shear) and that during the shear the layers grow further into the sample. The layering is more pronounced and occurs faster for the large strain (Fig. 5.10b) than for the small strain (Fig. 5.10a). We also found that in both regimes, particles first order into layers after which the hexagonal order within the layer starts to increase (compare Fig. 5.10 with Fig. 5.9d). This is most pronounced in the small strain regime. When both samples are completely layered (t/τ_B = 5), the global hexagonal order in the mid-plane at $z = 7\sigma$ for $\gamma_{max} = 0.3$ is small ($\Psi_6 < 0.1$) whereas for $\gamma_{max} = 0.6$ the global order parameter has almost reached its plateau value ($\Psi_6 \sim 0.6$).

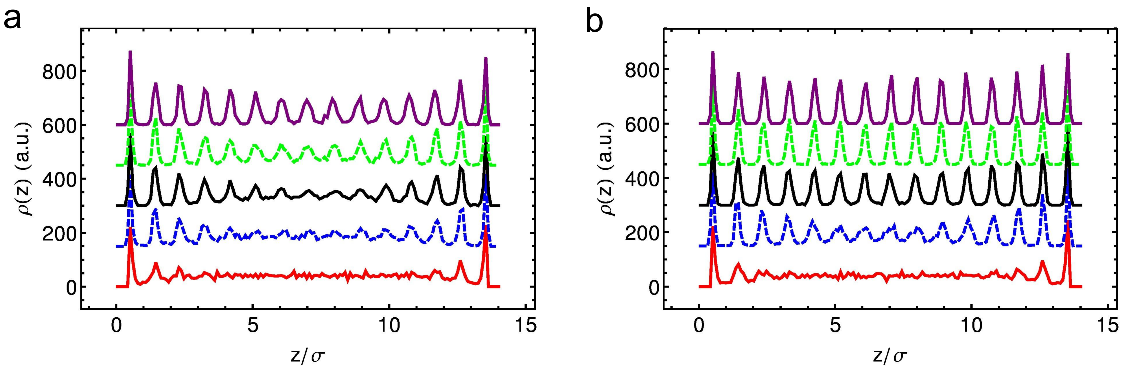

FIGURE 5.10. Density profiles of the two simulation results shown in Fig. 5.9. The profiles are shifted for better visualization. Oscillatory shear was applied with Peclet number $Pe = 4$ and strain amplitude of (a) $\gamma_{max} = 0.3$ and (b) $\gamma_{max} = 0.6$. Density profiles $\rho(z)$ are shown for times $t/\tau_B = 0$, 1.5, 2.5, 5 and 12.5 from bottom to top. Layering starts from the walls and is significantly faster in the large strain regime.

5.3.3. Melting after cessation of the shear

We end this chapter with preliminary experimental results on the melting of the shear-induced crystals upon cessation of the shear. The spheres used in these experiments had a diameter $\sigma = 2.64$ μm and polydispersity $\delta = 2.5$ %. The Brownian relaxation time $\tau_B = a^2/D_0$ for these particles was 23.4 s. Fig. 5.11a shows the melting of an oscillatory twinned fcc phase, induced by applying oscillatory shear with Peclet number $Pe = 2.0$ and maximum strain amplitude $\gamma_{max} = 0.3$ for a duration of 150 τ_B. The volume fraction $\phi = 0.46 \pm 0.02$. When the shear was stopped at $t = 0$, the shear-induced crystal started to melt and returned to its equilibrium fluid phase within $\sim$ 15 min, see also Movie 3 in Appendix B.1. The melting seemed to start uniformly throughout the sample, rather than nucleating at grain boundaries or defects [243].

In Fig. 5.11b, we show results on the melting of a sliding layer phase, induced by applying oscillatory shear with Peclet number $Pe = 1.0$ and maximum strain amplitude

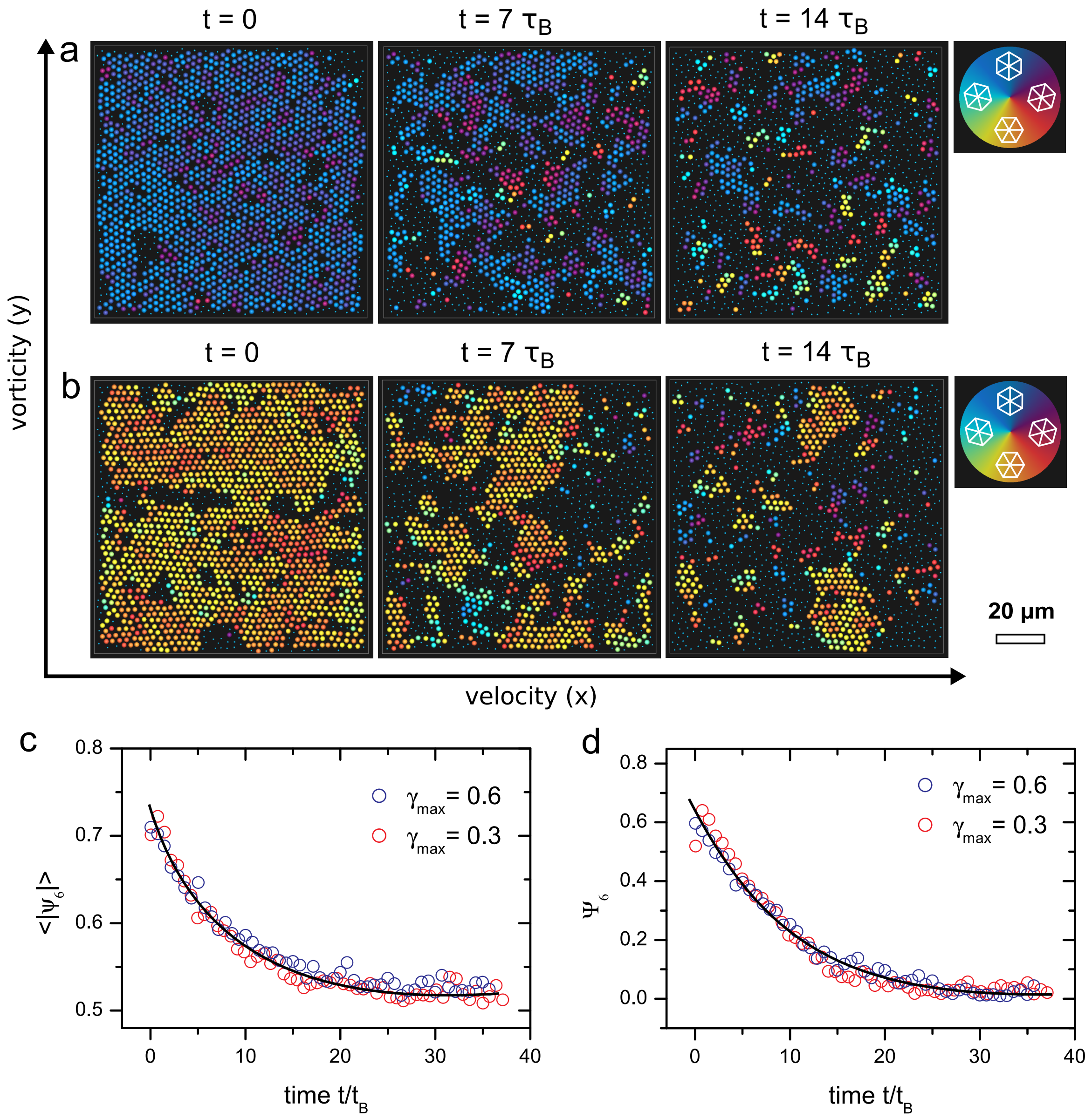

FIGURE 5.11. Experimental results on the melting of shear-induced phases after the shear was stopped at $t = 0$. (a) Melting of an oscillatory twinned fcc phase, induced by applying oscillatory shear with Peclet number $Pe = 2.0$ and maximum strain amplitude $\gamma_{max} = 0.3$ for a duration of 150 τ_B. The volume fraction $\phi = 0.46 \pm 0.02$. (b) Melting of a sliding layer phase, induced by applying oscillatory shear with Peclet number $Pe = 1.0$ and maximum strain amplitude $\gamma_{max} = 0.6$ for a duration of 79 τ_B. The volume fraction $\phi = 0.47 \pm 0.02$. (c) The average local hexagonal order parameter $\langle|\psi_6|\rangle$ and (d) the global hexagonal order parameter Ψ_6 as a function of time. Lines are drawn to guide the eye only.

$\gamma_{max} = 0.6$ for a duration of 79 τ_B. The volume fraction $\phi = 0.47 \pm 0.02$. Again, melting started immediately after the shear was stopped at $t = 0$, see also Movie 4 in Appendix B.1. Fig. 5.11c and Fig. 5.11d show that there was no difference between the two phases in both the rate of decrease of the local hexagonal order parameter $\langle|\psi_6|\rangle$ and the global hexagonal order parameter Ψ_6 respectively.

5.4. CONCLUSION

With both experiments on PMMA colloids and Brownian Dynamics simulations (without hydrodynamic interactions and an enforced linear shear profile) we have investigated two oscillatory shear-induced phases in hard-sphere fluids: an oscillating twinned fcc phase and a sliding layer phase. In both the experiments and in the simulation, these phases were *below* the coexistence density of hard-sphere freezing, i.e. they were in a fluid phase in equilibrium. For both phases, we characterized the crystallization kinetics during shear and the resulting 3D shear-induced structures. Because the simulation results were in strong agreement with the experiments, we conclude that deviations from a linear profile can be neglected in this work. Based on the same agreement, we also conclude that, except for large Peclet numbers, hydrodynamic interactions do not strongly affect the shear-induced structures. However, because the hydrodynamics play an important role in determining the absolute time scales in the system, we could not directly compare the crystallization rates.

Upon application of shear with a maximum strain amplitude of $\gamma_{max} = 0.3$, multiple crystalline domains were formed oriented *around* the vorticity direction. Upon continuation of the shear, these domains slowly coarsened, eventually forming an oscillatory twinned fcc phase where the particles oscillated between two neighbouring triangular voids of a neighbouring layer. The crystallization seemed to proceed via a nucleation-and-growth type of mechanism. A significantly different scenario was observed for a larger strain amplitude of $\gamma_{max} = 0.6$ (but equal Peclet number). Here, multiple crystal-like domains were formed that were all aligned with the velocity direction. These domains quickly grew into a large and uniform domain, forming a sliding layer phase with the hexagonal layers sliding in straight lines through the grooves formed by a neighbouring layer. This observation suggests a much more continuous crystallization process. Simulation results showed that for both phases, upon application of the shear, layering started at the walls and grew further into the sample until it became completely layered. After particles ordered into layers, the hexagonal order within the layer started to increase. Both the layer growth as well as the ordering within the layers was significantly slower for the oscillating fcc phase than for the sliding layer phase. We also presented preliminary experimental results on the melting of these phases, which occurred immediately after cessation of the shear. The melting seemed to start uniformly throughout the sample and we did not find any significant difference between the two phases in terms of decrease in hexagonal order as a function of time.

5.5. ACKNOWLEDGEMENTS

Parts of this chapter were based on work that was published in the MSc thesis of Thijs Besseling [236]. This work was done in collaboration with Michiel Hermes, Andrea Fortini and Marjolein Dijkstra. We thank Johan Stiefelhagen for particle synthesis.

6

Synthesis and Phase Behaviour of a Model System of Rod-like Silica Particles

Abstract

In this chapter we demonstrate quantitative real-space measurements on colloidal liquid crystal phases. First, we present three adjustments that were made to a recently developed synthesis procedure to produce fluorescent rod-like silica particles with large aspect ratio. When suspended in a solvent, these particles form equilibrium liquid crystal phases, such as nematic and smectic phases. With confocal microscopy and a particle fitting algorithm we determined all 3D positions and orientations of these particles, even in the most concentrated liquid crystal phases, for aspect ratios up to $l/d = 5.4$. Here, l is the end-to-end distance and d the diameter. This allowed us to directly compute the 3D orientation distribution function and investigate the (local) suspension structure. We found a smectic-B phase with small regions (approximately $10 \times 10 \times 5$ particles) of AAA-stacked crystalline layers. Additionally, we determined the complete equilibrium density profile of a sediment of coexisting isotropic and smectic-B phases in 3D real-space. At the isotropic - smectic-B interface, we found a difference between the inflection points of the density and the nematic order parameter, which agrees well with theoretical predictions. We also measured the 2D (projected) orientation distributions of both nematic and smectic phases of particles with aspect ratio $l/d > 7$. We compared our results to theory and simulations on both hard and soft spherocylinders and found a reasonable to good agreement. Preliminary results are also shown on super-resolution imaging of a smectic phase.

6.1. INTRODUCTION

The first experimental report on liquid crystals dates from 1888, when botanical physiologist Friedrich Reinitzer and physicist Otto Lehmann studied cholesterol based substances, now known as cholesteric liquid crystals [244, 245]. Before the discovery of liquid crystals by Reinitzer and Lehmann, three states of matter were known: solid, liquid and gas. The study of liquid crystals proved however, that also phases existed which had symmetry properties in between that of a liquid and a crystalline state, called mesophases. The classification of these phases was set out a few decades later, by Georges Friedel in 1922 [246]. Fig. 6.1 shows schematics of some of the mesophases that rod-like molecules or particles can form. The nematic phase, for example, is characterized by unidirectional orientational order, but liquid-like positional order. In the smectic phases, molecules are also aligned but, additionally, they are ordered into layers. In the smectic-A phase, the positional order within the layer is still liquid-like whereas in the smectic-B phase, molecules are hexagonally ordered. There are actually many different smectic phases, ranging from smectic-A to smectic-L, depending on the different types and degrees of positional and orientational order [20]. If there is long-ranged correlation between the hexagonal smectic-B layers, a crystal phase is formed. Depending on the stacking of the layers, this can either be an ABC crystal or AAA crystal, as indicated in Fig. 6.1. Also other liquid-crystalline phases exist, such as a columnar phase, where the hexagonal ordering is still present but the molecules are no longer ordered into layers. In general, liquid crystals can be divided into thermotropic and lyotropic phases. Thermotropic liquid crystals exhibit phase transitions as a function of temperature, whereas lyotropic liquid crystals exhibit phase transitions as a function of concentration [20]. Most of the molecular liquid crystals are thermotropic. In this chapter, however, we will focus on a *colloidal* liquid-crystal system, consisting of rod-like particles suspended in a solvent, which is an example of a lyotropic system.

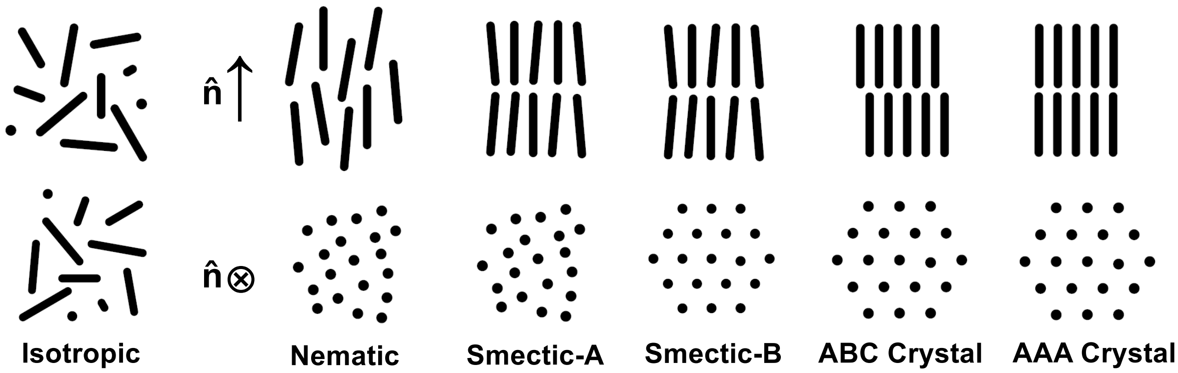

FIGURE 6.1. Schematics of the liquid crystal phases discussed in this chapter, with the imaging planes parallel (top) and perpendicular (bottom) to the average alignment in the system, or director, $\hat{\mathbf{n}}$.

In 1949, Lars Onsager gave one of the first theoretical explanations of the formation of a nematic phase of hard rods, based on excluded volume (and therefore entropy) alone [247]. Later, it was demonstrated with computer simulations that a smectic phase is also stable in a system of hard rods with sufficient aspect ratio [248]. Fig. 6.2 shows the packing fraction - aspect ratio phase diagram of a system of hard spherocylinders obtained with computer simulations by Bolhuis and Frenkel [209]. All phases shown in Fig. 6.1 are present in the phase diagram except for the smectic-B phase. In the simulations, the aspect ratio L/D is defined as the cylinder length over the diameter (see the inset in Fig. 6.2). Because the particles used in the experiments in this chapter are not identical in shape to a spherocylinder, but are more bullet-like, we define the end-to-end aspect ratio l/d, with l the average end-to-end length of the particle and d the diameter. Because the particles are also charged in suspension, as we will later discuss in detail, we also introduce an effective end-to-end length l^* and effective diameter d^*, resulting in an effective aspect ratio $l^*/d^* \approx L/D + 1$.

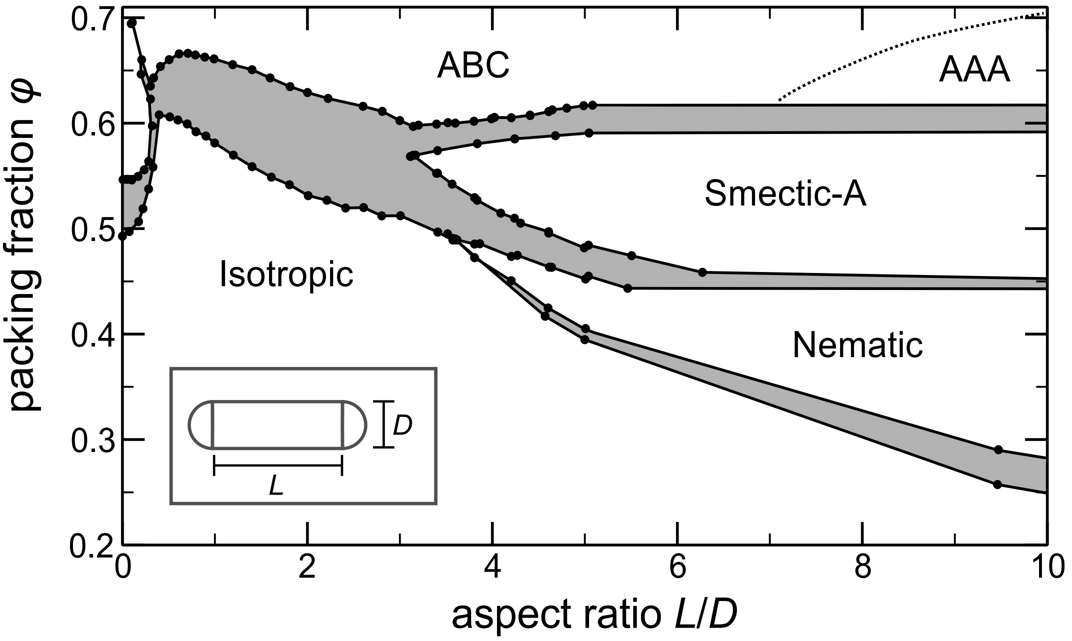

FIGURE 6.2. Phase diagram of hard spherocylinders, adapted from computer simulation results by Bolhuis and Frenkel [209]. The gray areas indicate coexistence regions. In the simulations, the aspect ratio L/D is defined as the length of the cylinder L over the diameter D (see inset). In the experiments in this chapter, however, we use the end-to-end length l, diameter d and aspect ratio l/d. Because the particles in the experiments are charged, we also define the effective end-to-end length l^*, effective diameter d^* and effective aspect ratio $l^*/d^* \approx L/D + 1$.

One of the first reports of an experimental colloidal liquid crystal system dates from 1925 by Zocher, who used needle-like vanadium pentoxide (V_2O_5) particles that formed nematic phases in suspension [18]. For a system of the tobacco mosaic virus (TMV), nematic phases were reported in the 1930s and smectic phases in the 1950s [19]. Since then, many different colloidal particles have been developed to study liquid crystal phase behaviour. We will however give a brief overview of the experimental systems consisting of *rod-like* colloids. Apart from the TMV system, various other bio-organic systems exist that form nematic, smectic and in some cases even crystalline phases, including the *fd*-virus [249, 250] and DNA [251]. Another class is that of the aluminium and iron hydroxides, including rod-like boehmite (AlOOH) particles [252], akaganeite (β-FeOOH) [21], goethite (α-FeOOH) [253] and spindle-like hematite (α-Fe$_2$O$_3$) [254,255]. For a review on liquid crystal formation in colloidal dispersions with mineral particles see Ref. 256. Another class of rod-like particles are the ellipsoidal polymer particles, made by mechanical stretching of spherical particles in a polymerized matrix. These ellipsoidal particles are usually made from poly(methyl methacrylate) (PMMA) [162] or polystyrene [257]. Furthermore, dumbbell-shaped polymer particles are also used as a model system for real-space studies of uniaxial anisotropic particles [165,258,259]. Our final examples of rod-like particles are nanorods made from gold [260] or semiconductor material, such as CdS [261], which can form large-scale smectic phases. See Refs. 262–264 for extensive reviews on the different types of colloidal (rod-like) self-assembly studies and liquid crystalline phase behaviour.

Early *real-space* experiments on colloidal liquid crystals were performed by Maeda and Maeda in 2003, who reported nematic and smectic phases of rod-like particles for a wide range of aspect ratios ($\sim$ 3 - 35), which they observed with an optical microscope [21]. The high refractive index of the particles, however, impeded observation of more than one or two layers of the sample. Nevertheless, they obtained quantitative data on the particle dynamics in a smectic phase [265] and also investigated the phase behaviour under strong confinement [266]. For some of the systems mentioned so far, the particles can be fluorescently dyed and index matched, which enables study of their phase behaviour with a confocal microscope. For the *fd*-viruses, which have a diameter much smaller than the resolution of a confocal microscope, this was only possible with fluorescently labelled tracers [26, 27]. However, this still enabled single particle measurements on the self-diffusion in a nematic [26] and in a smectic phase [27]. The larger PMMA and polystyrene ellipsoidal and dumbbell particles allowed for 3D study of systems where *all* the particles were fluorescent [44, 185]. However, hard dumbbells do not from liquid-crystal phases [267] and hard ellipsoids do not form stable smectic phases [268]. Therefore, external fields have been used to induce particle alignment over larger distances. Using a centrifugal field, nematic order was found in dense suspensions of ellipsoids [185] and crystalline order was induced with an external electric field for both dumbbells and ellipsoids and measured with 3D confocal microscopy [43, 44].

In contrast with the systems of ellipsoidal particles, it was recently shown by our group that a system of fluorescent rod-like silica particles does form nematic and smectic phases in equilibrium [25]. Further study showed that the phase behaviour could be mapped with qualitative agreement onto the hard-rod phase diagram shown in Fig. 6.2 [28]. However, there are several important differences with the computer simulation model. First of all, the particles in our experimental system are charged, resulting in both an effective length l^* and effective diameter d^*, which changes the aspect ratio (and therefore the phase behaviour) of the particles [28,269]. Additionally, the repulsive charge can also lead to a twisting effect [270]. Furthermore, computer simulations on parallel soft spherocylinders have shown that charge stabilizes a columnar phase, whereas a smectic and especially a nematic phase is destabilized [271]. Second, the particle systems that we use are not perfectly monodisperse, but have a polydispersity of 6% - 12% in both length and diameter, which is expected to have a significant effect on the stability of the smectic and crystalline phases [211, 272]. Finally, the particles in the experimental system are heavier than the dispersing solvent, resulting in sedimentation and, upon equilibration, a density profile along the direction of gravity. The equilibrium density profile is a fundamental property of the system that can be used to determine the equation of state, as has previously been done in real-space for colloidal spheres [273, 274]. Additionally, sedimentation has been used to study crystallization in the first layers of the sediment [14]. For recent developments and unsettled issues on colloidal sedimentation, see Ref. 275. Compared to studies on colloidal spheres, however, advancements in sedimentation phenomena of rod-like particles strongly lag behind [275]. Nevertheless, several theoretical studies have been put forward, e.g. on the concentration dependence of the sedimentation velocity of colloidal rods [276] or on the nematic ordering of rods during sedimentation [277]. A notable computer simulation study is by Savenko and Dijkstra who studied hard spherocylinders with

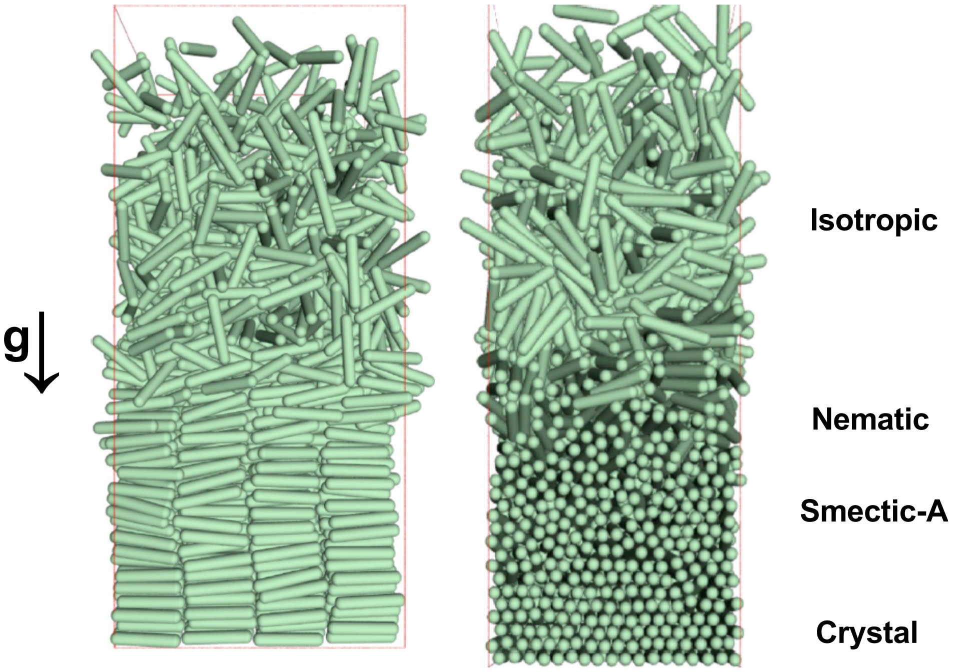

Figure 6.3. A snapshot of a computer simulation by Savenko and Dijkstra on hard spherocylinders with aspect ratio $L/D = 5$, subjected to a gravitational field [278]. The number of particles per unit surface $n_s D^2 = 4.34$ and inverse gravitational length $D/l_g = 0.75$. The snapshot shows isotropic-nematic-smectic-A-crystal phase coexistence.

aspect ratio $L/D = 5$ in a gravitational field [278]. Fig. 6.3 shows a snapshot from this study, indicating isotropic-nematic-smectic-crystal phase equilibrium, determined from analysis of the sedimentation profile. Real-space experimental measurements of rod-like particles under sedimentation remain however scarce [28] and, quoting Roberto Piazza, “a comprehensive experimental analysis of rod concentration profiles, allowing for instance a comparison with detailed theoretical predictions for nematic ordering in the presence of gravity, is yet to come” [275].

In this chapter, we demonstrate novel strategies that allow for real-space quantitative analysis of experiments on rod-like particles under gravity. We first show results on adjustments made to a recently developed synthesis procedure to produce fluorescent rod-like particles [25, 28, 72]. After the particles had been left to sediment and form concentrated liquid-crystal phases, we acquired 3D confocal microscopy data stacks and applied our particle fitting algorithm, described in Chapter 4, to obtain their 3D positions and orientations. From these data, we analysed the phase behaviour of the particles, for aspect ratios $l/d = 4$ - 20, and compared the results with predictions from both theory and simulation.

6.2. METHODS

6.2.1. Rods in a gravitational field

The sedimentation profile of a colloidal suspension is the result of fundamental equilibrium properties of the system. The profile arises due to the competing effects of minimal gravitational energy and maximal entropy. This competition results in a gravitational pressure on the particles being balanced by an osmotic pressure gradient, which is given by

$$\frac{\mathrm{d}\,\Pi(z)}{\mathrm{d}\,z} = -g(\rho_p - \rho_s)\phi(z). \tag{6.1}$$

Here, $\Pi(z)$ is the osmotic pressure at height z, ρ_p the mass density of the particle, ρ_s the mass density of the solvent and $\phi(z) = \rho(z)\,v_p$ the particle volume fraction at height z, with $\rho(z)$ the particle number density at height z and v_p the volume of the colloid. Equation (6.1) is only valid if the thermodynamic quantities, such as the density and pressure, are locally well-defined [279]. We assume the rods in this chapter to be spherocylindrical in shape, with a volume given by

$$v_p = \pi\left(\frac{l\,d^2}{4} - \frac{d^3}{12}\right), \tag{6.2}$$

with l the end-to-end length of the particle and d the diameter. In the ideal gas limit, the density profile is barometric and the solution to equation (6.1) is the well known barometric height distribution

$$\phi(z) = \phi_0 \exp(-z/l_g), \tag{6.3}$$

with l_g the gravitational length, given by $l_g = k_B T/mg$, where m is the buoyant mass of the particle, i.e. $m = (\rho_p - \rho_s)\,v_p$. For higher densities, where particles start to interact, the system can undergo phase transitions and an integrated sedimentation profile allows for a determination of the equation of state. First, the sedimentation profile is integrated from z to the top of the sample h to give the pressure

$$\Pi(h) - \Pi(z) = -g\,(\rho_p - \rho_s)\int_z^h \phi(z')dz'. \tag{6.4}$$

Next, elimination of z between $\Pi(z)$ and $\phi(z)$ directly leads to the equation of state $\Pi(\phi)$. On the other hand, if the equation of state $\Pi(\phi)$ is explicitly known, equation (6.1) can be used to obtain the density profile for given l_g [280]. Moreover, equation (6.4) can be used to estimate the number of layers in the sediment N needed to reach the pressure for the bottom layer to undergo a phase transition [281]. We therefore assume that the volume fraction of the entire sediment is constant. If we also assume a constant layer thickness ξ, then equation (6.4) becomes

$$\Pi = g\,(\rho_p - \rho_s)\,\phi\,\xi\,N. \tag{6.5}$$

We will now estimate N for a spherocylinder with diameter D = 500 nm, cylinder length L = 2.5 μm and aspect ratio L/D = 5.0. For the mass densities we used ρ_p = 1.9 g/ml and ρ_s = 1.0 g/ml. Based on the computer simulations by Bolhuis and

Frenkel, we expect the isotropic to nematic phase transition to occur at a pressure $\Pi = 0.036$ N/m^2 and volume fraction $\phi = 0.40$ [209]. Assuming a layer thickness $\xi = 600$ nm, we obtain from equation (6.5) that $N = 17$ layers are needed for the bottom layer to become nematic. Similarly, for a nematic to smectic-A transition ($\Pi = 0.047$ N/m^2 and $\phi = 0.47$) we find $N = 19$ layers and for the smectic-A to solid transition ($\Pi = 0.076$ N/m^2 and $\phi = 0.60$) we expect that $N = 24$ layers are needed for the bottom layer to crystallize.

Because the density profile can vary rapidly due to layering of particles, a coarse-grained density profile is sometimes used to obtain the equation of state [279,282], given by

$$\bar{\phi}(z) = \int_0^\infty \phi(z)w(z-z')dz', \tag{6.6}$$

with $w(z)$ a normalized resolution function, e.g. a triangular or top-hat function [279].

To quantify the interface region of two coexisting phases, we fitted a tangent hyperbolic function to both the nematic order parameter S_{3D} and the particle number density ρ, given by [283]

$$\alpha(z) = \frac{1}{2}(\alpha_1 + \alpha_2) + \frac{1}{2}(\alpha_1 - \alpha_2)\tanh(z - z_0)/\Delta, \tag{6.7}$$

with z_0 the position of the interface, Δ the thickness of the interface and $\alpha = \{S_{3D}, \rho\}$.

To estimate the sedimentation velocity at infinite dilution, assuming complete decoupling of rotations, translations and sedimentation [196], we use the Svedberg equation [197]

$$v_{sed} = \frac{v_p\, D_t\, g\,(\rho_p - \rho_s)}{k_B\, T}, \tag{6.8}$$

with D_t the rotationally averaged translational diffusion coefficient at infinite dilution.

6.2.2. Rod-like particle suspensions

Synthesis of particle cores. Fluorescent silica rods were prepared following the method of Kuijk *et al.* [25,72]. Two types of adjustments were made to increase the aspect ratio of the rods. The first adjustment was a seeded growth method. For this method, 30 g of polyvinylpyrrolidone (PVP, average molecular weight $M_n = 40.000$, Sigma-Aldrich) was disssolved in 300 ml of 1-pentanol ($\geq$ 99% Sigma-Aldrich) by ultra-sonication for 2 hours in a 500 ml glass laboratory bottle. After all the PVP had dissolved, 30 ml of absolute ethanol (Baker) was added to the pentanol, together with 8-10 ml of ultrapure water (Millipore system) and 2 ml of 0.18 M sodium citrate dihydrate (NaCit, 99%, Aldrich). Afterwards, the flask was shaken by hand several times until the solution became turbid. Next, 6.75 ml of ammonia (25 wt%, Merck) and 3.0 ml of tetraethyl orthosilicate (TEOS, $\geq$ 98%, Fluka) was added to the mixture. After both additions, the flask was shaken by hand several times. After the mixture was left to react for 6 hours, an additional amount of 3 ml TEOS was added after which the flask was gently shaken again and left unagitated. This growth step was repeated up to a maximum of 3 times, each with a minimum time interval of 6 hours. After the last addition of TEOS, the reaction was allowed to proceed overnight.

The second method consisted of a scaled-up synthesis, using a 1 L glass bottle, with slightly different concentrations as described before: 80 g of PVP, 800 ml of 1-pentanol, 80 ml ethanol, 19 - 20 ml water, 8 ml of 0.18 M NaCit, 16 - 18 ml ammonia and 8.0-8.5 ml TEOS. The TEOS was added once at the beginning of the synthesis and, after shaking by hand several times, the reaction was left to proceed for at least 48 hours. All reactions were carried out at room temperature except for one, which was carried out at $30 \pm 1\,^{\circ}$C using an incubator (RS-IF-203, Revolutionary Science).

The synthesis was stopped by centrifuging the reaction mixture at 1500 g for 1 hour after which the supernatant was removed and particles in the sediment were redispersed in ethanol by vortex mixing and by brief sonication. This procedure was repeated at 1500 g for 20 minutes, 2 times with ethanol, 2 times with water and finally with ethanol again.

To narrow the particle size distribution and purify the sample, we removed both large and small particles and we removed aggregates. To remove the smaller particles, the sample was centrifuged with varying centrifugation speeds (150 - 700 g), depending on the average size of the particles. The centrifugation speed was chosen such that after 15 minutes of centrifugation, there was both a dense sediment at the bottom and still a turbid supernatant on top. The supernatant was removed and the rods in the sediment were redispersed in ethanol. This procedure was repeated at least four times and the centrifugation speed was lowered if the height of the turbid supernatant became smaller. Large particles and aggregates were removed by transferring the sample to a 40 ml vial and leaving it to sediment for approximately 2 hours, until a sediment was visible at the bottom, a turbid supernatant in the middle and a clear supernatant at the top. The clear supernatant was removed and approximately the same volume of turbid supernatant was separated for further use. This procedure was repeated several times to increase the yield of the final suspension containing rod-like particle cores with a relatively narrow size distribution.

Fluorescent labelling. To fluorescently label the rods, we followed the method described in Ref. 72. We used two methods to label the rods: the first resulted in a gradient in fluorescent intensity along the main axis of the particle core, the second method resulted in a uniform fluorescent shell around the core. For both methods we dissolved 25 mg of fluorescein isothiocyanate (FITC, isomer I, 90%, Sigma-Aldrich) in 5 ml of absolute ethanol (Baker), after which 35 μl of (3-aminopropyl)triethoxysilane (APS) was added. The mixture was left to react overnight. Alternatively, 35 mg of rhodamine isothiocyanate (RITC, mixed isomers, Aldrich) was used instead of 25 mg FITC. For the first method, the dye-APS mixture was added during the rod synthesis, described in the previous section, directly after addition of the TEOS. Because the availability of dye is higher during the beginning of the rod-growth, this method resulted in a gradient of dye molecules along the rod axis. To label the particles with a fluorescent shell, the as prepared particle cores ($\sim$ 0.5 g) were dispersed in 300 ml of ethanol in a round bottom flask. Under gentle magnetic stirring, we added 10 ml of ultrapure water, 10 ml of ammonia and 1.0 ml of TEOS together with the dye-APS mixture. After the mixture reacted overnight, it was centrifuged at 700 g for 30 minutes and washed three times with ethanol and once with water. This procedure resulted in a homogeneous fluorescent shell of 30 - 60 nm. When RITC was used instead of FITC, particles were not stable in ethanol, since RITC is cationic and the silica rods have a negative charge. Therefore a mixture of ammonia and ethanol was used (5 ml ammonia per 100 ml of ethanol) to wash the particles. The particles were stable in ethanol again after growing a non-fluorescent outer silica shell around the RITC-dyed particles (see details below).

The particles with a fluorescent shell enable a more accurate determination of the center of mass from confocal microscopy images, compared to gradient-dyed rods, and are therefore the preferred type of particles. However, there were often problems with (partial) aggregation during the shell coating procedure, rendering the batch useless about half the time. The gradient dyed rods did not have any stability problems and, additionally, break the up-down symmetry of the rods optically, enabling unique determination of the tip of the particle. In Chapter 4, we show in Fig. 4.2i the intensity histograms of two fluorescently labelled rods that were oriented parallel to the xy image plane of the confocal microscope. The continuous (red) line shows the intensity histogram of a rod with a fluorescent shell and the dashed (green) line that of a gradient-dyed rod.

To resolve individual particles with confocal microscopy, even when the concentration is high, non-fluorescent silica shells were grown around the particles. The fluorescent rods ($\sim$ 0.7 g) were dispersed in 300 ml of ethanol in a round bottom flask together with 10 ml of water. Under gentle magnetic stirring, 10 ml of ammonia was added and 0.5 - 1.5 ml TEOS after which the reaction mixture was left to react overnight, which resulted in a non-fluorescent silica shell around the particles. Afterwards, the particles were centrifuged at 700 g for 30 minutes and washed three times with ethanol and once with water. The thickness of the shell depended on the particle dimensions and TEOS concentration, but was usually between 30 - 60 nm. The shell growth step was repeated several times until the desired thickness ($\sim$ 100 - 200 nm) was reached.

Index matching. Particle suspensions were prepared for confocal microscopy imaging by dispersing the rods in an index-matching mixture $n_D^{21} = 1.45$ of either dimethylsulfoxide (DMSO, $\geq$ 99%, Sigma-Aldrich) and ultrapure water (Millipore system) or glycerol ($>$ 99 %, Sigma-Aldrich) and ultrapure water. The particles were dispersed in DMSO or glycerol first, after which water was added until the suspension was carefully index-matched by eye. This resulted in mixtures of 91 wt% DMSO in water and 85 wt% glycerol in water.

6.2.3. Confocal microscopy & image restoration

Sample cells. To record confocal microscopy images, three types of sample cells were used. The first consisted of normal glass capillaries (0.1 × 1.0 mm^2 and 0.2 × 2.0 mm^2, Vitrocom) which were sealed at both ends with UV-glue (Norland No. 68). This type of capillary was used only for qualitative inspection of the samples because they provide poor imaging, which is partially due to their manufacturing process and also due to the low and probably non-uniform refractive index ($n_D^{23} = 1.47$). For high quality images, sample cells were constructed with standard glass coverslips (Menzel Gläzer). These glass coverslips have a high flatness (≤ 5.0 %) and a refractive index ($n_D^{23} = 1.523$) close to the refractive index of the oil-immersion liquid (Type F, Leica, $n_D^{23} = 1.515$) used for imaging. The second type of sample cell consisted of such a glass coverslip (No. 1.0, thickness between 130 - 160 μm) and a standard microscopy slide (Menzel Gläzer) which were separated by two strips of a No. 1.0 coverslip acting as spacers. All components were glued together with UV-glue, leaving a small channel of $\sim 0.2 \times 4 \times 20$ mm^3 (height × width × depth) which was filled with suspension and sealed at both ends with either UV-glue or two component epoxy glue (Bison Combi Rapide).

The third and final sample cell was used to accommodate a column of sedimenting particles. This cell was constructed as follows (see the schematic in Fig. 6.4). First, the broad end of a glass pasteur pipette (WU Mainz) was cut to 2 cm in length. One of the open ends was then glued on a No. 1.0 or No. 1.5 coverslip (Menzel Gläzer) with UV curing glue (Norland 68). Then, the pipette was slid through a circular hole of 7 mm that was drilled in the middle of a standard microscopy slide (Menzel Gläzer) and attached permanently by gluing the coverslip to the microscopy slide with UV glue. This created a vertical cylindrical sample holder of 5 mm in diameter and 2 cm in height, with a volume of ~ 400 μl, see Fig. 6.4. The sample cell was filled by either adding 350 μl of suspension with initial volume fraction $\phi = 0.04\%$ or by adding 5 μl of suspension with volume fraction $\phi = 3\%$ on top of a column of 345 μl of glycerol/water that was recovered from the same sample by centrifugation. After filling, the sample was sealed with cotton wool wrapped in parafilm, followed by candle wax. This prevented any significant evaporation of the suspension for at least several weeks.

Conventional confocal microscopy. The samples were imaged with a confocal microscope (Leica SP2 or Leica SP8) using a 63×/1.4 or 100×/1.4 oil-immersion confocal

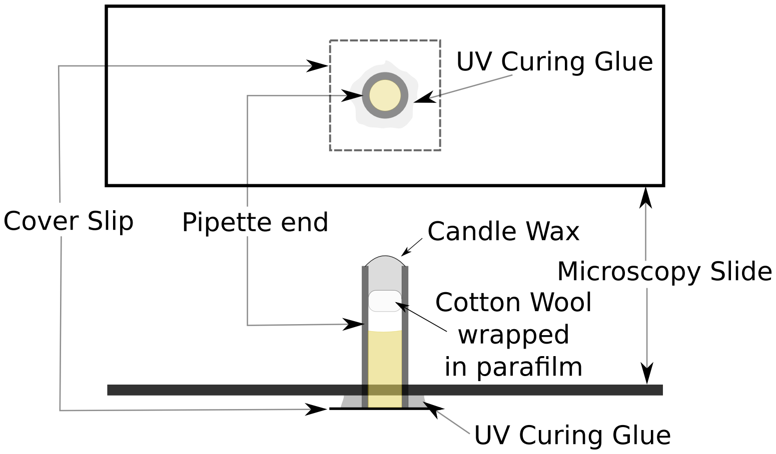

FIGURE 6.4. Sample cell used for study of the sedimentation profile of rod-like particles with 3D confocal microscopy.

objective (Leica) and an excitation wavelength of either 488 nm or 542 nm. We corrected the 3D images for distortion of the axial (z) distances due to the refractive index mismatch between sample ($n_D^{21} = 1.45$) and immersion oil ($n_D^{21} = 1.51$), which results in an increase of axial distances by 5%, see Chapter 3. Typical dimensions of a single 3D image stack were 30 × 30 × 50 μm^3 with voxel size of 50 × 50 × 100 nm^3. This is roughly four times smaller than the resolution of the Leica SP8 confocal microscope used (190 nm in the lateral and 490 nm in the axial direction, see Chapter 3) and close to the Nyquist sampling rate, which is 43 × 43 × 130 nm^3 for a numerical aperture of 1.4, oil-immersion ($n_D = 1.515$) and an excitation wavelength of 488 nm [93, 94].

Stimulated Emission Depletion. Continuous Wave Stimulated Emission Depletion (CW-STED) images were taken with a Leica SP8 STED confocal microscope. Images were taken with a white light continuum laser with a pulsed excitation at 488 nm and a 592 nm STED beam. Typical image dimensions were 10 × 10 μm^2 with a pixel size of 20 × 20 nm^2.

Image deconvolution. Some of the 2D and 3D confocal microscopy data were deconvolved to suppress noise and improve both contrast and resolution [187]. All deconvolutions were performed using commercially available software (Huygens Professional 4.4, Scientific Volume Imaging) using the classic maximum likelihood estimation restoration method [90]. A theoretical point spread function (PSF) was used when there was a mismatch between the refractive index of the sample and the immersion fluid and for the STED data, otherwise the measured PSF shown in Chapter 3 was used.

6.2.4. Particle fitting

We determined the position and orientation of the fluorescent rods from 3D confocal microscopy data-stacks using the algorithm described in Chapter 4. We applied the algorithm to both raw and deconvolved data, depending on the quality of the data stacks.

6.2.5. Structure tensor

Some systems that we studied did not have a (large) non-fluorescent outer layer, resulting in strongly overlapping particle signals. When the overlap was too severe to apply our particle fitting algorithm with enough accuracy, we used the publicly available ImageJ routine OrientationJ to quantify the orientational order in 2D confocal microscopy images [284–286]. This routine computes the structure tensor J for each pixel in the image, given by the 2 × 2 symmetric matrix

$$J = \begin{pmatrix} \langle f_x, f_x \rangle & \langle f_x, f_y \rangle \\ \langle f_x, f_y \rangle & \langle f_y, f_y \rangle \end{pmatrix}, \tag{6.9}$$

with f_i the spatial derivatives of the image $f(x, y)$, which were calculated using a cubic B-spline interpolation [285]. The brackets denote a weighted inner product given by

$$\langle a, b \rangle_w = \iint_{R^2} w(x, y) a(x, y) b(x, y), \tag{6.10}$$

with $w(x, y)$ a Gaussian function that specifies the area of interest. The eigenvector corresponding to the largest eigenvalue of the tensor then gives the local predominant orientation of each pixel [285]. We used a Gaussian window with standard deviation σ of 3 pixels. From the pixel orientation distribution we then calculated the projected 2D nematic director and nematic order parameter as described in the next section.

6.2.6. 3D and 2D projected nematic order parameters

To quantify the global 3D orientational order in our systems we calculated the 3D nematic order parameter defined by

$$S_{3D} = \frac{3}{2}\langle \cos^2\theta \rangle - \frac{1}{2}, \tag{6.11}$$

where $\cos\theta = \hat{\mathbf{u}} \cdot \hat{\mathbf{n}}$, with $\hat{\mathbf{u}}$ the unit vector along the main axis of the rod and $\hat{\mathbf{n}}$ the nematic director, i.e. the direction of the average alignment in the system. We find S_{3D} and $\hat{\mathbf{n}}$ by calculating the largest eigenvalue and corresponding eigenvector of the standard 3 × 3 nematic order parameter tensor

$$Q^{3D}_{\alpha\beta} = \frac{1}{N}\sum_{i=1}^{N}\left(\frac{3\, u_{i\alpha}u_{i\beta} - \delta_{\alpha\beta}}{2}\right), \tag{6.12}$$

with $u_{i\alpha}$ the α-component of the unit vector pointing along the main axis of particle i and $\alpha, \beta = x, y, z$. $\delta_{\alpha\beta}$ is the Kronecker delta and N is the total number of particles in the system.

We also determined the *local* nematic order parameter S^i_{3D} given by

$$S^i_{3D} = \frac{1}{n_i}\sum_{j=1}^{n_i}\left(\frac{3}{2}|\mathbf{u}_i \cdot \mathbf{u}_j|^2 - \frac{1}{2}\right) \tag{6.13}$$

with n_i the number of (nearest) neighbours of particle i. A particle is assigned as a neighbour j if its center falls within a cylinder concentric with particle i with length and diameter approximately three times that of particle i.

In cases where only 2D information was available, we quantified the (projected) 2D order in the system by calculation of the 2D nematic order parameter, given by

$$S_{2D'} = 2\langle \cos^2\psi \rangle - 1, \tag{6.14}$$

with ψ the angle between the projected main axis of the rod $\hat{\mathbf{u}}'$ and the projected nematic director $\hat{\mathbf{n}}'$, i.e. ψ is the in-plane projected angle that maximizes equation (6.14). Similarly, we calculated the 2 × 2 nematic order parameter tensor given by

$$Q^{2D}_{\alpha\beta} = \frac{1}{N}\sum_{i=1}^{N}\left(2\, u'_{i\alpha}u'_{i\beta} - \delta_{\alpha\beta}\right), \tag{6.15}$$

with $u'_{i\alpha}$ the α-component of the unit vector pointing along the projected main axis of particle i, $\delta_{\alpha\beta}$ the Kronecker delta and $\alpha = x, y$.

6.2.7. Fast Fourier Transform

We applied a Fast Fourier Transform (FFT) algorithm on 2D confocal microscopy images to visualize the observed structures in Fourier space. This allows for a (qualitative) comparison with existing light scattering or X-ray diffraction experiments on rod-like particles. We used a custom written C++ algorithm involving a Hanning window to avoid artefacts caused by the finite size of the images [287].

6.3. Results

6.3.1. Control over particle geometry

From the phase diagram of hard spherocylinders shown in Fig. 6.2, we can see that for both the nematic and smectic liquid crystal phases to be stable for an appreciable range of density, a minimum cylinder length aspect ratio L/D of approximately 6 is needed, or equivalently, an end-to-end length aspect ratio l/d of 7. Fortunately, it is well within the limit of the method of Kuijk *et al.* [25] to synthesize particle cores with such an aspect ratio. Fig. 6.5a shows a transmission electron microscopy (TEM) images of particles directly after synthesis with $l/d = 9.4$. However, to perform quantitative 3D real-space analysis in concentrated phases with confocal microscopy, the fluorescent parts of the rods need to be separated by approximately 500 nm, which is roughly the resolution of the confocal microscope in the lateral (z) direction. If we assume that the repulsive potential of the particles adds about 100 nm of separation to each rod (which will be discussed in more detail in section 6.3.2), then the particle cores need to be coated with a non-fluorescent outer layer with a minimum thickness of approximately 150 nm. Because the thickness of the fluorescent layer ($\sim$ 25 nm) also needs to be taken into account (if the cores themselves are not made fluorescent), a minimum shell thickness of 175 nm is needed. The problem that now arises is that the shell coating decreases the particle aspect ratio quite dramatically. Fig. 6.5b shows that an initial aspect ratio of $l/d = 9.4$ decreased to $l/d = 4.7$ after coating the particles with a 162 nm shell. Fig. 6.5c further demonstrates this effect. The continuous lines show the decrease in aspect ratio for a rod with an initial diameter of 250 nm and initial aspect ratio $l/d =$ 8,10,12,14 and 16, assuming that a layer of uniform thickness is formed all around the rod. The gray area in Fig. 6.5c marks the approximate total shell thickness needed for quantitative 3D real-space measurement. The dashed line in Fig. 6.5c indicates that to

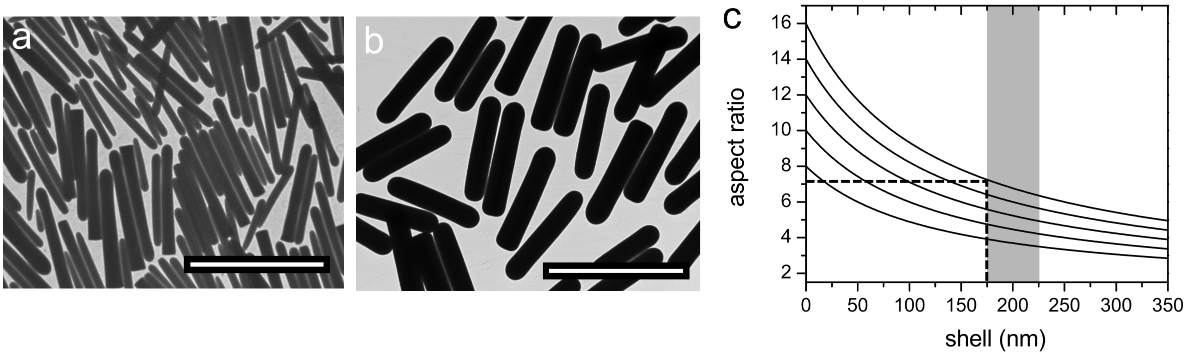

Figure 6.5. The effect of shell coating on the particle aspect ratio. (a) Transmission electron microscopy (TEM) image of particle cores with $l/d =$ 9.4, directly after synthesis. (b) After coating the cores with a 162 nm shell, the aspect ratio decreased to $l/d = 4.7$. Both scale bars are 3 μm. (c) Change in aspect ratio l/d as a function of shell thickness for a rod with a core diameter of 250 nm. The gray area indicates the approximate non-fluorescent shell thickness needed to resolve individual particles with 3D confocal microscopy.

end up with particles with $l/d = 7$, coated with a 175 nm shell, an initial aspect ratio of $l/d = 16$ is needed, which stretches the limits of the current synthesis procedure. We therefore used three adjustments to the rod synthesis procedure to obtain particles with significantly larger aspect ratio.

The first adjustment was a seeded growth procedure where the original recipe was followed with the exception that additional TEOS was added in steps of 3 ml with a time interval of 6 hours. We used a maximum of 4 additions of TEOS in total, resulting in rods with increased aspect ratio. An additional observation is that within the same batch, the thickest rods were always bent. With careful centrifugation and sedimentation steps it was possible to almost completely remove them. Shaking as opposed to just tumbling the synthesis bottle several times after the addition of TEOS did not have a significant effect on rods being straight or bent. A list of syntheses performed using this growth method is given in Table 6.1. A maximum of 4 growth steps resulted in particles with an aspect ratio of $l/d = 20.4$ (TH6). In Fig. 6.6 TEM images are shown for three particle systems with, all other concentrations kept constant, increasing number of growth steps: one time ($l/d = 5.3$, Fig. 6.6a), two times ($l/d = 9.1$, Fig. 6.6b) and four times ($l/d = 20.4$, Fig. 6.6c). The results are summarized in Figs. 6.7a-b, showing that the aspect ratio increases almost linearly with TEOS concentration. For a fixed number of 3 growth steps we also varied the water concentration, which is known to be inversely proportional to the final length of the rods obtained [25]. By lowering the water concentration we could indeed increase the aspect ratio of the particles (see Figs. 6.7c-d). However, below a critical water content of 9 ml, almost all rods were curly or bent.

	H_2O (ml)	NH_3 (aq) (ml)	TEOS (ml)	l (μm)	d (μm)	l/d
THB7	10	6.75	1 × 3 ml	1.7	0.32	5.3
TH2	10	6.75	2 × 3 ml	2.3	0.33	7.0
TH4	8.4	6.75	2 × 3 ml	2.6	0.28	9.1
TH9	8	6.75	3 × 3 ml	5.5	0.30	18.3
TH7	9	6.75	3 × 3 ml	5.7	0.43	13.2
TH8	10	6.75	3 × 3 ml	4.8	0.44	10.9
TH6	10	6.75	4 × 3 ml	10.0	0.49	20.4

Table 6.1. Reagent concentrations of the seeded growth syntheses. All syntheses were performed with 300 ml of 1-pentanol, 30 g PVP, 30 ml ethanol and 2 ml of 0.18 M sodium citrate dihydrate solution in a 500 ml glass laboratory bottle. There was always a minimum of 6 hours between additions of TEOS. All rods were straight and bullet shaped except for TH9, which contained many particles which had a kink along their major axis. Here, l is the average end-to-end length, d the average diameter and l/d the aspect ratio.

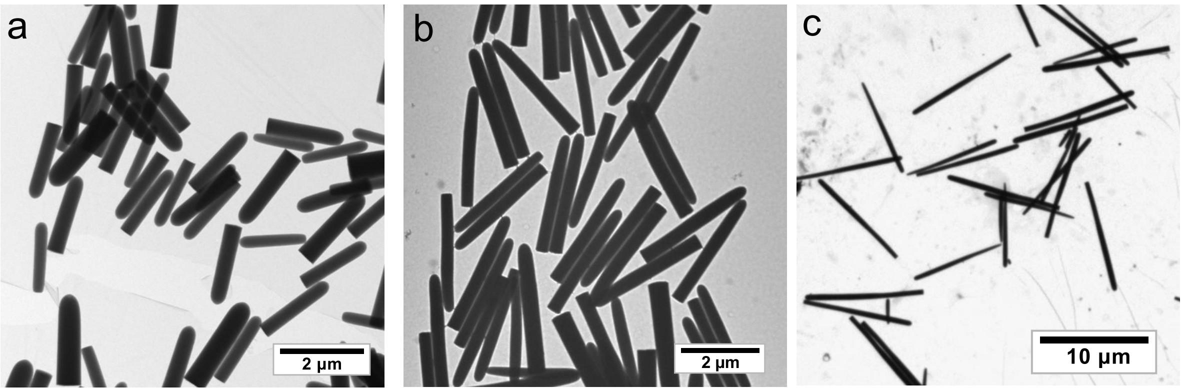

FIGURE 6.6. TEM images of rod-like particle cores. (a) Aspect ratio $l/d = 5.3$ (THB7). (b) Aspect ratio $l/d = 9.1$ (TH4). (c) Aspect ratio $l/d = 20.4$ (TH6). A larger aspect ratio was achieved by a seeded growth procedure, with a maximum of 4 additions of 3 ml TEOS. Reagent concentrations and particle dimensions are listed in Table 6.1.

Although the seeded growth method could be used to produce rods with aspect ratios as large as $l/d = 20$, it also produced very large (and heavy) rods. This is not ideal, since Brownian relaxation times and sedimentation speed increase strongly as a function of size. Therefore, equilibrium phases are more easily surpassed by metastable disordered phases. For a particle with length $l = 5.7$ μm and diameter $d = 430$ nm (TH7) dispersed in 91 wt% DMSO in water, the rotational relaxation time $\tau_r = 23$ s, the time to translate over its own length $\tau_L = 70$ s, the gravitational length $l_g = 0.64$ μm and the sedimentation velocity at infinite dilution $v_s = 10$ μm/min. Due to subsequent shell coatings, these values will increase even more. We therefore investigated an alternative method to obtain particles with large aspect ratio but with small length and diameter. This method consisted of a scaled-up synthesis, using larger amounts of reagent in a 1 L glass bottle and different water and sodium citrate concentrations. Details of all the reagent concentrations and resulting particle dimensions are listed in Table 6.2. Compared to the original synthesis procedure, we used for the first synthesis listed in Table 6.2 (CT1) 25% less water and 50% more sodium citrate solution. All other concentrations were kept constant. We added 8 ml of TEOS only once and the reaction was left to proceed for 72 hours. This resulted in rods with average length $l = 3.0$ μm, diameter $d = 0.21$ μm and $l/d = 14.4$. Although these particles had both a large aspect ratio and a small diameter, their shape was less well defined, see Fig. 6.8a for a TEM image of the particles after several purification steps. Many of the particles were not perfectly straight, and especially the larger ones had an asparagus-like shape. However, most of the large particles could be removed by sedimentation, and shell coating improved the uniformity of the particle shape significantly. When we increased the ammonia concentration from 16 ml to 18 ml (see CT2 in Table 6.2), which is known to result in smaller and less curly rods [25], the particles were indeed more straight and well defined. However, the resulting aspect ratio $l/d = 5.6$ was not high enough for our phase behaviour studies as these particles will have a final aspect ratio of approximately

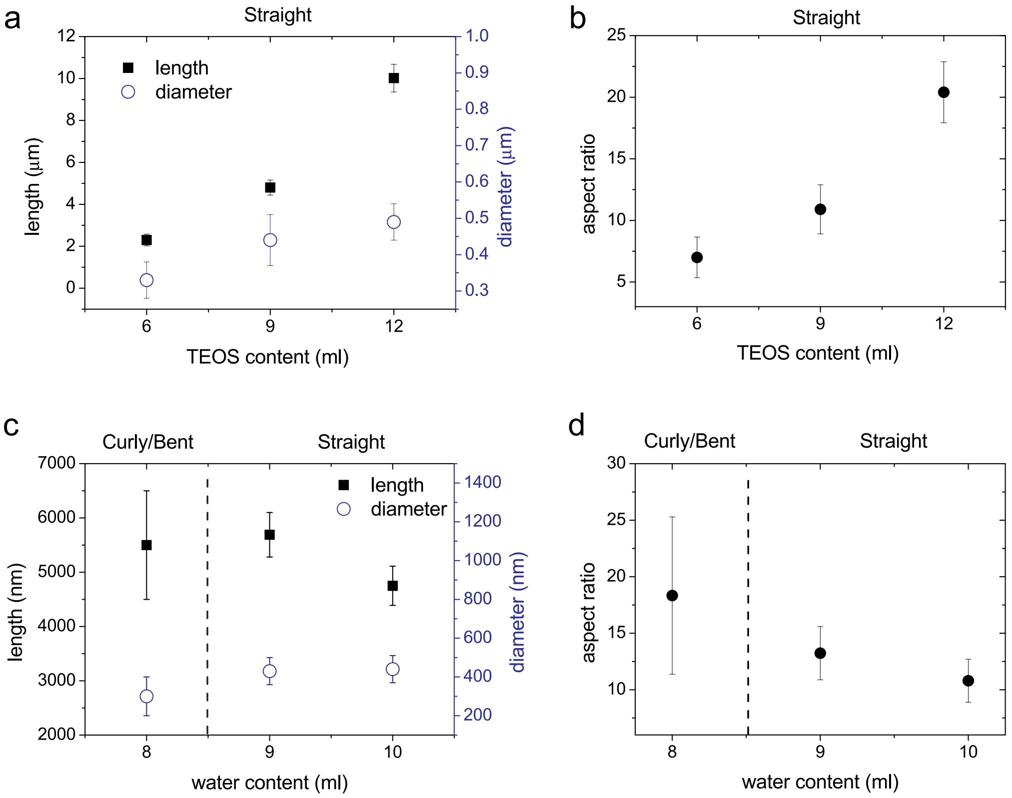

Figure 6.7. Dependence of reagent concentrations on the particle size and shape. Change in length, diameter and aspect ratio are shown as a function of (a-b) TEOS concentration and (c-b) water concentration, with all other concentrations being constant. TEOS was always added in steps of 3 ml with a minimum time interval of 6 hours. Below a critical water concentration, the rods became curly or bent. Error bars indicate the s.d. of the distribution. Complete reagent concentrations are listed in Table 6.1.

3 if a 175 nm shell is coated around these particles. A lower water concentration and lower ammonia concentration (see CT3 in Table 6.2) increased the aspect ratio again to $l/d = 9.4$, with most of the rods straight (see Fig. 6.8b).

To increase the aspect ratio even further we carried out a synthesis at elevated temperature, since it was recently shown that the diameter of the rods can be controlled by regulating the reaction temperature during synthesis, with higher temperatures resulting in smaller diameters [288]. Although the diameter still responded to temperatures up to 90 °C, rods already started to become curved when they were grown at a constant temperature of 40 °C [288]. We therefore carried out our synthesis at a constant temperature of $30 \pm 1\,^{\circ}$C using an incubator to maintain a constant and uniform temperature throughout the duration of the synthesis. This resulted in particles with aspect ratio $l/d = 15.4$ (CT5), see Table 6.2 for details and Fig. 6.8c for a TEM image of the particles.

	H_2O (ml)	NH_3 (aq) (ml)	TEOS (ml)	l (μm)	d (nm)	l/d
CT1	20	16	8.0	3.0	210	14.4
CT2	20	18	8.0	1.7	305	5.6
CT3	19	17	8.5	2.1	226	9.4
CT5	19	17	8.5	3.2	209	15.4

TABLE 6.2. Reagent concentrations for syntheses that were scaled-up and changed in composition compared to the ones listed in Table 6.1. All syntheses were performed with 800 ml of 1-pentanol, 80 g PVP, 80 ml ethanol, 8 ml of 0.18 M sodium citrate dihydrate solution in a 1 L glass laboratory bottle. TEOS was added once at the beginning of the synthesis. All reactions were carried out at room temperature with the exception of CT5 which was incubated at 30°C. Here, l is the average end-to-end length, d the average diameter and l/d the aspect ratio.

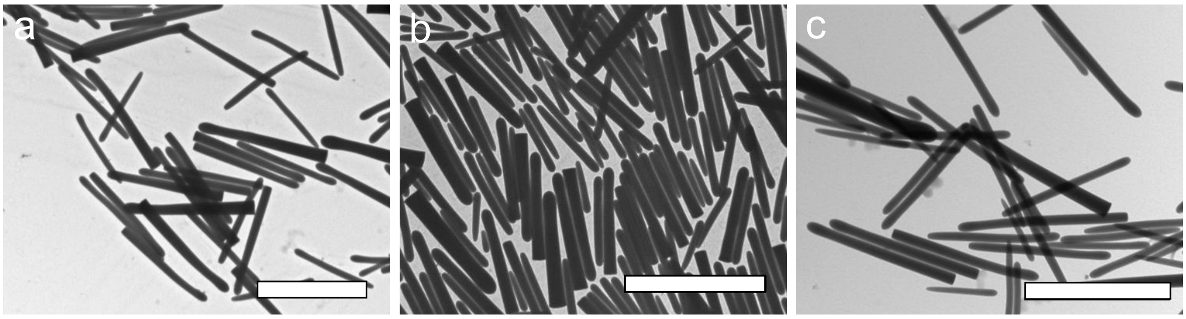

FIGURE 6.8. TEM images of particle cores, with varying aspect ratio, directly after synthesis. (a) Synthesis performed in a larger volume, with 25% higher water concentration (CT1), aspect ratio $l/d = 14.4$. Notice that not all particles are straight. (b) Synthesis performed at room temperature (CT3), aspect ratio $l/d = 9.4$. (c) Synthesis performed at an elevated temperature of 30° C (CT5), aspect ratio $l/d = 15.4$. All scale bars are 3 μm. Particle dimensions and reagent concentrations are listed in Table 6.2.

6.3.2. Phase behaviour

Particle systems. In Table 6.3 we listed the particle systems used for phase behaviour studies for increasing end-to-end aspect ratio l/d. Systems B31, B48 and B35 were used in earlier studies, which are reported in Ref. 28. Two systems had a fluorescent dye-gradient along the main axis of the rods: system B48 (rhodamine isothiocyanate, RITC) and system THB4 (fluorescein isothiocyanate, FITC). Three systems had an FITC fluorescent shell: system B31 (30 nm), system CT1 (57 nm) and system B35 (30 nm). The system TH6 consisted of non-fluorescent particle cores. To image these particles with confocal microscopy, we dyed the solvent with FITC and inverted the images.

	l (μm)	d (μm)	l/d	shell (nm)	solvent	l_g (μm)	$l^*/d^* - 1$
B31	2.4 (10%)	0.64 (8%)	3.8	190	glycerol/water	0.84	2.1
B48	2.6 (9%)	0.63 (6%)	4.1	175	DMSO/water	0.69	2.4
CT1	3.4 (12%)	0.63 (7%)	5.4	137	glycerol/water	0.59	3.3
B35	3.3 (10%)	0.55 (11%)	6.0	105	glycerol/water	0.80	3.7
THB4	4.3 (12%)	0.59 (12%)	7.3	76	DMSO/water	0.46	4.6
TH6	10.0 (7%)	0.49 (10%)	20.4	-	DMSO/water/FITC	0.28	13.8

TABLE 6.3. Properties of the particles used for the phase-behaviour studies in this chapter, with l the average end-to-end length of the rod, d the average diameter, and the percentages in brackets the polydispersity. Also listed is the hard-core end-to-end aspect ratio l/d, the thickness of the outer non-fluorescent shell, the composition of the dispersing solvent, the corresponding gravitational length l_g and an estimate of the effective aspect ratio minus one $l^*/d^* - 1$.

Table 6.3 further lists the thickness of the outer non-fluorescent shell of the particles, the composition of the dispersing solvent and the corresponding gravitational length l_g. As explained in section 6.3.1, a crude estimate of the minimum thickness of the non-fluorescent layer needed for particle fitting of 3D confocal microscopy data is ~ 150 nm (see also Fig. 6.5c). The systems B31 and B48 were above this limit and it was indeed possible to determine accurate 3D positions and orientations of these particles, as shown in detail in Chapter 4. For system CT1, this was only possible after deconvolution of the 3D image stacks and for systems B35, THB4 and TH6 this was not possible. Later in this chapter we will demonstrate, however, that a 2D analysis of the (projected) orientations was nevertheless still possible for these systems.

It is known for these systems, that the silica rods have a negative charge and therefore have a repulsive electrostatic potential [28]. Using an effective diameter d^* and effective length $l^* = l + d^* - d$, with l and d the hard-rod dimensions as measured by TEM, it was possible to map the phase behaviour to reasonable extent onto the hard-spherocylinder phase diagram [28], in analogy with the mapping of charged silica spheres onto the hard-sphere phase diagram, see e.g. Refs. 13,14. In contrast with spheres, however, the (increased) effective dimensions of anisotropic particles also changes the aspect ratio (and therefore also the phase behaviour) [269, 289]. In Ref. 28, the value $d^* - d$ was found to be roughly constant for the five different systems that were used (including systems B31, B48 and B35), which was approximately 200 nm. We therefore used this value to estimate an effective aspect ratio for all of our systems, which we reduced by 1, to enable direct comparison with the phase diagram of hard spherocylinders (see Fig. 6.2 and Ref. 209), where the cylinder length-to-diameter L/D is used. Based on computer simulations, Bolhuis and Frenkel predict the smectic-A phase to be stable for $L/D > 3.1$ and the nematic phase for $L/D > 3.7$. They also estimate the transition between the ABC crystal and AAA crystal to happen at $L/D \approx 7$ [209]. We can immediately see that for the first three systems (B31, B48 and CT1) we do not expect nematic phases.

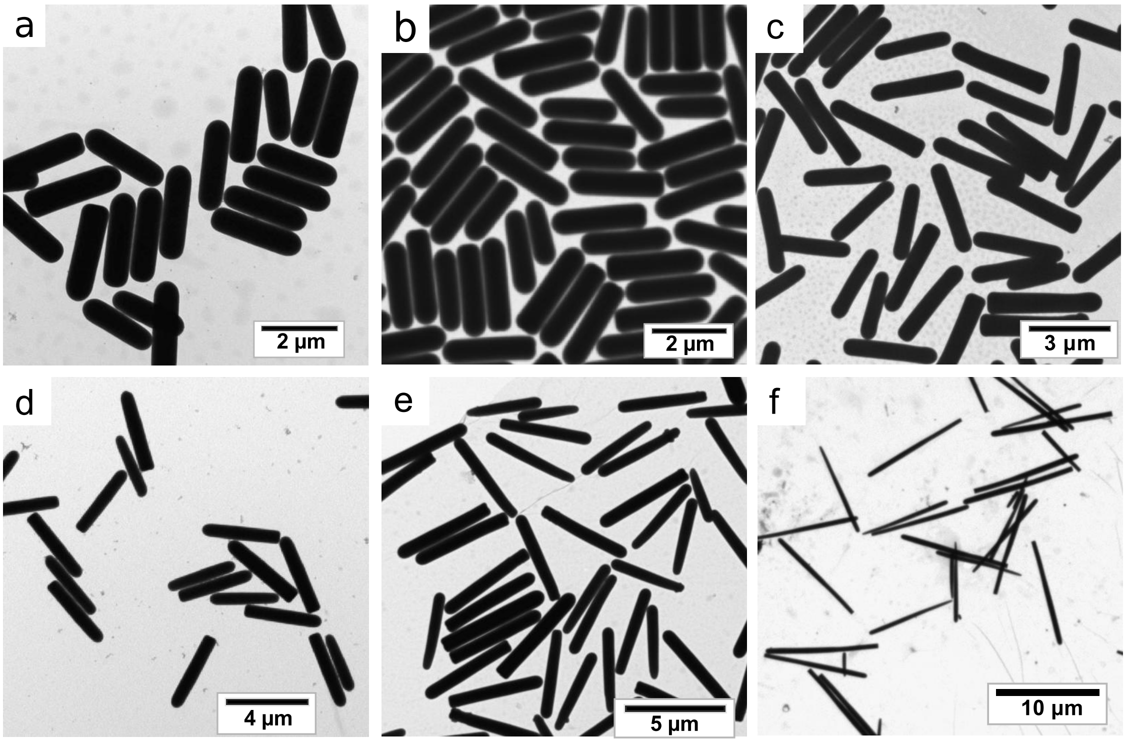

FIGURE 6.9. TEM images of the particles used for phase-behavior studies. (a) B31 (b) B48 (c) CT1 (d) B35 (e) THB4 (f) TH6. Particle dimensions are summarized in Table 6.3.

Fig. 6.9 shows TEM images of the systems listed in Table 6.3. Figs. 6.9a-c show the systems with a non-fluorescent shell ≥ 137 nm which were used for quantitative 3D analysis. Although the shell coating decreased the aspect ratio significantly, it did have a positive effect on the particle system; particles became more uniform in size and more spherocylinder-like in shape compared to the cores that were obtained directly after synthesis.

Aspect ratio $l/d = 4.1$. In this section we present results for system B48, which consists of particles with length $l = 2.6$ μm ($\delta = 8.5\%$), $d = 630$ nm ($\delta = 6.3\%$) and aspect ratio $l/d = 4.1$. The estimated effective aspect ratio minus one $l^*/d^* - 1 = 2.4$, which means that based on computer simulations we only expect an isotropic phase and an ABC crystal to be stable (see Fig. 6.2). However, we always observed that the particles, when left to sediment, ordered into either a smectic-B phase or an AAA stacked solid. Fig. 6.10a-c show that particles ordered into smectic layers (Fig. 6.10a) and within the layers we always found hexagonal order (Fig. 6.10b). Figs. 6.10d-f show Figs. 6.10a-c after 3D deconvolution with a theoretical point spread function. The deconvolution not only suppressed noise but also increased both contrast and resolution, where the improvement in resolution is most clearly visible in the z (lateral) direction. This allowed us the investigate the registry between the smectic layers in more detail, as shown in the 3D projections in Fig. 6.11. Often there was no clear registry between the layers, indicating that there was no long-ranged order or large-scale crystalline phase present. We expect that this is due to the polydispersity of the sample, resulting in the formation of a smectic-B phase, whereas in the simulations on monodisperse hard-rods an ABC solid is found [209]. It is likely however, that the charges on the particle also stabilize a smectic-B phase, as simulations on monodisperse parallel soft spherocylinders indicated a continuous crystal to smectic-B transition [290], whereas in

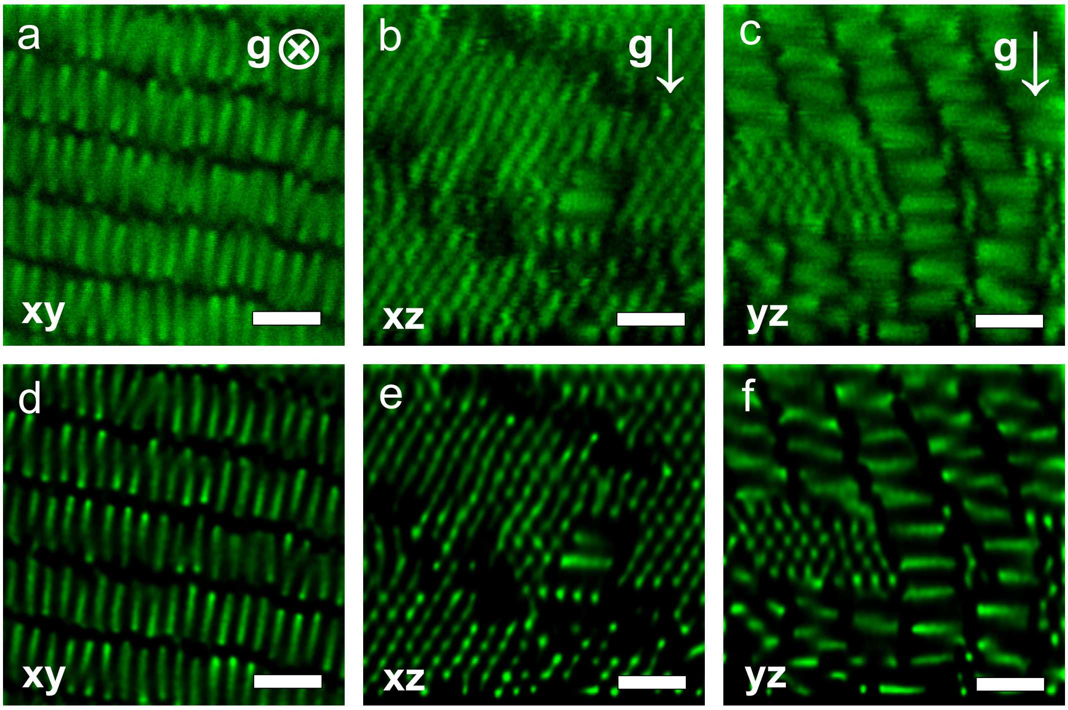

FIGURE 6.10. Smectic-B phase formed by particles with aspect ratio $l/d = 4.1$ (B48). (a-c) Orthogonal views from a 3D confocal microscopy data stack. Particles ordered into smectic layers and within the layers there was hexagonal order. (d-f) The same images as in (a-c) after 3D deconvolution with a theoretical point spread function. All scale bars are 3 μm.

the phase diagram for hard spherocylinders the smectic-B phase is completely absent [209]. However, we did find small regions were there was registry between the layers, showing an AAA-crystal-like stacking (Fig. 6.11). Bolhuis and Frenkel predict that the ABC stacked crystal is stable up to the point where the distance between layers decreases to become of the order of the diameter D, which is for $L/D \lesssim 7$ [209]. Beyond that point, the hemispherical caps of the rods start to feel each other and the AAA crystal is more stable because the number of interactions in the ABC crystal is much larger than for the AAA crystal; a rod in ABC stacking interacts on average with 6 rods from neighbouring layers whereas in the AAA stacking this number reduces to 2. The AAA crystal-like stacking that we found for $l^*/d^* - 1 = 2.4$ is probably due to the polydispersity of the system ($\delta_l = 8.5\%$ and $\delta_d = 6.3\%$). For the B31 system, which

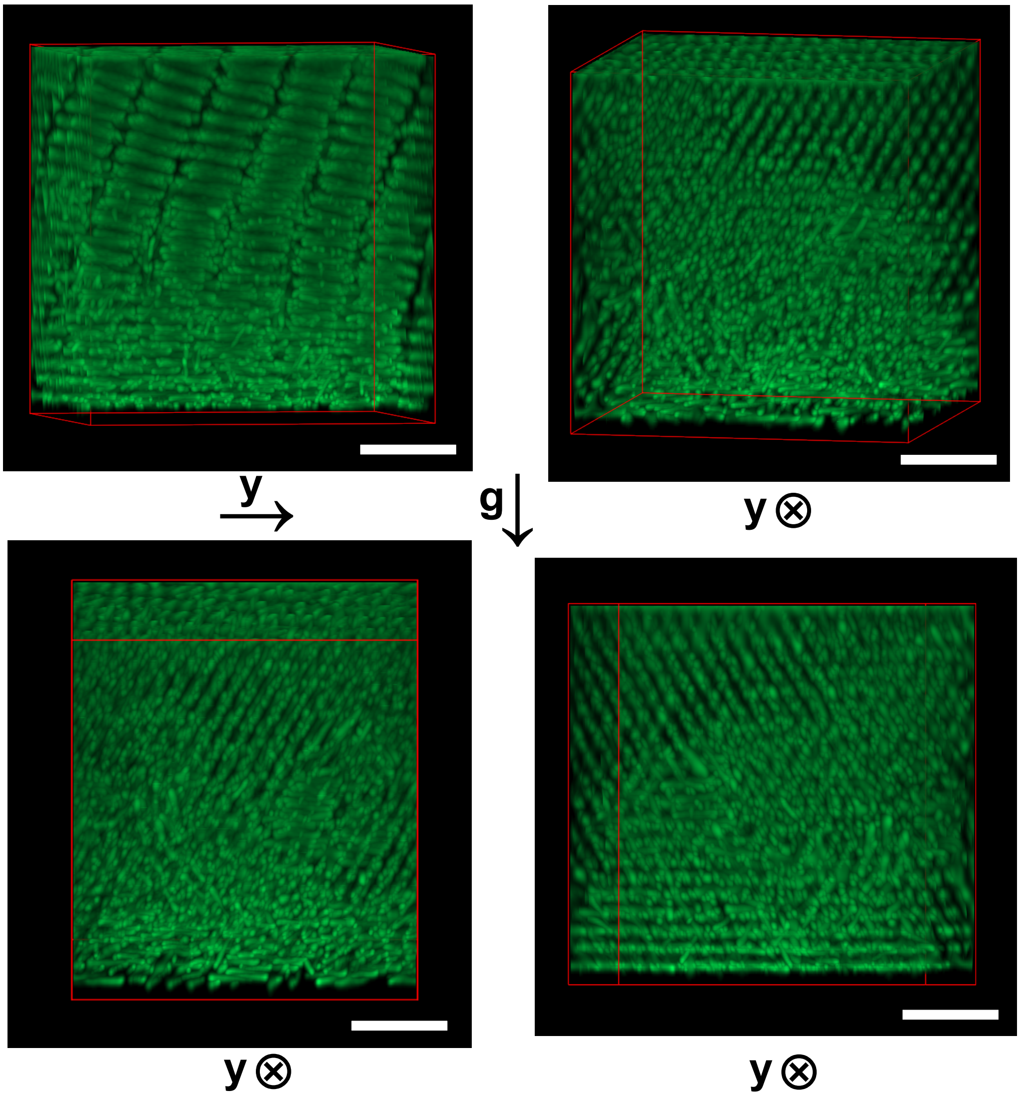

FIGURE 6.11. 3D views of deconvolved data of a dense sediment of particles with aspect ratio $l/d = 4.1$ (B48). Small AAA-stacked crystalline regions are visible. The direction of gravity is indicated with g. All scale bars are 4 μm.

has similar dimensions but slightly higher polydispersity ($\delta_l = 10\%$ and $\delta_d = 7.5\%$, see Table 6.3), we never observed any regular stacking between smectic layers, i.e. we always found a smectic-B phase at the bottom of the sediment. We therefore expect for rods with $L/D < 7$ the following transition as a function of increasing polydispersity: ABC crystal → AAA crystal → Smectic-B phase, given that the polydispersity in length stays below a certain level ($\delta_l \lesssim 10\%$) since otherwise it is likely that a columnar phase will form at high density [211, 272].

In Fig. 6.12 we show a 3D reconstruction after particle fitting the data shown in Fig. 6.10a-c, i.e. without an initial deconvolution. We determined the 3D positions and orientations of 1699 particles in total, which we color-coded according to their orientation. Figs. 6.12a-d show that there were small domains of particles with deviating orientation and also single, transverse interlayer particles, which were predicted by computer simulations [291, 292]. In Fig. 6.12e particles are shown 1/2 of their original size. The AAA-crystalline region in the top left corner is clearly visible. It is also visible that both positional and orientational order was less pronounced towards the bottom region of the sample where the particles were horizontally aligned with the glass wall, which will be discussed in more detail in the next section. We also calculated the nematic order parameter S_{3D} and the nematic director $\hat{\mathbf{n}}$, indicating the average alignment in the system, using equation (6.12). We found $S_{3D} = 0.78$ and $\hat{\mathbf{n}} = \{-0.19, 0.98, -0.07\}$ confirming the strong alignment in the y-direction. In Fig. 6.12f we show the distribution of the angle θ, defined by $\cos\theta = \hat{\mathbf{u}} \cdot \hat{\mathbf{n}}$, with $\hat{\mathbf{u}}$ the unit vector along the main axis of a rod. Here, we also define ϕ as the angle in the plane perpendicular to the director, with $\phi = 0$ indicating alignment with the horizontal. The large peak in Fig. 6.12f, close to $\theta/\pi = 0$, is from the particles aligned with the director, whereas the small secondary peak close to $\theta/\pi = 0.5$ shows that the (domains of) interlayer particles were on average oriented perpendicular to the nematic director. Additionally, these particles were also more often orientated along the hexagonal close-packed directions of the smectic-B layer ($\phi \approx 0, \pi/3$ and $2\pi/3$) or orientated parallel to gravity ($\phi \approx \pi/2$), which is indicated by the red, purple and blue particles respectively in Figs. 6.12a-e.

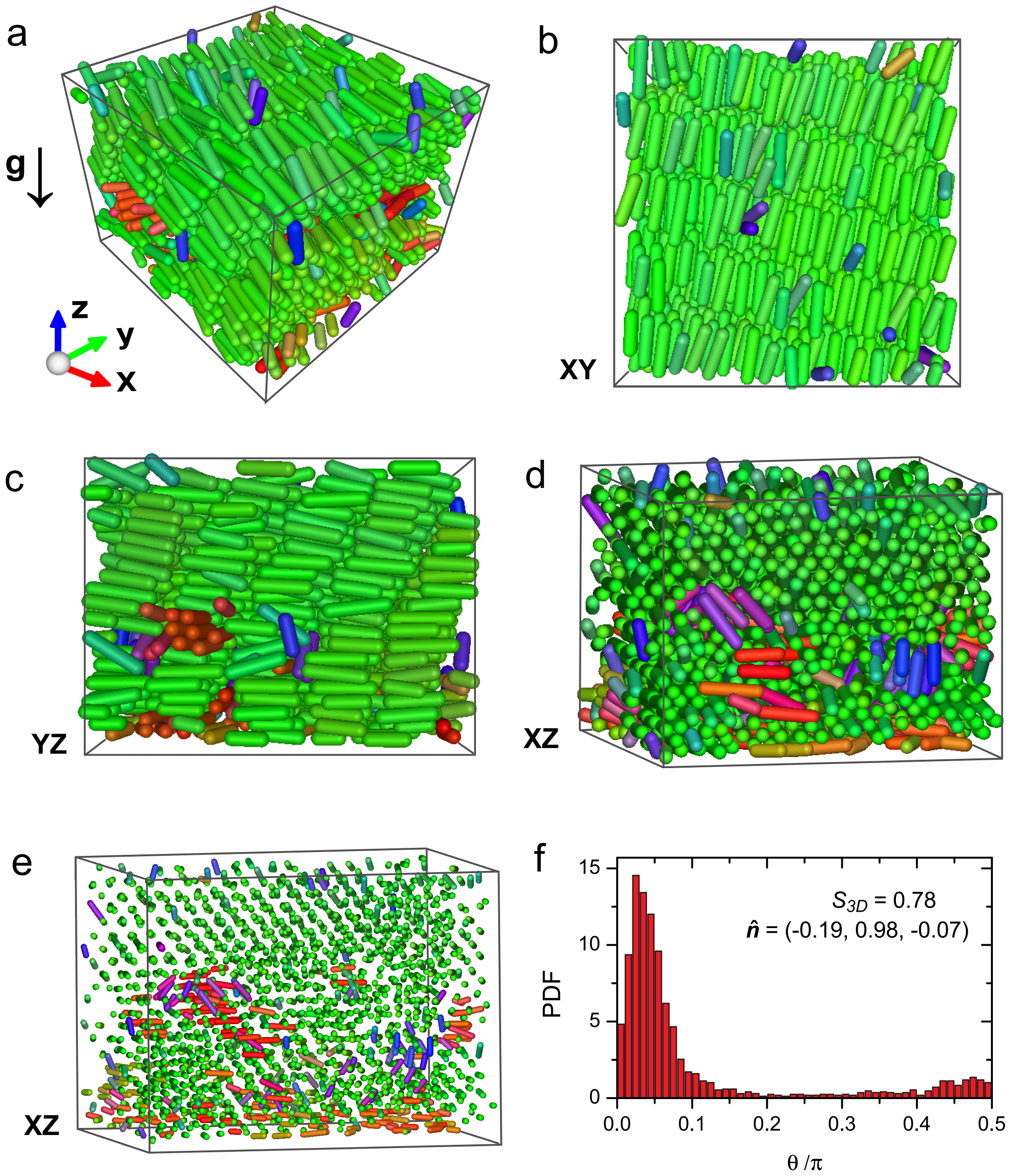

FIGURE 6.12. 3D reconstruction from confocal microscopy data of a dense sediment of rods with aspect ratio $l/d = 4.1$ (B48). (a-e) Colors indicate the 3D orientation of the particles. Small deviating domains and transverse interlayer particles are clearly visible. (f) Orientation distribution function of the angle θ, defined by $\cos\theta = \hat{\mathbf{u}} \cdot \hat{\mathbf{n}}$.

Aspect ratio $l/d = 5.4$. In Fig. 6.13, we show deconvolved confocal microscopy images of a sediment of the CT1 system which consists of particles with average length $l =$ 3.4 μm (12%), diameter d = 630 nm (7%) and aspect ratio $l/d = 5.4$ dispersed in glycerol/water. The images in Fig. 6.13 were acquired after the sample had been left to sediment for 90 days. We did not find a significant difference in structure with data acquired 47 days after sample preparation. The estimated effective aspect ratio minus one $l^*/d^* - 1 = 3.3$ for this system (see Table 6.3). At this aspect ratio, the equation of state of monodisperse hard spherocylinders shows isotropic - smectic-A - ABC solid transitions [209]. Fig. 6.13a shows that we observed a dilute isotropic phase at the top of the sediment (see also Fig. 6.13b). Closer to the bottom of the sediment, we found a hexagonally stacked dense phase, which we identify as a smectic-B phase (see Fig. 6.13a and Fig. 6.13c). Furthermore, we found that the smectic phase was more disordered closer to the glass bottom wall (Figs. 6.13d-f), which will later be discussed in more detail.

In Fig. 6.14 we show a quantitative 3D analysis of a part of the sediment (acquired 47 days after sample preparation), based on confocal microscopy data stacks of $25 \times 20 \times 54$ μm^3, with a voxelsize of 51 nm in x,y and 84 nm in z. Fig. 6.14a shows a 3D reconstruction, with colours indicating the 3D orientation of the particles. Notice the strong similarity with the computer simulation result shown in Fig. 6.3, which is for hard spherocylinders with aspect ratio $L/D = 5$, inverse gravitational length $D/\,l_g = 0.75$ and number of particles per unit surface $n_s\, D^2 = 4.34$, defined as $n_s \equiv \int_0^\infty dz\, \rho(z)$ [278]. The similarity is because these three parameters are in reasonable correspondence with the ones in our experimental system; the estimated effective aspect ratio minus one $l^*/d^* - 1 = 3.3$, the inverse gravitational length $d^*/\,l_g = 0.75$ and the number density per unit surface $n_s\, d^{*2} = 6.5$. Here, we have used an estimated effective end-to-end length l^* = 3.6 μm, effective diameter d^* = 0.83 μm and a gravitational length measured from the dilute top region of the sediment, which will be discussed later in this section. However, the difference in the phases that we observed, compared to the simulations, are due to the (non-negligible) difference in aspect ratio and likely due to polydispersity. For hard spherocylinders with aspect ratio $L/D = 3.3$, the nematic phase is not stable and the density region where the smectic-A phase is stable in the simulations is so narrow that it is unlikely to be observed in our experimental system. Similarly as before, we expect the presence of the smectic-B phase (instead of the predicted ABC solid) to be caused by the polydispersity of the system. We did not find any indication of (AAA) crystalline order in this sample. Fig. 6.14b shows a projection of the rods centres-of-mass, with colours indicating the values of the average local nematic order parameter $\langle S^i_{3D} \rangle$, given by equation (6.13). The smectic layers are clearly visible in Fig. 6.14b, as well as the positionally and orientationally disordered isotropic phase. Close to the bottom glass wall ($z = 0$), we observed wall induced layering of the rods, however, both positional and orientational order were lower than in the smectic region above (as can be seen from the lower part of Fig. 6.14b). This type of disorder is unexpected because a wall aligns the particles and computer simulations on monodisperse hard rods have shown that a thick

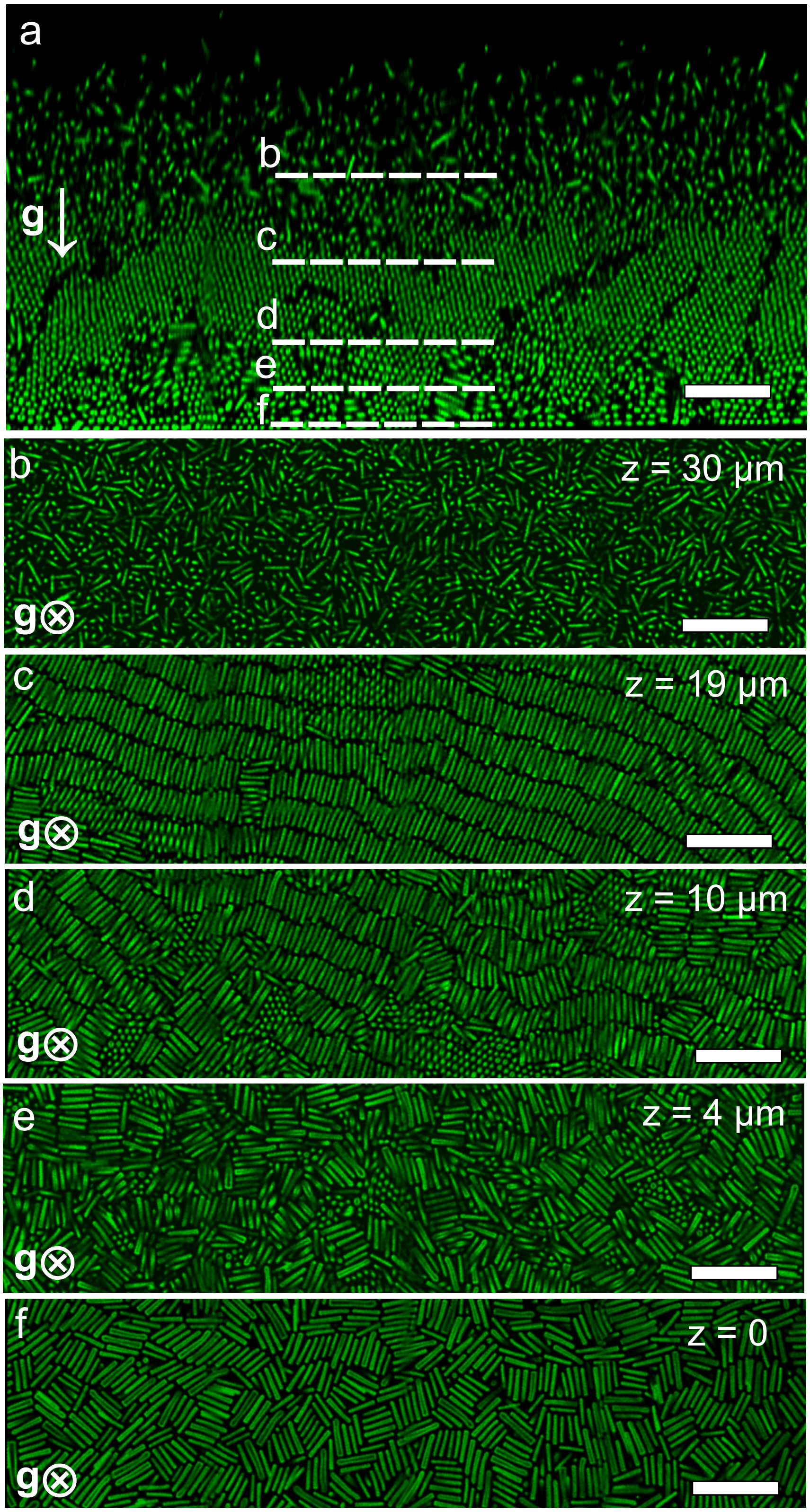

FIGURE 6.13. Deconvolved confocal microscopy images of a sediment of particles with aspect ratio $l/d = 5.4$ (CT1). Images are shown (a) parallel to gravity (xz-direction) and (b-f) perpendicular to gravity (xy-direction). The dashed horizontal lines in (a) indicate the height were images (b-f) were acquired. All scale bars are 10 μm.

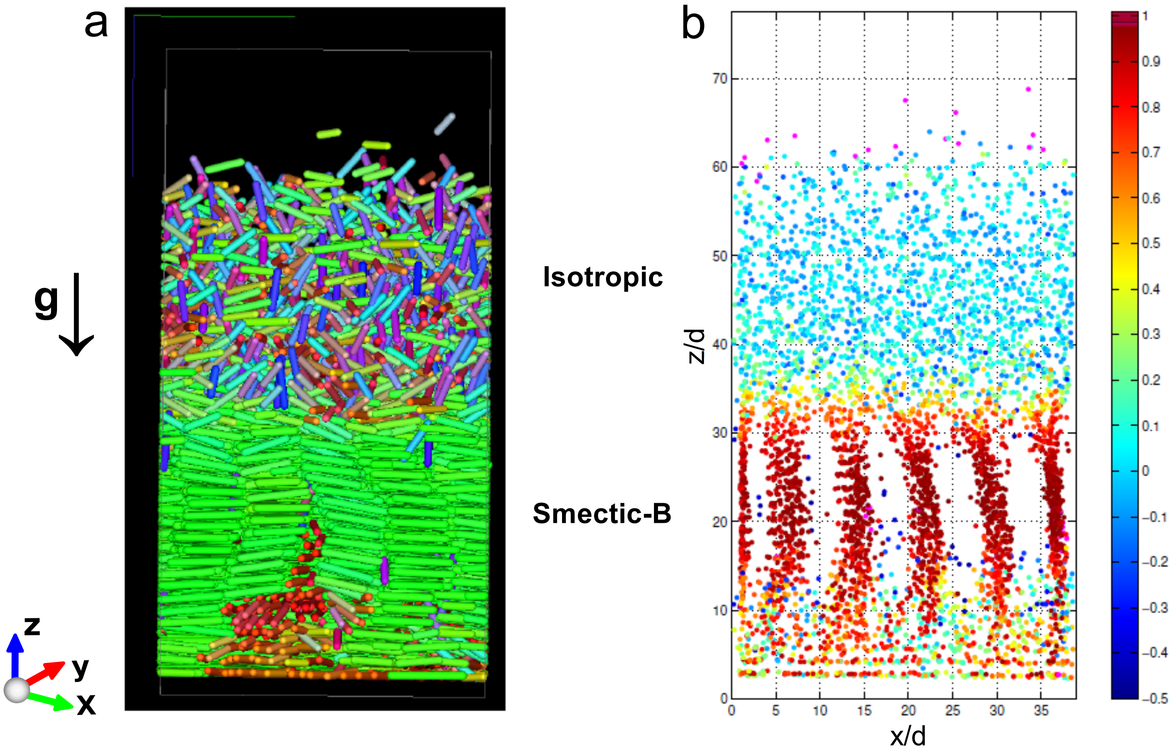

FIGURE 6.14. Quantitative analysis from 3D confocal microscopy data stacks of particles with aspect ratio $l/d = 5.4$ (CT1). (a) 3D reconstruction from a sediment, 47 days after sample preparation. Colours indicate 3D particle orientation. (b) Distribution of the rods centres-of-mass. The colours indicate the value of the average local nematic order parameter $\langle S^i_{3D} \rangle$, as indicated in the colour-bar.

nematic film forms at the wall, already below the isotropic-nematic coexistence density, which grows logarithmically when nearing the bulk phase transition [293]. Close to the wall, however, we always found small domains of particles with various orientations, together with orientationally disordered regions (see Figs. 6.13e,f) which extended at least 10 layers into the bulk. The disorder is likely caused by particle segregation during sedimentation. After sedimentation, the concentration of the larger particles was higher at the bottom of the sediment (Figs. 6.13e,f) than in the middle or top part of the sediment (Figs. 6.13b-d).

In Fig. 6.15a we show the density profile over the full length of the sediment, averaged over 24 image stacks collected at different xy position. The continuous (green) line shows the local density profile ρd^3, with d the particle diameter as measured with TEM. The (red) dashed line shows a coarse grained density profile $\bar{\rho} d^3$, obtained by convolving the data with a top hat function of $5d$ in width. The profiles were obtained by averaging over 175.728 particles in total. The (blue) dashed-dotted line in Fig. 6.15a shows the average value of the local nematic order parameter $\langle S^i_{3D} \rangle$. After ~ 17 μm, the order parameter reaches a plateau level in the smectic-B phase ($\langle S^i_{3D} \rangle \sim 0.85$), until

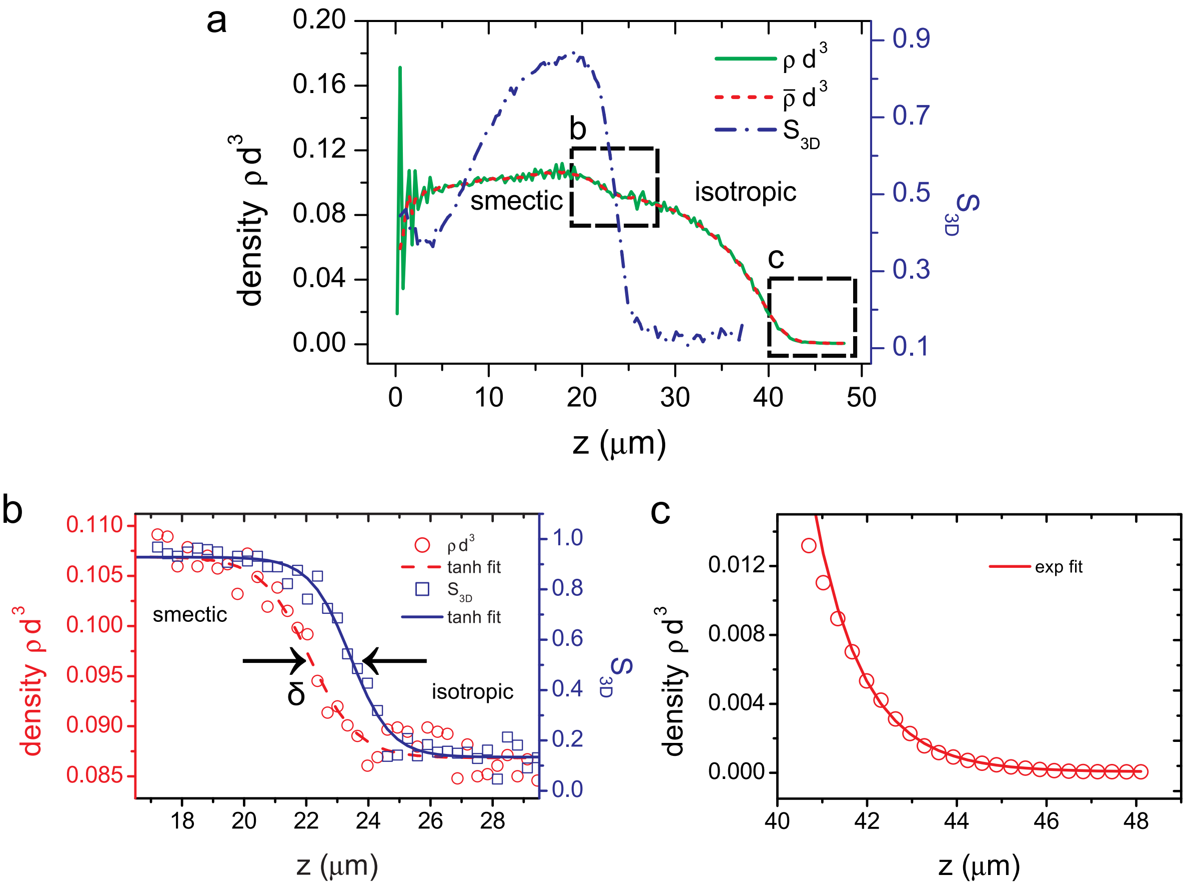

FIGURE 6.15. Density profile for particles with aspect ratio $l/d = 5.4$ (CT1), obtained from 3D confocal microscopy data. (a) Profiles of the particle number density $\rho\, d^3$, the coarse grained number density $\bar{\rho}\, d^3$ and the average local nematic order parameter $\langle S^i_{3D} \rangle$. Here, d is the hard-core particle diameter (630 nm). (b) Number density $\rho\, d^3$ and average local nematic order parameter $\langle S^i_{3D} \rangle$ at the isotropic - smectic-B interface. (c) Density profile of the dilute top region of the sediment.

it drops at the smectic-B - isotropic interface, where there is also a change in number density $\rho\, d^3$.

We investigated the interface region of a single data stack in more detail, as shown in Fig. 6.15b. The dashed and continuous lines are tangent hyperbolic fits, given by equation (6.7). It is clear that the nematic order persisted higher up in the sample, compared to the density. This phenomenon was predicted by both theory and simulation for an isotropic-nematic interface of hard spherocylinders and is due to planar alignment of particles close to the interface [294, 295]. We determined the difference between the two inflection points to be $\delta/(l^* - d^*) \equiv (z_0^{S_{3D}} - z_0^{\rho\, d^3})/(l^* - d^*) = 0.48 \pm 0.04$, which agrees well with density functional theory ($\delta/L = 0.45$) and computer simulations of hard spherocylinders with $L/D = 15$ ($\delta/L = 0.38$) [295]. Furthermore, we obtained for the density in the isotropic and smectic-B phase respectively $\rho_1\, d^3 = 0.088$ and $\rho_2\, d^3 = 0.107$. If we convert these values to volume fractions, assuming an effective length $l^* = 3.6\ \mu$m and effective diameter $d^* = 0.83\ \mu$m, we find $\phi_I = 0.63$ and $\phi_{Sm} = 0.77$. These values are higher than predicted by computer simulations for the isotropic-ABC solid transition for hard spherocylinders with $L/D = 3.4$, which are $\phi_I^{HSC} = 0.50$ and $\phi_{Solid}^{HSC} = 0.60$ [209]. However, determining colloidal volume fractions via confocal microscopy is difficult, even for hard-sphere like suspensions [15]. This is even more so the case for the charged, anisotropic particles used in this chapter since the effective dimensions, which are only estimates, can shift the final volume fractions considerably. For comparison, if we use the hard-particle diameters obtained from TEM ($l = 3.4\ \mu$m and $d = 0.63\ \mu$m) we find $\phi_I = 0.35$ and $\phi_{Sm} = 0.43$. Furthermore, other phenomena that influence the volume fraction determination are the assumption about the particle shape (bullet-like or spherocylindrical-like) and the polydispersity of the particles. Nevertheless, the relative increase in density $(\phi_{Sm} - \phi_I)/\phi_I = 22\%$ does compare well with the 20% increase predicted by the simulations [209], however, it is likely that the polydispersity of the system actually broadens this range [296–298]. For the average values of the local 3D nematic order parameter we found for the isotropic phase $\langle S_{3D}^i \rangle_I = 0.13$ and for the smectic-B phase $\langle S_{3D}^i \rangle_{Sm} = 0.92$, which are in reasonable agreement with the values that were expected for hard spherocylinders [209].

The last part of the density profile that we investigated was the dilute top regime, indicated in Fig. 6.15c. We fitted the tail of the density profile ($z > 42\ \mu$m) to a barometric height distribution $\rho\, d^3(z) = \rho_0 \exp(-z/l_g)$, indicated by the continuous line in Fig. 6.15c. From this fit, we obtained for the gravitational length $l_g = 1.10 \pm 0.02\ \mu$m, corresponding to a reduced inverse gravitational length $d^*/l_g = 0.75$, which is almost twice the value expected from the hard-rod dimensions ($l_g = 0.59\ \mu$m). It is known from simulation that a polydispersity of $\sim 5\%$ in a hard-sphere system results in an increase of the gravitational length of $\sim 8\%$ [274]. We expect a similar but larger effect in our system, since the polydispersities are $\delta_l = 12\%$ and $\delta_d = 7\%$ for the particle length and diameter respectively. Although the particles in our system are charged, they are significantly screened since the inter-particle spacing of two parallel rods at the bottom of the sediment is $\sim 0.3\, d$, with d the hard-core particle diameter obtained from TEM. We therefore do not expect that charge separation, which results in extended gravitational lengths in unscreened systems of spherical colloids [274, 280], can fully explain our observations.

Determination of in-plane orientations. In the previous sections (and in Chapter 4) we showed that individual particle detection from 3D confocal microscopy images is only possible when there is a large enough non-fluorescent layer grown around the particle (approximately 150 nm). This limits however the aspect ratio of the rods, which is why the systems described so far did not form nematic phases in equilibrium. We therefore also synthesized rods that have a non-fluorescent layer of only 76 nm but a relatively high aspect ratio $l/d = 7.3$ and estimated effective aspect ratio minus one $l^*/d^* - 1 = 4.6$ (system THB4, see Table 6.3). We also used a particle system consisting of non-fluorescent cores only with aspect ratio $l/d = 20.4$ and estimated effective aspect ratio minus one $l^*/d^* - 1 = 13.8$ (TH6, see Fig. 6.6c). At this (effective) aspect ratio, the range of volume fractions at which a nematic phase is predicted to be stable is quite large: $\phi = 0.18 - 0.45$ [209]. However, their size (average length $l = 10.0$ μm and diameter $d = 0.49$ μm), makes them almost non-Brownian: when dispersed in DMSO/water, the rotational relaxation time $\tau_r = 102$ s. Nevertheless, we dispersed a small amount of the rods in a refractive matching mixture of 91 wt% DMSO in water and added FITC dye to this mixture to image the non-fluorescent particle cores, eliminating the need for shell coating, which would have reduced the aspect ratio and increased their size even further.

Although these two systems (with a minimum inter-particle separation of $\sim$ 200 - 300 nm) do not allow for quantitative 3D measurements, Fig. 6.16 shows that the orientations of the particles can nevertheless be quantified in 2D real-space, even for concentrated phases. Fig. 6.16a shows a raw xy confocal microscopy image of particles with an aspect ratio $l/d = 7.3$, dispersed in DMSO/water (THB4). The image was acquired close to the bottom glass wall of the sample container, after the particles had sedimented for 2 days. We quantified the orientational order in the system by calculation of a structure tensor of each pixel individually [285]. We used a Gaussian window function with a standard deviation $\sigma = 3$ pixels to specify the region of interest. The eigenvector corresponding to the largest eigenvalue of the tensor gives the predominant orientation in that region. These orientations are shown in Fig. 6.16b, with colouring according to the colormap on the right. Fig. 6.16b shows a close-up of a nematic-like phase, indicated by the predominant green and yellow in the image. A small domain with different orientation (magenta), is visible in the top right of Fig. 6.16b. The same procedure was followed for our second system (TH6), consisting of non-fluorescent cores with aspect ratio $l/d = 20.4$, also dispersed in DMSO/water. Because the dispersing solvent was made fluorescent, instead of the particles, we inverted the confocal microscopy image shown in Fig. 6.16c before processing. Figs. 6.16b,d clearly show that this method is capable of quantifying the (in-plane) orientational order in the system, with accuracy almost on the single particle level.

Aspect ratio $l/d = 7.3$. In this section, we report investigations on the phase behaviour of particles with an average end-to-end length $l = 4.3$ μm (12%), average diameter $d = 0.59$ μm (11%), aspect ratio $l/d = 7.3$ and estimated effective aspect ratio $l^*/d^* - 1 = 4.6$,

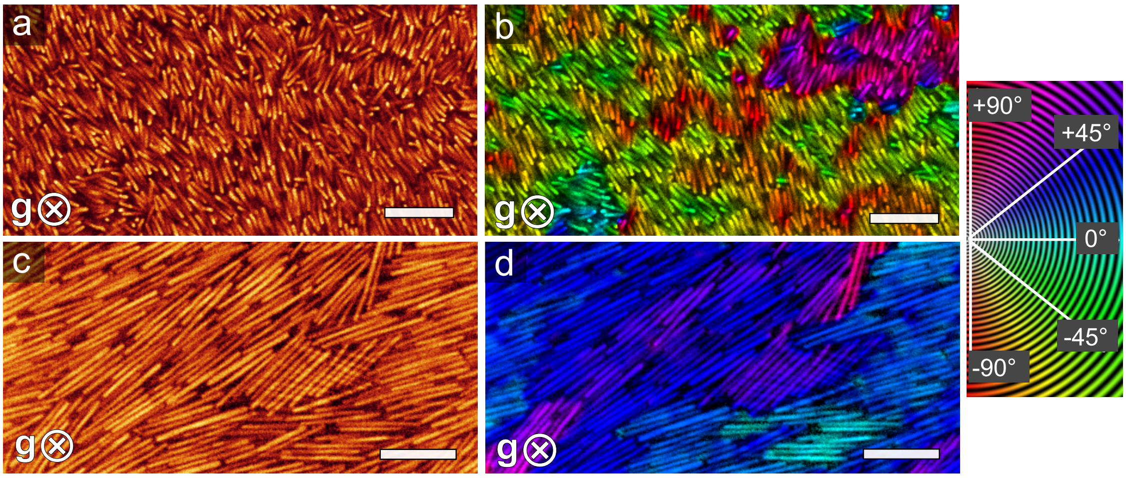

Figure 6.16. Determination of the in-plane particle orientations. Orientations were determined by calculation of the structure tensor for each pixel individually, using a Gaussian window function with $\sigma = 3$ pixels [285]. Colours correspond to the orientations indicated in the colormap. (a) Raw xy confocal microscopy image and (b) processed image of particles with aspect ratio $l/d = 7.3$ (THB4). (c) Inverted xy confocal microscopy image and (d) processed image of particles with aspect ratio $l/d = 20.4$ (TH6). Both particle systems were dispersed in an index-matching mixture of DMSO/water. All scale bars are 10 μm.

dispersed in DMSO/water (THB4). Fig. 6.17 shows a processed confocal microscopy image (perpendicular to gravity), obtained after the particles had sedimented for 2 days. In this single microscopy image, three phases were observed: an isotropic phase, a nematic phase and a smectic phase are clearly visible, with colours indicating the in-plane orientations of the particles. Bolhuis and Frenkel estimated the isotropic-nematic-smectic triple point at $L/D \approx 3.7$ [209], which is in the vicinity of the estimated effective aspect ratio of our system l^*/d^* - 1 = 4.6. However, it is likely that the sample shown in Fig. 6.17 was under a small angle with respect to gravity, due to the common fact that the capillaries are never stored perfectly vertically or placed vertically under the confocal microscope. Combined with the small gravitational length of the rods ($l_g = 0.46$ μm), it is likely that the image shows a (small) section through the density profile and therefore shows regions with slightly different densities, instead of a single phase point.

We further analysed the two liquid-crystal phases individually, shown in Fig. 6.18. Figs. 6.18a,b show processed xy confocal microscopy images obtained at different heights in the sediment, 4 days after sample preparation. Fig. 6.18a shows an image of a nematic phase, acquired approximately 20 μm above the bottom wall, whereas Fig. 6.18b shows an image of a smectic phase, acquired approximately 15 μm above the bottom wall. The arrows in the inset of Fig. 6.18b highlight transverse interlayer particles, which have an orientation perpendicular to the director, which were predicted by both theory and computer simulations [291, 292]. Figs. 6.18c,e show a Fast Fourier Transform (FFT)

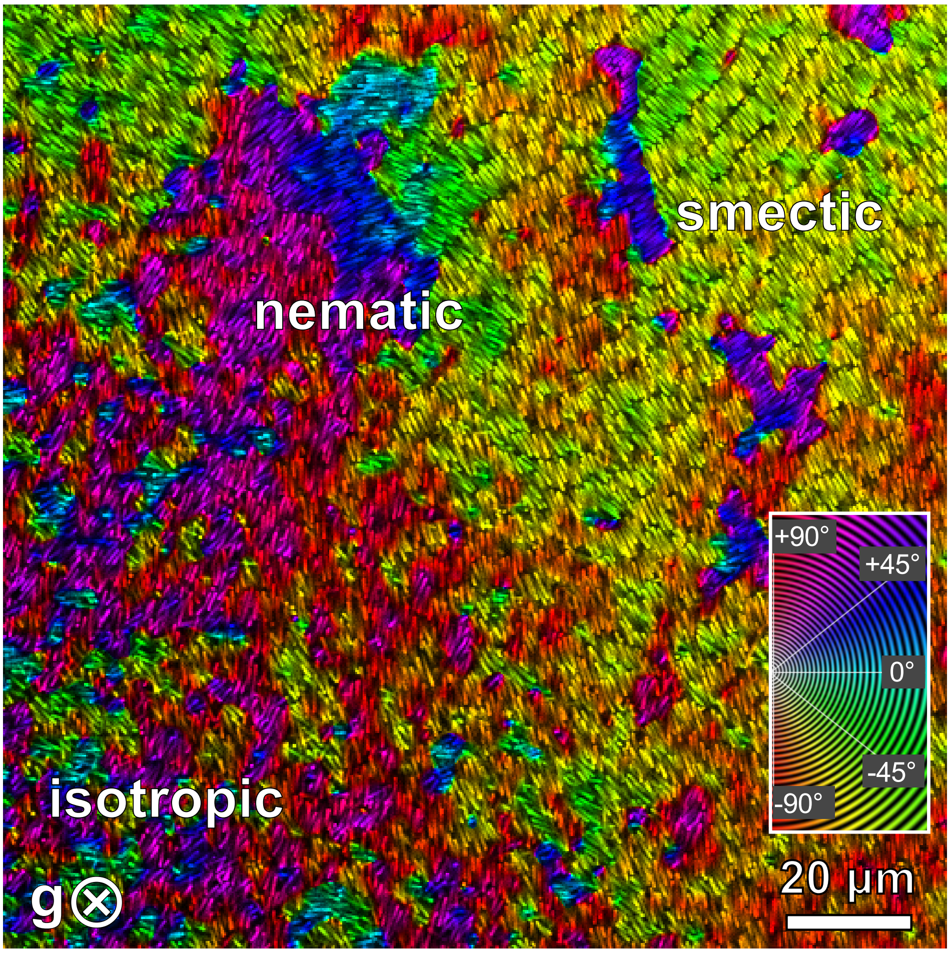

FIGURE 6.17. Phase behaviour of particles with aspect ratio $l/d = 7.3$, dispersed in an index matching mixture of DMSO/water. In a single confocal microscopy image, which was acquired perpendicular to gravity, three phases were observed: an isotropic, a nematic and a smectic phase.

of the images in Figs. 6.18a,b respectively, plotted with logarithmic intensity scale. The FFTs clearly indicate the long-range (orientational) order in the system. The orientation probability density functions (PDFs) shown in Figs. 6.18d,f were obtained from structure tensor calculations for all the individual pixels (1024 × 1024) of the images shown in Figs. 6.18a,b. From these distributions, we calculated the projected 2D nematic order parameter $S_{2D'}$ and the nematic director $\hat{\mathbf{n}}'$. As long as the angle between the director and the plane of observation is small, we have found the value of the 2D projected nematic order parameter to be a good estimate of the true 3D nematic order in the system (at the same height in the sample), which is demonstrated in Chapter 4. Fig. 6.18d shows the projected orientation distribution of the nematic phase, from which we obtained $S_{2D'} = 0.88$. The projected nematic director was at an angle of $-48.6\,^\circ$ with the horizontal, indicated by the double-sided arrow in Fig. 6.18a. For the smectic phase, we found $S_{2D'} = 0.97$ (Fig. 6.18f) and a nematic director that was at an angle of $+1.4\,^\circ$ with the horizontal, as shown in Fig. 6.18b. Bolhuis and

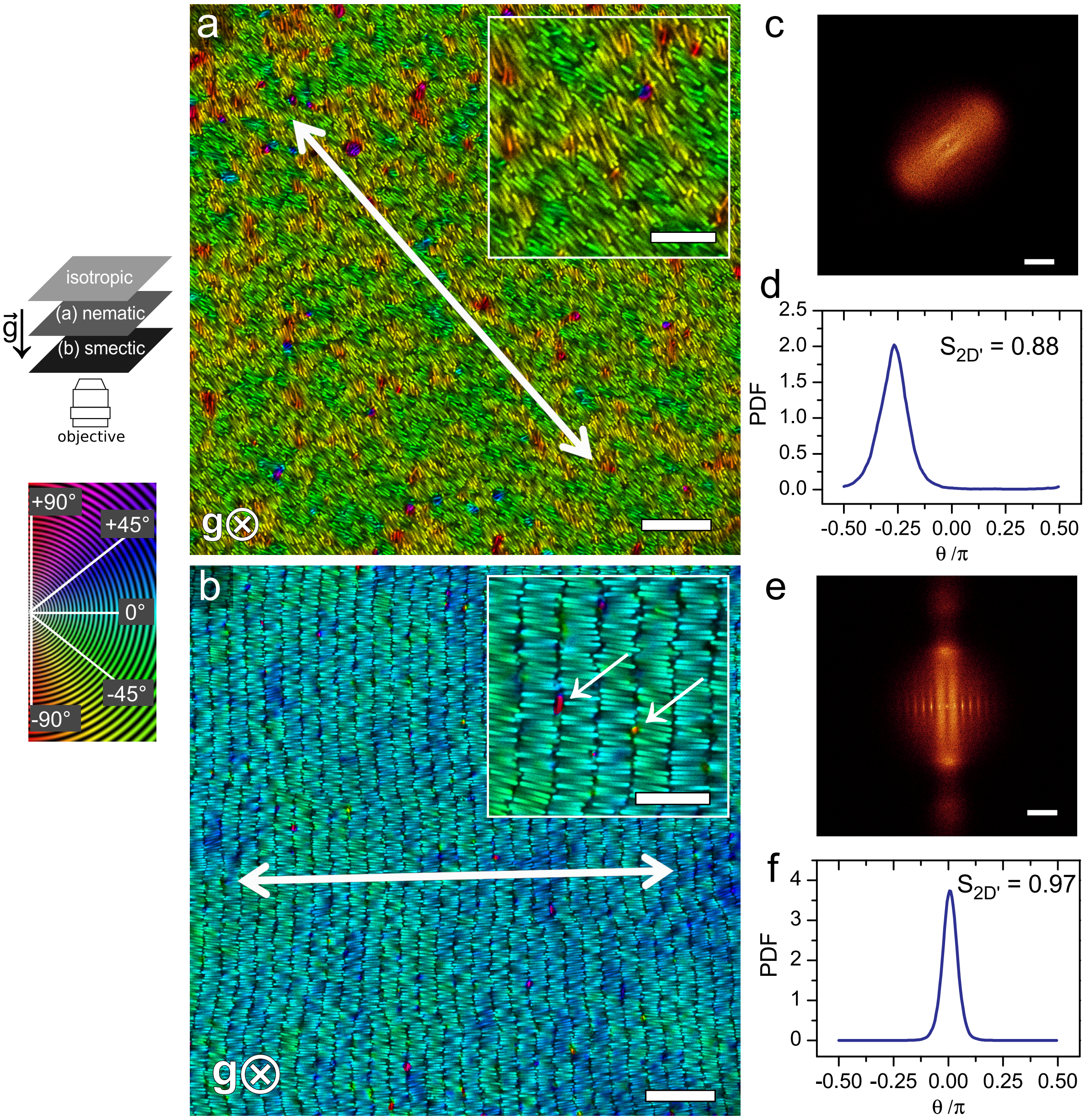

FIGURE 6.18. Liquid crystalline phase-behaviour for particles with aspect ratio $l/d = 7.3$. (a) Nematic phase. (b) Smectic phase. The arrows in the inset highlight transverse interlayer particles. The colours in (a) and (b) indicate the in-plane orientation of the particles as indicated by the colormap. (c,e) Fast Fourier Transforms (FFTs) of the images in (a,b) respectively, plotted on a logarithmic intensity scale. (d,f) Probability density function (PDF) of the in-plane orientations, which were used to determine the projected nematic order parameter $S_{2D'}$ and the projected nematic director $\hat{\mathbf{n}}'$. The nematic director $\hat{\mathbf{n}}'$ is indicated in both (a) and (b) with an double sided arrow. The scale bars are 20 μm in (a) and (b), 10 μm in the insets of (a) and (b) and 5 μm^{-1} in (c) and (e).

Frenkel demonstrated that although the isotropic-nematic transition is a first-order transition, the density jump and the hysteresis were too small to be observed in the simulations for $L/D \leq 5$ [209]. For an aspect ratio $L/D = 5.0$, corresponding to the effective aspect ratio of our system, they estimated the isotropic-nematic transition to take place at $\phi = 0.40$ with an order parameter value $S_{3D} \sim 0.4$ [209]. Notice that this value very low compared to Onsager theory ($L/D \rightarrow \infty$), which predicts $S_{3D} = 0.79$ in the coexisting nematic phase [247]. The nematic to smectic-A transition is however a more pronounced first-order transition for hard spherocylinders with $L/D = 5.0$, with coexisting densities $\phi_1 = 0.45$ and $\phi_2 = 0.48$ and order parameter values $S_1 = 0.74$ and $S_2 = 0.90$ for the nematic and smectic-A phase respectively [209], which is in reasonable agreement with the values shown in Fig. 6.18. Unfortunately, due to the limited resolution in the axial (z) direction (parallel to gravity), we could not determine the order within nor between the smectic layers shown in Fig. 6.18b, and therefore we could not distinguish between smectic-A, smectic-B or crystalline phases.

Aspect ratio $l/d = 20.4$. In this section, we present results on the phase behaviour of particles with a significantly larger aspect ratio than in the previous section. The particle system that was used consisted of non-fluorescent cores with average length $l = 10.0$ μm (7%), diameter $d = 0.49$ μm (10%), aspect ratio $l/d = 20.4$ and estimated effective aspect ratio minus one l^*/d^* - 1 = 13.8 (TH6, see Fig. 6.6c and Figs. 6.16c,d). The non-fluorescent particles were dispersed in a DMSO/water mixture, dyed with FITC. Despite their long rotational relaxation time, a nematic phase was formed close to the bottom wall of the sample, within an hour after sample preparation. Fig. 6.19a shows a processed confocal microscopy image, acquired three layers above the glass bottom wall, indicating that large nematic domains were formed, with the director gradually changing as a function of xy position. Fig. 6.19b shows the bottom layer of particles, directly on top of the glass bottom wall: here, particles were ordered in small nematic domains with random orientation. A smectic phase was not observed, probably because a high enough density was not reached in this sample. Figs. 6.19c,e show FFTs of the images in Figs. 6.19a,b respectively. The measured orientation distributions, shown in Figs. 6.19d,f, resulted in a nematic order parameter $S_{2D'} = 0.92$ for the nematic phase (Fig. 6.19a) and $S_{2D'} = 0.38$ for the multi-domain nematic (Fig. 6.19b). The disorder in the bottom layer of the sample is unexpected because a wall aligns the particles and computer simulations on monodisperse hard rods have shown that a thick nematic film forms at the wall, already below the isotropic-nematic coexistence density [293]. We expect that the lower orientational order close to the bottom wall is due to the polydispersity of the sample, which is likely to couple to the sedimentation process, i.e. we expect the number of longer rods to be at enhanced at the bottom of the sample. Additionally, we suspect that although the wall aligns the particles, (too) fast sedimentation and long relaxation times impede the coarsening into larger domains close to the wall. Furthermore, it is likely that due to the same effect, the nematic phase (Fig. 6.19a) was not in equilibrium but trapped in a glassy state. To circumvent these

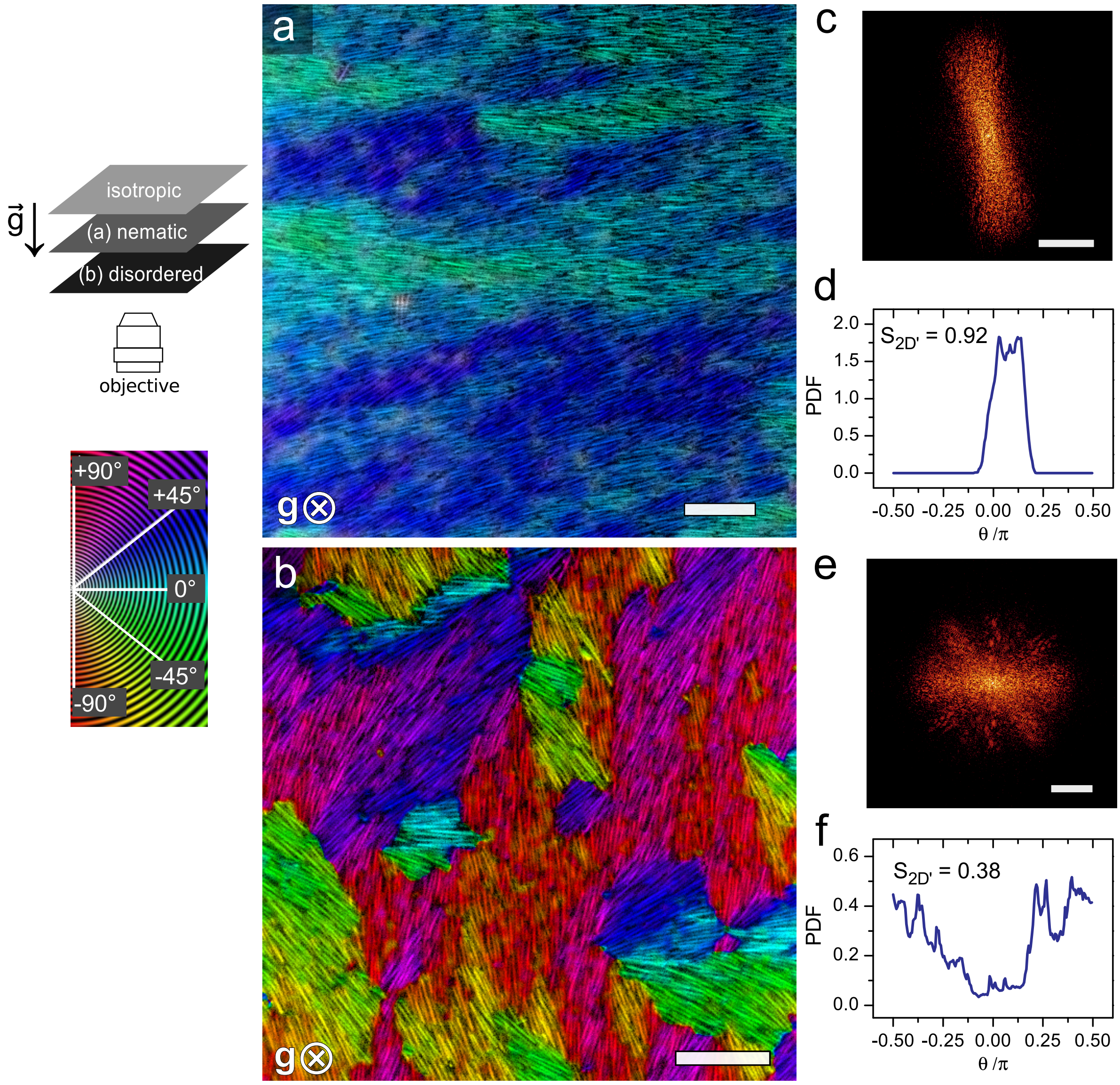

Figure 6.19. Phase behaviour of particles with aspect ratio $l/d = 20.4$. (a) Three layers above the bottom wall, a nematic phase was formed. (b) At the glass bottom wall, particles ordered in small nematic domains with random orientation. The colours in (a) and (b) indicate the in-plane orientation of the particles as indicated by the colormap. (c,e) Fast Fourier Transforms (FFTs) of the images in (a,b) respectively, plotted on a logarithmic intensity scale. (d,f) Probability density function (PDF) of the in-plane orientations which were used to determine the projected nematic order parameter $S_{2D'}$. The scale bars are 20 μm in (a) and (b) and 5 μm^{-1} in (c) and (e).

limitations, it would be worthwhile to synthesize rods with a smaller diameter, while keeping the aspect ratio unchanged. This could done by further tuning of the reagent concentrations [25], or by elevating the temperature of the reaction mixture [288].

6.3.3. Super-resolution imaging

As a final addition to this chapter, we present a preliminary result of 2D super-resolution imaging of a smectic liquid-crystalline phase using STED confocal microscopy [89]. Fig. 6.20a shows a conventional confocal microscopy image of particles with average length $l = 3.3$ μm (10%), average diameter $d = 0.55$ μm (11%) and aspect ratio $l/d = 6.0$ (B35). The particles had a non-fluorescent core, a 30 nm FITC fluorescent shell and a 105 nm non-fluorescent outer shell. Furthermore, particles were dispersed in an index matching mixture of 85 wt% glycerol in water. Data were acquired approximately two months after sample preparation. On the bottom of the sample cell, particles were ordered in a smectic phase. Often the particles in the smectic layers were aligned parallel with the glass bottom wall of the sample cell, however, small domains existed were particles were oriented perpendicular to the walls. In Figs. 6.20b,c, we show CW-STED images acquired using a pulsed excitation at 488 nm with a white light laser, a 592 nm STED beam and a 100×/1.4 STED oil-immersion objective. The 30 nm fluorescent shells of the particles are clearly visible. Figs. 6.20d,e show the images after deconvolution using a theoretical point spread function (PSF). The deconvolution further increased the resolution of the images and additionally, increased the contrast and suppressed pixel noise.

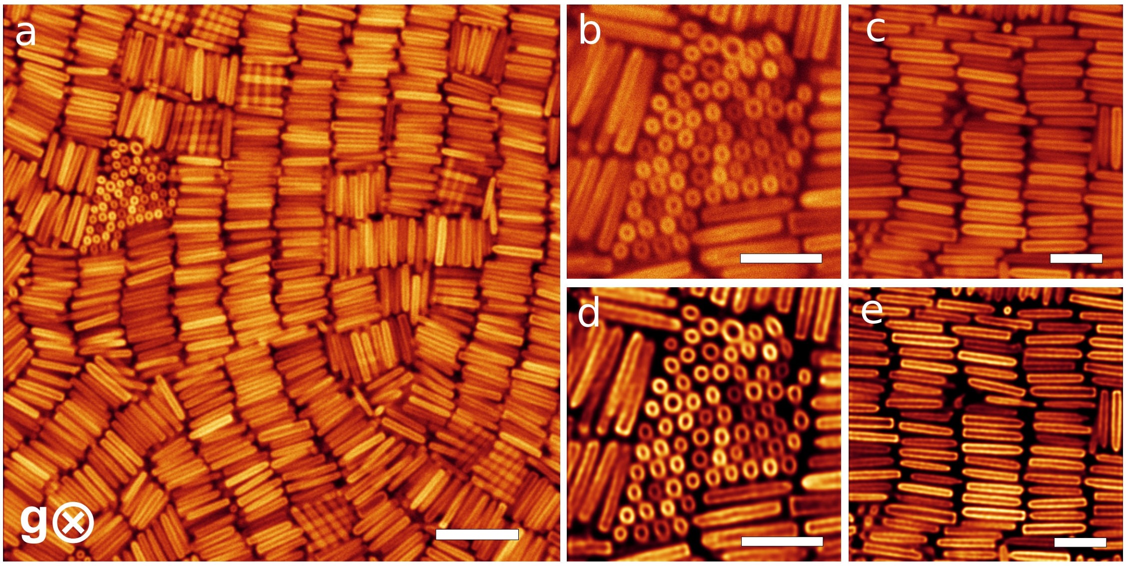

Figure 6.20. Super-resolution imaging of a smectic phase formed by particles with aspect ratio $l/d = 6.0$ (B35). (a) Conventional microscopy image. Scale bar is 6 μm. (b-c) CW-STED images of the same region of the sample, using a pulsed white light laser at 488 nm and a 592 nm STED beam. The thin FITC fluorescent shells of 30 nm are clearly visible. (d-e) Images after deconvolution, which further increased the resolution and also increased contrast and suppressed noise. All scale bars in (b-e) are 3 μm.

Super-resolution imaging can be a useful technique to image particles that are not well resolved with conventional confocal microscopy. This allows for quantitative measurements on thinner silica rods (with a higher aspect ratio) compared to the systems described in this chapter, and therefore enables study of systems which show more pronounced liquid crystalline phase behaviour.

6.4. Summary and Discussion

In this chapter we presented quantitative real-space measurements on colloidal liquid crystal phases. We first described three adjustments to a recently developed synthesis procedure to produce rod-like silica particles. The adjustments were targeted at increasing the aspect ratio of the rods. The first adjustment consisted of a seeded growth procedure, the second adjustment consisted of a synthesis at larger volume using 25% lower water concentration and the third was an adjustment of the reaction temperature, which was raised to a constant value of 30 °C [288]. All adjustments increased the particle aspect ratio significantly, reaching values up to 20, with the rods still being straight. However, the seeded growth procedure resulted in large and heavy particles. Therefore, the synthesis at larger volume using lower water concentration in combination with an elevated reaction temperature is preferred.

Furthermore, we used six different particle systems for quantitative real-space study of liquid-crystalline phase behaviour in a gravitational field and compared them to predictions from theory and simulation. In the simulations, the aspect ratio L/D is defined as the cylinder length over the diameter (see Fig. 6.2 and Ref. 209). Because the particles used in the experiments in this chapter were not identical in shape to a spherocylinder, but are more bullet-like, we defined the end-to-end aspect ratio l/d, with l the average end-to-end length of the particle and d the average diameter. Additionally, because the particles are electrically charged in suspension, we also introduced an effective end-to-end length l^* and effective diameter d^*, resulting in an effective aspect ratio l^*/d^*. Based on these effective dimensions, the rod-like silica systems are known to be in qualitative agreement with the phase diagram for hard spherocylinders, with $l^*/d^* - 1 \approx L/D$ [28].

Three of the systems had a non-fluorescent shell $\gtrsim$ 150 nm, which allowed for individual 3D particle detection from confocal microscopy data. In a dense sediment of particles with aspect ratio $l/d = 4.1$, we observed a smectic-B phase with small regions (approximately $10 \times 10 \times 5$ particles) of AAA-stacked crystalline layers, instead of the ABC-crystalline phase predicted by simulations. Both the occurrence of the smectic-B phase and the AAA-crystal-like regions are likely due to the polydispersity in the system and possibly also due to subtle charge effects [211,271,290]. As far as we are aware, this is the first real-space demonstration of an AAA crystalline region in a colloidal liquid crystal system. There are for instance many examples of crystal-like columnar phases of mineral particles, observed with small angle X-ray diffraction (SAXS) [253,299,300], but columnar phases were not observed in our system. Additionally, for a system of *fd*-viruses a hexagonal AAA crystalline phase has been reported, however, the crystal structure could again only be determined with SAXS and the phase was only formed after slow drying of the sample [250].

Apart from the positional structure, we also determined the orientational distribution function for the system with aspect ratio $l/d = 4.1$. We found that the inter-layer particles were always aligned perpendicular to the director, as was predicted by both theory and simulation [291, 292]. Additionally, we determined the complete equilibrium density profile of a sediment of particles with aspect ratio $l/d = 5.4$. We found that close to the wall, there was a large region that was disordered both in particle position and in orientation. This was unexpected given the fact that the wall aligns the particles and that simulations predict a thick nematic film to form already below the isotropic-nematic coexistence density [293]. We believe that our observation was caused by a size-segregation process during sedimentation with the larger particles from the size distribution ending up more frequently at the bottom of the sediment. This phenomenon bears resemblance to a fractionation process, or partitioning of colloidal components over coexisting phases, as predicted by theory and observed for colloidal particles with high polydispersity [253, 296, 300, 301].

Higher up in the sample, at the isotropic-smectic-B interface, we found a difference in the inflection points of the density and the nematic order parameter $\delta/(l^* - d^*) = 0.48 \pm 0.04$. Such a shift was predicted by both theory and simulations for the isotropic-nematic interface of hard spherocylinders [294, 295]. The coexisting densities that we obtained were higher compared to the hard spherocylinder phase diagram, however, both the relative density change $(\phi_{Sm} - \phi_I)/\phi_I \sim 22\%$ and the coexisting values of the nematic order parameter ($S_I^{3D} = 0.13$ and $S_{Sm}^{3D} = 0.92$) were in agreement with the simulations [209]. We expect that both the polydispersity and the charge on the particles influences these values significantly and it would be interesting to incorporate these in simulations on spherocylinders for further investigation. Finally, we found an increased gravitational length ($l_g/d^* = 1.3$), obtained from a fit to the dilute upper part of the sediment, which is almost twice the value expected from the hard-rod dimensions. The polydispersity is likely to contribute to this increase [274]. We do not expect that charge separation can explain our observation, as the charges on the particles in our system are significantly screened [274, 280].

The thick non-fluorescent shells of the first three systems, needed for individual 3D particle detection, decreased the particle aspect ratio strongly. As a result, none of these systems showed a nematic phase in equilibrium. We therefore also used a system with a small 76 nm outer shell (resulting in an aspect ratio $l/d = 7.3$) and one without an outer shell at all (with aspect ratio $l/d = 20.4$). Although both 2D and 3D particle detection from confocal microscopy images was not accurate enough for these systems, we found that calculation of the structure tensor for each pixel individually nevertheless enabled the determination of the (projected) 2D nematic order parameter and nematic director. As shown in Chapter 4, the 2D projected nematic order parameter is almost equal to the value of the 3D nematic order parameter, as long as the angle between the director and the plane of observation is not close to $\pi/2$. For the system with aspect ratio l/d

= 7.3, we found a three-phase coexistence region of isotropic-nematic-smectic phases. Bolhuis and Frenkel estimated the isotropic-nematic-smectic triple point to be at $L/D \approx 3.7$ [209], which is in the vicinity of the estimated effective aspect ratio minus of our system, which was $l^*/d^* - 1 = 4.6$. The values of the order parameter in the nematic phase ($S_{2D'} = 0.88$) and in the smectic phase ($S_{2D'} = 0.97$) were in good agreement with the values for the 3D nematic order parameter of a coexisting nematic and smectic phase (with the same aspect ratio) obtained from computer simulation [209]. Our last system, with aspect ratio $l/d = 20.4$, formed large-scale nematic phases within 1 hour. However, the large size of the particles made them almost non-Brownian and it is likely that the observed nematic phase did not reach equilibrium but became frozen-in or glassy within several hours. Nevertheless, this system showed clearly that the bottom layer of the sediment was more disordered in orientation than the layers above it.

As a final example of the novel possibilities of this liquid-crystal model system, we showed preliminary result on super-resolution imaging of a smectic phase of rods using 2D stimulated emission depletion (STED). The particles were labelled with a thin (30 nm) fluorescein isothiocyanate (FITC) shell, which was clearly visible in the (deconvolved) STED images.

6.5. Conclusion

We produced 6 different suspensions of rod-like particles and investigated their liquid-crystalline phase behaviour in real-space. We found that a non-fluorescent outer shell of approximately 150 nm or larger enabled quantitative 3D real-space measurements using a combination of confocal microscopy and a novel particle fitting algorithm. However, the thick non-fluorescent layer limited in practice the end-to-end aspect ratio of the particle systems to $l/d \leq 5.4$. For particle systems with aspect ratio $l/d \geq 6.0$, we could not obtain 3D coordinates, however, it was still possible to obtain the in-plane orientation distribution from 2D confocal microscopy images. We compared our experimental results to both simulations and theory of hard spherocylinders, using effective particle dimensions to account for the small but non-negligible Debye screening length in our systems. In general, we found reasonable agreement regarding the formation of isotropic, nematic, smectic and crystalline phases. However, the ABC-stacked crystal predicted from simulation was replaced by either a smectic-B or AAA-stacked crystal in the experiments. We expect that this was due to the polydispersity in the experimental systems and possibly also due to subtle charge effects. We did not observe a columnar phase, which is not unexpected because the polydispersities for all our particle systems were always $\leq 12\%$. Furthermore, we determined the full equilibrium sedimentation profile of a system of rods with aspect ratio $l/d = 5.4$. At the isotropic - smectic-B interface, we found a difference in height between the inflection points of the 3D nematic order parameter and the density. Both the magnitude of this difference as well as the values for the nematic order parameter were in good agreement with predictions from both theory and simulation on an isotropic - nematic interface of hard spherocylinders with similar aspect ratio. The (effective) volume fractions that we obtained for both phases were higher than expected, however, the magnitude of the relative density jump was in good agreement with the values from simulation. Additionally, we found that the gravitational length, obtained from a fit to the dilute upper part of the sediment, was almost twice the value expected from the hard-rod dimensions. We expect that this discrepancy can only partially be explained by the polydispersity in the system and a full explanation is left for further study. Finally, we showed preliminary results of stimulated emission depletion (STED) imaging of rod-like particles coated with a thin (30 nm) uniform fluorescent shell. The results indicated that STED is a successful method to study thinner rods at high resolution, thus enabling quantitative real-space study of particles with higher aspect ratio compared to conventional confocal microscopy.

6.6. Acknowledgements

This work was done in collaboration with Anke Kuijk, Michiel Hermes and Chris Kennedy. Anke Kuijk performed particle synthesis of systems B31, B35 and B48. Chris Kennedy performed in collaboration particle synthesis of systems CT1 - CT5 and the experiments on and analysis of the CT1 sedimentation profile. We thank Henriëtte Bakker, Bo Peng, Simone Dussi, Marjolein Dijkstra and René van Roij for many useful discussions and we also thank Simone Dussi for the adapted phase diagram of hard spherocylinders. Furthermore, we thank Simone Dussi and Henriëtte Bakker for critical reading of this chapter.

7

Rheology and Real-Space Analysis of Colloidal Silica Rods under Shear

Abstract

In this chapter we describe the shear-induced phase behaviour of colloidal silica rods. We used two different shear cell configurations that both allowed simultaneous confocal microscopy measurements to be made while the system was sheared. The first configuration was a parallel-plate shear cell and the second configuration was a stress controlled rheometer, both mounted on top of a confocal microscope. With the parallel-plate shear cell, steady shear flow was successfully applied to align rods with an aspect ratio of 6.0, and create shear-aligned para-nematic and para-columnar liquid crystal phases. The application of oscillatory shear led to the formation of para-smectic-like domains in a sample that was previously in a shear-aligned para-nematic state. Rheological measurements on rod-like particles with aspect ratio 7.8 and initial volume fraction $\phi \sim 0.3$, were characterized by pronounced shear thinning behaviour, a Newtonian regime and (the onset of) shear-thickening for increasing shear rate. We also found large non-periodic fluctuations in the viscosity (as a function of time) for shear rates $< 1.0\ s^{-1}$. However, these fluctuations could not be directly correlated with the micro-structure of the suspension. Although these experiments are only preliminary, they give a strong indication that shear is a powerful external field to align colloidal liquid-crystal phases over larger areas. This could for instance be applied in spin coating of colloidal liquid crystals.

7.1. Introduction

Dense systems of liquid crystals exhibit rich phase behaviour when subjected to shear flow. Early theoretical investigations on hard rods under shear by Hess [34] and by Doi and Edwards [35] produced an equation that governed the time development of the orientational distribution function. The Doi-Edwards-Hess (DEH) theory predicts that the average direction of alignment, the nematic director, can undergo different motion depending on its initial state, volume fraction and shear rate. If the system is initially in a nematic liquid crystal phase with the director in the velocity-gradient plane, the induced flow can bring it in a quasi-stationary state for which the local director describes a periodic 'tumbling' orbit for low shear rates. At intermediate shear rates the director can also describe an orbit oblique to the gradient-velocity plane, called a 'kayaking' state. Other time-periodic orbits are 'wagging', where the director oscillates between two angles in the velocity-gradient plane and 'log-rolling', a state where the director remains perpendicular to the gradient-velocity plane. For higher shear rates the director aligns with the flow and a para-nematic is formed. The tumbling, wagging and flow aligning states were experimentally found using colloidal suspensions of *fd* viruses [36, 37] and with Brownian Dynamics computer simulations for rods with large aspect ratio ($20 < l/d < 60$) [38, 39]. A Brownian Dynamics simulation study on ellipsoids demonstrated that particles with much shorter aspect ratio ($l/d = 3$) can also exhibit tumbling, wagging and flow aligning states [302]. Additionally, both theory and experiments have identified that the stationary viscosity as a function of shear rate decreases, i.e. the system behaves as a shear-thinning fluid, as the sample progresses from tumbling to wagging to flow-alignment [37]. Moreover, a hesitation in the decrease of the viscosity with increasing shear rate has been interpreted as a signature of the transition from a tumbling to a wagging state [37, 303]. Although recent real-space studies on colloidal hard-sphere suspensions have clarified the correlation between shear-thinning, shear-thickening and the micro-structural changes in the suspension [62, 235], similar work on rod-like suspensions has not been performed as far as we know.

As mentioned, the above described shear-induced liquid crystal phases all have concentrations such that they are in a nematic phase in the absence of shear. It is, however, known that shear flow also has a significant effect on more concentrated phases, such as a smectic phase. The effect of shear flow on smectic phases has often been studied in the configuration where the layers are parallel to the planes of constant velocity. For instance, theoretical models inspired by experimental results are treated in Refs. 304, 305. In this configuration, the layering is stable up to a certain critical shear rate. At higher shear rates, the director and the smectic layers were found to adjust their alignment through undulations of the layers and realignment of the director relative to the layers to end up in a state where the layers are parallel to the gradient-velocity plane, as experimentally shown in Refs. 306, 307. Theory and computer simulations show that shear that is applied to smectic phases that are oriented with their layers parallel to the gradient-vorticity plane, also causes structural changes [308, 309]. It was found that the layers tilt progressively with increasing shear. At a critical shear, however, the particles were found to rearrange themselves; the sample melts near the center and reforms with a reduced tilt consistent with the layers that are still present at the walls. Shear induced melting and recrystallization was also measured experimentally in smectic-A and smectic-B phases of butyloxy-benzylidene-octylaniline [310].

In this chapter, we present preliminary results of experiments on the combined effect of shear and gravity on concentrated dispersions of silica rods, which we analysed in 2D real-space on the single particle level. The silica rods, opposed to e.g. polymeric systems, are affected significantly by gravity. Here, we use the concentrating effect of gravity to create shear aligned dense phases in systems that were initially in an isotropic phase. Using a parallel plate shear cell, which previously was used to study dispersions of spheres (see Refs. 63, 238, 240 and Chapter 5), we were able to follow the dynamics of particles in the zero-velocity plane for an extended period of time. Using a hybrid combination of a confocal microscope and a rheometer (known as a confocal rheoscope [52,311]), we also investigated the correlation between the suspension viscosity and the particle micro-structure.

7.2. Methods

7.2.1. Suspensions

Two different suspensions of rod-like particles were used for the shear experiments described in this chapter. The properties of these systems are summarized in Table 7.1. The B35 particles consisted of a 280 nm non-fluorescent core, a 30 nm fluorescein isothiocyanate (FITC) dyed inner shell and a 105 nm non-fluorescent outer shell. The THB5 particles had a 380 nm core that contained a gradient of FITC dye along the rod main axis and were coated with a 145 nm non-fluorescent outer shell, see Ref. 72 and Chapters 2 and 6 for details.

The B35 particles were dispersed in a mixture of dimethylsulfoxide (DMSO, $\geq$ 99%, Sigma-Aldrich) and de-ionized water (Millipore system) and the THB5 particles were dispersed on a mixture of glycerol ($\geq$ 99%, Sigma-Aldrich) and de-ionized water (Millipore system). Both the B35 and the THB5 particle suspensions were index-matched by eye, which resulted in 93 wt% DMSO in water and 85 wt% glycerol in water mixtures respectively. The properties of these solvent mixtures are summarized in Table 7.2. Using the particle dimensions and the solvent properties, we calculated two quantities of interest, as indicated in Table 7.1: the gravitational length l_g and the rotational self-diffusion coefficient D_r at infinite dilution [198]. For both these calculations the effects of a double layer (repulsion) that was caused by the charges present on the rods and the concentration of counter and other ions in the solvent were neglected.

7.2.2. Shear cells

We used two different shear cells to investigate the properties of the rod-like suspensions under shear. The first is a parallel-plate shear cell that was mounted on top of an inverted confocal microscope (SP2, Leica). A schematic representation can be

	l (μm)	σ_l (%)	d (μm)	σ_d (%)	l/d	ϕ	l_g (μm)	D_r (rad^2/s)
B35	3.3	10	0.55	11	6.0	0.30	0.70	$5.3 \cdot 10^{-2}$
THB5	5.2	11	0.67	8	7.8	0.25/0.33	0.35	$4.5 \cdot 10^{-4}$

Table 7.1. Properties of the particles used in this chapter, with l the end-to-end length of the rod, d the diamter, σ_i the polydispersity, l/d the aspect ratio and ϕ the volume fraction. For the solvent properties summarized in Table 7.2, we also calculated the gravitational length l_g and the rotational diffusion coefficient D_r at infinite dilution [198].

solvent mixture	ρ (g/ml)	n_D	η (cP)
93 wt% DMSO/water	1.096 (25°C) [73]	1.472 (20°C)	2.6 (22°C)
85 wt% glycerol/water	1.222 (20°C) [199]	1.452 (20°C)	92 (22°C)

Table 7.2. Properties of solvents used in this chapter, with ρ the density, n_D the refractive index and η the absolute viscosity. The values for the density are obtained from the literature.

seen in Fig. 7.1a and a detailed description of the setup can be found in Ref. 238. The top plate was a standard No. 5 microscopy slide (Menzel Gläzer, thickness 0.5 - 0.6 mm) which was cut to 15 mm × 30 mm. The bottom plate was a No. 1 slide (Menzel Gläzer, thickness 0.13 - 0.16 mm) of 24 mm × 50 mm. The glass slides were attached to translational stages that could be displaced by piezostepper motors. The maximum travel of the stages was $\sim$ 10 mm. Because both plates can move in opposite directions, there is a plane of zero velocity, indicated by the dashed (red) line in Fig. 7.1a. This zero-velocity plane enables observation of the particles under shear for an extended period of time. The alignment of the plates and the spacing between the plates was set prior to the experiment with confocal microscopy in reflection mode using a HeNe 543 nm laser and a 20×/0.7 air objective (Leica). Values for the spacing between the plates h in this chapter were between 30 - 50 μm. The cell was filled with $\sim$ 60 μl suspension and a metal vapour-lock was used to avoid evaporation of the sample. Prior to the experiment, a value can be chosen for the sum of the amplitudes of the upper and lower slide $A = A_T + A_B$, the sum of the velocities $v = v_T + v_B$ and the ratio between the two velocities $k = v_B/v_T$. Combined with the value for the distance between the plates h, this determines the shear rate $\dot{\gamma} = v/h$, the strain amplitude $\gamma = A/h$ and the position of the zero-velocity plane $z_{zvp} = h/(1/k + 1)$. Additionally, it is possible to choose between steady shear or oscillatory shear. We applied both types of shear, where in the latter the shear rate and strain amplitude become time dependent, as described in Chapter 5.

The second shear cell that we used was a confocal-rheoscope setup, indicated in Fig. 7.1b. This setup is a combination of a fast confocal microscope (VT-Eye, Visitech)

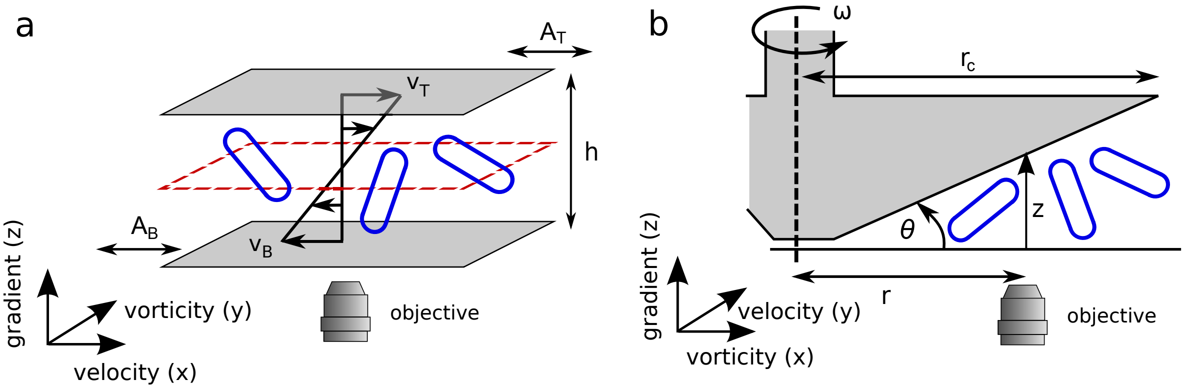

FIGURE 7.1. Schematic representations of the shear cells used. (a) Parallel-plate shear cell mounted on top of an inverted confocal microscope [238]. The height between the two plates h, the sum of the amplitude of the upper and lower plate $A = A_T + A_B$, the sum of the speeds $v = v_T + v_B$ and the ratio between the two velocities $k = v_B/v_T$ can be set during the experiment. Because both plates move in opposite directions, there is a zero velocity plane (ZVP), indicated by the dashed (red) line. The position of the ZVP can be adjusted by changing the ratio k. (b) Confocal rheoscope setup [52]. This setup consists of a stress controlled cone-plate rheometer coupled to an inverted confocal microscope, which enables measurement of rheological properties during imaging. The rotation speed ω and distance of observation r can be set during the experiment. The lower plate consists of a stationary glass plate, which enables confocal microscopy imaging but does not allow for a ZVP to be moved away from the lower wall.

and a stress controlled rheometer (Physica MCR 301, Anton Paar) [52]. The cone-plate rheometer had a custom-built open construction that allowed for simultaneous imaging and rheological measurements. The bottom (transparent) plate of the rheometer was stationary, whereas the truncated cone was able to rotate. This resulted in a velocity profile with constant shear rate throughout the gap, given by $\dot{\gamma} = \omega/\tan\theta$, with ω the angular velocity of the cone and θ the angle between the cone and plate, see Fig. 7.1b. In our experiments, a stainless steel cone was used with radius $r_c = 20$ mm and cone angle $\theta = 1°$. The plate of the rheometer consisted of a glass microscopy slide (thickness $\sim$ 180 μm, radius 25 mm) attached to an aluminium plate. The aluminium plate could be aligned prior to the experiment using three adjustments screws. We filled the cell with $\sim$ 0.5 ml of suspension. We measured flow curves of the suspensions using logarithmic up- and down ramps spanning four decades of shear rate ($\dot{\gamma} = 0.01$ - 100 s^{-1}). Longer measurement were performed for smaller shear rates to adjust for differences in particle displacement (or strain magnitude), with a maximum of 300 s. We further monitored the viscosity as a function of time for various shear rates, with a maximum duration of 600 s. A 100×/1.4 oil-immersion objective (Nikon) mounted on a piezo-element was used for focussing in the z-direction. The distance between the axes of the objective and the cone r (see Fig. 7.1b) could be adjusted during the experiment. The confocal microscope was equipped with an acousto-optic deflector (AOD) for scanning in the

x-direction and a galvanometer mirror for scanning in the y-direction. A solid state 488 nm laser was used to excite the fluorescent particles. Scan speeds are up to 40 fps for images of 1024 × 1024 pixels and 110 fps for images of 512 × 512 pixels. These high scan speeds result in a typical acquisition time of a 3D-image of $\sim$ 1 s. Because the lower plate of the setup was stationary, there was no zero-velocity plane, which makes it hard to follow particles for an extended period in time. However, because of the fast image acquisition, it is possible to follow the 3D structure for a limited period of time for shear rates up to ~ 0.05 s^{-1} and in 2D for shear rates up to ~ 50 s^{-1}.

7.2.3. Image analysis

Confocal microscopy is a technique especially suited for 3D measurements and several algorithms exist that are optimized for 2D and 3D particle tracking under flow [52, 53, 60]. We found, however, that 3D image analysis of concentrated samples of rod-like particles under flow was not (yet) possible with the suspensions and setups described in this chapter. We therefore analysed 2D time-series of confocal microscopy images only. Using the 2D particle fitting algorithm described in Chapter 6, we obtained the projected positions $\mathbf{r}'$ and orientations $\hat{\mathbf{u}}'$ of the rod-like particles under shear. We quantified the (projected) 2D order in the system by calculating the 2D nematic order parameter, given by

$$S_{2D'} = 2\langle\cos^2\psi\rangle - 1, \tag{7.1}$$

with ψ the angle between the projected main axis of the rod $\hat{\mathbf{u}}'$ and the projected nematic director $\mathbf{n}'$, i.e. ψ is the in-plane projected angle that maximizes equation (8.12). To find the projected nematic director, we calculated the 2 × 2 nematic order parameter tensor given by

$$Q^{2D}_{\alpha\beta} = \frac{1}{N}\sum_{i=1}^{N}\left(2\,u'_{i\alpha}u'_{i\beta} - \delta_{\alpha\beta}\right), \tag{7.2}$$

with $u'_{i\alpha}$ the α-component of the unit vector pointing along the projected main axis of particle i and $\alpha, \beta = x, y$. $\delta_{\alpha\beta}$ is the Kronecker delta and N is the total number of particles in the system.

We also calculated the (local) orientation of the particles via the structure tensor using an existing ImageJ plugin [285], as described in Chapter 4, which was used for visualization of the orientations of the particles.

To determine local shear rates, we used a coarse-grained method similar to a particle image velocimetry (PIV) technique [60, 312]. For different heights in the velocity-gradient (z) direction, we recorded xy time-series of confocal microscopy images. By calculating the cross-correlation between consecutive time-frames, we obtained the average displacement of the particles per frame (without the need for individual particle tracking), which are then divided by the time step to obtain the average velocity as a function of z. We also used these displacements to shift the images such that we obtained a view from the co-moving frame, i.e. the frame that moves with the average speed of the suspension. This enables better visualization of the non-affine motion of the particles.

Finally, for a quantitative comparison between experiments, we calculate the rotational Peclet number Pe_r, which we define as

$$Pe_r = \frac{\dot{\gamma}}{2\,D_r} \tag{7.3}$$

This dimensionless quantity is the ratio of the orientational relaxation time $(1/2\,D_r)$ and the typical time-scale associated with flow $(1/\dot{\gamma})$. If $Pe_r < 1$, Brownian motion is dominant and no large deviations from equilibrium phase behaviour are expected. However, if $Pe_r > 1$, the time-scale for flow is dominant and shear-induced motion can be expected.

7.3. RESULTS

7.3.1. Shear-induced alignment

In Fig. 7.2 we show preliminary results of a suspension of silica rods (B35) with aspect ratio $l/d = 6.0$, suspended in a mixture of 93 wt% dimethylsulfoxide (DMSO) in ultrapure water, with initial volume fraction $\phi = 0.3$. Figs. 7.2a-c show close-ups of confocal microscopy images of the suspension under steady shear (shear rate $\dot{\gamma} = 33$ s^{-1}, Peclet number $Pe_r = 311$) applied with the parallel plate shear cell. The view is from the velocity-vorticity plane, close to the zero-velocity plane. The colors indicate the projected 2D orientation of the particles. Initially, the particles in the field-of-view were in an isotropic phase. However, shortly after the shear was applied, particles aligned in the velocity direction forming a shear-induced nematic phase (or para-nematic phase). Figs. 7.2b shows that after the shear was stopped, the system relaxed back towards the equilibrium isotropic phase. However, some (local) order still remained after approximately 38 s. After re-applying the shear, the system aligned with the velocity direction again (within $\sim$ 3 s), see Fig. 7.2c. In Fig. 7.2d we show the projected 2D nematic order parameter $S_{2D'}$ as a function of time, calculated for approximately 650 particles per time-step ($\Delta t = 0.66$ s). The red line is an average over 7 consecutive time-steps. When the shear was applied, the value for the 2D order parameter reached a plateau of approximately $S_{2D'} = 0.7$. Because the nematic director is approximately parallel to the plane of observation, this value (of the 2D projected nematic order parameter) will be almost equal to the value of the 3D nematic order parameter, as shown in Chapter 4.

7.3.2. Rheology measurements

To complement the shear measurements with the parallel plate shear cell, we also investigated the behaviour of a suspension of rods with a rheo-confocal setup [52]. The particles used for this study (THB5) had a slightly larger aspect ratio of $l/d = 7.8$ and were dispersed in a mixture of 85 wt% glycerol in water. Fig. 7.3a shows an average over three independent flow curves for a suspension with volume fraction $\phi = 0.25$. A clear shear-thinning regime is observed for shear rates $\dot{\gamma} = 0.01$ - 3 s^{-1}, corresponding to Pe_r $\sim$ 10 - 10^3. In this regime, we observed both a non-monotonic decrease of the viscosity for individual measurements and significant variations between measurements, resulting

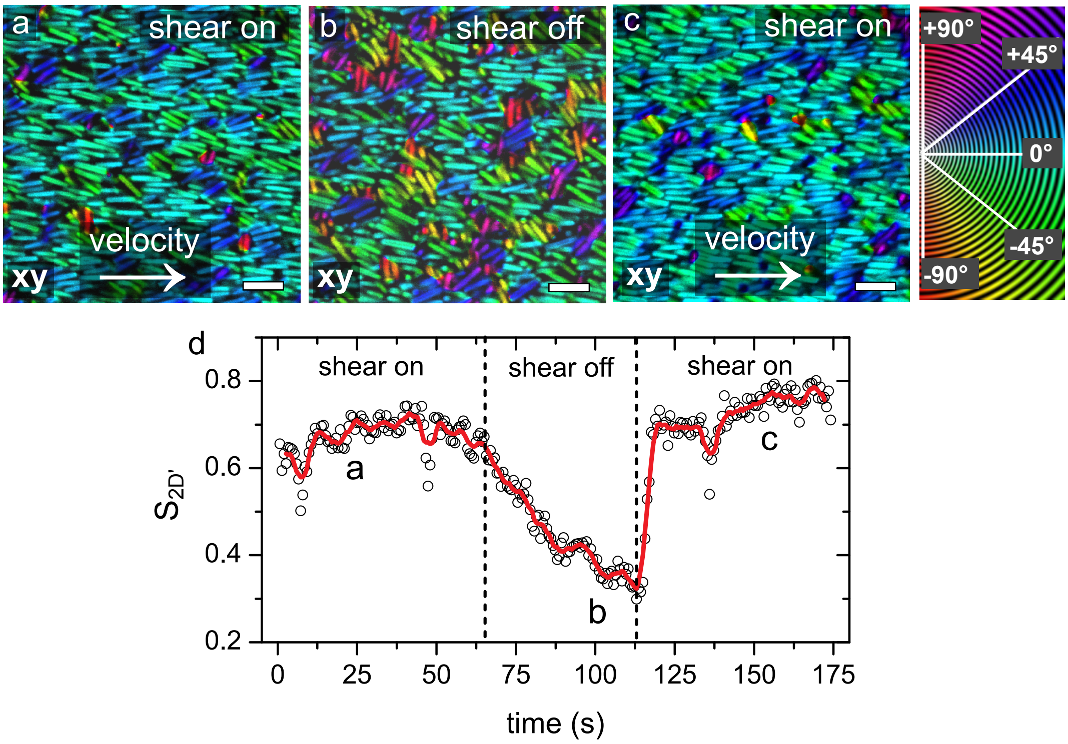

Figure 7.2. Shear alignment of rods with $l/d = 6.0$ by application of steady shear with shear rate $\dot{\gamma} = 33$/s using a parallel-plate shear cell. The particles in the zero-velocity plane were initially in an isotropic phase. (a-c) Close-ups of confocal microscopy images in the velocity-vorticity (xy) plane. The colors indicate the (projected) orientation of the particles in the 2D plane, as indicated by the colorwheel. The scale bars indicate 5 μm. (a) Directly after application of the shear, a shear-induced nematic phase was formed. (b) Approximately 38 s after the shear was stopped, the distribution of orientations was almost isotropic again. (c) Particles aligned almost instantly when the shear was re-applied. (d) The projected 2D nematic order parameter $S_{2D'}$ as a function of time. The (red) line is an average over 7 consecutive measurement points ($\Delta t = 4.6$ s).

in the large error-bars shown in Fig. 7.3a. Furthermore, we found that for shear rates $\dot{\gamma} = 3$ - 10 s^{-1} ($Pe_r \sim 10^3$ - 10^4) the suspension behaved approximately Newtonian. Finally, we observed a small increase in viscosity, i.e. shear thickening, for shear rates $\dot{\gamma} > 10$ s^{-1} ($Pe_r > 10^4$), as can be seen in the inset in Fig. 7.3a. To further investigate the rheological behaviour of the suspensions, viscosity measurements were taken as a function of time for varying shear rates. Fig. 7.3b shows that for the shear rates in the shear thinning regime ($\dot{\gamma} = 0.01$ - 3 s^{-1}), significant (non-periodic) fluctuations existed, whereas for the largest shear rates, a constant value was measured. Notice that the plateau value in the viscosity for $\dot{\gamma} = 5$ s^{-1} (pink triangles) is lower than for $\dot{\gamma} = 20$ s^{-1} (blue diamonds), since these values are in the shear thickening regime.

A hesitation in the decrease of the viscosity, such as shown in Fig. 7.3a, was also observed for *fd* viruses under shear and was interpreted as a signature of the transition from a tumbling to a wagging state [37]. It is also probable that the large fluctuations in the viscosity, shown in Fig. 7.3b, were (partially) a result of tumbling, wagging or kayaking behavior of the rods. However, we could not identify such micro-structural changes in the confocal microscopy images acquired during shear. Movies 1 - 3 in Appendix B.2 show confocal microscopy time-series of the velocity-vorticity plane, for shear rates $\dot{\gamma} = 1$, 2 and 5 s^{-1}. Images were shifted backwards with the average displacement of the particles, which enables a clear view of how the local micro-structure and any non-affine motion was influenced by the flow. For shear rate 1 s^{-1} we observed a (weak) average alignment with velocity direction, however we did not observe any rearrangements during the time that the particles were in the field of view of the microscope. For shear rate 2 s^{-1} the particles were, on average, still aligned with the flow, and particles rotated of tumbled, however not collectively. For shear rate = 5 s^{-1} (which is at the upper limit of the Newtonian regime) we observed more non-collective rotations of the rods and for shear rates > 10 s^{-1} (which is in the shear-thickening regime) the non-affine motion of the rods looked turbulent. The fluctuations were not a result of the resolution of the rheometer, as for a shear rate $\dot{\gamma} = 0.05$ s^{-1} we measured a stress $\sigma \sim 0.02$ Pa and torque $\tau \sim 0.7$ μNm, which is well above the torque resolution of the rheometer of 0.1 nNm. Also, the period of rotation of the cone ($T = 3600$s for $\dot{\gamma}$ $= 0.1$ s^{-1}) is much larger that the time of a typical fluctuation.

Although the microscopy observations did not identify the expected time-periodic motion of the directors, Movies 1 - 3 in Appendix B.2 are a clear illustration of shear-enhanced rotational motion, a form of Taylor dispersion, which was recently reported for dumbbell particles at infinite dilution under oscillatory shear as well [40].

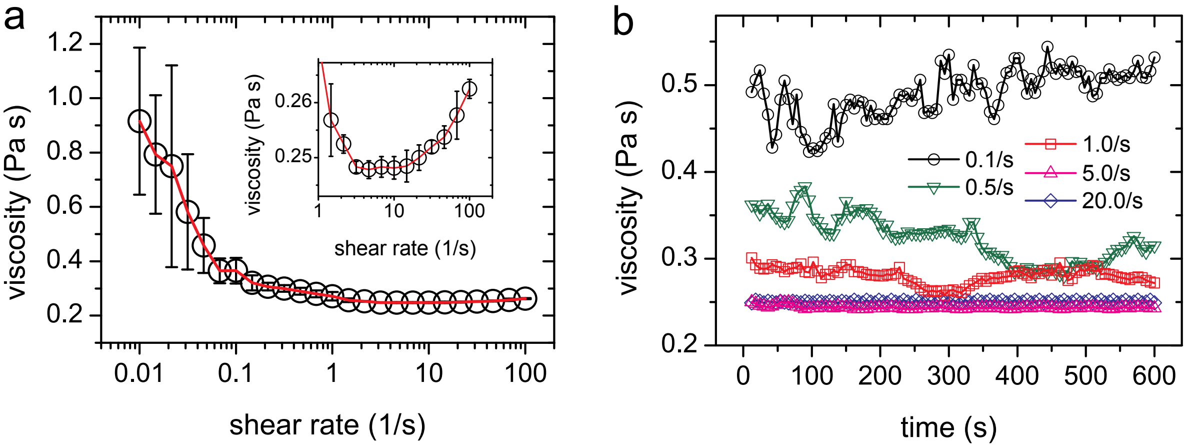

FIGURE 7.3. Rheology measurements for a suspensions of rod-like particles with length $l = 5.2$ μm, aspect ratio $l/d = 7.8$ and volume fraction $\phi = 0.25$. (a) For increasing shear rate we observed shear-thinning, Newtonian and shear-thickening behaviour. (b) Viscosity as a function of time for four different shear rates. For the lowest shear rates, we systematically observed large, non-periodic fluctuations whereas for the largest shear rates, a constant value was measured.

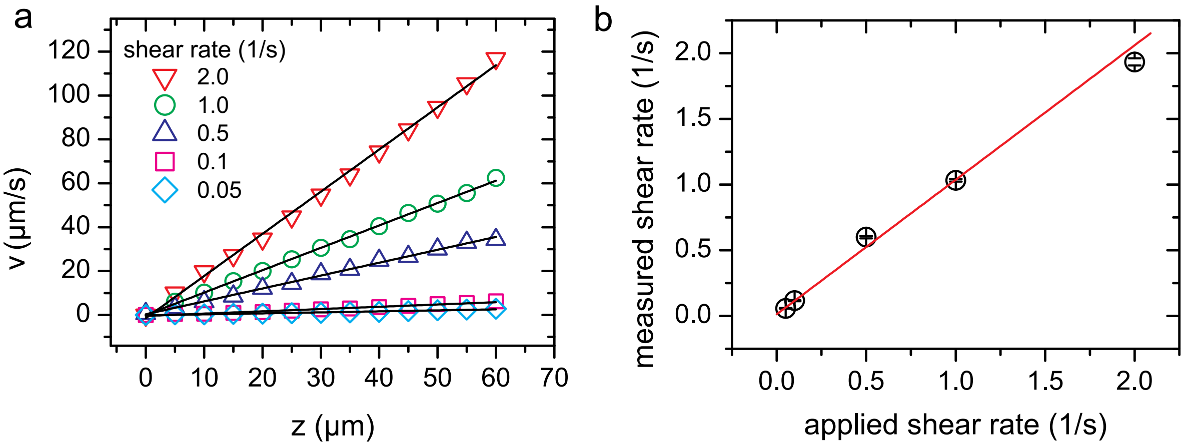

Figure 7.4. Velocity profiles for a suspensions of rod-like particles with length $l = 5.2\ \mu$m, aspect ratio $l/d = 7.8$ and volume fraction $\phi = 0.25$. (a) The slopes are all close to linear. Measured shear rates were obtained from linear fits to the data. (b) The applied versus measured shear rates are almost identical.

As a final addition to the rheology measurements, we measured the local velocity profile for various shear rates, indicated in Fig. 7.4a. The slopes are all close to linear and the measured shear rates (linear fits) correspond well to the applied values, as indicated in Fig. 7.4b. These results indicate an absence of shear banding and suggest little to no slip.

7.3.3. Shear aligned columnar and smectic-B phases

Combining the ability of shear flow to align the rods and that of gravity to increase concentration, it was possible to create a shear-aligned columnar, or a shear aligned smectic phase on the bottom of the shear cell. Which phase was formed depended on when the shear was stopped. The columnar phase was created by applying steady shear, with a shear rate of 2.6 s^{-1} and a strain amplitude of 5.3, for 3.5 hours. In this time, the volume fraction of rods on the bottom of the sample increased sufficiently to allow for a phase transition from a shear aligned nematic, with its director pointing in the velocity direction, to a shear induced columnar phase. Figs. 7.5a-c show confocal images of the columnar phase through three different planes. In the velocity-gradient (xz) plane as well as in the velocity-vorticity (xy) plane, the rods were ordered in horizontally oriented columns. The hexagonal stacking of the columns is visible in the vorticity-gradient (yz) plane. Subjecting the columnar phase to a shear flow with a shear rate of 13.2 s^{-1} and strain amplitude of 26.3, destroyed the 3D order of the sample, but an average orientation of the rods in the velocity direction remained (para-nematic phase). The volume fraction of the rods on the bottom of the sample was sufficiently high at this point to maintain the alignment caused by the shear when the flow was stopped. After cessation of the shear and subsequent sedimentation, the particles ordered in a shear-aligned smectic phase within 1 hour, as shown in Figs. 7.5d-f. The rods in the smectic layers of this phase were ordered hexagonally, as shown in Fig. 7.5e. The structure was therefore identified as a smectic-B phase [28].

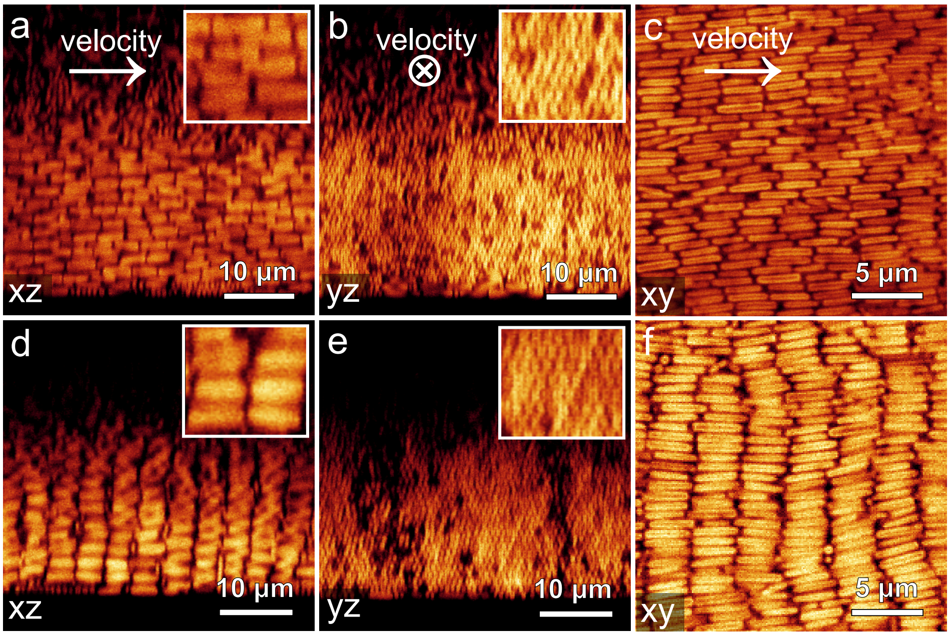

Figure 7.5. Shear aligned columnar and smectic phases in different planes. x is the velocity direction, y the vorticity direction and z the velocity gradient direction. (a-c) When subjected to a shear flow with a shear rate of 2.6 s^{-1} and a strain amplitude of 5.3, a sample with initial volume fraction of 0.3 ordered into a shear aligned columnar phase. (d-f) After shear melting the sample to a para-nematic and leaving it to sediment in the absence of shear, the sample was almost completely smectic within 1 hour.

7.3.4. Oscillatory shear

Besides steady shear, the rods were also subjected to oscillatory shear. Oscillatory shear has been used in several recent experiments to increase the crystalline order of nearly jammed, glassy and gel systems of colloidal spheres [213, 313]. Even in equilibrium fluids of hard-sphere colloids, ordered structures can be formed under the influence of oscillatory shear [31, 63], which is described in detail in Chapter 5 of this thesis. The effect of oscillatory shear on a sedimented sample of rods is shown in Fig. 7.6. Before applying oscillatory shear, the rods were subjected to steady shear (shear rate 33 s^{-1}, strain amplitude of 7) and afterwards left to sediment. In this manner, a shear aligned smectic formed with a nematic order parameter value of 0.94 (Fig. 7.6d). This was the initial state of the system at $t = 0$, shown in Fig. 7.6a. Subsequently, the smectic phase was shear melted to a para-nematic phase with $S_{2D'} = 0.85$ by applying large amplitude ($\sim$ 25) steady shear (Fig. 7.6b). Upon the application of oscillatory shear, with a shear rate of 33 s^{-1} and a strain amplitude of 7, small smectic or columnar-like domains were formed (Fig. 7.6c). The average nematic order parameter $S_{2D'}$ first decreased and then significantly increased during shear, as can be clearly seen in Fig. 7.6d. Details about this intriguing phenomenon, such as its stability and development in time, require more experimental work.

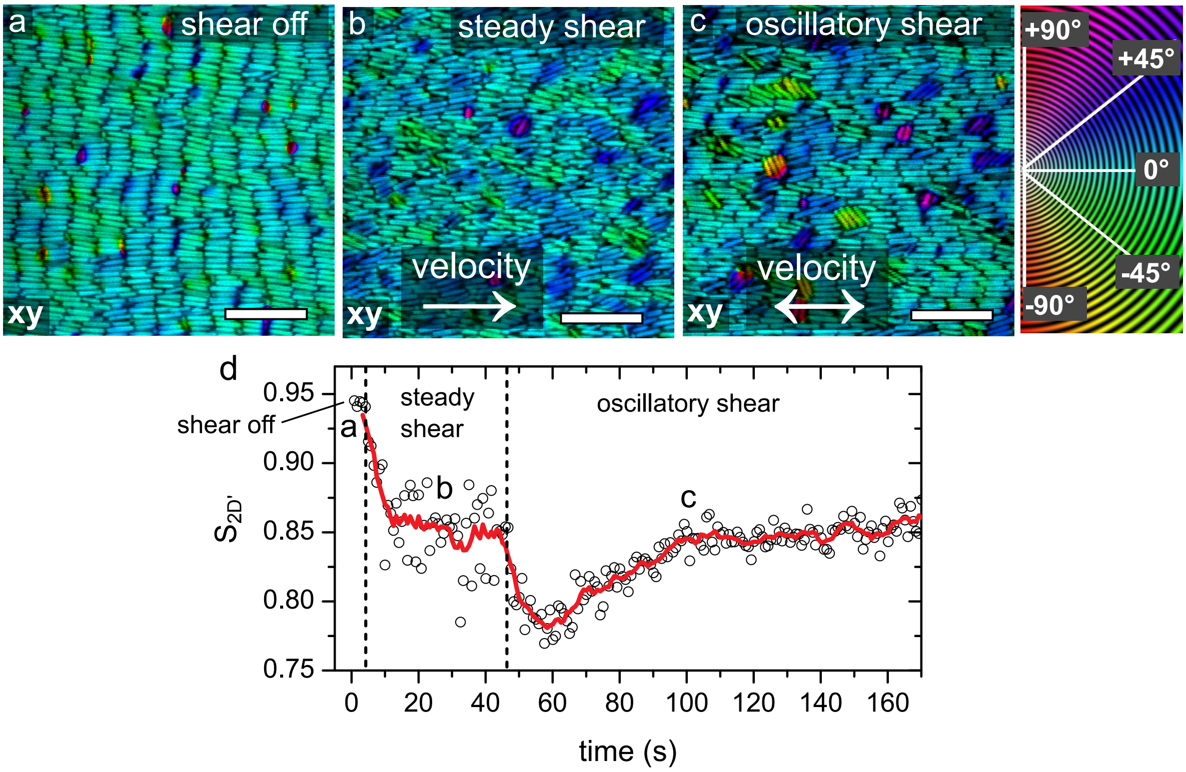

FIGURE 7.6. Application of oscillatory shear to a dispersion of rods. (a) A sedimentation induced shear-aligned smectic phase. (b) Shear melting into a para-nematic. (c) After applying oscillatory shear (shear rate 33 s^{-1}, strain amplitude 7), ordered columnar/smectic-like domains were induced in the para-nematic sample. (d) The nematic order parameter $S_{2D'}$ first decreased and then increased significantly when oscillatory shear was applied to the sample. Scale bars indicate 10 μm.

7.4. DISCUSSION AND CONCLUSION

Steady shear flow was successfully applied to align rod-like silica particles and create shear-induced nematic, columnar and smectic liquid crystal phases. Upon application of steady shear to rods in the isotropic phase, a shear-induced nematic was almost instantly formed and the nematic order parameter was determined from 2D confocal microscopy time-series. With a combination of fast confocal microscopy and simultaneous rheological measurements we investigated the correlation between the suspension micro-structure and its rheological properties. For increasing shear rate, we found pronounced shear thinning, a Newtonian regime and (the onset of) shear-thickening. We also found large non-periodic fluctuations in the viscosity over time for shear rates $\dot{\gamma} < 1.0$ s^{-1}. Although these fluctuations could be an indication of tumbling, wagging or kayaking behavior of the rods, we could not identify such micro-structural changes in the confocal microscopy images acquired during shear. As the measured velocity profiles were all linear and indicated no slip nor shear-banding, we rule out any non-linear shear flow as the origin of the fluctuations. Also the torque resolution of the rheometer was more than adequate to resolve the fluctuations and the period of rotation of the cone was orders of magnitude larger than the fluctuations.

While it would be interesting to study tumbling, wagging or kayaking behavior on the single particle level, which our system in principle does allow for, it is also difficult to get the sample in the right state. Tumbling, wagging or kayaking has been observed for nematic liquid crystals only. Our system of rods with aspect ratio $l/d = 6$ - 8 in principle has a nematic phase (see Chapter 6), but only in a small range of volume fractions. Due to the sensitivity of the rods to gravity, the samples tended to form a smectic rather than a nematic phase upon concentration. Therefore, careful fine-tuning of the dispersion's concentration will be required to make these measurements possible. Alternatively, a mixture of rods with different dimensions and aspect ratios can be used to frustrate the formation of a smectic phase. The time-scale of tumbling, with periods between 10 s for shear rates of 1 s^{-1} and 0.2 s for shear rates of 100 s^{-1} that were measured in *fd*-virus suspensions [37], are accessible using confocal microscopy. The viscous solvent for one of the samples in this chapter slows down Brownian dynamics enough to track the motion of a quiescent particle in 3D (see Chapter 4). However, it also shifts shear rates two orders of magnitude down, if we want to compare data with equal Peclet numbers, which can also obscure observation of tumbling or wagging motion using microscopy.

The largest changes observed in the suspension micro-structure were beyond the shear-thinning regime ($\dot{\gamma} > 2$ s^{-1}) and indicated an enhanced (non-collective) shear-induced rotational motion that increased in magnitude while approaching the shear-thickening regime. Although various studies exist on shear thickening of colloidal spheres, little is known about this behaviour for rods. We believe that rheo-confocal studies such as described in this chapter, can also elucidate the micro-structural origin of shear thickening in rod-like suspensions. However, more research is needed for this to be achieved.

Combining the ability of shear flow to align the rods and that of gravity to increase concentration, it was possible to create shear-aligned dense phases on the bottom of the shear cell. After sufficient sedimentation, the alignment induced by the shear was maintained in the sample when the shear was stopped and upon further sedimentation a shear aligned smectic-B phase was formed. When the shear was continuously applied during sedimentation a columnar phase was formed, with its director in the velocity direction. Although these first experiments are preliminary, it is already clear that shear is a powerful field to induce order over large distances as could for instance be applied by spin coating, which is often used in industry. The application of oscillatory shear to a shear aligned nematic resulted in the formation of para-smectic-like domains. More experiments are required to examine this phenomenon in more detail.

7.5. Acknowledgements

This work was done in collaboration with Anke Kuijk, Michiel Hermes and Rut Besseling. We thank Michiel Hermes and Rut Besseling for facilitating a research visit to the University of Edinburgh and for help with the rheo-confocal setup and image processing. We thank the European Soft Matter Infrastructure (ESMI) network for funding. We thank Henriëtte Bakker for critical reading of this chapter.

8

Switching Plastic Crystals of Colloidal Rods with Electric Fields

ABSTRACT

When a crystal melts into a liquid both long-ranged positional and orientational order are lost, and long-time translational and rotational self-diffusion appear. Sometimes, these properties do not change at once, but in stages, allowing states of matter such as liquid crystals or plastic crystals with unique combinations of properties. Plastic crystals/glasses are characterized by long-ranged positional order/frozen-in-disorder but short-ranged orientational order, which is dynamic. Here we show by quantitative three-dimensional studies that charged rod-like colloidal particles form three-dimensional plastic crystals and glasses if their repulsions extend significantly beyond their length. These plastic phases can be reversibly switched to full crystals by an electric field. These new phases provide insight into the role of rotations in phase behaviour and could be useful for photonic applications.

8.1. Introduction

Owing to their size, colloidal particles are an interesting model system for condensed matter, because Brownian motion ensures that the phase behaviour is analogous to that of atomic and molecular systems [314, 315] and particle coordinates can be obtained quantitatively in three-dimensional (3D) real space on a single particle level [12, 46, 56, 59]. In addition to the system being able to reach equilibrium on experimental time scales, the interaction potentials between the particles can be tuned extensively [12]. For instance, rod-like and plate-like particles have a nematic liquid crystal phase where translational order is short ranged, and there is unconstrained 3D translational motion, but one orientational degree of freedom is still long ranged [314]. This combination of properties makes liquid crystals perfectly suitable for display applications. As such, liquid crystals are the positional-rotational opposite of plastic crystals (PCs). The term ‘plastic crystals’ was chosen by Timmermans [316] when he found that some of the molecular plastic crystals could not even support their own weight as a direct consequence of the reduced strength of this solid phase of matter by the rotational dynamics of the molecules on their lattice [316, 317]. Colloidal liquid crystals are well known [262]; plastic crystals, however, have hardly been studied experimentally, despite their intriguing structure and dynamics, which are a mixture of those of a liquid and those of a solid. In recent experiments two-dimensional (2D) plastic crystals have been found [179, 318], but, as the dimension affects dynamics and structure strongly, these are not the same as 3D systems. For instance, 2D crystals do not have long-ranged order, and a system of disks does not have a glass transition. The only work we are aware of that mentions a 3D colloidal plastic crystal is the recent work by Zukoski *et al.* [319]. They studied slightly anisotropic ‘dicolloids’ for which the shape closely approximated two interpenetrating spheres by x-ray scattering. For certain parameters, it was concluded that a plastic crystal with a long-ranged positional, but random orientational, order had formed. However, because only static scattering experiments were performed, the question of rotations of the particles on their lattice sites on experimental time scales could not be addressed, which leaves open the possibility that the random orientations of the dicolloids were actually frozen in. Such plastic crystals are perhaps better characterized as ‘aperiodic crystals’, as they have sharp diffraction peaks but no true lattice periodicity due to the absence of rotations on an experimental time scale [320]. Similar to the particles as in Ref. 319, almost all molecular plastic crystals for which rotation around one or more axes is possible [316, 317] consist of an almost spherical shape around their rotation axis (for some examples, see Refs. 321–323).

Here, we take advantage of the possibility to realize extremely long-ranged repulsions in colloidal systems. By making this range longer than the rod-like particles in our system, we demonstrate that even for colloidal rods of 3.3 μm length and a length/diameter (l/d) ratio as large as 5.6 plastic crystals and, at higher densities, plastic glasses are found in a large range of volume fractions. We also demonstrate by scattering experiments, described later, that field-induced switching of these new plastic crystal phases offers new opportunities for photonic applications.

8.2. METHODS

8.2.1. Particle synthesis

Fluorescent silica rod-like particles were synthesized as described in Chapter 2. The particles were dyed using fluorescein isothiocyanate (FITC, isomer I, 90%, Sigma-Aldrich). The particles consisted of a three layered structure: a non-fluorescent core, an FITC labelled shell (*ca.* 40 nm) and a non-fluorescent outer shell (*ca.* 100 nm). In the second step, we modified the silica rods with octadecyltrimethoxylsilane (OTMOS, 90%, Sigma-Aldrich) by a ultrasonic-assisted coating procedure. In brief, a solution of OTMOS, butylamine (BA, 99.5%, Sigma-Aldrich) and dried toluene (1:1:10 v/v/v) was prepared, and then 10 wt% of silica rods, that had been dried under a nitrogen flow, were added to this solution. The suspension was sonicated at 30 - 55 °C for 4 hours (Branson 2250). Afterwards, the colloidal rods were washed in turn with toluene, cyclohexane and cyclohexylchloride (CHC, $>$ 98%, Merck). Finally, the colloidal rods were dispersed in deionized CHC for further use.

We used three systems of fluorescent colloidal silica rods, named R1, R2 and R3. R1: $l = 2.36$ μm (6.3%), $d = 0.58$ μm (10.6%), $l/d = 4.1$; R2: $l = 2.29$ μm (6.0%), $d = 0.60$ μm (6.5%), $l/d = 3.8$; R3: $l = 3.30$ μm (6.3%), $d = 0.59$ μm (8.7%), $l/d = 5.6$. Here, l and d are the mean end-to-end length and diameter respectively with the polydispersity (standard deviation divided by the mean) between parentheses.

8.2.2. Sample preparation & Electric field setup

The particles were suspended in cyclohexyl chloride (CHC). The received CHC (conductivity $\gg$ 1.000 pS/cm) was deionized by using molecular sieves (0.4 nm, Aldrich) and activated aluminium oxide (Aldrich). After purification, CHC had a conductivity as low as 5 - 10 pS/cm. Rectangular glass capillaries (0.1 × 2 mm^2, 0.1 × 2 mm^2, 0.5 × 0.5 mm^2, VitroCom, UK) were used as sample cells. Electrodes consisting of a 3 nm layer of Cr and a 6 - 10 nm layer of Au were sputter-coated on two opposing outer surfaces of these capillaries. Thermocouple alloy wires (diameter 50 μm, Goodfellow) were connected to the electrodes with silverpaint (SPI-paint). The ends of the wires were wrapped around standard electronic wires that in turn were connected to the electrical set-up. We used a function generator (Agilent 33120A) to generate a sinusoidal signal with a frequency of 1 MHz and an amplitude of 2.0 V (peak-to-peak). This signal was sent to the sample via a wide band amplifier (Krohn-Hite, 7602M) used to vary the field strength in the sample. We applied a high frequency AC field to prevent polarization of the electric double layer of the particles. After filling the capillaries, they were fixed on a glass slide and sealed with UV-cured glue (Norland, No. 68).

8.2.3. Electric field calculation

Because the electrodes were on the outside of the capillaries, there were three layers of material between the two electrodes. In this case, the field strength is given by [281]

$$E = \frac{V}{\epsilon_0}\left(\frac{\epsilon_1\epsilon_2\epsilon_3}{d_1\epsilon_2\epsilon_3 + d_2\epsilon_1\epsilon_3 + d_3\epsilon_1\epsilon_2}\right), \tag{8.1}$$

with V the applied voltage, ϵ_0 the dielectric constant of the sample, ϵ_{1-3} the dielectric constant of layers 1-3 and d_{1-3} the thickness of layers 1-3. In our experiments, layer 1 and 3 are the glass capillary walls, (thickness $d \sim 0.1$ mm and $\epsilon = 3.5$) and layer 2 is (primarily) the solvent CHC (thickness $d \sim 0.1$ mm and $\epsilon = 7.6$). The field strength is thus given by $E = 1.9 \times 10^{-3}\,V$ (V/μm). All field strengths in this chapter are given in units V_{RMS}/μm.

8.2.4. Electrical conductivity measurement

We estimated the Debye screening length by measuring the conductivity of the deionized solvent CHC with a Scientifica 627 conductivity meter. For the calculation of ionic strength, we made use of Walden's rule [12, 77] which states that the product of the limiting equivalent conductance and the viscosity is a constant between different media, that is, $\Lambda_0^{Ethanol}\,\eta_0^{Ethanol} = \Lambda_0^{CHC}\,\eta_0^{CHC}$. We used literature values for the limiting equivalent conductance of HCl in ethanol [79] and the viscosity of 1.57 mPa·s for CHC [69]. The Debye screening length κ^{-1} can then be estimated by

$$\kappa^{-1} = (8\pi\lambda_B c)^{-1/2}. \tag{8.2}$$

Here, $\lambda_B = e^2/(4\pi\epsilon\epsilon_0 k_B T)$ is the Bjerrum length, and ϵ and ϵ_0 are the dielectric constant of the solvent and the permittivity of vacuum. e is the elementary charge, k_B is Boltzmann's constant and T is the absolute temperature. A final conductivity of *ca.* 10 pS/cm for particle-free CHC corresponded to κ^{-1} of *ca.* 5 μm, estimated using equation (8.2).

8.2.5. Electrophoretic mobility measurement

To estimate the surface charge of our particles, we measured the electrophoretic mobility of a dilute suspension (volume fraction $\phi = 0.0005$) with confocal microscopy [53]. The sample cell was a 0.1 × 2 mm^2 capillary with two parallel nickel-alloy wires (diameter 50 μm) running along the side walls. We filled the cell with our sample and sealed it with UV-glue. The z-position of the stationary layer was calculated as described before [53]. In a direct current (DC) electric field, the motion of particles in the stationary layer was determined from time series of confocal microscopy images. From the mobility we then obtained the zeta potential using the Hückel equation, which applies to ideal dilute suspensions with large Debye screening length.

8.2.6. Confocal microscopy measurement

The samples were studied with a laser scanning confocal microscope (Leica TCS SP2 and Leica TCS SP8 equipped with a 12 kHz resonant scanner). All images were taken in fluorescence mode. The excitation wavelength was 488 nm. To obtain 3D data for dynamical measurements, care was taken to ensure that rods did not move or rotate too much during the collection of the 3D data set. The measured rotational relaxation time was 2.7 s for sample R2. The time to acquire a single 3D data-set was 0.26 s, achieved by scanning an area of 54 × 18 × 7 μm^3, with a pixel size of 178 nm in x-y and 396 nm in z.

8.2.7. Rod-like particle tracking

We determined the positions and orientations of the rods from both 2D and 3D confocal micrscopy data sets, using the algorithm described in Chapter 4. To uniquely track the tip of the (nearly up-down symmetric) rods, it is required that the rotation angle of individual rods between successive frames was less than $\pi/2$. It was therefore verified that the rotations larger than $\pi/2$ were negligible at a time-step of 0.26 s.

8.2.8. Translational motion

To quantify the rotationally averaged translational motion in the plastic crystalline phases, we used an expression for the diffusive motion of a harmonically bound Brownian particle. Following the work of Uhlenbeck and Ornstein [324], we derived an expression for the mean squared displacement (MSD) in three dimensions of a Brownian particle trapped in a harmonic potential [325]

$$\langle|\mathbf{r}-\mathbf{r}_0|^2\rangle = \frac{3}{\beta\,k}[1-\exp\left(-2\,D_t\,\beta\,k\,t\right)] + \mathbf{r}_0^2\,[1-\exp\left(-D_t\,\beta\,k\,t\right)]^2, \tag{8.3}$$

with $\mathbf{r}$ the (radial) distance to the minimum of the harmonic potential, $\mathbf{r}_0$ the position of the particles at $t = 0$, $\beta = 1/(k_BT)$ the inverse temperature, D_t the rotationally averaged translational diffusion coefficient and k the spring constant. For $t \to \infty$ and $\mathbf{r}_0 = 0$ we find the equipartition theory

$$\frac{1}{2}k\langle\mathbf{r}^2\rangle = \frac{3}{2}k_BT. \tag{8.4}$$

Equation (8.3) is valid for an ensemble of particles that all start to diffuse at the same starting position $\mathbf{r}_0$ at $t = 0$. In the experiments, however, the particles are at a random position at any given time, also for $t = 0$, which is given by a Boltzmann distribution

$$P(\mathbf{r}) = \left(\frac{\beta\,k}{2\pi}\right)^{3/2}\exp\left(-\frac{1}{2}\,\beta\,k\,\mathbf{r}^2\right). \tag{8.5}$$

It is not difficult to show that in this situation, the expression for the MSD is given by [325]

$$\langle\langle|\mathbf{r}-\mathbf{r}_0|^2\rangle\rangle_{\mathbf{r}_0} = \frac{6}{\beta\,k}\,[1-\exp(-D_t\,\beta\,k\,(t-\frac{\tau}{3})] + 6\,\epsilon_t^2, \tag{8.6}$$

with the outermost brackets indicating an average over starting positions $\mathbf{r}_0$. Here, we have included τ to account for the time to acquire a 3D data set and ϵ_t to account for positional measurement error [193]. Equation (8.6) shows that for a Boltzmann distribution of starting points $\mathbf{r}_0$, there is a factor of 2 difference in both the decay constant of the exponent as well as the prefactor of the expression for the MSD, compared to equation (8.3) with $\mathbf{r}_0 = 0$.

An alternative method to measure the effective spring constant k is by calculating the probability of an excursion of a particle away from its center position $P(\mathbf{r})$ for any given time (see equation (8.5)). Taking the logarithm of this distribution gives the effective potential well $-\ln P(r) = \beta\, U(r)$. Weiss *et al.* showed for charged spherical colloids that this effective well is harmonic for excursions within 10% of the lattice spacing [326]

$$\beta\, U(r) = \frac{1}{2}\beta\, k\, \mathbf{r}^2. \tag{8.7}$$

8.2.9. Rotational motion

We quantified the rotational motion of the particles by determination of the rotational auto-correlation function, given by

$$C(t) = \langle \hat{\mathbf{u}}(0) \cdot \hat{\mathbf{u}}(t) \rangle, \tag{8.8}$$

with the brackets denoting an ensemble average, and $\hat{\mathbf{u}}(t)$ the orientation of the rod. The angular coordinates of the rods were obtained from time-series of 3D confocal microscopy data sets. The rotational auto-correlation function was calculated by averaging over 35 particles and over 494 time steps. The auto-correlation function was then fitted to the expression

$$C(t) = (1 - \epsilon_r^2) \exp(-2D_r(t - \frac{\tau}{3})). \tag{8.9}$$

This expression is derived from the equation for the mean squared angular displacement used in Ref. 195. Here, ϵ_r is the term accounting for the statistical error in measurements of $\hat{\mathbf{u}}(t)$ and τ is the time to acquire a single 3D data set. As demonstrated in Chapter 4, ϵ_r can be as low as $4\,^\circ$ using our in-house developed rod-fitting algorithm. However, the value of ϵ_r in this chapter was significantly higher due to the fast rotational motion of the particles, i.e. the angular resolution was time-limited due to motion blur. Therefore, we found a relatively high angular uncertainty of $\epsilon_r = 24\,^\circ$, which is close to the average angular displacement during the time that a 3D data set was acquired $\sqrt{\langle \theta^{\,2} \rangle_\tau} = 25\,^\circ$, with $\tau = 0.26$ s.

We compared our measurement of the rotational diffusion coefficient with the value for a freely rotating cylinder at infinite dilution, given by [198]

$$D_r^0 = \frac{3k_BT}{\pi\,\eta\, l^3}(\log p + \delta_r), \tag{8.10}$$

$$\delta_r = -0.662 + 0.917/p - 0.050/p^2, \tag{8.11}$$

with l the end-to-end length of the rod, $p = l/d$ the aspect ratio, k_B the Boltzmann constant, $T = 294$ K the temperature and $\eta = 1.57$ mPa·s the viscosity of the solvent. The term δ_r is to correct for the finite size of the particle. The calculated D_r^0 for rod system R2 is 0.19 $(\text{rad})^2$/s.

8.2.10. Nematic order parameter calculation

To quantify the (projected) 2D order in the system we calculated the 2D nematic order parameter, given by

$$S_{2D'} = 2\langle \cos^2 \psi \rangle - 1, \tag{8.12}$$

with ψ the angle between the projected main axis of the rod $\hat{u}'$ and the projected nematic director $\hat{n}'$, i.e. ψ is the in-plane projected angle that maximizes equation (8.12). To determine both $\hat{n}'$ and ψ, we calculated the 2 × 2 nematic order parameter tensor given by

$$Q^{2D}_{\alpha\beta} = \frac{1}{N}\sum_{i=1}^{N}\Big(2\, u'_{i\alpha}u'_{i\beta} - \delta_{\alpha\beta}\Big), \tag{8.13}$$

with $u'_{i\alpha}$ the α-component of the unit vector pointing along the projected main axis of particle i and $\alpha = x, y$ and $\delta_{\alpha\beta}$ the Kronecker delta. Although the 2D projection of 3D orientations changes the orientation distribution significantly, we showed in Chapter 4 that the 2D projected nematic order parameter is almost equal to the value of the 3D nematic order parameter, as long as the the director lies approximately in the plane of observation. Given that circumstance, measurements of the projected 2D nematic order parameter are therefore a strong indication of the actual 3D nematic order in the system.

8.2.11. Low polar viscous solvents

At the end of this chapter we present preliminary results on plastic crystals where particle dynamics were slowed down due to the use of low polar viscous solvents. We used cyclohexyl chloride (CHC) mixed with either dioctyl phthalate (DOP, 99%, Aldrich) or tris(2-ethylhexyl)trimellitate (TEHTM, 99%, Aldrich). The solvents were de-ionized as described in Section 8.2.2, resulting in similar conductivity values as obtained for pure CHC (5 - 10 pS/cm). Results are presented for particles dispersed in a mixture of 83 wt% DOP in CHC. The viscosity of this solvent $\eta = 22.5$ mPa·s (23 °C), as measured with a SV10 viscometer (A&D Company) and the refractive index $n_D^{23} = 1.482$, as measured with a refractometer (Atago 3T). Confocal microscopy data stacks were acquired with a Leica SP2 confocal microscope. The dimensions of a single 3D stack was 44.5 × 34.8 × 51.6 μm^3 with a voxel size of 174 nm in x,y and 311 nm in z. The time to record the stack was 28 s (using a 1 kHz scanner).

8.3. RESULTS

8.3.1. Charged colloidal rods

We and others have shown previously for spherical colloids that it is not difficult to achieve electrostatic screening lengths (κ^{-1}) of several micrometer in solvents with a relative dielectric constant approximately in between 4 and 10 [12, 327]. In this study, we used a recently developed fluorescent model system of micron-sized colloidal silica rods that can be fluorescently labelled [25] and dispersed in the index matching solvent cyclohexylchloride (CHC). In addition to carrying a negative charge (surface potential -70 mV), the colloidal silica rods were sterically stabilized by grafting with short C18 alkane chains and almost index-matched to reduce van der Waals forces and allow for quantitative confocal microscopy measurements > 100 μm deep inside the sample. We studied three different rod lengths from 2.3 to 3.3 μm and aspect ratios from 3.8 to 5.6 (see Methods). For relatively high concentrations of an added salt, and thus short screening lengths, nematic and smectic liquid crystal phases were found (not shown here) in accordance with a recent real space study of our group (see Ref. 28 and Chapter 6). On the other hand, at low concentrations of salt, the effective repulsive interactions between the rods should become increasingly less anisotropic. On the basis of results of spherical particles [12, 17], we expected to obtain crystals with a body centred cubic (BCC) structure in which the rods have the freedom to rotate. The screening lengths for the systems studied in this chapter were maximized by extensively deionizing the solvent to reach screening lengths of about 5 μm, as determined from the conductivity. This screening length was sufficient to result in plastic crystals over a range of volume fractions ($\phi \approx 0.005$ - 0.015). In the following, we first describe the structures observed without an external electric field.

8.3.2. Plastic crystal structure

As Fig. 8.1 shows in detail, the 3D lattice on which the rods rotate is indeed of BCC symmetry (see Fig. 8.1a-e). In addition, it is clear that the softness of the interparticle potential as well as the rotations of the individual rods on their 3D lattice makes visual identification of the actual structure from (sets of) individual images relatively hard. However, as a testament to the true 3D long-ranged periodicity and stability of these crystals, an average of 150 frames taken over 5 min produced an almost perfect lattice, shown in Fig. 8.1c (also see Movies 1 and 2 in Appendix B.3). The sharp peaks from first to even fifth order in the corresponding Fourier transform shown in Fig. 8.1d illustrate the nearly perfect crystallinity present even over the relatively long averaging period. We further illustrated the softness and the positional order of the crystal with two-dimensional (2D) pair correlation functions $g(r)$ (Fig. 8.1f) with (red) and without averaging (blue). The peaks from the timeaveraged image match well with a perfect (110) plane of a BCC phase (black). The position of the first peak at 2.2 times the length of the rods again illustrates the long range repulsion between the rods. The resulting extremely low effective mass density of these crystals explains why gravity hardly affected the lattice spacing as a function of height in the samples studied. Unfortunately, a theoretical description of systems of anisotropic particles with electrostatic double layers the size of the particles is not available yet as the interparticle interactions are quite difficult to solve [269].

8.3.3. 3D particle dynamics

Translational motion. Using fast confocal microscopy, we were able to study the dynamics of the particles in the plastic crystal phases in 3D real-space. Prior to these measurements, the confocal microscope was carefully calibrated in all three directions and we corrected for the refractive index mismatch between the sample and oil-immersion (see Chapter 3). In Fig. 8.2a, we show a 3D reconstruction from a confocal microscopy

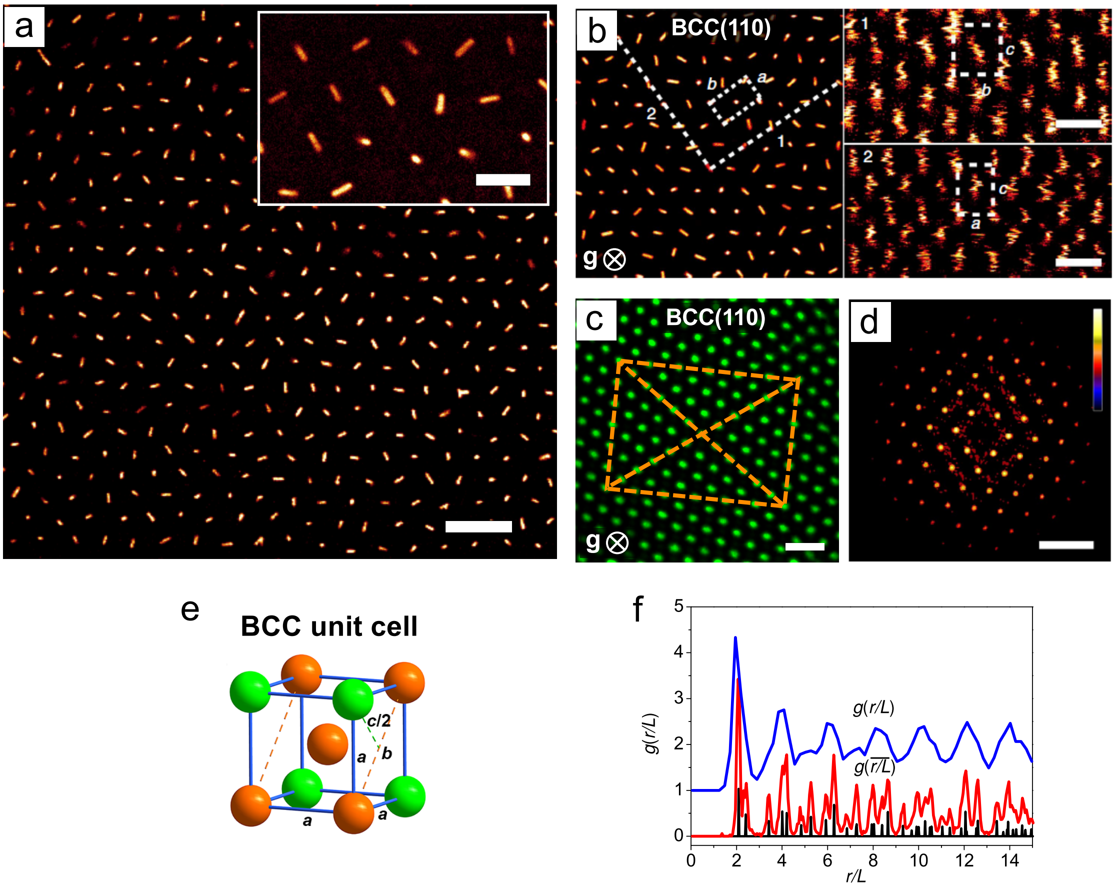

Figure 8.1. Body centred cubic (BCC) plastic crystal structure. Silica rods R1 with $\phi = 0.005$. (a) 2D confocal microscopy image of a 3D plastic crystal of silica rods. The scale bar is 15 μm and the scale bar in the inset 5 μm. (b) Confocal microscopy images indicating the BCC plastic crystal structure, left: (110) plane; top right: (001) plane; bottom right: $(1\bar{1}0)$ plane. The images for the (001) and $(1\bar{1}0)$ planes were reconstructed from the same 3D data stack. (c) The average of 150 frames, measured over a time of 300 s. The dashed (orange) lines correspond to the plane of the orange spheres in the BCC model shown in (e). (d) Fourier transform calculated from the monochrome real space image shown in (c). The colour bar indicates the logarithmic intensity scale. (e) Schematic BCC model defining the lattice vectors shown in (b) and (c). (f) Pair correlation function $g(r)$ found, from top to bottom, by calculating the $g(r)$ of a single frame, by calculating the $g(r)$ of the average of 150 frames, and from a perfect BCC lattice. The scale bars in (b) and (c) are 10 μm, and the scale bar in (d) is 3 μm^{-1}.

data set. To minimize the time-interval to record the stack ($\tau = 0.26$ s, see Sections 8.2.6 - 8.2.7) only a thin 3D slab was acquired containing 1 crystalline layer, covering a volume of 54 × 18 × 7 μm^3. In Fig. 8.2b, we show the xy projections of the 3D translational trajectories of all the particles in the 3D volume, for a total time of 128 s. The xy-plane in Fig. 8.2b shows a view of the BCC(110) plane of the plastic crystal (see

Figs. 8.1a,b). Drift was removed by subtraction of the center of mass of the system from the particle coordinates at each time step. The trajectory of the particle highlighted with the dashed circle in Fig. 8.2b, is shown in 3D in Fig. 8.2c. From the nearly isotropic shape of the trajectory we can infer that diffusion in the x, y and z direction was almost equal. In Fig. 8.2d, we show the probability distributions of an excursion away from the average lattice position of a particle in the x, y and z direction, averaged over all particles and time-steps. The lines are Gaussian fits to equation (8.5). By taking the logarithm of these distributions and fitting to equation (8.7) for each spatial direction, we obtained for the effective spring constants $\beta\, k_x = 32.3 \pm 0.5\, l^{-2}$, $\beta\, k_y = 21.1 \pm 0.5\, l^{-2}$ and $\beta\, k_z = 29.0 \pm 0.6\, l^{-2}$, with $\beta = 1/(k_B T)$ the inverse temperature and

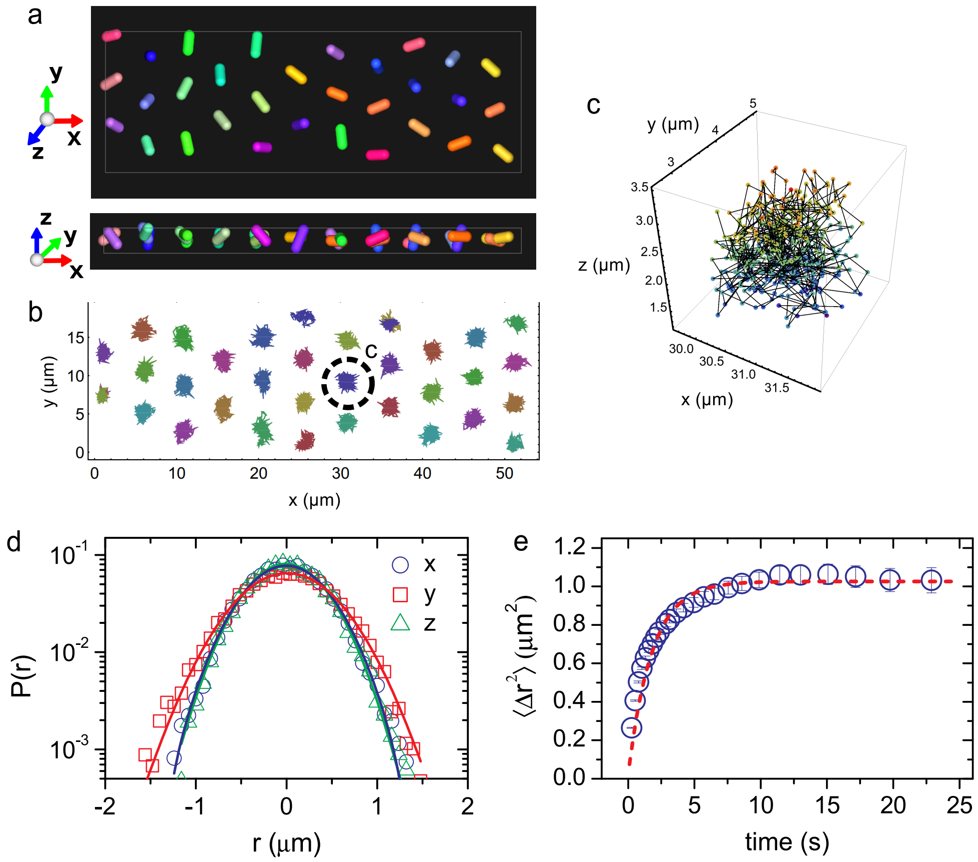

FIGURE 8.2. Translational dynamics of silica rods (R2) in a plastic crystal phase, with volume fraction $\phi = 0.005$. (a) 3D reconstruction from a confocal microscopy data set containing a single layer of the crystal. Colours indicate the 3D orientation of the particles. (b) Projection in the xy plane of the 3D translational trajectories, showing a view of the BBC(110) plane of the plastic crystal. (c) The complete 3D trajectory of the particle highlighted with the dashed circle in (b). (d) Probability distribution of excursions from the center of the lattice position in the x, y and z direction, averaged over all particles and all time-steps. The lines are Gaussian fits to equation (8.5). (e) Rotationally averaged mean squared displacement $\langle \Delta \mathbf{r}^2(t) \rangle$, averaged over 35 particles. The (red) dashed line is a fit to equation (8.6).

$l = 2.29$ μm the average length of the rods. The effective potential well is weaker in the y than in the x or z direction, which is likely due to the orientation of the BCC crystalline lattice (see Fig. 8.2b). In Fig. 8.2e, we show the rotationally averaged mean squared displacement $\langle \Delta \mathbf{r}^2(t) \rangle$. The dashed (red) line in Fig. 8.2e is a fit to equation (8.6), which is an expression for the mean squared displacement of Brownian particles trapped in a harmonic potential with random starting positions. From this fit, we obtain for the average spring constant $\beta\, k = 30.7 \pm 0.5\, l^{-2}$, which is in agreement with the previous stated values. In Ref. 77, a similar calculation was done on crystals of spherical particles with a long-range repulsion (inverse screening length $\kappa\sigma = 5$ and potential at contact $\beta\epsilon = 140$), which resulted in $\beta\, k \approx 60\ \sigma^{-2}$, with $\sigma = 2$ μm the diameter of the sphere. This shows that the (effective) potential in which the rods in our experiments were trapped was significantly weaker. Furthermore, we obtained from the fit to equation (8.6) the rotationally averaged translational diffusion equation $D_t = 0.118 \pm 0.007$ μm^2/s, which is significantly smaller than the theoretical value for particles at infinite dilution $D_t = 0.22$ μm^2/s. We also obtained the average vibrational amplitude $\sqrt{\langle \mathbf{r}^2 \rangle} = \sqrt{\langle \Delta \mathbf{r}^2 \rangle / 2} = 0.71$ μm, which is 14% of the average inter-particle spacing in the crystal (obtained from the first peak in the $g(r)$, see Fig. 8.1f). These (extremely) large lattice displacements further illustrate the softness of the crystal.

Rotational motion. We explored the nature of the rotational motion of the rods on their BCC lattice and investigated whether rods influence each other's rotation at the lowest volume fractions $\phi = 0.005$. In Fig. 8.3a, we show the superposition of a time sequence of 300 frames taken over 100.8 s. Already from the symmetry of the pattern, we can reasonably infer that the rods explore all the orientations. This is confirmed by the absence of structure in the orientation distribution of the rods as projected in the 2D imaging plane (Fig. 8.3b). To further verify the free rotation of the rods, we also measured a 3D rotational trajectory of a single rod on its lattice position by extracting its angular coordinates from a time series of 3D confocal microscopy data sets (see section 8.2.7-8.2.9). The orientation distribution on the unit sphere is homogeneous, showing that the rod explores all orientations (see Fig. 8.3c and Movie 2 in Appendix B.3). From an average over the trajectories of 35 rods, we calculated the rotational autocorrelation function $C(t)$, as shown in Fig. 8.3d. The (red) continuous line in Fig. 8.3d is a fit to equation (8.9), from which we obtained the rotational diffusion coefficient $D_r = 0.18 \pm 0.04$ (rad)^2/s. This value is close to the theoretical value for a freely rotating rod $D_r^0 = 0.19$ (rad)^2/s, which is indicated by the (black) dotted line in Fig. 8.3d.

When ϕ was increased above 0.005 the plastic crystalline behaviour was still observed, although the (almost) free rotations demonstrated in Fig. 8.3 became more and more influenced by neighbouring particles. Interestingly though, not the rotational degrees of freedom were lost when ϕ was increased above roughly 0.018, but it was the positional order that was lost (Fig. 8.4a). This loss of positional order, without appreciable translational diffusion, but with significant rotational mobility is clearly seen by comparing

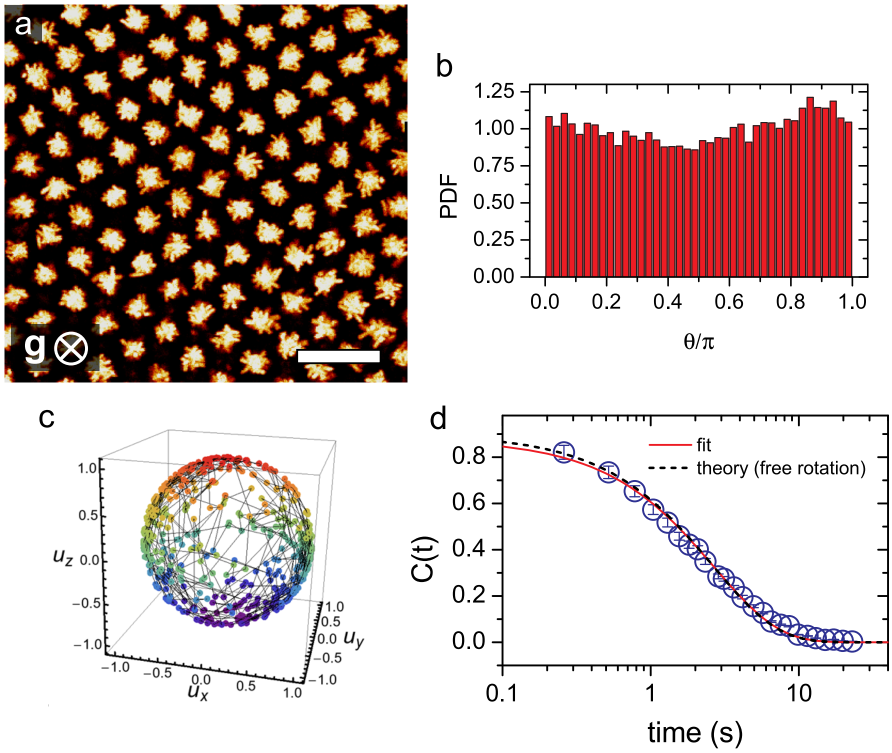

FIGURE 8.3. Rotational dynamics of silica rods (R2) in a plastic crystal phase, with volume fraction $\phi = 0.005$. (a) A superposition of 300 frames measured over 100.8 s. The scale bar is 10 μm. (b) The orientation distribution function of in-plane angles. (c) The rotational trajectory of a single rod on the unit sphere surface. (d) Orientational autocorrelation function $C(t)$, averaged over 35 particles. The (red) continuous line is a fit to equation (8.9), whereas the (black) dotted line is obtained from theory for a freely rotating particle at infinite dilution.

Fig. 8.4b and c with Fig. 8.1b and c. In Movie 3 in Appendix B.3, the rotations of many of the rods can be clearly observed, while positionally there is no relaxation. This plastic glass phase is a remarkable demonstration of the decoupling of the glass transitions of the positional and rotational degrees of freedom, as has been discussed earlier based on simulations and theory (for examples, see Refs. 328–330). The ability to follow the 3D rotations of the particles quantitatively in real-space gives unprecedented possibilities to study this new type of glass transition, which is investigated in more detail in Chapter 9. Moreover, the positional glass can be reversibly switched to a crystalline state by an external electric field as will be demonstrated below.

8.3.4. Alignment under an electric field

Electric fields are known to couple strongly to the alignment of liquid crystal phases, enabling many applications [262]. To examine whether the particle orientations in plastic crystals can also be controlled, we applied a homogeneous external electric field with a frequency of 1 MHz so that the double layer is not able to follow the field and only effects of dielectric polarization of the particles remain [12]. Because the

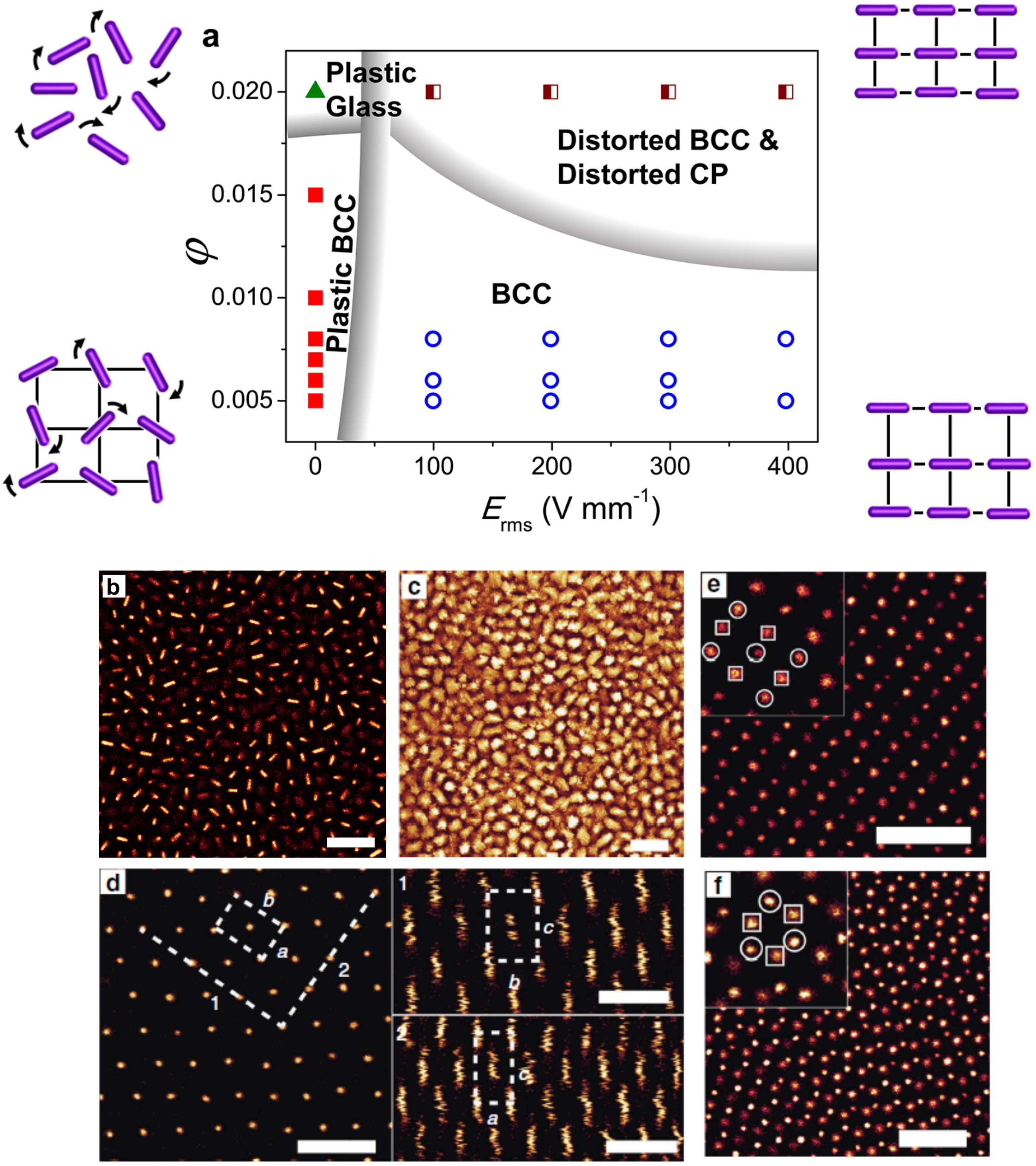

FIGURE 8.4. Volume fraction - electric field state diagram. Silica rods R2 with $\phi \sim 0.005 - 0.02$. (a) The state diagram. Thick grey lines indicate approximate phase boundaries. (b) Confocal image of a plastic glass phase. (c) A superposition of 120 frames of a plastic glass measured over 98 s. (d) Confocal images of a 3D crystal with BCC symmetry, left: (110) plane; top right: (001) plane; bottom right: $(1\bar{1}0)$ plane. The images for the (001) and $(1\bar{1}0)$ planes were reconstructed from the same 3D data stack. (e) Distorted BCC phase and (f) distorted close packed phase at $\phi = 0.02$, the focal plane is in between two neighbouring layers. In inset images, squares represent one layer, and circles represent one neighbouring layer. The scale bars from (b) to (f) are 10 μm.

long range of the particle repulsion, coupling of induced dipoles between particles is significantly weaker than the thermal energy at almost all field strengths used, so in the systems studied here induced dipoles couple only to the external field (see Figs. A.1-A.2 in Appendix A). Nevertheless, as shown qualitatively in Fig. 8.4 and quantitatively in Fig. 8.5, fields of sufficient strength align the rods, fully arresting the rotational freedom of the plastic crystals, thus switching from a plastic crystal to a fully ordered 3D crystalline state (Fig. 8.5a,b). As expected from the lack of dipole-dipole coupling (Appendix A), the lattice symmetry was preserved in this transition as illustrated in Fig. 8.4d and Movie 4 in Appendix B.3.

To investigate the nature of the transition from a plastic to a full BCC crystal, we quantified the projected angular distributions measured by taking 2D time series of (110) crystal planes (Fig. 8.5c, $\phi = 0.005$) as a function of the electric field strength with the field parallel to the imaging plane (Fig. 8.5a). Already at a field strength of 25 V_{rms}/mm, the rotations became highly restricted (Fig. 8.5c). However, there was no

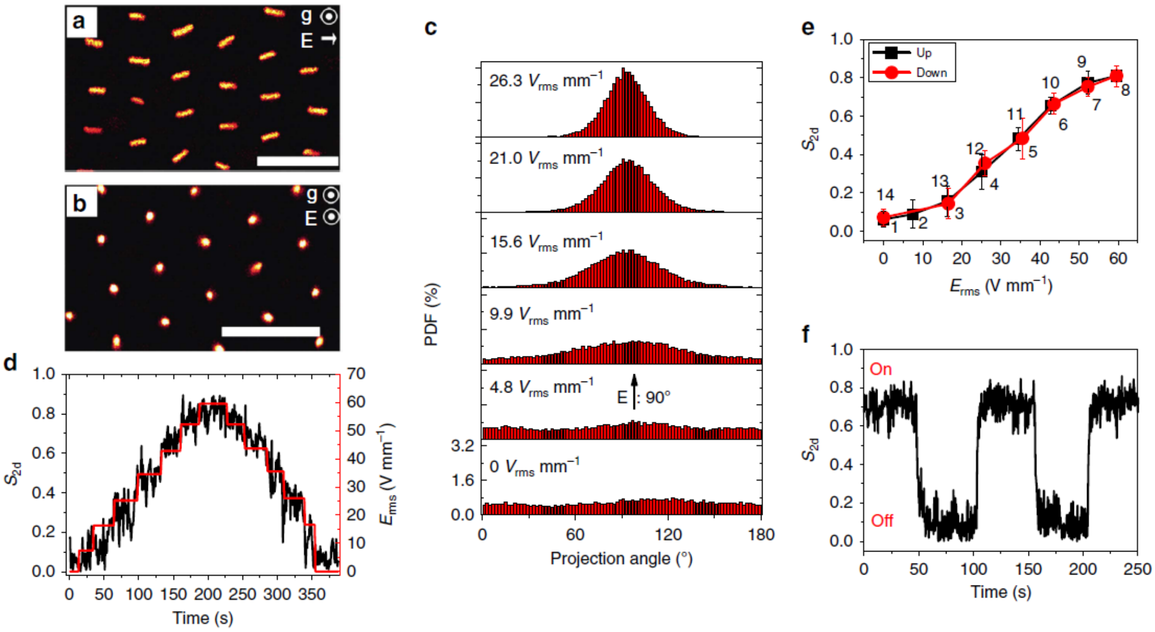

FIGURE 8.5. Manipulation of the rotation using an external electric field. Silica rods R2 (a,b,d-f) and R3 (c) with $\phi = 0.005$. (a,b) Confocal images of the rods oriented by different field directions. (c) In-plane angular distribution of rods on a crystal lattice as a function of field strength. (d) Nematic order parameter (2D) and corresponding field strength as a function of time. (e) Nematic order parameter (2D) versus field strength, showing the absence of hysteresis. The time points were 0, 14, 35, 65, 89, 133, 161, 188, 228, 253, 286, 310, 340, 355 s. The vertical error bars are the standard deviation of the calculated values displayed. (f) Fast switching between the on-state (same orientation) and off-state (random orientation). The scale bars in (a) and (b) represent 10 μm.

indication of a sudden jump in the angular distribution or the nematic order parameter S_{2d} of in-plane angles, indicating that the transition as a function of the field was continuous at this volume fraction. This is also borne out by the absence of any hysteresis when the field was slowly cycled from low to high values and back (Fig. 8.5d,e). Figure 8.5f gives an indication of the switching speed. When the field is switched on/off instantaneously, it takes a few seconds to achieve full alignment/randomization of the rods (see also Movie 5 in Appendix B.3). Fully in line with expectations, such switching did not affect the crystallinity.

At higher volume fractions ($\phi \gtrsim 0.015$) and for field strengths where the positional order was not lost, we observed a relatively large region where distorted BCC crystal (see Fig. 8.4a) was found mixed with crystals with a different stacking and symmetry (compare Fig. 8.4e,f). These other crystals were similar to those observed for hard spheres: randomly stacked close packed (CP) layers. The distortion consisted of an elongation of the crystal lattice along the electric-field direction and is investigated in more detail in Chapter 9. There was not a sharp transition region in the state diagram between BCC and the randomly close packed layers, quite similar to the case reported for spheres in a similar inter-particle distance range [331]. As mentioned, there are unfortunately no simulations or theory for comparison. It is also quite intriguing that at the higher volume fractions and relatively low field strengths there is a transition between the already mentioned plastic glass and a 3D fully crystalline state that is completely reversible. Apparently and intriguingly, without a field the plastic glass is more stable than the crystal. In Chapter 9, we characterize this transition in more detail in real-space and on the single particle level.

8.3.5. Apolar viscous solvents

We end this chapter with an outlook on real-space quantitative measurement on particles in a plastic crystal phase, dispersed in an apolar viscous solvent mixture. The rotational diffusion coefficient that we measured when particles were dispersed in CHC ($D_r = 0.18 \pm 0.04$ (rad)^2/s, Fig. 8.3), is three orders of magnitude larger than previously accessible with 3D confocal microscopy [181]. However, due to this rapid rotational motion, only small 3D volumes can be acquired, even with a 12 kHz scanner, as shown in Fig. 8.2. We therefore increased the solvent viscosity to slow down the dynamics in the system [181, 332]. We used two low-polar viscous solvents: dioctyl phthalate (DOP) and tris(2-ethylhexyl)trimellitate (TEHTM). DOP has been used earlier as

	ρ (g/ml) (25 °C)	n_D^{21}	η (cP) (25 °C)	ϵ_r
DOP	0.980 ^{1}	1.4862 ^{1}	54.8 ^{1}	5.1 ^{2}
TEHTEM	0.985 ^{3}	1.4856 ^{3}	213.4 ^{3}	4.6 ^{2}

Table 8.1. Properties of two low-polar viscous solvents. Here, ρ is the density, n_D the refractive index, η the absolute viscosity and ϵ_r the dielectric constant. All entries are literature values, taken from Refs. 333 (1), 334 (2) and 335 (3).

a dispersing solvent for PMMA spheres to measure shear-induced structure with 3D confocal microscopy [223] and TEHTM has similar properties but is more viscous (and less toxic) than DOP, see Table 8.1.

We found that the particles were not stable in either DOP or TEHTEM alone, which is likely due to the limited charge that the particles acquire in these solvents. We therefore dispersed the particles in solvent mixtures of CHC and DOP or CHC and TEHTEM. Fig. 8.6a shows a confocal microscopy image of particles with volume fraction $\phi \sim 0.005$ dispersed in a mixture of 83 wt% DOP in CHC. It is clear that also in this mixture, the particles had a long range repulsion and that they were able to from a plastic crystal phase. The viscosity of this solvent mixture was $\eta = 22.5$ mPa·s, corresponding to a rotational relaxation time $\tau_r = 38$ s, which is 14 times larger than

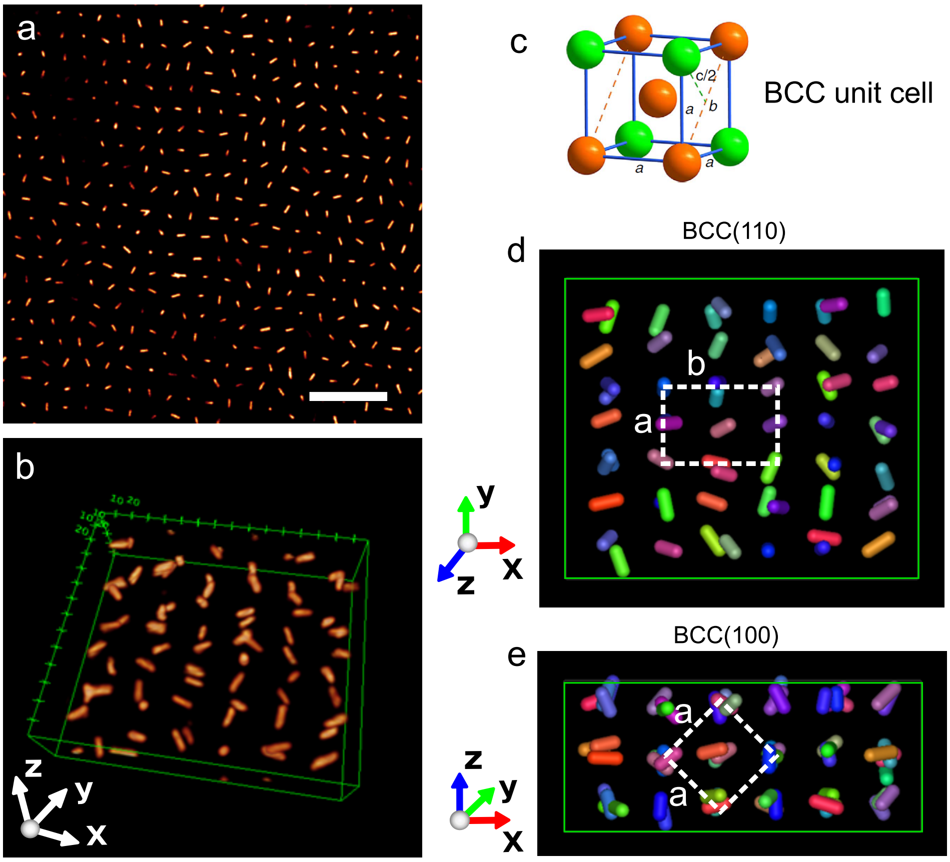

Figure 8.6. Rod system R2 dispersed in a mixture of 83 wt% dioctyl phthalate (DOP) in cyclohexyl chloride (CHC). The viscosity of this solvent mixture $\eta = 22.5$ mPa·s. (a) Confocal microscopy image showing that also in this solvent, repulsions remained long-range and a plastic crystal phase was formed. The scale bar is 20 μm. (b) Close-up view of a 3D confocal microscopy image stack. Time to acquire the 3D stack shown was 8.5 s. (c) BCC unit cell. (d-e) 3D particle reconstructions from the image stack shown in (b). The colours indicate the 3D orientation of the particles. (d) View from the BCC(110) plane. (e) View from the BCC(100) plane.

for pure CHC ($\eta = 1.57$ mPa·s). Fig. 8.6b shows a close-up of a 3D confocal microscopy data stack, with total dimensions of 44.5 × 34.8 × 51.6 μm^3 with a voxel size of 174 nm in x,y and 311 nm in z. The time to record the complete stack was 28 s (with a 1 kHz scanner) and the time to record the close-up shown in Fig. 8.6b was 8.5 s. Since this is significantly smaller than the rotational relaxation time ($\tau_r = 38$ s), there is no motion-blur visible in the 3D image, enabling (more) accurate measurement of the particle coordinates (compare Fig. 8.1b and Fig. 8.6b). In Figs. 8.6d,e we show 3D reconstructions of the BCC(110) and BCC(100) planes respectively, showing that the orientations of *all* the nearest neighbours of a particle were determined, which could be further improved if a fast (12 kHz) scanner was used, as in Fig. 8.2. The white dashed lines in Fig. 8.6d-e indicate the BCC unit cell, shown in Fig. 8.6c.

Accurate determination of particle positions and orientations over larger areas allows for detailed study of the 3D structure in real-space and for calculation of quantities such as the spatial orientation correlation function.

8.4. Discussion

Because the rods studied here are quite long and their aspect ratio is quite high, we expect that switchable plastic crystals can be obtained with a broad range of other monodisperse anisotropic particles in combination with sufficiently long-range charged repulsions. Such repulsions can be achieved in a large range of solvents but should be accessible also in water for anisotropic particles of a smaller size. It is quite clear that the systems studied here were not yet optimized for applications. For instance, clear improvements in switching speed by going to smaller rods and a much more marked photonic switching will be possible, for instance, with gold rods, which are known to have two strongly different plasmonic resonances excitable by changing the orientation of the rods [336]. As another example, rod-like superparticles built up from nanorods with strongly anisotropic luminescent light emission have recently been realized as well [337]. Results on other rod-like systems have already indicated that at lower electric field frequencies a phase diagram as studied here will become richer as a result of strong coupling of the double layers to the external field [338]. Finally, the demonstrated ability to quantitatively analyse rotations on the single particle level in strongly interacting systems will no doubt lead to new insights into the role played by rotations in fundamental processes such as crystallization and the glass transition.

8.5. Acknowledgements

This work was done in collaboration with Bing Liu, Michiel Hermes and Ahmet Demirörs. Bing Liu performed particle synthesis and the work on the state diagram and the switching of the plastic crystals. We thank Anke Kuijk, Bo Peng and Anand Yethiraj for helpful discussion.

9

Plastic Glass to Crystal Transition in a System of Long-Range Repulsive Rods

ABSTRACT

We demonstrate that when the volume fraction of a suspension of long-range repulsive silica rods is increased above a critical value ($\phi \sim 0.015$), the system fails to crystallize into a plastic crystal phase. Instead, a plastic glass was found. In this phase, particles lacked long-ranged positional order and translational motion was frozen-in, whereas rotational motion remained almost free. This phenomenon is a remarkable demonstration of the decoupling of the glass transitions associated with the positional and rotational degrees of freedom. Moreover, this glassy phase could completely crystallize into a stretched body-centered-cubic (bcc) lattice upon application of an AC electric field. Intriguingly, when the field was turned off, the crystal became unstable and the system returned to the plastic glass phase. The ability to follow the 3D rotations of the particles quantitatively in real-space gives unprecedented possibilities to study this new type of glass transition and its connection to crystallization.

9.1. INTRODUCTION

When a liquid is slowly cooled below its melting point, it may crystallize. However, if the temperature decrease is fast enough, the liquid can bypass crystallization and forms instead a *supercooled liquid*, which is metastable since the thermodynamically stable state is a crystal. If the cooling is fast enough, the viscosity increases dramatically upon further cooling, until it can be considered an amorphous solid, known as a *glass*. How dramatic the viscosity changes, depends on the fragility of the material. Liquid that are very sensitive to changes in temperature are known as 'fragile' glass formers, whereas liquids that are much less sensitive to temperature changes are known as 'strong' glass formers. The formation of a glass happens at the glass transition temperature T_g and the transition of a material that approaches T_g from $T > T_g$ is known as the *glass transition* [339]. Although glasses are ubiquitous in nature, many aspects of glasses and the glass transition are far from understood and highly debated, and current theories, such as mode coupling theory (MCT), only partially explain experimental measurements [340]. This is why P.W. Anderson is often cited, who remarked that "the deepest and most interesting unsolved problem in solid state theory is probably the theory of the nature of glass and the glass transition." [341]. In recent years, colloids have proven to be a fruitful model system to study both glasses and the glass transition. See Ref. 342 for a general overview and for an in-depth comparison between molecular and colloidal glasses. Hard-sphere colloids in particular have been used as the standard model system and, combined with confocal microscopy, allowed for pivotal study of colloidal glasses on the particle level [46, 58, 59]. Later, also other types of particles have been used such as hydrogel particles, which interact via a soft repulsion [343, 344], or more complex systems such as colloids combined with polymers which results in an attraction between the particles [345]. Recently, glasses composed of spherical particles with a long-range repulsive Yukawa potential were studied both experimentally [346], and with computer simulation [347] and revealed that the structure of these 'soft glasses' was remarkably similar to the structure of their hard-sphere counterparts. Interestingly, studies on both hydrogel particles and spheres with a long-range repulsive Yukawa potential showed that these 'soft particles' form stronger glasses than hard particles [343, 347]. Apart from particle interaction, both MCT and simulations have shown that shape anisotropy deeply modifies the nature of the glass transition [348–351]. Experimentally, anisotropic particles with a (nearly) hard repulsive potential have been used to study the effect of shape on the glass transition [176, 255, 329]. Zheng *et al.* used ellipsoidal particles in a quasi-2D configuration combined with bright-field microscopy and found a two-step glass transition where the rotational degrees of freedom freeze in first (as a function of density), followed by the translational degrees of freedom. In between these two transitions, they found an *orientational glass*, which has frozen-in rotational motion while the center-of-mass motion remained ergodic [177, 352]. A similar two-step glass transition was found with ellipsoidal particles that were repulsive as well as attractive [178]. Highly charged and thin rods, in the form of *fd*-viruses, exhibit a glass transition far beyond the isotropic-nematic coexistence region

[353, 354]. Although these studies with *fd*-viruses are one of the few examples of a glass transition study of rod-like particles with a long-ranged potential, they cannot be resolved individually and therefore do not provide information on the particle level. As far as we know, the only glass-transition study of anisotropic particles in 3D real-space has been performed by Edmond *et al.*, who used tetrahedral clusters as tracers in a host of a colloidal supercooled fluid of hard-sphere particles [167]. The researchers showed that rotational and translation diffusion decouple while approaching the glass transition point; the rotational diffusion remained coupled with the viscosity for the full range of volume fractions, whereas the translational diffusion decoupled for high enough volume fractions. However, experimental real-space studies on the glass transition of particles that form *plastic crystals* in equilibrium, remain absent. We therefore used our system of long-ranged repulsive rod-like particles, that forms equilibrium plastic crystals [186], to investigate particle diffusion when the volume fraction is increased towards the glass transition point. From a theoretical point of view, a plastic crystal (or rotator phase) of infinitely thin hard needles has been proposed as an ideal model system to study the dynamics of the orientational glass transition [330]. Neutron scattering experiments on ethanol confirmed the presence of such a transition in a molecular system [355].

In this chapter, we demonstrate that our system fails to crystallize above a certain volume fraction. However, surprisingly, the particles form a *plastic glass*; in this phase, rotational motion is almost free while translational motion becomes glassy. This phase can therefore be considered as the inverse of the previously described orientational glass. We demonstrate that the plastic glass can reversibly crystallize when an electric field is applied to the sample. Finally, we analyse both structure and dynamics of this transition in detail as a function of electric field strength.

9.2. METHODS

9.2.1. Particle synthesis

Fluorescent silica rod-like particles were synthesized as described in Chapter 2. The particles were dyed using fluorescein isothiocyanate (FITC, isomer I, 90%, Sigma-Aldrich). The particles consisted of a three layered structure: a non-fluorescent core, an FITC labelled shell (*ca.* 40 nm) and a non-fluorescent outer shell (*ca.* 100 nm). In the second step, we modified the silica rods with octadecyltrimethoxysilane (OTMOS, 90%, Sigma-Aldrich) by an ultrasonic-assisted coating procedure. In brief, a solution of OTMOS, butylamine (BA, 99.5%, Sigma-Aldrich) and dried toluene (1:1:10 v/v/v) was prepared, and then 10 wt% of silica rods, that had been dried under nitrogen flow, were added to this solution. The suspension was sonicated at 30 - 55 °C for 4 hours (Branson 2250). Afterwards, the colloidal rods were washed in turn with toluene, cyclohexane and cyclohexylchloride (CHC, > 98%, Merck). Finally, the colloidal rods were dispersed in deionized CHC for further use. The particles used in this chapter had an end-to-end length $l = 2.29$ μm ($\delta = 6.0\%$), diameter $d = 600$ nm ($\delta = 6.5\%$), and aspect ratio $l/d = 3.8$. Here, l and d are the mean length and diameter and δ is the polydispersity (standard deviation divided by the mean).

9.2.2. Sample preparation & Electric field setup

The particles were suspended in cyclohexyl chloride (CHC). The as received CHC (conductivity $\gg$ 1.000 pS/cm) was deionized by using molecular sieves (0.4 nm, Aldrich) and activated aluminium oxide (Aldrich). After purification, the CHC had a conductivity as low as 5 - 10 pS/cm. In this solvent, the particles acquired a negative charge (surface potential -70 mV) and a Debye screening length $\kappa^{-1} \sim 5$ μm (see Chapter 8 for details). The sample was concentrated to a volume fraction $\phi \sim 0.02$ by either sedimentation under gravity or by centrifugation with a maximum of 60 g. Rectangular fused quartz capillaries (0.1 × 2 mm^2 and 0.2 × 2 mm^2, VitroCom, UK) were used as sample cells. Electrodes consisting of a 3 nm layer of Cr and a 6 - 10 nm layer of Au were sputter-coated on two opposing outer surfaces of these capillaries. Thermocouple alloy wires (diameter 50 μm, Goodfellow) were connected to the electrodes with silverpaint (SPI-paint). The ends of the wires were wrapped around standard electronic wires that in turn were connected to the electrical set-up. We used a function generator (Agilent 33120A) to generate a sinusoidal signal with a frequency of 1 MHz and an amplitude of 2.0 V (peak-to-peak). This signal was sent to the sample via a wide band amplifier (Krohn-Hite, 7602M) used to vary the field strength in the sample. The field strength was measured with a digital phosphor oscilloscope (Tektronix TDS3052). We applied a high frequency AC field to prevent polarization of the electric double layer of the particles. After filling the capillaries, they were fixed on a glass slide and sealed with UV-cured glue (Norland, No. 68).

9.2.3. Electric field calculation

Because the electrodes were on the outside of the capillaries, there were three layers of material between the two electrodes. In this case, the field strength is given by [281]

$$E = \frac{V}{\epsilon_0}\left(\frac{\epsilon_1\epsilon_2\epsilon_3}{d_1\epsilon_2\epsilon_3 + d_2\epsilon_1\epsilon_3 + d_3\epsilon_1\epsilon_2}\right) \tag{9.1}$$

with V the applied voltage, ϵ_0 the dielectric constant of the sample, $\epsilon_{1,-3}$ the dielectric constant of layers 1-3 and d_{1-3} the thickness of layers 1-3. In our experiments, layer 1 and 3 are the glass capillary walls, (thickness $d \sim 0.1$ mm and $\epsilon = 3.5$) and layer 2 is (primarily) the solvent CHC (thickness $d \sim 0.1$ mm and $\epsilon = 7.6$). The field strength is thus given by $E = 1.9 \times 10^{-3}\, V$ (V/μm). All field strengths in this chapter are given in units V$_{RMS}$/μm.

9.2.4. Confocal microscopy measurements

Particles were imaged using a confocal microscope (Leica SP8) equipped with a fast 12 kHz resonant scanner and a GaAsP hybrid detector (Leica HyD^{TM}). Images with 8-bit pixel-depth were acquired using a white light laser with a selected wavelength of 488 nm. A confocal glycerol immersion objective 63x/1.3 (Leica) was used, which is optimized for refractive index $n_D = 1.45$ [91]. To avoid hydrodynamic interactions with the wall, particles were imaged at least 20 μm deep into the sample. To investigate the 3D structure of the suspensions, data stacks were recorded with typical dimensions of

512 × 256 × 120 pixels^3 with voxel size 160 × 160 × 321 nm^3, corresponding to 82 × 41 × 39 μm^3, which were recorded with a frame-rate of 0.3 fps. To track the 3D particle motion, data-stacks were acquired with typical dimensions of 512 × 65 × 25 pixels^3 with voxel size 160 × 160 × 321 nm^3, corresponding to a volume of 82 × 10 × 8 μm^3. The frame-rate for recording these 3D volumes was typically 4 fps. 2D confocal microscopy images had dimensions of 512 × 512 pixels^2 and pixel size of 150 × 150 nm^2, corresponding to typically 75 × 75 μm^2. The 2D images were recorded with a frame-rate of 2 - 20 fps.

9.2.5. Analysis of static structure

Radial distribution function. To determine the average static structure in our samples, we calculated the radial distribution function $g(r)$. For a given particle, this function describes the probability of finding another particle a distance r away and is given by

$$g(r) = \frac{1}{\rho^2}\langle\sum_{i=1}^{N}\sum_{j\neq i}^{N}\delta(\mathbf{r}_i)\delta(\mathbf{r}_j - \mathbf{r})\rangle \tag{9.2}$$

with δ the Dirac delta function, ρ the bulk number density and the angular brackets denoting an ensemble average. N is the total number of particles in the system. The distribution is normalized such that $g(r \to \infty) = 1$.

Nematic order parameter. To quantify the 3D orientational order we calculated the 3D nematic order parameter defined by

$$S_{3D} = \frac{3}{2}\langle\cos^2\theta\rangle - \frac{1}{2}, \tag{9.3}$$

with θ the angle between the main axis of the rod $\hat{\mathbf{u}}$ and the nematic director $\hat{\mathbf{n}}$. We find S_{3D} and $\hat{\mathbf{n}}$ by calculating the largest eigenvalue and corresponding eigenvector of the standard 3 × 3 nematic order parameter tensor

$$Q^{3D}_{\alpha\beta} = \frac{1}{N}\sum_{i=1}^{N}\left(\frac{3\,u_{i\alpha}u_{i\beta} - \delta_{\alpha\beta}}{2}\right), \tag{9.4}$$

with $u_{i\alpha}$ the α-component of the unit vector pointing along the main axis of particle i and $\alpha = x, y, z$.

Hexagonal bond order parameter. To quantify the 2D positional order we used the local hexagonal bond-orientational order parameter ψ_{6_k} given by

$$\psi_{6_k} = \frac{1}{n_c(k)}\sum_{j=1}^{n_c(k)}\exp(i6\theta(\mathbf{r}_{jk})) \tag{9.5}$$

with $n_c(k)$ the number of neighbors of particle k (which is taken to be the number of particles that are within a certain cut-off distance r_c of the particle), $\mathbf{r}_{jk}$ the vector connecting particle k and its neighbour j, $\theta(\mathbf{r}_{jk})$ the angle between $\mathbf{r}_{jk}$ and an arbitrary reference axis and i in the exponent the imaginary unit. In a perfect hexagonal layer, the angles $\theta(\mathbf{r}_{jk})$ are multiples of 60° and $|\psi_{6_k}| = 1$.

Voronoi cell construction. The Voronoi cell of a particle contains all the points in space that are closer to the particle than to any other particle in the system. For monodisperse particles these cells consist of flat faces and straight edges, called polyhedra. We used a publicly available Voronoi software library (Voro++ [356]) to calculate 3D Voronoi cells, the number of Voronoi nearest neigbours, the number of edges per Voronoi face and the average Voronoi cell volume.

9.2.6. Analysis of particle dynamics

To study the particle dynamics, we applied our particle-fitting algorithm to time-series of 3D confocal microscopy data-stacks, as described in detail in Chapter 4. We calculated the mean squared displacement (MSD) given by

$$\Delta\mathbf{r}^2(t) \equiv \langle|\mathbf{r}(t) - \mathbf{r}(0)|^2\rangle, \tag{9.6}$$

which we fitted to the expression

$$\Delta\mathbf{r}^2(t) = 6\,D_t\,t + 6\,\epsilon_t^2, \tag{9.7}$$

with D_t the rotationally averaged translational diffusion coefficient and ϵ_t the error in measurement of each of the coordinates of the particle [193].

We projected the displacements to the particle body-frame using the expressions [195]

$$\langle\Delta\mathbf{r}_{\parallel}{}^2(t)\rangle \equiv \langle|[\mathbf{r}(t) - \mathbf{r}(0)] \cdot \hat{\mathbf{u}}(0)|^2\rangle = 2\,D_{\parallel}\,t + 2\,\epsilon_{\parallel}^2, \tag{9.8}$$

$$\langle\Delta\mathbf{r}_{\perp}{}^2(t)\rangle \equiv \langle|[\mathbf{r}(t) - \mathbf{r}(0)] \times \hat{\mathbf{u}}(0)|^2\rangle = 4\,D_{\perp}\,t + 4\,\epsilon_{\perp}^2, \tag{9.9}$$

with $D_{\parallel}$ the parallel and $D_{\perp}$ the perpendicular translational diffusion coefficient, which are related to the rotationally averaged translational diffusion coefficient via the equation

$$D_t = (D_{\parallel} + 2D_{\perp})/3. \tag{9.10}$$

To quantify the rotational motion of the particles, we calculated the orientation autocorrelation function

$$C(t) = \langle\hat{\mathbf{u}}(0) \cdot \hat{\mathbf{u}}(t)\rangle \tag{9.11}$$

which we fitted with a stretched exponential function, given by

$$C(t) = (1 - \epsilon_r^2)\exp(-(t/\tau_r)^{\beta}) \tag{9.12}$$

with ϵ_r the measurement error in the determination of the direction of the main axis of the rods, τ_r the typical orientation relaxation time and β the Kohlrausch exponent. At infinite dilution we have $\beta = 1$ and $\tau_r = 1/(2\,D_r)$ with D_r the rotational diffusion coefficient [194].

9.2.7. Expressions for the diffusion coefficients at infinite dilution

To compare our measurements with diffusion coefficients valid for $\lim_{\phi\to 0}$, we used the analytical expressions for hard cylinders at infinite dilution, as proposed by Tirado, Martinez and de la Torre [198],

$$D_\perp^0 = \frac{k_B T}{4\pi\,\eta\,l}(\log p + \delta_\perp), \tag{9.13}$$

$$D_\parallel^0 = \frac{k_B T}{2\pi\,\eta\,l}(\log p + \delta_\parallel), \tag{9.14}$$

$$D_t^0 = \frac{2}{3}D_\perp + \frac{1}{3}D_\parallel, \tag{9.15}$$

$$D_r^0 = \frac{3k_B T}{\pi\,\eta\,l^3}(\log p + \delta_r), \tag{9.16}$$

with η the solvent viscosity, $p = l/d$ the aspect ratio of the particle and δ_i a correction term for the finite aspect ratio of the cylinders, given by [198]

$$\delta_\perp = 0.839 + 0.185/p + 0.233/p^2, \tag{9.17}$$

$$\delta_\parallel = -0.207 + 0.980/p - 0.133/p^2, \tag{9.18}$$

$$\delta_r = -0.662 + 0.917/p - 0.050/p^2. \tag{9.19}$$

Substituting $l = 2.29$ μm, $p = 3.8$ and $\eta = 1.5$ cP, results in $D_t^0 = 0.23$ μm^2/s, $D_\parallel^0 = 0.26$ μm^2/s, $D_\perp^0 = 0.21$ μm^2/s and $D_r^0 = 0.20$ rad^2/s and $\tau_R^0 = 2.5$ s.

9.3. RESULTS

9.3.1. Plastic glass phase

When the volume fraction of the suspension of long-ranged repulsive silica rods exceeded approximately $\phi = 0.015$, the system failed to crystallize into a plastic crystal (see Ref. 186 and Chapter 8), but instead formed a ‘plastic glass’. This phase lacked long-ranged positional order, as can be clearly seen in Fig. 9.1a for a suspension with $\phi \sim 0.02$. The particles were caged by their neighbours, and therefore translational motion was slowed down dramatically, whereas rotational motion remained almost free. This is illustrated by the superposition of 125 frames, measured over a time-interval $\Delta t = 12.5$ s, in Fig. 9.1b. This time interval corresponds to $\Delta t = 5\,\tau_r^0$, with τ_r^0 the orientation relaxation time at infinite dilution, or equivalently to $\Delta t = 48\,\tau_t^0$, with τ_t^0 the time for the rod to diffuse over its own diameter at infinite dilution.

On longer time-scales, however, there were significant positional rearrangements in the sample. These rearrangements are indicated in Fig. 9.1c, which shows an intensity average over 2000 frames, corresponding to a time interval of $\Delta t = 200.0$ s. Expressed in units of relaxation times at infinite dilution, this time interval is given by $\Delta t = 79\,\tau_r^0$ or $\Delta t = 757\,\tau_t^0$. In Fig. 9.1c, particles with low mobility appear as spherical spots, whereas the local rearrangements resulted in blurred lines. It is clear that the dynamics in the system were spatially heterogeneous, reminiscent of the dynamical heterogeneities observed in suspensions of hard spheres on approach of the glass transition [58, 59].

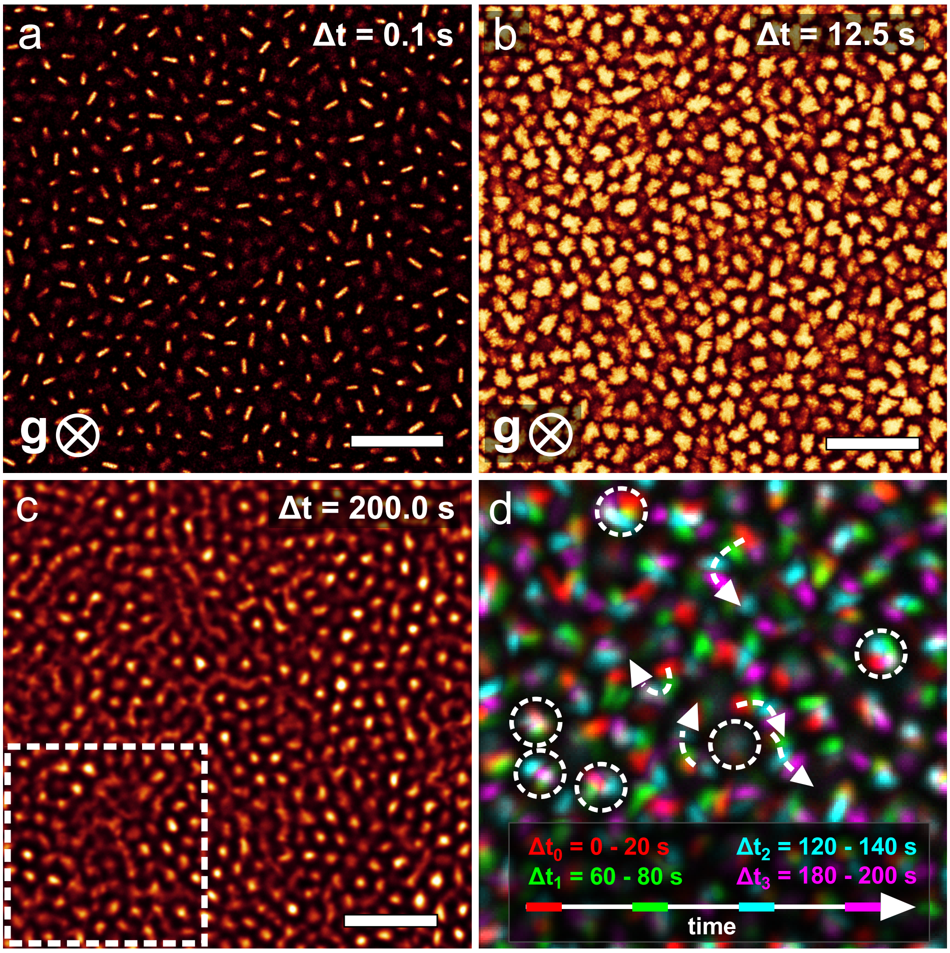

Figure 9.1. A 'plastic glass' phase of long-ranged repulsive rods. The volume fraction $\phi \sim 0.02$, which is higher than the volume fraction where a plastic crystal phase becomes stable. (a) A single confocal microscopy snapshot shows the absence of long-ranged positional order. (b) A maximum projection of 125 individual images, measured over 12.5 s, shows that although there was significant rotational motion, the rods were positionally caged during this time interval. (c) An average of 2000 frames, measured over 200 s, shows that there were spatially heterogeneous rearrangements during this time interval. (d) Close-up of the region indicated in (c) with the (white) dashed line. The colours correspond to averages over time-intervals of 20 s (as indicated in the figure). The dotted circles indicate particles with low mobility, whereas the dashed arrows indicate particles with high mobility. All scale bars are 15 μm.

Fig. 9.1d shows a close-up of the region indicated with the white dashed line in Fig. 9.1c. The colours correspond to averages over time-intervals of $\Delta t = 20$ s (as indicated in the figure). The dotted circles indicate particles with low mobility, whereas the dashed arrows indicate local (collective) rearrangements of particles with higher mobility. We found that these collective rearrangements occurred often in a circular motion, or loop, around a less mobile particle. Due to these rearrangements, the average translational motion was not completely frozen-in and therefore this phase can be described as a supercooled plastic liquid close to the glass transition. We however prefer the term 'plastic glass' and will use this terminology in the rest of this chapter.

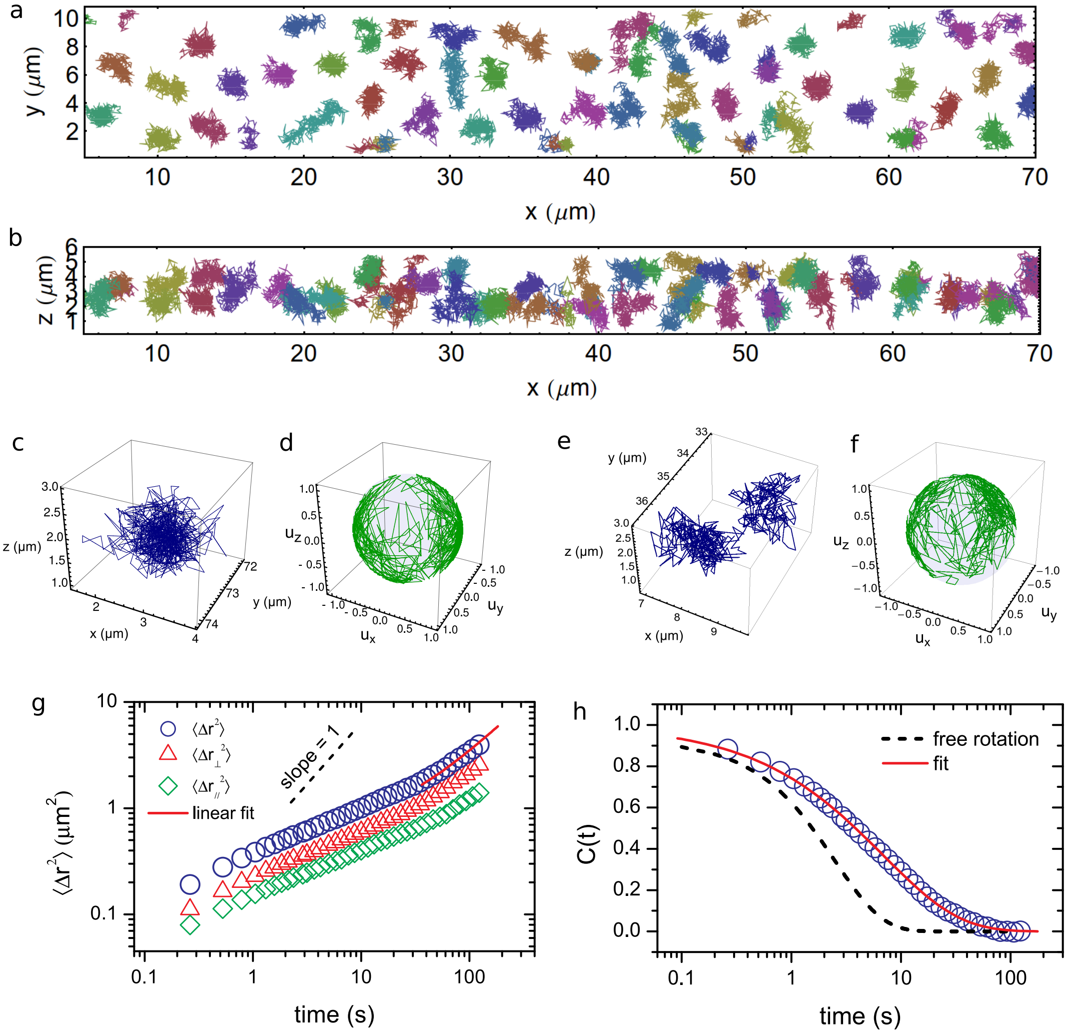

FIGURE 9.2. 3D quantitative analysis of the dynamics in the 'plastic glass' phase. (a) xy- and (b) xz-projections of the translational trajectories of the rods. (c) Positional and (d) rotational trajectory of a particle that remained caged during the time of the experiment. (e) Positional and (f) rotational trajectory of a particle that escaped its cage. (g) The mean squared displacement. Parallel and perpendicular components as indicated in the figure. The (black) dashed line has unity slope, the (red) continuous line is a linear fit for $t > 80$ s and was used to extract a value for the rotationally averaged diffusion coefficient $D_t/D_t^0 = 0.016$. (h) The orientation correlation function. The (black) dashed line is for free rotation, the (red) continuous line is a fit to equation (9.12), resulting in $\tau_r^0/\tau_r = 0.36$ and $\beta = 0.63$.

In Fig. 9.2, we show results of a quantitative 3D analysis of the plastic glass. We tracked approximately 150 particles over 526 s. Projections of the individual translational trajectories in the xy-plane (Fig. 9.2a) and xz-plane (Fig. 9.2b) over a time interval of 132 s confirm that particle motion was strongly confined. However, particle trajectories were often irregularly shaped and elongated, which was due to the local structure and the local rearrangements. A translational trajectory and corresponding rotational trajectory of a particle that remained caged during the time of the experiment is shown in Fig. 9.2c and Fig. 9.2d respectively. In Fig. 9.2e, a translational trajectory in shown of a particle that escaped its cage and Fig. 9.2f shows its corresponding rotational trajectory. Notice that although Fig. 9.2d and Fig. 9.2f indicate significant rotational motion, not all angles were visited with equal probability.

To quantify the average translational motion, we calculated the rotationally averaged mean squared displacement (MSD), as shown in Fig. 9.2g, as well as the parallel $\langle \Delta \mathbf{r}_{\|}^2 \rangle$ and perpendicular $\langle \Delta \mathbf{r}_{\perp}^2 \rangle$ components. Although the MSD does not show a pronounced plateau, the slope at intermediate time-scale is significantly lower than unity ($\Delta \mathbf{r}^2 \sim t^{0.42}$ for 5 s $< t <$ 12 s). The lack of a pronounced plateau is possibly due to the extreme long-range repulsions (or softness) in the system. Fitting the MSD to equation (9.7) for $t >$ 80 s (indicated by the red line in Fig. 9.2g) resulted in $D_t/D_t^0 = 0.016$, which indicates that the translational diffusion at that time-interval was slowed down by two orders of magnitude compared to the diffusion at infinite dilution. For $t >$ 80 s, we measured that $\Delta \mathbf{r}^2 \sim t^{0.66}$ indicating that the process was still sub-diffusive.

The rotational motion, however, was much less hindered. We calculated the orientation auto-correlation function $C(t)$. A fit to expression (9.12) resulted in $\tau_r^0/\tau_r = 0.36$ and $\beta = 0.63$, indicating that the rotational motion was slowed down by only a factor of 3 and not yet ‘glassy’ or frozen-in. This means that there is an order of magnitude difference in the slowing down of the translational and rotational motion of these soft rod-like particles, which is a remarkable example of strong decoupling of the glass transitions of the positional and rotational degrees of freedom.

9.3.2. Reversible electric field switch

Although the plastic glass described in the previous section lacks long-ranged order, it is possible to induce complete crystallization of the sample, with particles aligned and on a 3D lattice, by applying a high frequency AC electric field. It is quite intriguing, however, that when the field is turned off, the crystal returns to the plastic glass phase. This transition is illustrated in Fig. 9.3 and in Supporting Movies 1-2 in Appendix B.4.

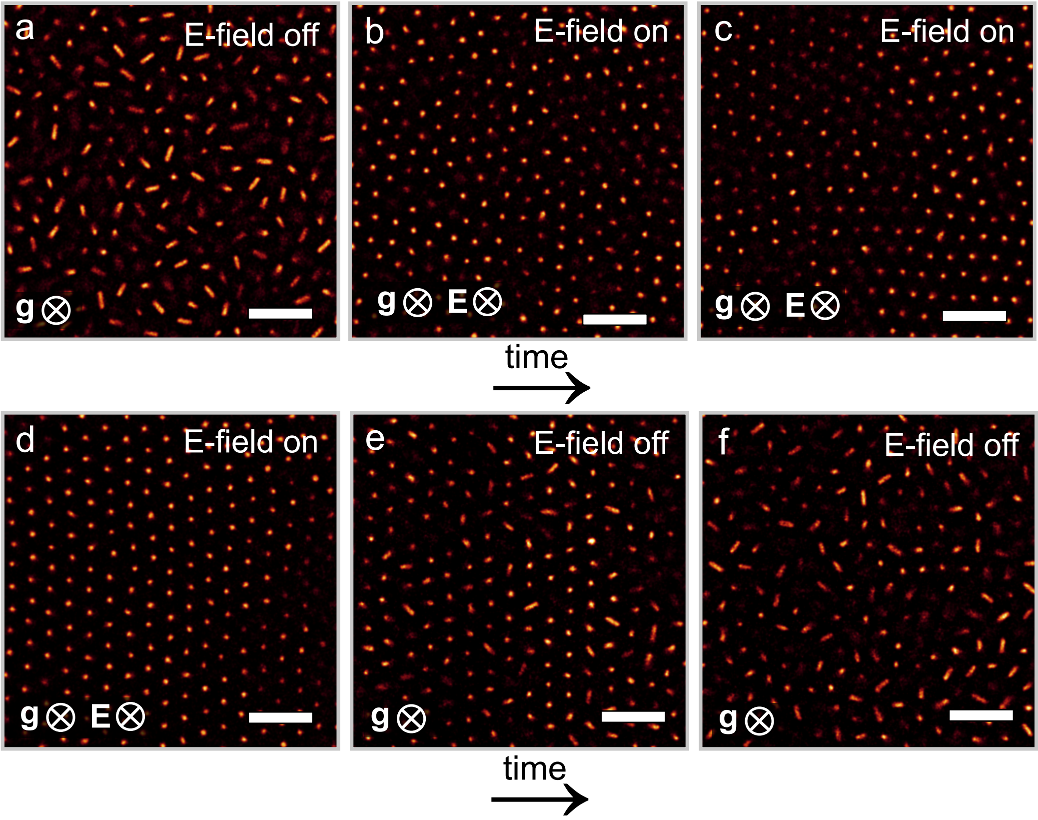

FIGURE 9.3. Reversible switching between a plastic glass and a crystal. (a) Particles rotated, though they were positionally 'caged' without any long-ranged positional order. (b) Directly after application of an AC electric field ($E = 90$ V/mm, turned on by hand in ~ 5 s), particles aligned with the field. (c) Ordered clusters were formed that grew larger in time. (d) After 40 min the sample was fully crystalline. (e) Directly after the field had been turned off, an intermediate plastic crystal-like phase was observed. (f) After ~ 2 min, the long-ranged positional order was lost, particle orientations became random and the particles remained positionally caged. All scale-bars are 10 μm.

Initially, the field was off (Fig. 9.3a) and particles could rotate significantly (see also Fig. 9.2). When the AC electric field (1 MHz, $E = 90$ V/mm) was increased to full strength in ~ 5 s, all particles aligned immediately with the field direction (Fig. 9.3b). Because the positions were still disordered, this can be seen as a *plastic glass* $\rightarrow$ *glass* transition. Within minutes, positionally ordered clusters started to form and grew larger as a function of time, see the bottom right corner in Fig. 9.3c. After approximately 40 minutes, the sample was completely crystalline (Fig. 9.3d), completing this nucleation-and-growth type of transition from *glass → crystal.* Directly after the field had been turned off (Fig. 9.3e), some particles started to rotate, although not uniformly at all, while the crystalline lattice was still preserved, resulting in a *crystal → plastic crystal* transition. However, the plastic-crystal lattice remained stable for only a brief period of time ($\sim$ 2 min), after which all long-ranged order disappeared and rotational motion increased, resulting in a final *plastic crystal → plastic glass* transition.

9.3.3. 3D structure analysis of the plastic glass and the crystal phase

Before we analyse the dynamics of the plastic glass to crystal transition, we first show results of the 3D static structure of both phases. Figs. 9.4a,b show a 3D reconstruction of the plastic glass, obtained from confocal microscopy data. The total volume of the data stack was $50 \times 50 \times 48$ μm^3, containing 2567 particles. The colours in Figs. 9.4a,b correspond to the 3D orientation of the particles. The orientation distribution in Fig. 9.4c shows that all angles were accessible with, on average, equal probability, i.e. there was no average orientational order in the system. Figs. 9.4d,e show a 3D reconstruction of a crystalline phase that was formed under application of an electric field of $E = 90$ V/mm. The volume of the data stack was $45 \times 46 \times 41$ μm^3, containing 2379 particles. The particles ordered into a body centred cubic (bcc) phase that was elongated in the field (z) direction. A view from the bcc(110) plane (Fig. 9.4d) shows the large inter-particle spacing and the long-ranged 3D crystalline order. The view from the bcc(100) plane (Fig. 9.4e) shows that there is a significant elongation in the field (z) direction. For a perfect bcc lattice, the (red) dashed diamond should be a square. We measured inscribed angles of 76° and 104°, corresponding to an elongation factor in the z-direction of 1.28. The strong alignment of the particles is indicated by the orientation distribution of the particles in Fig. 9.4f.

Results on the calculation of the radial distribution function $g(r/l)$ are shown in Fig. 9.5, with the average end-to-end length of the rods $l = 2.29$ μm. The green line in Fig. 9.5a corresponds to the plastic glass and indicates the liquid-like order of this phase. The position of the first peak indicates the large inter-particle spacing ($r = 1.5\,l$), which is due to the long-range repulsion between the rods. The red line corresponds to the crystalline phase, formed under application of an electric field of $E = 90$ V/mm. The inter-particle spacing remained approximately the same ($r = 1.4\,l$), however, the well-defined peaks correspond (to a large extent) with the black peaks of a perfect bcc latice. The subtle mismatch with a perfect bcc lattice is due to the elongation in the z-direction. The blue line in Fig. 9.5b shows the same data for the crystalline phase but with all z coordinates scaled with 0.75, which resulted in the best fit with the perfect bcc lattice (in steps of 0.05).

In Appendix A, we estimated the strength of the dipole-dipole interactions in our system of long-ranged repulsive rods, for various particle configurations and field strengths E, which can also be found in the Supplementary Information of Ref. 186. For particles aligned by an electric field $E = 90$ V/mm, we found an average inter-particle distance

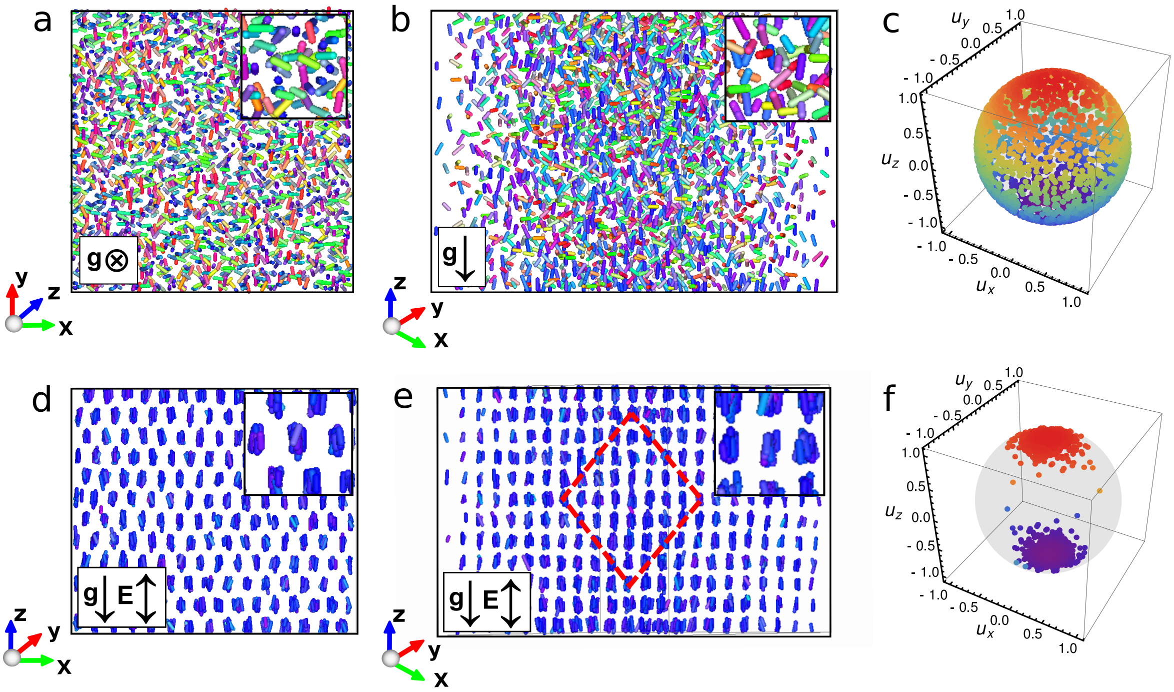

FIGURE 9.4. Static structure of the plastic glass and the crystalline phase. (a-b) 3D reconstruction of a plastic glass phase and (d-e) of the crystalline phase, obtained from 3D confocal microscopy data analysis. Particles are color-coded according to their orientation. (c) The orientation distribution of the particles in the plastic glass phase shows that all angles are accessible, with equal probability. (d-e) Crystalline phase formed under application of an electric field $E = 90$ V/mm. The particles formed a body centered cubic (bcc) phase that was elongated in the field (z) direction. (d) View from the bcc(110) plane. (e) The view from the bcc(100) plane shows that there is a significant elongation in the field (z) direction. For a perfect bcc lattice, the (red) dashed diamond should be a square. (f) The distribution of the orientations of the particles in the crystalline phase indicates the alignment with the electric field.

of $r = 1.4\,l$, determined from the $g(r/l)$ of the crystalline phase in Fig. 9.5. For these two parameters, assuming completely aligned particles, the dipole-dipole interaction is much smaller than k_BT. This demonstrates that the contribution of the dipole-dipole interactions to the stability of the crystal phase can be neglected. The elongation of the bcc lattice along the field direction must therefore be completely due to the anisotropy of the particle and its electrostatic repulsive potential. Calculations based on rod-like particles with a screened Yukawa potential should give further insight into the observed phenomenon, which is left for future research.

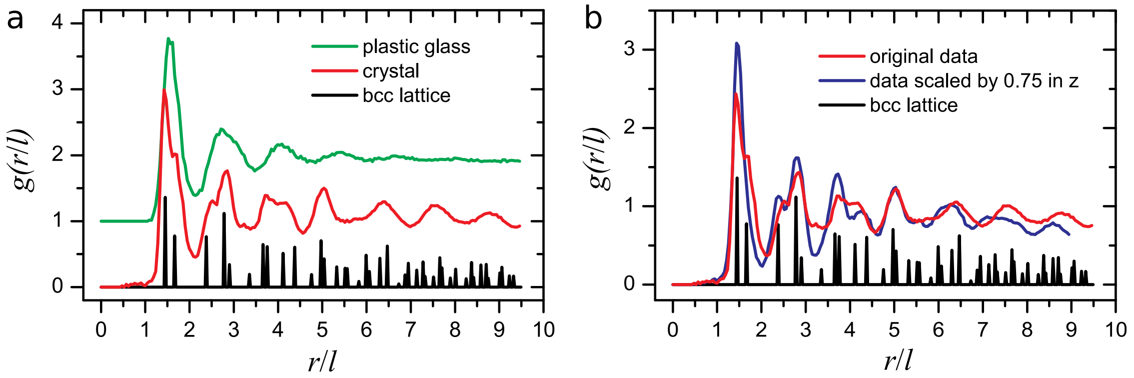

FIGURE 9.5. 3D radial distribution functions $g(r/l)$, with the end-to-end length of the particle $l = 2.29$ μm. (a) The green line corresponds to the plastic glass, with no field applied. The red line is for a crystalline phase formed under application of an electric field $E = 90$ V/mm. Notice the large inter-particle spacing (first peak positioned at $1.4\,l$), the long-ranged order in the sample and the subtle mismatch with the perfect bcc lattice. (b) 3D radial distribution function for the original data of the crystal (red) and the same data with all z-coordinates scaled by 0.75 (blue)

The final analysis that we performed on the 3D structures is based on a calculation of Voronoi cells, shown in Fig. 9.6. The particles in the plastic glass had on average 14 Voronoi nearest neighbours (Fig. 9.6a) and Voronoi faces with on average 5 edges (Fig. 9.6b), representing the number of particles surrounding a near-neighbour bond. These two distributions are almost identical to the distributions of a glass consisting of hard spheres [46] or spheres with a long-range repulsive potential [346, 347]. During the transition to a crystal, the distribution of Voronoi neighbours became strongly peaked, however, an average number of 14 remained (Fig. 9.6c). Additionally, the distribution of the edges per Voronoi face was split into two peaks positioned at 4 and 6 (Fig. 9.6d). These values correspond well with the Voronoi cell of a perfect bcc crystal-lattice which is a truncated octahedron. A schematic of a truncated octahedron is shown in Fig. 9.6e, which shows that it contains 6 faces with 4 edges and 8 faces with 6 edges. Although the number of nearest neighbours stayed constant during the transition, we will later show in more detail that the transition proceeded via a heterogeneous, nucleation-and-growth type of process.

Finally, we determined the distribution of the Voronoi cell volumes, shown in Fig. 9.6f. The distribution of the crystal is narrower but its average (34.9 ± 0.02 μm^3) is close to the value for the glass (34.3 ± 0.03 μm^3). Using the hard-core particle dimensions (as measured with TEM), both values correspond to a volume fraction of $\phi = 0.017$. This value is indeed higher than the range of volume fractions where a plastic-crystal phase was found (see Chapter 8 and Ref. 186). Interestingly, if we assume for a rotating particle in the glass phase an 'effective spherical particle volume' with diameter $d_{\text{eff}} \approx 1.5\,l$ (based on the first peak in the $g(r)$, see Fig. 9.5a), we find $\phi_{\text{eff}} \approx 0.59$, a value remarkably close to the glass transition volume fraction for hard-spheres.

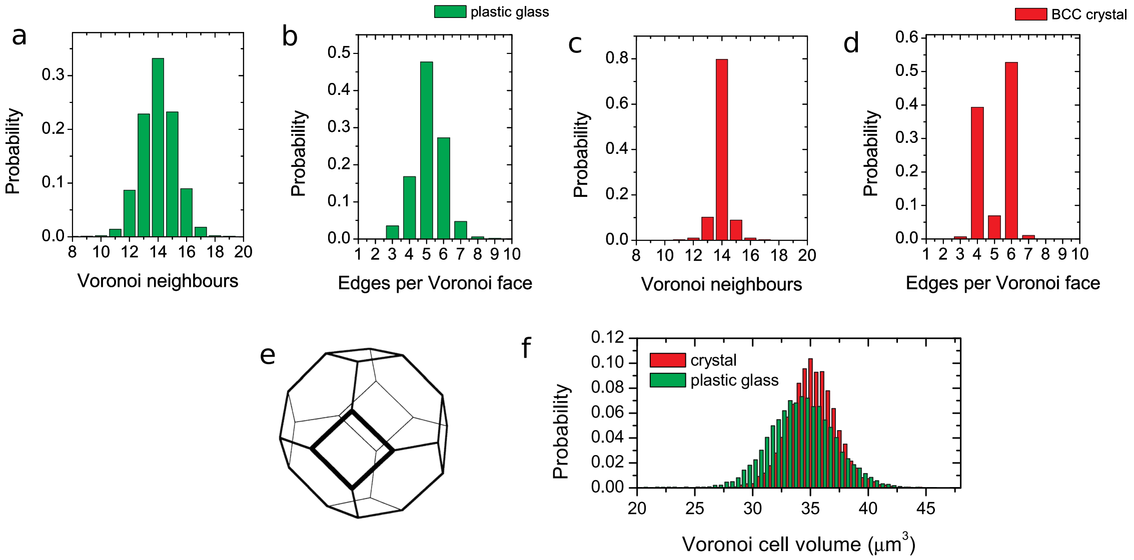

FIGURE 9.6. 3D Voronoi analysis. (a-b) The distribution of the plastic glass has on average 14 Voronoi neighbours and Voronoi faces with on average 5 edges. (c-d) The number of neighbours of the crystal is strongly peaked at 14 and the number of edges peaked at 4 and 6, which is in correspondence with the Voronoi cell of a perfect bcc crystal, i.e. a truncated octahedron (e). (f) Distribution of the Voronoi cell volume, which is inversely proportional to the local particle volume fraction. The distribution of the crystal is narrower but its average (34.9 ± 0.02 μm^3) is close to the value for the glass (34.3 ± 0.03 μm^3). Using the hard-core particle dimensions, these values correspond to a volume fraction of approximately $\phi = 0.017$.

9.3.4. Plastic glass to crystal transition as a function of electric field strength

We will now focus our attention to the reversibility of the transition between the plastic glass and the crystal as a function of field strength. Fig. 9.7 shows a step wise up-ramp in electric field strength in steps of 22.5 V/mm. The duration of each measurement was 141 s and the time interval between measurements was 4 min. Figs. 9.7b-e show that upon increasing the electric field strength, positional order increased. For the highest field strength (Fig. 9.7e, E = 90 V/mm), the particles were strongly aligned with the field direction and particles locally ordered into a regular 3D lattice. However, the sample was poly-crystalline over larger distances (approximately 100 μm) and, additionally, small unordered domains still existed. We therefore let the sample equilibrate for approximately 1 hour under a constant field strength of E = 90 V/mm. During this time interval, the sample became completely crystalline. Before we discuss the results on the crystallization (and coarsening of domains) during this 1 hour time-interval (shown in Fig. 9.11), we will show results on the changes in the system when the field was turned down again (in the same number of steps as the up-ramp), indicated in Fig. 9.8. Notice that it is already clear from comparing Fig. 9.7e and Fig. 9.8a (both under constant field strength E = 90 V/mm but with the 1 hour time-interval between them) that positional order increased significantly.

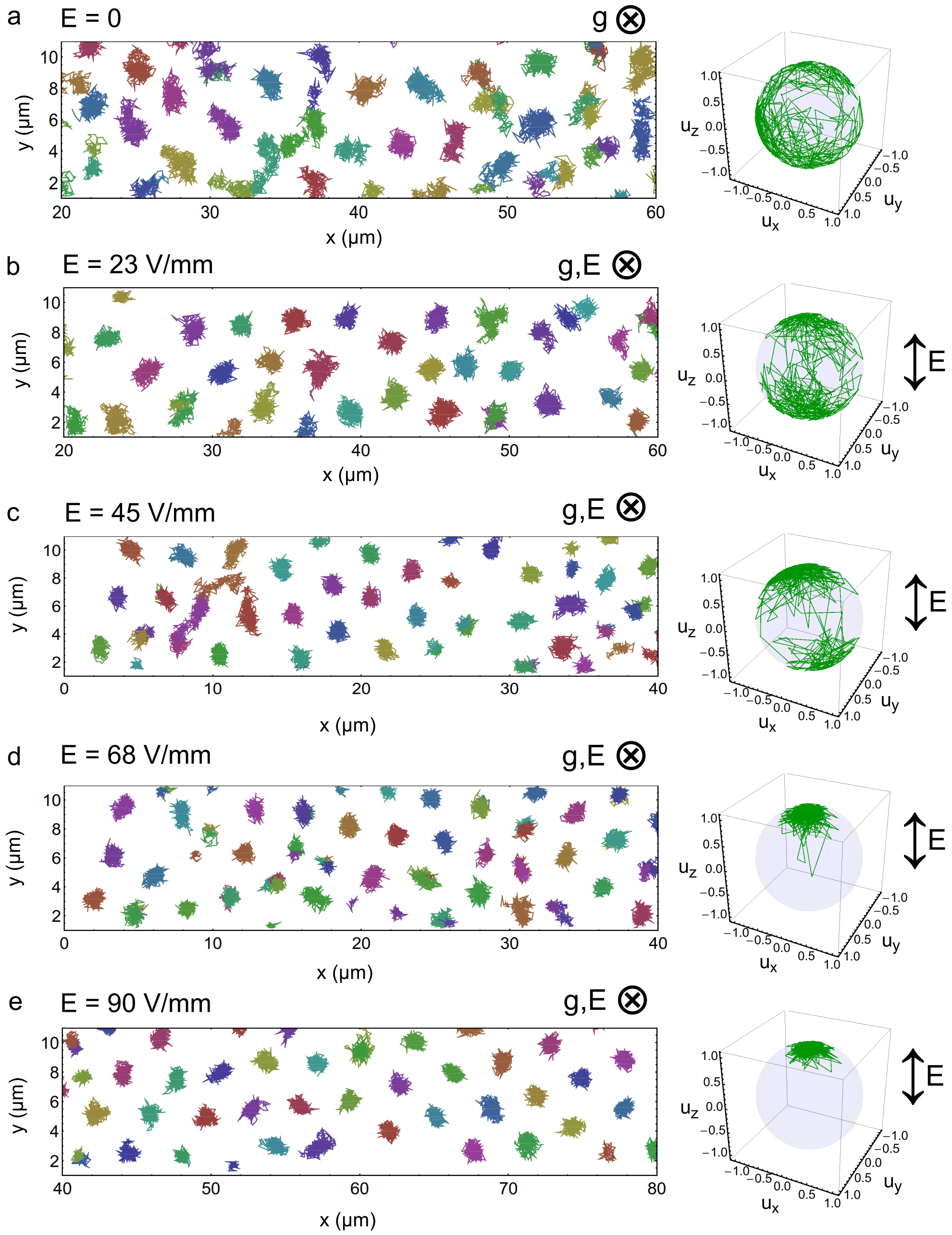

FIGURE 9.7. Electric field induced transition from a plastic glass phase to a crystalline phase. The duration of each measurement was 141 s and the time interval between measurements was 4 min. The left shows projections of the 3D translational trajectories in the xy-plane. The right shows a typical rotational trajectory of a single particle. (a) Plastic glass phase. (b) Weak alignment of the particles with the field. (c) Some rotational motion was still possible, local regions with higher positional order started to appear. (d) Strong alignment of the particles, however complete crystalline order was not yet present. (e) Ordered domains of particles were present.

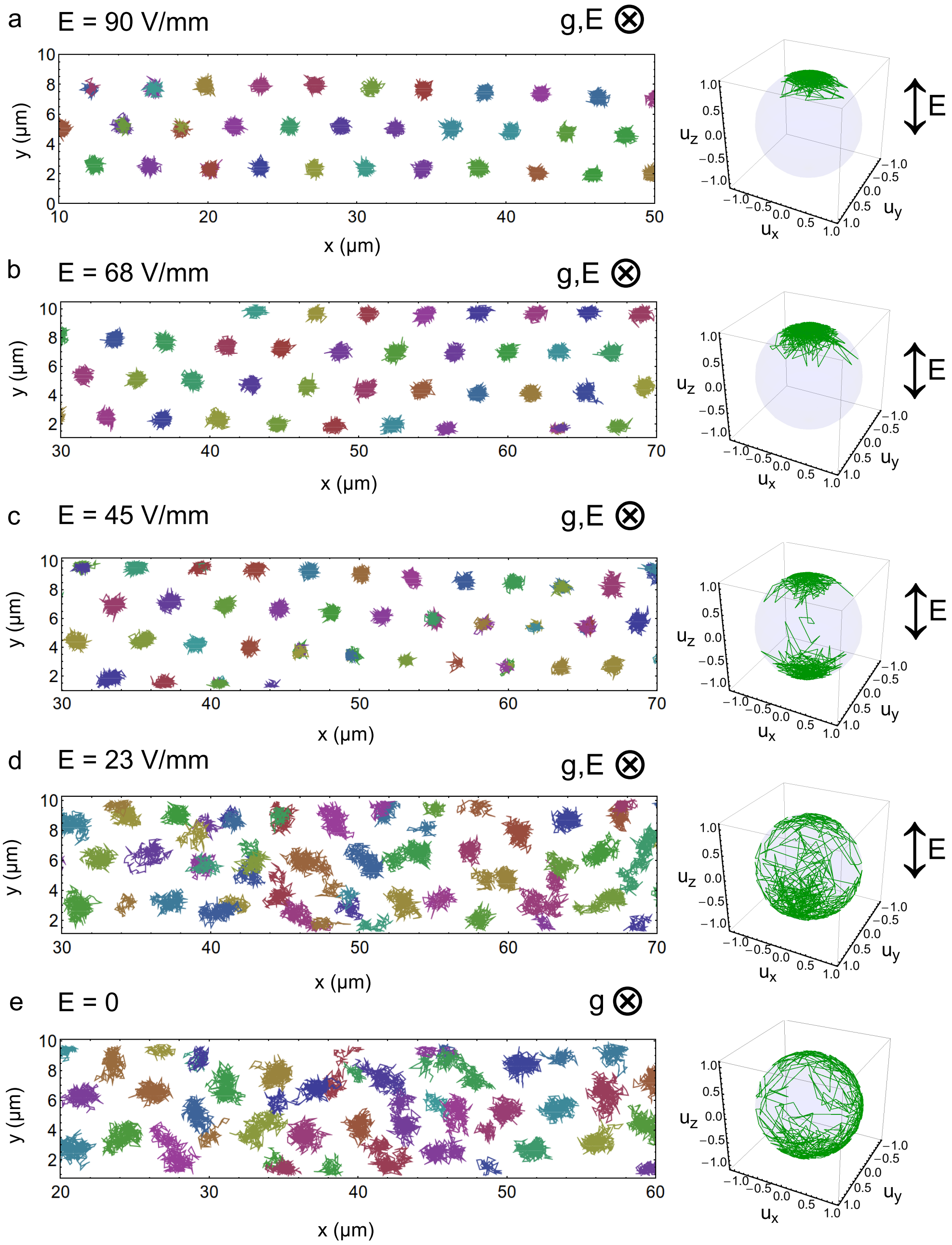

FIGURE 9.8. Electric field induced transition from a crystalline phase to a plastic glass phase. The duration of each measurement was 141s and the time interval between measurements was 4 min. The left shows projections of the 3D translational trajectories in the *xy*-plane. The right shows a typical rotational trajectory of a single particle. (a) Particles were aligned with the field direction and the sample was completely crystalline. (b) Crystalline order still persisted upon lowering the field strength. (c) Intermediate plastic crystal phase. (d) Significant particle rotation was possible at this field strength and the crystalline lattice disappeared completely. (e) The sample was again in the plastic glass phase.

Starting form the fully crystalline state (Fig. 9.8a), the electric field strength was lowered in steps and particles regained their rotational freedom. Eventually, the crystalline lattice became unstable until it completely disappeared (Fig. 9.8e) and the system returned to the plastic glass phase. For an electric field strength $E = 45$ V/mm (Fig. 9.8c), short-ranged positional order was still present while particles were able to rotate significantly, i.e. there was an intermediate plastic-crystal phase present. Notice that this plastic-crystal phase was not observed during the up-ramp (Fig. 9.7c). When the field strength was further lowered to $E = 23$ V/mm (Fig. 9.8d), rotational motion significantly increased and the crystal lattice became unstable.

For each of the 3D data sets illustrated in Fig. 9.7 and Fig. 9.8, we calculated the nematic order parameter S_{3D}, the rotational relaxation time τ_r, the average local hexagonal bond-order parameter $\langle|\psi_6|\rangle$ and the translational diffusion coefficient D_t. The results are summarized in Fig. 9.9. The normalized translational diffusion coefficient D_t/D_t^0 was determined from a fit to equation (9.7) in the intermediate diffusion regime (between $\Delta t = 7$ s and $\Delta t = 16$ s), which corresponds to either the motion of the particle in its cage or to the motion around its lattice position for particles in a plastic

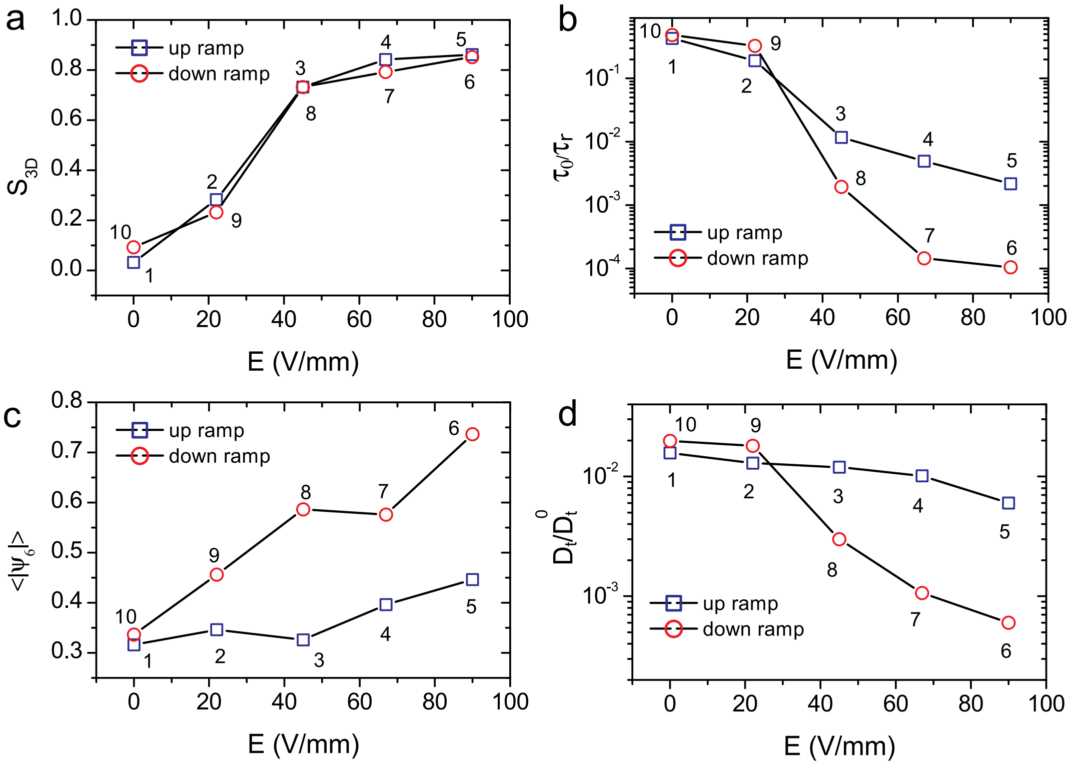

FIGURE 9.9. Reversible electric field switching (in stages) between a plastic glass phase and a crystalline phase. There was 4 min between each measurement, except between point 5 and 6, which was approximately 1 hour. (a) Nematic order parameter S_{3D}. (b) Rotational relaxation time τ_0/τ_r. (c) Average local hexagonal bond-order parameter $\langle|\psi_6|\rangle$. (d) Intermediate rotationally averaged diffusion coefficient D_t/D_t^0.

glass or a crystalline phase respectively. The normalized (inverse) rotational relaxation time τ_0/τ_r was obtained from a fit to equation (9.12). The bond-order parameter ψ_6 was determined from the xy-coordinates of particles in a thin 3D volume (perpendicular to the field) with $\Delta z = 4.5$ μm, which corresponds approximately to the first minimum in the $g(r)$ of both the glassy phase and crystalline phase (Fig. 9.5a).

Fig. 9.9a shows that during the up-ramp, particles became aligned. The largest increase in particle alignment was between step 2 and 3 (E = 23 V/mm to E = 45 V/mm) where the nematic order parameter S_{3D} increased from 0.22 to 0.72. This increase was accompanied by an order of magnitude decrease of the rotational correlation time (Fig. 9.9b). The rotational motion further decreased as a function of field strength, however, when the field was turned down again, there was a strong hysteresis effect in the rotational relaxation times (Fig. 9.9b). This effect cannot be explained by field alignment alone, since the orientational order in the system did not show any hysteresis (Fig. 9.9a). The reason for it is that the positional structure also changed as a function of field strength (and time). Upon application of the field, particles aligned and started to order, indicated by the increase of $\langle|\psi_6|\rangle$ during the up-ramp (Fig. 9.9c). The increase in positional order was accompanied by a decrease in both translational motion (Fig. 9.9d) and rotational motion (Fig. 9.9b). However, notice that the rotational relaxation time τ_0/τ_r (Fig. 9.9b) drops one order of magnitude between step 2 and 3 (E = 23 V/mm and E = 45 V/mm), which is distinctly different from its translational counterpart, which stays almost constant at that point. Between point 5 and 6, there was 1 hour of equilibration time during which the sample became fully crystalline, explaining the large increase in $\langle|\psi_6|\rangle$ at constant field strength (Fig. 9.9c). This resulted in significant hysteresis in all the parameters except for the nematic order parameter (Fig. 9.9a). In contrast with the up-ramp, there was now a metastable plastic crystal phase at step 8 (E = 45 V/mm). When the field was decreased from E = 45 V/mm to E = 23 V/mm (step 8 to 9), rotational motion increased two orders of magnitude (Fig. 9.9b) and the plastic crystalline lattice melted almost completely (Fig. 9.9c). This step was also accompanied by the strongest increase in translational motion (one order of magnitude).

To summarize, we can conclude that upon stepwise increase of an electric field, particles aligned first and then started to order positionally. This process was accompanied by a decrease of more than one order of magnitude in both translational and rotation motion. However, the crystallization process was not completed until approximately 1 hour, resulting in strong hysteresis in both translational and rotational motion when the field was turned down again. When the field strength dropped below approximately E = 45 V/mm, the (plastic) crystalline lattice became unstable, and completely melted within minutes, returning to its original plastic glassy state.

In Fig. 9.10 we further illustrate another characteristic of the electric-field induced transition. Fig. 9.10a shows that the x, y and z components of the mean squared displacement (MSD) for particles in the plastic glass phase are equal, i.e. translational motion, as measured in the laboratory-frame, was isotropic. In the fully crystalline phase (formed under field strength $E = 90$ V/mm), the MSD reached a distinct plateau after ~ 5 s (indicating that particles were confined to a lattice), however, there was a clear difference between the plateau values perpendicular to the field ($\alpha_\perp = \sqrt{\langle \Delta x^2 \rangle} = 0.31$ μm or $\alpha_\perp = \sqrt{\langle \Delta y^2 \rangle} = 0.30$ μm) and parallel to the field ($\alpha_\parallel = \sqrt{\langle \Delta z^2 \rangle} = 0.37$ μm). The ratio $\alpha_\parallel / \alpha_\perp = 1.19 - 1.23$ seems to agree with the elongation of the bcc lattice in the z-direction (see Fig. 9.4e). The average vibrational amplitude $\sqrt{\langle \Delta r^2 \rangle / 2}$ was 0.40 μm (see Chapter 8 for the explanation of the factor 2), which is 13% of the inter-particle spacing of 3.2 μm and is due to the softness of the crystal.

To monitor the anisotropy in the diffusion (along the field direction) as a function of field strength, we calculated the ratio of the MSD displacement in the z and x directions after a fixed time-interval $\tau = 16$ s, given by $\langle \Delta z^2 \rangle_\tau / \langle \Delta x^2 \rangle_\tau$. We used this quantity because at lower field strength, where there were no well defined crystalline lattices, the plateau values in the MSD were also not well defined. Fig. 9.10c shows that during the

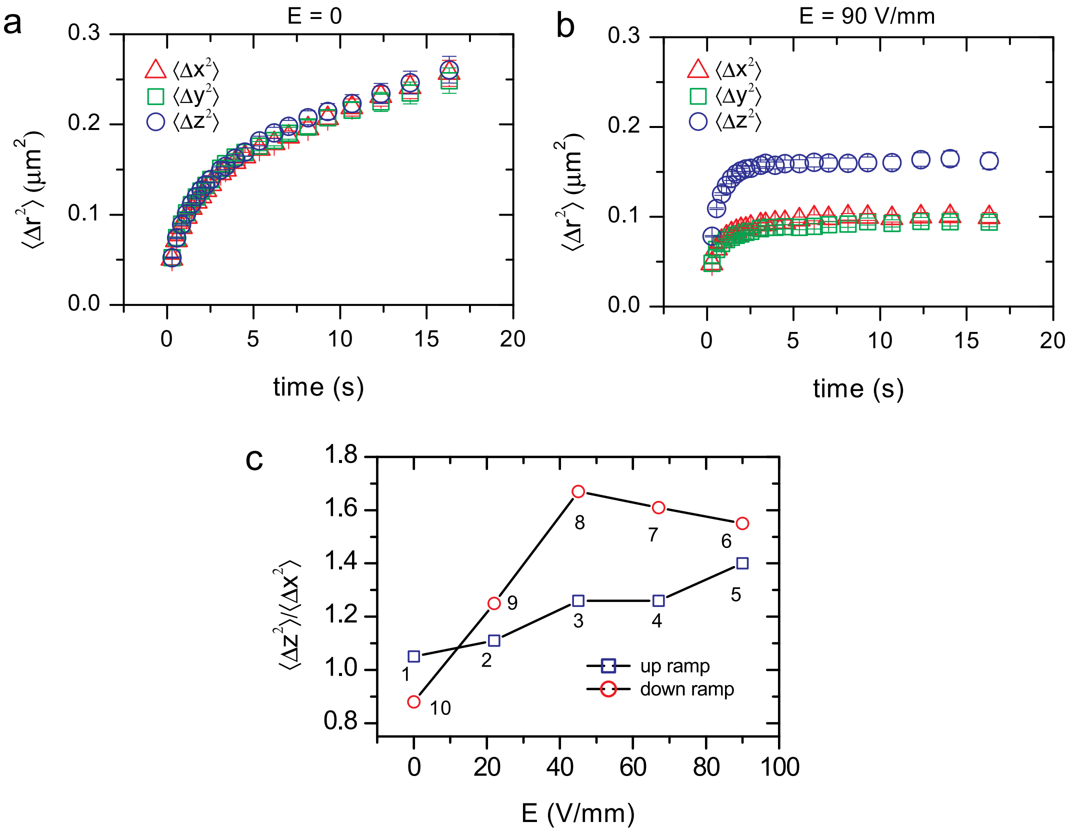

FIGURE 9.10. Anisotropic diffusion in the crystalline phases. The x, y and z components of the mean squared displacement (MSD) are shown for (a) the plastic glass phase ($E = 0$) and (b) the crystalline phase ($E = 90$ V/mm). The ratio of the plateau values in the crystalline phase $\sqrt{\langle \Delta z^2 \rangle / \langle \Delta y^2 \rangle} = 1.23$ seems to correspond with the elongation of the crystalline lattice in the z-direction (see Fig.9.4e). (c) Ratio of the MSD displacement in the z and x direction ($\langle \Delta z^2 \rangle_\tau / \langle \Delta x^2 \rangle_\tau$) with $\tau = 16$ s.

down-ramp (step 6 to 8), this quantity first increased, until the lattice became unstable (between step 8 and 9) after which we found isotropic diffusion again.

Finally, we show some details on the crystallization process at constant electric field strength. Fig. 9.11 shows image sequences of the crystallization process after the field had been increased in steps of 22.5 V/mm to a final field strength of $E = 90$ V/mm, as shown in Fig. 9.7. Figs. 9.11a-d show superpositions of 200 xy confocal microscopy images each (measured over 100 s). The total time time between Fig. 9.11a and Fig. 9.11d was 28 min. Because the images were acquired under application of constant electric field $E = 90$ V/mm, all particles were strongly aligned with the field (perpendicular to the page). Initially, regions with high positional order and regions with less positional order were found to exist together (Fig. 9.11a). Over time, the highly ordered regions grew larger and coarsened until the sample was completely crystalline (Fig. 9.11d). The crystallization process thus seemed to proceed via a nucleation-and-growth type of mechanism. Figs. 9.11e-h show close-ups of local positional rearrangements during the crystallization process, both in the more disordered and in the crystalline phase. Similar to the rearrangements in the (unaligned) plastic glass phase (Fig. 9.1d), the

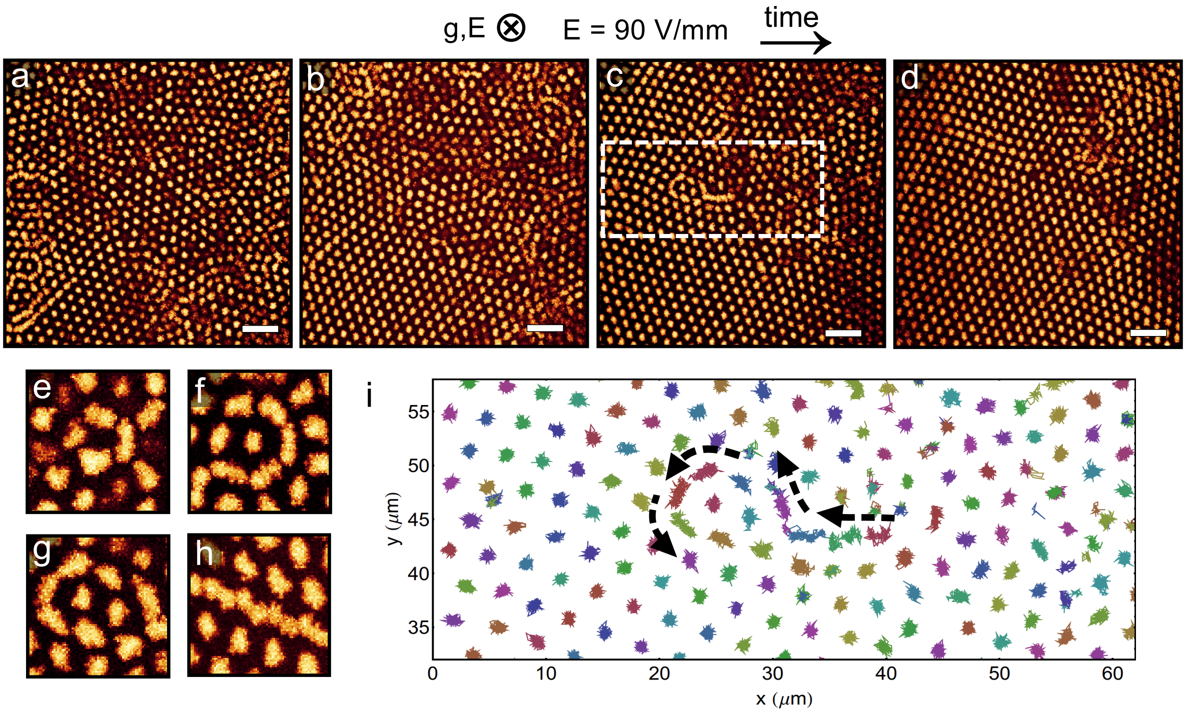

FIGURE 9.11. Crystallization after the electric field was step-wise increased to $E = 90$ V/mm. (a-d) Superpositions of 200 xy confocal microscopy images measured over 100 s. The total time between (a) and (d) is 28 min. All scalebars are 10 μm. (e-h) Close-up of local rearrangements in both disordered and ordered regions. (i) Positional trajectories of particles, from the region indicated by the white dashed line in (c), obtained after 2D particle tracking (total duration 100 s). The local rearrangement (loop) is clearly visible.

rearrangements in the less ordered regions (Figs. 9.11e-g) were often found to occur in a (circular) loop. The rearrangements in the highly ordered (or crystalline) regions (Fig. 9.11h) were along the lattice direction of the crystal. Fig. 9.11i shows the projected particle trajectories from the region indicated by the white dashed line in Fig. 9.11c. The rearrangement loop, close to the disordered-ordered ‘interface’ is clearly visible.

9.4. Conclusion

We demonstrated that when the volume fraction of a suspension of long-ranged repulsive silica rods is increased above a critical value ($\phi \sim 0.015$), the system failed to crystallize into a plastic crystal phase. Instead of forming an orientational glass, a *plastic glass* was found. Particles lacked long-ranged positional order and translational motion was slowed down by two orders of magnitude, whereas rotational motion remained almost free, which is a remarkable demonstration of the decoupling of the glass transitions of the positional and rotational degrees of freedom. Interestingly, this plastic glass phase could be switched reversibly to a fully ordered crystal upon application of a high frequency AC electric field. Upon stepwise increase of the field strength, particles in the plastic glass phase aligned with the field direction first and then started to crystallize. The crystallization process resembled a nucleation-and-growth type of mechanism and was not completed until approximately 1 hour. During this process, both translational and rotational motion decreased by more than one order of magnitude. We determined that the particles ordered into a stretched *bcc* crystalline lattice, which was elongated in the electric field direction by $\sim 25\%$. When the field strength was decreased in steps again, strong hysteresis and a metastable plastic crystal phase were found. When the field strength dropped below approximately $E = 45$ V/mm, the crystalline lattice became unstable, and completely melted within minutes, returning to its original plastic glassy state again. Apparently, the crystal is destabilized by free particle rotations, and a plastic crystal is unstable with respect to a plastic glass.

The ability to follow the 3D rotations of the particles quantitatively in real-space gives unprecedented possibilities to study this new type of glass transition. Although we determined that the dipole-dipole interactions are almost negligible, future work is needed to better understand the stability of both phases, such as the contribution of the anisotropic repulsive potential and the entropy, as well as (metastable) dynamical phenomena such as the collective rearrangements and a possible coupling between translational motion, rotational motion and positional order (as a function of volume fraction).

9.5. Acknowledgements

This work was done in collaboration with Bing Liu and Michiel Hermes. We thank Laura Filion and Zdenek Preisler for useful discussion. We also thank Laura Filion for critical reading of this chapter.

Bibliography

[1] Graham, T. Liquid diffusion applied to analysis. *Philos. Trans. R. Soc. London*, 151:183, 1861.

[2] Larson, R. *The Structure and Rheology of Complex Fluids*. Oxford University Press, 1999.

[3] Brown, R. A brief account of microscopical observations made in the months of June, July and August, 1827, on the particles contained in the pollen of plants; and on the general existence of active molecules in organic and inorganic bodies. *Philos. Mag.*, 4:161–173, 1828.

[4] Einstein, A. Über die von der molekularkinetischen Theorie der Wärme geforderte Bewegung von in ruhenden Flüssigkeiten suspendierten Teilchen. *Ann. Phys.*, 322(8):549–560, 1905.

[5] Perrin, J. Mouvement brownien et réalité moléculaire. *Ann. Chim. Phys.*, 18:5–114, 1909.

[6] Perrin, J. *Atoms*. Constable & Company Ltd, 1916.

[7] Alder, B.J. and Wainwright, T.E. Phase Transition for a Hard Sphere System. *J. Chem. Phys.*, 27(5):1208, 1957.

[8] Hoover, W.G. and Ree, F.H. Melting transition and communal entropy for hard spheres. *J. Chem. Phys.*, 49(8):3609, 1968.

[9] Pusey, P.N. and van Megen, W. Phase behaviour of concentrated suspensions of nearly hard colloidal spheres. *Nature*, 320(6060):340–342, 1986.

[10] van Blaaderen, A. and Vrij, A. Synthesis and characterization of colloidal dispersions of fluorescent, monodisperse silica spheres. *Langmuir*, 8(12):2921–2931, 1992.

[11] Royall, C.P., Poon, W.C.K., and Weeks, E.R. In search of colloidal hard spheres. *Soft Matter*, 9(1):17, 2013.

[12] Yethiraj, A. and van Blaaderen, A. A colloidal model system with an interaction tunable from hard sphere to soft and dipolar. *Nature*, 421(6922):513–517, 2003.

[13] van Blaaderen, A., Peetermans, J., Maret, G., and Dhont, J.K.G. Long-time self-diffusion of spherical colloidal particles measured with fluorescence recovery after photobleaching. *J. Chem. Phys.*, 96(6):4591–4603, 1992.

[14] Hoogenboom, J.P., Vergeer, P., and van Blaaderen, A. A real-space analysis of colloidal crystallization in a gravitational field at a flat bottom wall. *J. Chem. Phys.*, 119(6):3371, 2003.

[15] Poon, W.C.K., Weeks, E.R., and Royall, C.P. On measuring colloidal volume fractions. *Soft Matter*, 8(1):21, 2012.

[16] Sirota, E.B., Ou-Yang, H.D., Sinha, S.K., and Chaikin, P.M. Complete phase diagram of a charged colloidal system: A synchro-tron x-ray scattering study. *Phys. Rev. Lett.*, 62(13):1524–1527, 1989.

[17] Hynninen, A.P. and Dijkstra, M. Phase behavior of dipolar hard and soft spheres. *Phys. Rev. E*, 72(5):051402, 2005.

[18] Zocher, H. Über freiwillige Strukturbildung in Solen: eine neue Art anisotrop flüssiger Medien [Spontaneous structure formation in sols: a new kind of anisotropic liquid media]. *Z. Anorg. Allg. Chem.*, 147:91–110, 1925.

[19] Oster, G. Two-phase formation in solutions of tobacco mosaic virus and the problem of long-range forces. *J. Gen. Physiol.*, 33(3):445–473, 1950.

[20] de Gennes, P.G. and Prost, J. *The Physics of Liquid Crystals*. Oxford University Press, New York, 1993.

[21] Maeda, H. and Maeda, Y. Liquid Crystal Formation in Suspensions of Hard Rodlike Colloidal Particles: Direct Observation of Particle Arrangement and Self-Ordering Behavior. *Phys. Rev. Lett.*, 90(1):1–4, 2003.

[22] Johnson, P.M., van Kats, C.M., and van Blaaderen, A. Synthesis of colloidal silica dumbbells. *Langmuir*, 21(24):11510–11517, 2005.

[23] Lee, S.H., Song, Y., Hosein, I.D., and Liddell, C.M. Magnetically responsive and hollow colloids from nonspherical core-shell particles of peanut-like shape. *J. Mater. Chem.*, 19(3):350, 2009.

[24] Sacanna, S., Rossi, L., Kuipers, B.W.M., and Philipse, A.P. Fluorescent monodisperse silica ellipsoids for optical rotational diffusion studies. *Langmuir*, 22(4):1822–7, 2006.

[25] Kuijk, A., van Blaaderen, A., and Imhof, A. Synthesis of monodisperse, rodlike silica colloids with tunable aspect ratio. *J. Am. Chem. Soc.*, 133(8):2346–2349, 2011.

[26] Lettinga, M.P., Barry, E., and Dogic, Z. Self-diffusion of rod-like viruses in the nematic phase. *Europhys. Lett.*, 71(4):692–698, 2005.

[27] Lettinga, M. and Grelet, E. Self-Diffusion of Rodlike Viruses through Smectic Layers. *Phys. Rev. Lett.*, 99(19):197802, 2007.

[28] Kuijk, A., Byelov, D.V., Petukhov, A.V., van Blaaderen, A., and Imhof, A. Phase behavior of colloidal silica rods. *Faraday Discuss.*, 159:181–199, 2012.

[29] Grelet, E. Hard-Rod Behavior in Dense Mesophases of Semiflexible and Rigid Charged Viruses. *Phys. Rev. X*, V:1–8, 2014.

[30] Vermant, J. and Solomon, M.J. Flow-induced structure in colloidal suspensions. *J. Phys. Condens. Matter*, 17:R187–R216, 2005.

[31] Ackerson, B.J. Shear-Induced Order in Suspensions of Hard Spheres. *Phys. Rev. Lett.*, 61(8):1033, 1988.

[32] Ackerson, B.J. Shear induced order and shear processing of model hard sphere suspensions. *J. Rheol.*, 34(4):553, 1990.

[33] Baulin, V.A. and Khokhlov, A.R. Nematic ordering of rigid rods in a gravitational field. *Phys. Rev. E. Stat. Phys. Plasmas. Fluids. Relat. Interdiscip. Topics*, 60(3):2973–7, 1999.

[34] Hess, S. Fokker-Planck-Equation Approach to Flow Alignment in Liquid Crystals. *Z. Naturforsch.*, 31:1034–1037, 1976.

[35] Doi, M. and Edwards, S. *The Theory of Polymer Dynamics*. Oxford Univ. Press, Oxford, 1986.

[36] Lettinga, M.P. and Dhont, J.K.G. Non-equilibrium phase behaviour of rod-like viruses under shear flow. *J. Phys. Condens. Matter*, 16(38):S3929–S3939, 2004.

[37] Lettinga, M.P., Dogic, Z., Wang, H., and Vermant, J. Flow behavior of colloidal rodlike viruses in the nematic phase. *Langmuir*, 21(17):8048–57, 2005.

[38] Tao, Y.G., den Otter, W., and Briels, W. Kayaking and Wagging of Rods in Shear Flow. *Phys. Rev. Lett.*, 95(23):1–4, 2005.

[39] Tao, Y.G., den Otter, W.K., and Briels, W.J. Kayaking and wagging of liquid crystals under shear: Comparing director and mesogen motions. *EPL*, 86(5):56005, 2009.

[40] Leahy, B.D., Cheng, X., Ong, D.C., Liddell-Watson, C., and Cohen, I. Enhancing Rotational Diffusion Using Oscillatory Shear. *Phys. Rev. Lett.*, 110(22):228301, 2013.

[41] Kuijk, A., Troppenz, T., Filion, L., Imhof, A., van Roij, R., Dijkstra, M., and van Blaaderen, A. Effect of external electric fields on the phase behavior of colloidal silica rods. *Soft Matter*, 10:6249–6255, 2014.

[42] Kwaadgras, B.W., Besseling, T.H., Coopmans, T.J., Kuijk, A., Imhof, A., van Blaaderen, A., Dijkstra, M., and van Roij, R. Orientation of a dielectric rod near a planar electrode. *Phys. Chem. Chem. Phys.*, 2014.

[43] Demirörs, A.F., Johnson, P.M., van Kats, C.M., van Blaaderen, A., and Imhof, A. Directed self-assembly of colloidal dumbbells with an electric field. *Langmuir*, 26(18):14466–71, 2010.

[44] Shah, A.A., Kang, H., Kohlstedt, K.L., Ahn, K.H., Glotzer, S.C., Monroe, C.W., and Solomon, M.J. Liquid crystal order in colloidal suspensions of spheroidal particles by direct current electric field assembly. *Small*, 8(10):1551–62, 2012.

[45] Crocker, J.C. and Grier, D.G. Methods of digital video microscopy for colloidal studies. *J. Colloid Interface Sci.*, 179(1):298–310, 1996.

[46] van Blaaderen, A. and Wiltzius, P. Real-Space Structure of Colloidal Hard-Sphere Glasses. *Science*, 270(5239):1177–1179, 1995.

[47] Dassanayake, U., Fraden, S., and van Blaaderen, A. Structure of electrorheological fluids. *J. Chem. Phys.*, 112(8):3851–3858, 2000.

[48] Dinsmore, A.D., Weeks, E.R., Prasad, V., Levitt, A.C., and Weitz, D.A. Three-dimensional confocal microscopy of colloids. *Appl. Opt.*, 40(24):4152–4159, 2001.

[49] Lu, P.J., Sims, P.A., Oki, H., Macarthur, J.B., and Weitz, D.A. Target-locking acquisition with real-time confocal (TARC) microscopy. *Opt. Express*, 15(14):8702–8712, 2007.

[50] Jenkins, M.C. and Egelhaaf, S.U. Confocal microscopy of colloidal particles: towards reliable, optimum coordinates. *Adv. Colloid Interface Sci.*, 136(1-2):65–92, 2008.

[51] Gao, Y. and Kilfoil, M. Accurate detection and complete tracking of large populations of features in three dimensions. *Opt. Express*, 17(6):4685, 2009.

[52] Besseling, R., Isa, L., Weeks, E.R., and Poon, W.C. Quantitative imaging of colloidal flows. *Adv. Colloid Interface Sci.*, 146(1-2):1–17, 2009.

[53] Vissers, T., Imhof, A., Carrique, F., Delgado, A.V., and van Blaaderen, A. Electrophoresis of concentrated colloidal dispersions in low-polar solvents. *J. Colloid Interface Sci.*, 361(2):443–55, 2011.

[54] Kurita, R., Ruffner, D.B., and Weeks, E.R. Measuring the size of individual particles from three-dimensional imaging experiments. *Nat. Commun.*, 3:1127, 2012.

[55] Leocmach, M. and Tanaka, H. A novel particle tracking method with individual particle size measurement and its application to ordering in glassy hard sphere colloids. *Soft Matter*, 9(5):1447, 2013.

[56] Gasser, U., Weeks, E.R., Schofield, A., Pusey, P.N., and Weitz, D.A. Real-space imaging of nucleation and growth in colloidal crystallization. *Science*, 292(5515):258–262, 2001.

[57] Schall, P., Cohen, I., Weitz, D.A., and Spaepen, F. Visualization of dislocation dynamics in colloidal crystals. *Science*, 305(5692):1944–8, 2004.

[58] Kegel, W.K. and van Blaaderen, A. Direct Observation of Dynamical Heterogeneities in Colloidal Hard-Sphere Suspensions. *Science*, 287(5451):290–293, 2000.

[59] Weeks, E.R. Three-Dimensional Direct Imaging of Structural Relaxation Near the Colloidal Glass Transition. *Science*, 287(5453):627–631, 2000.

[60] Derks, D., Wisman, H., van Blaaderen, A., and Imhof, A. Confocal microscopy of colloidal dispersions in shear flow using a counter-rotating cone-plate shear cell. *J. Phys. Condens. Matter*, 16:3917–3928, 2004.

[61] Cohen, I., Davidovitch, B., Schofield, A.B., Brenner, M.P., and Weitz, D.A. Slip, Yield, and Bands in Colloidal Crystals under Oscillatory Shear. *Phys. Rev. Lett.*, 97(21):215502, 2006.

[62] Cheng, X., McCoy, J.H., Israelachvili, J.N., and Cohen, I. Imaging the microscopic structure of shear thinning and thickening colloidal suspensions. *Science*, 333(6047):1276–1279, 2011.

[63] Besseling, T.H., Hermes, M., Fortini, A., Dijkstra, M., Imhof, A., and van Blaaderen, A. Oscillatory shear-induced 3D crystalline order in colloidal hard-sphere fluids. *Soft Matter*, 8(26):6931–6939, 2012.

[64] Heston, W.M., Hennelly, E.J., and Smyth, C.P. Dielectric Constants, Viscosities, Densities, Refractive Indices and Dipole Moment Calculations for Some Organic Halides. *J. Am. Chem. Soc.*, 72:2071–2075, 1950.

[65] Zéberg-Mikkelsen, C.K., Barrouhou, M., Baylaucq, A., and Boned, C. Viscosity and density measurements of binary mixtures composed of methylcyclohexane + cis-decalin versus temperature and pressure. *Int. J. Thermophys.*, 24(2):361–374, 2003.

[66] Leunissen, M. *Manipulating Colloids with Charges & Electric Fields.* Ph.D. thesis, Utrecht University, 2007.

[67] Staudhammer, P. and Seyer, W.F. The Dielectric Constant of cis- and trans-Decahydronaphthalene and Cyclohexane as a Function of Temperature and Frequency. *J. Am. Chem. Soc.*, 80:6491–6494, 1958.

[68] Vissers, T. *Oppositely Charged Colloids Out of Equilibrium.* Ph.D. thesis, Utrecht University, 2010.

[69] Rodríguez, S., Lafuente, C., Cea, P., Royo, F.M., and Urieta, J.S. Densities and viscosities of binary mixtures of some cyclic ethers + chlorocyclohexane at 298.15 and 313.15 K. *J. Chem. Eng. Data*, 42:1285–1289, 1997.

[70] Crowe, R. and Smyth, C. The Dielectric and Polymorphic Behavior of Cyclohexanol, Cyclohexanone, Chlorocyclohexane and Cyclohexane. *J. Am. Chem. Soc.*, 73(11):5406–5411, 1951.

[71] Williams, J.W. The dielectric constants of binary mixtures. X. The electric moments of simple derivatives of cyclohexane and of dioxan. *J. Am. Chem. Soc.*, 52(5):1831–1837, 1930.

[72] Kuijk, A., Imhof, A., Verkuijlen, M.H.W., Besseling, T.H., van Eck, E.R.H., and van Blaaderen, A. Colloidal Silica Rods: Material Properties and Fluorescent Labeling. *Part. Part. Syst. Charact.*, 31(6):706–713, 2014.

[73] LeBel, R. and Goring, D. Density, Viscosity, Refractive Index, and Hygroscopicity of Mixtures of Water and Dimethyl Sulfoxide. *J. Chem. Eng. Data*, 7(1):100–101, 1962.

[74] Puranik, S.M., Kumbharkhane, A.C., and Mehrotra, S.C. Dielectric study of dimethyl sulfoxide-water mixtures using the time-domain technique. *J. Chem. Soc. Faraday Trans.*, 88(3):433, 1992.

[75] Glycerine Producers' Association. *Physical Properties of Glycerine and Its Solutions.* Gulf Publishing Company, 1967.

[76] Akerlof, G. Dielectric constants of some organic solvent-water mixtures at various temperatures. *J. Am. Chem. Soc.*, 54(11):4125–4139, 1932.

[77] Royall, C.P., Leunissen, M.E., and Blaaderen, A.V. A new colloidal model system to study long-range interactions quantitatively in real space. *J. Phys. Condens. Matter*, 15:3581–3596, 2003.

[78] Walden, P. Organic solvents and ionization media. III. Interior friction and its relation to conductivity. *Z. Phys. Chem.*, 55:207 – 249, 1906.

[79] Janz, G.J. and Danyluk, S.S. Conductances of Hydrogen Halides in Anhydrous Polar Organic Solvents. *Chem. Rev.*, 60:209–234, 1960.

[80] Bosma, G., Pathmamanoharan, C., de Hoog, E.H.A., Kegel, W.K., van Blaaderen, A., and Lekkerkerker, H.N.W. Preparation of monodisperse, fluorescent PMMA-latex colloids by dispersion polymerization. *J. Colloid Interface Sci.*, 245(2):292–300, 2002.

[81] Royall, C.P., Poon, W.C.K., and Weeks, E.R. In search of colloidal hard spheres. *Soft Matter*, 9(1), 2012.

[82] van Blaaderen, A., Ruel, R., and Wiltzius, P. Template-directed colloidal crystallization. *Nature*, 385(6614):321–324, 1997.

[83] Wilson, T. and Sheppard, C.J.R. *Theory and Practice of Scanning Optical Microscopy.* Academic Press, London, 1984.

[84] Pawley, J.E. *Handbook of Biological Confocal Microscopy.* Springer, Berlin, 3rd edition, 2006.

[85] Minksy, M. Microscopy apparatus. *U.S. Patent 3.013.467*, 1961.

[86] Brakenhoff, G.J., Blom, P., and Barends, P. Confocal scanning light microscopy with high aperture immersion lenses. *J. Microsc.*, 117:219–232, 1979.

[87] Carlsson, K. and Aslund, N. Confocal imaging for 3-D digital microscopy. *Appl. Opt.*, 26(16):3232–8, 1987.

[88] Hell, S., Reiner, G., Cremer, C., and Stelzer, E.H.K. Aberrations in confocal fluorescence microscopy induced by mismatches in refractive index. *J. Microsc.*, 169(3):391–405, 1993.

[89] Hell, S.W. Far-field optical nanoscopy. *Science*, 316(5828):1153–8, 2007.

[90] van der Voort, H.T.M. and Strasters, K.C. Restoration of confocal images for quantitative image analysis. *J. Microsc.*, 178(2):165–181, 1995.

[91] Martini, N., Bewersdorf, J., and Hell, S.W. A new high-aperture glycerol immersion objective lens and its application to 3D-fluorescence microscopy. *J. Microsc.*, 206(Pt 2):146–51, 2002.

[92] Art, J. Photon Detectors for Confocal Microscopy. In J.B. Pawley, editor, *Handbook of Biological Confocal Microscopy*, chapter 12, pages 251–264. Springer Science+Business Media, New York, third edition, 2006.

[93] Nyquist, H. Certain topics in telegraph transmission theory. *Tans. AIEE*, 46:617–644, 1928.

[94] SVI. Nyquist rate calculator, http://www.svi.nl/NyquistCalculator, 2014.

[95] Sheppard, C.J.R., Gan, X., Gu, M., and Roy, M. Signal-to-Noise Ratio in Confocal Microscopes. In J.B. Pawley, editor, *Handbook of Biological Confocal Microscopy*, chapter 22, pages 442–452. Springer Science+Business Media, New York, third edition, 2006.

[96] SVI. Signal-to-Noise ratio, http://www.svi.nl/SignalToNoiseRatio. 2014.

[97] Requejo-Isidro, J. Fluorescence nanoscopy. Methods and applications. *J. Chem. Biol.*, 6(3):97–120, 2013.

[98] Hell, S.W. Microscopy and its focal switch. *Nat. Methods*, 6(1):24–32, 2009.

[99] Klar, T.A., Jakobs, S., Dyba, M., Egner, A., and Hell, S.W. Fluorescence microscopy with diffraction resolution barrier broken by stimulated emission. *Proc. Natl. Acad. Sci. U.S.A.*, 97(15):8206–8210, 2000.

[100] Willig, K.I., Harke, B., Medda, R., and Hell, S.W. STED microscopy with continuous wave beams. *Nat. Methods*, 4(11):915–918, 2007.

[101] Wildanger, D., Medda, R., Kastrup, L., and Hell, S.W. A compact STED microscope providing 3D nanoscale resolution. *J. Microsc.*, 236(1):35–43, 2009.

[102] Wilson, T. *Confocal Microscopy.* Academic Press, 1990.

[103] White, N.S. and Errington, R.J. Fluorescence techniques for drug delivery research: theory and practice. *Adv. Drug Deliv. Rev.*, 57(1):17–42, 2005.

[104] Prasad, V., Semwogerere, D., and Weeks, E.R. Confocal microscopy of colloids. *J. Phys. Condens. Matter*, 19(11):113102, 2007.

[105] Visser, T., Oud, J., and Brakenhoff, G.J. Refractive index and axial distance measurements in 3-D microscopy. *Optik*, 90:17–19, 1992.

[106] Visser, T. and Oud, J. Volume measurements in three-dimensional microscopy. *Scanning*, page 198, 1994.

[107] Egner, A. and Hell, S. Aberrations in confocal and multi-photon fluorescence microscopy induced by refractive index mismatch. In J.B. Pawley, editor, *Handbook of Biological Confocal Microscopy*, chapter 20, pages 404–413. Springer, New York, 2006.

[108] Sheppard, C.J., Gu, M., Brain, K., and Zhou, H. Influence of spherical aberration on axial imaging of confocal reflection microscopy. *Appl. Opt.*, 33(4):616–24, 1994.

[109] Sheppard, C. Effects of specimen refractive index on confocal imaging. *J. Microsc.*, 185(3):366–374, 1997.

[110] Wiersma, S.H., Török, P., Visser, T.D., and Varga, P. Comparison of different theories for focusing through a plane interface. *J. Opt. Soc. Am. A*, 14(7):1482, 1997.

[111] de Grauw, C.J., Vroom, J.M., van der Voort, H.T., and Gerritsen, H.C. Imaging properties in two-photon excitation microscopy and effects of refractive-index mismatch in thick specimens. *Appl. Opt.*, 38(28):5995–6003, 1999.

[112] Diaspro, A., Federici, F., and Robello, M. Influence of refractive-index mismatch in high-resolution three-dimensional confocal microscopy. *Appl. Opt.*, 41(4):685–90, 2002.

[113] Neuman, K.C., Abbondanzieri, E.A., and Block, S.M. Measurement of the effective focal shift in an optical trap. *Opt. Lett.*, 30(11):1318–20, 2005.

[114] Shaevitz, J.W. and Fletcher, D.A. Enhanced three-dimensional deconvolution microscopy using a measured depth-varying point-spread function. *J. Opt. Soc. Am. A. Opt. Image Sci. Vis.*, 24(9):2622–7, 2007.

[115] Jacobsen, H. and Hell, S. Effect of the specimen refractive index on the imaging of a confocal fluorescence microscope employing high aperture oil immersion lenses. *Bioimaging*, 3(1):39–47, 1995.

[116] White, N. and Errington, R. Aberration control in quantitative imaging of botanical specimens by multidimensional fluorescence microscopy. *J. Microsc.*, 181:99–116, 1996.

[117] Boddeke, F.R., Vliet, L.J.V., and Young, I.T. Calibration of the automated z-axis of a microscope using focus functions. *J. Microsc.*, 186:270–274, 1997.

[118] Bornfleth, H., Saetzler, K., Eils, R., and Cremer, C. distance measurements and volume-conserving segmentation of objects near and below the resolution limit in three-dimensional confocal fluorescence microscopy. *J. Microsc.*, 189:118–136, 1998.

[119] Jensen, K.E., Weitz, D.A., and Spaepen, F. Note: A three-dimensional calibration device for the confocal microscope. *Rev. Sci. Instrum.*, 84(1):016108, 2013.

[120] Kasarova, S.N., Sultanova, N.G., Ivanov, C.D., and Nikolov, I.D. Analysis of the dispersion of optical plastic materials. *Opt. Mater.*, 29(11):1481–1490, 2007.

[121] Rasband, W.S. ImageJ, National Institutes of Health, Bethesda, Maryland, USA, http://imagej.nih.gov/ij/.

[122] Jiang, P., Bertone, J.F., Hwang, K.S., and Colvin, V.L. Single-Crystal Colloidal Multilayers of Controlled Thickness. *Chem. Mater.*, 11(8):2132–2140, 1999.

[123] Cole, R.W., Jinadasa, T., and Brown, C.M. Measuring and interpreting point spread functions to determine confocal microscope resolution and ensure quality control. *Nat. Protoc.*, 6(12):1929–41, 2011.

[124] Wilhelm, S., Gröbler, B., Gluch, M., and Heinz, H. *Carl Zeiss Principles*. Carl Zeiss, 1997.

[125] Thijssen, J.H.J., Petukhov, A.V., t Hart, D.C., Imhof, A., van der Werf, C.H.M., Schropp, R.E.I., and van Blaaderen, A. Characterization of Photonic Colloidal Single Crystals by Microradian X-ray Diffraction. *Adv. Mater.*, 18(13):1662–1666, 2006.

[126] Haw, M. *Middle World: The Restless Heart of Matter and Life*. Macmillan Science, New York, 2007.

[127] Zsigmondy, R.A. Properties of Colloids. *Nobel Lect.*, 1926.

[128] Mappes, T., Jahr, N., Csaki, A., Vogler, N., Popp, J., and Fritzsche, W. The invention of immersion ultramicroscopy in 1912-the birth of nanotechnology? *Angew. Chem., Int. Ed.*, 51(45):11208–12, 2012.

[129] Walter, N.G., Huang, C.y., Manzo, A.J., and Sobhy, M.A. Do-it-yourself guide : how to use the modern single-molecule toolkit. *Nat. Methods*, 5(6):475–489, 2008.

[130] Lee, S.H., Roichman, Y., Yi, G.R., Kim, S.H., Yang, S.M., van Blaaderen, A., van Oostrum, P., and Grier, D.G. Characterizing and tracking single colloidal particles with video holographic microscopy. *Opt. Express*, 15(26):18275–18282, 2007.

[131] Fung, J., Perry, R.W., Dimiduk, T.G., and Manoharan, V.N. Imaging multiple colloidal particles by fitting electromagnetic scattering solutions to digital holograms. *J. Quant. Spectrosc. Radiat. Transf.*, 113(18):2482–2489, 2012.

[132] van Blaaderen, A., Imhof, A., Hage, W., and Vrij, A. Three-dimensional imaging of submicrometer colloidal particles in concentrated suspensions using confocal scanning laser microscopy. *Langmuir*, 2(l):3–6, 1992.

[133] van Blaaderen, A. Imaging individual particles in concentrated colloidal dispersions by confocal scanning light microscopy. *Adv. Mater.*, 5(1):52–54, 1993.

[134] Ito, K., Yoshida, H., and Ise, N. Void structure in colloidal dispersions. *Science*, 263(5143):66–68, 1994.

[135] Kose, A., Ozaki, M., Takano, K., Kobayashi, Y., and Hachisu, S. Direct observation of ordered latex suspension by metallurgical microscope. *J. Colloid Interface Sci.*, 44(2):330–338, 1973.

[136] Hachisu, S. and Yoshimura, S. Optical demonstration of crystalline superstructures in binary mixtures of latex globules. *Nature*, 283:188–189, 1980.

[137] Murray, C.A. and Grier, D.G. Video Microscopy of Monodisperse Colloidal Systems. *Annu. Rev. Phys. Chem.*, 47(1):421–462, 1996.

[138] Weeks, E. www.physics.emory.edu/˜weeks/idl/, 2013.

[139] Ramírez-Saito, A., Bechinger, C., and Arauz-Lara, J. Optical microscopy measurement of pair correlation functions. *Phys. Rev. E*, 74(3):030401, 2006.

[140] Baumgartl, J., Arauz-Lara, J.L., and Bechinger, C. Like-charge attraction in confinement: myth or truth? *Soft Matter*, 2(8):631, 2006.

[141] Besseling, T.H., Jose, J., and van Blaaderen, A. Methods to calibrate and scale axial distances in confocal microscopy as a function of refractive index. *submitted*, 2014.

[142] Lu, P.J., Shutman, M., Sloutskin, E., and Butenko, A.V. Locating particles accurately in microscope images requires image-processing kernels to be rotationally symmetric. *Opt. Express*, 21(25):30755, 2013.

[143] van Loenhout, M.T.J., Kerssemakers, J.W.J., De Vlaminck, I., and Dekker, C. Non-bias-limited tracking of spherical particles, enabling nanometer resolution at low magnification. *Biophys. J.*, 102(10):2362–71, 2012.

[144] MacKintosh, F. and Schmidt, C. Microrheology. *Curr. Opin. Colloid Interface Sci.*, 4:300–307, 1999.

[145] Crocker, J.C., Valentine, M.T., Weeks, E.R., Gisler, T., Kaplan, P.D., Yodh, A.G., and Weitz, D.A. Two-point microrheology of inhomogeneous soft materials. *Phys. Rev. Lett.*, 85(4):888–891, 2000.

[146] Cicuta, P. and Donald, A.M. Microrheology: a review of the method and applications. *Soft Matter*, 3(12):1449, 2007.

[147] Gal, N., Lechtman-Goldstein, D., and Weihs, D. Particle tracking in living cells: a review of the mean square displacement method and beyond. *Rheol. Acta*, 52(5):425–443, 2013.

[148] Moschakis, T. Microrheology and particle tracking in food gels and emulsions. *Curr. Opin. Colloid Interface Sci.*, 18(4):311–323, 2013.

[149] Toiya, M., Hettinga, J., and Losert, W. 3D Imaging of particle motion during penetrometer testing. *Granul. Matter*, 9(5):323–329, 2007.

[150] Dijksman, J.A., Rietz, F., Lorincz, K.A., van Hecke, M., and Losert, W. Invited Article: Refractive index matched scanning of dense granular materials. *Rev. Sci. Instrum.*, 83(1):011301, 2012.

[151] Maas, H., Gruen, A., and Papantoniou, D. Particle tracking velocimetry in three-dimensional flows. *Exp. Fluids*, 146:133–146, 1993.

[152] Cierpka, C. and Kähler, C.J. Particle imaging techniques for volumetric three-component (3D3C) velocity measurements in microfluidics. *J. Vis.*, 15(1):1–31, 2011.

[153] Dunderdale, G., Ebbens, S., Fairclough, P., and Howse, J. Importance of particle tracking and calculating the mean-squared displacement in distinguishing nanopropulsion from other processes. *Langmuir*, 28(30):10997–1006, 2012.

[154] Miño, G., Mallouk, T.E., Darnige, T., Hoyos, M., Dauchet, J., Dunstan, J., Soto, R., Wang, Y., Rousselet, A., and Clement, E. Enhanced Diffusion due to Active Swimmers at a Solid Surface. *Phys. Rev. Lett.*, 106(4):048102, 2011.

[155] Poon, W. From Clarkia to Escherichia and Janus: the physics of natural and synthetic active colloids. *arXiv Prepr. arXiv1306.4799*, pages 317–386, 2013.

[156] Friedrich, H., Gommes, C.J., Overgaag, K., Meeldijk, J.D., Evers, W.H., de Nijs, B., Boneschanscher, M.P., de Jongh, P.E., Verkleij, A.J., de Jong, K.P., van Blaaderen, A., and Vanmaekelbergh, D. Quantitative structural analysis of binary nanocrystal superlattices by electron tomography. *Nano Lett.*, 9(7):2719–24, 2009.

[157] Evers, W.H., Friedrich, H., Filion, L., Dijkstra, M., and Vanmaekelbergh, D. Observation of a ternary nanocrystal superlattice and its structural characterization by electron tomography. *Angew. Chem., Int. Ed.*, 48(51):9655–7, 2009.

[158] de Nijs, B., Dussi, S., Smallenburg, F., Meeldijk, J.D., Groenendijk, D.J., Filion, L., Imhof, A., Dijkstra, D., and van Blaaderen, A. Entropy-driven Formation of Large Icosahedral Colloidal Clusters by Spherical Confinement. 2014.

[159] Midgley, P.A. and Dunin-Borkowski, R.E. Electron tomography and holography in materials science. *Nat. Mater.*, 8(4):271–80, 2009.

[160] Huang, P.Y., Kurasch, S., Alden, J.S., Shekhawat, A., Alemi, A.A., McEuen, P.L., Sethna, J.P., Kaiser, U., and Muller, D.A. Imaging Atomic Rearrangements in Two-Dimensional Silica Glass: Watching Silica's Dance. *Science*, 342(6155):224–227, 2013.

[161] Wenzl, J., Seto, R., Roth, M., Butt, H.J., and Auernhammer, G.K. Measurement of rotation of individual spherical particles in cohesive granulates. *Granul. Matter*, 15(4):391–400, 2012.

[162] Mohraz, A. and Solomon, M.J. Direct visualization of colloidal rod assembly by confocal microscopy. *Langmuir*, 21(12):5298–306, 2005.

[163] Rossi, L., Sacanna, S., Irvine, W.T.M., Chaikin, P.M., Pine, D.J., and Philipse, A.P. Cubic crystals from cubic colloids. *Soft Matter*, 7(9):4139–4142, 2011.

[164] Elsesser, M.T., Hollingsworth, A.D., Edmond, K.V., and Pine, D.J. Large core-shell poly(methyl methacrylate) colloidal clusters: synthesis, characterization, and tracking. *Langmuir*, 27(3):917–27, 2011.

[165] Peng, B., Vutukuri, H.R., van Blaaderen, A., and Imhof, A. Synthesis of fluorescent monodisperse non-spherical dumbbell-like model colloids. *J. Mater. Chem.*, 22(41):21893—-21900, 2012.

[166] Hunter, G.L., Edmond, K.V., Elsesser, M.T., and Weeks, E.R. Tracking rotational diffusion of colloidal clusters. *Opt. Express*, 19(18):17189–17202, 2011.

[167] Edmond, K.V., Elsesser, M.T., Hunter, G.L., Pine, D.J., and Weeks, E.R. Decoupling of rotational and translational diffusion in supercooled colloidal fluids. *Proc. Natl. Acad. Sci. U.S.A.*, 109(44):17891–6, 2012.

[168] Kraft, D.J., Wittkowski, R., ten Hagen, B., Edmond, K.V., Pine, D.J., and Löwen, H. Brownian motion and the hydrodynamic friction tensor for colloidal particles of complex shape. *Phys. Rev. E*, 88(5):050301, 2013.

[169] Anthony, S.M., Hong, L., Kim, M., and Granick, S. Single-particle colloid tracking in four dimensions. *Langmuir*, 22(24):9812–5, 2006.

[170] Hong, L., Anthony, S.M., and Granick, S. Rotation in suspension of a rod-shaped colloid. *Langmuir*, 22(17):7128–31, 2006.

[171] Han, Y., Alsayed, A.M., Nobili, M., Zhang, J., Lubensky, T.C., and Yodh, A.G. Brownian motion of an ellipsoid. *Science*, 314(5799):626–30, 2006.

[172] Han, Y., Alsayed, A., Nobili, M., and Yodh, A.G. Quasi-two-dimensional diffusion of single ellipsoids: Aspect ratio and confinement effects. *Phys. Rev. E*, 80(1):1–6, 2009.

[173] Zheng, Z. and Han, Y. Self-diffusion in two-dimensional hard ellipsoid suspensions. *J. Chem. Phys.*, 133(12):124509, 2010.

[174] Chakrabarty, A., Wang, F., Fan, C.Z., Sun, K., and Wei, Q.H. High-precision tracking of brownian boomerang colloidal particles confined in quasi two dimensions. *Langmuir*, 29(47):14396–14402, 2013.

[175] Chakrabarty, A., Konya, A., Wang, F., Selinger, J.V., Sun, K., and Wei, Q.H. Brownian Motion of Boomerang Colloidal Particles. *Phys. Rev. Lett.*, 111(16):160603, 2013.

[176] Yunker, P., Chen, K., Zhang, Z., Ellenbroek, W.G., Liu, A.J., and Yodh, A.G. Rotational and translational phonon modes in glasses composed of ellipsoidal particles. *Phys. Rev. E*, pages 1–6, 2011.

[177] Zheng, Z., Wang, F., and Han, Y. Glass Transitions in Quasi-Two-Dimensional Suspensions of Colloidal Ellipsoids. *Phys. Rev. Lett.*, 107(6):065702, 2011.

[178] Mishra, C.K., Rangarajan, A., and Ganapathy, R. Two-Step Glass Transition Induced by Attractive Interactions in Quasi-Two-Dimensional Suspensions of Ellipsoidal Particles. *Phys. Rev. Lett.*, 110(18):188301, 2013.

[179] Zhao, K., Bruinsma, R., and Mason, T.G. Entropic crystal-crystal transitions of Brownian squares. *Proc. Natl. Acad. Sci. U.S.A.*, 108(7):2684–7, 2011.

[180] Zhao, K., Bruinsma, R., and Mason, T.G. Local chiral symmetry breaking in triatic liquid crystals. *Nat. Commun.*, 3:801, 2012.

[181] Mukhija, D. and Solomon, M.J. Translational and rotational dynamics of colloidal rods by direct visualization with confocal microscopy. *J. Colloid Interface Sci.*, 314(1):98–106, 2007.

[182] Cohen, A.P., Janai, E., Mogilko, E., Schofield, A.B., and Sloutskin, E. Fluid Suspensions of Colloidal Ellipsoids: Direct Structural Measurements. *Phys. Rev. Lett.*, 107(23):238301, 2011.

[183] Cohen, A.P., Janai, E., Rapaport, D.C., Schofield, A.B., and Sloutskin, E. Structure and interactions in fluids of prolate colloidal ellipsoids: comparison between experiment, theory, and simulation. *J. Chem. Phys.*, 137(18):184505, 2012.

[184] Shah, A.A., Schultz, B., Kohlstedt, K.L., Glotzer, S.C., and Solomon, M.J. Synthesis, assembly, and image analysis of spheroidal patchy particles. *Langmuir*, 29(15):4688–96, 2013.

[185] Mukhija, D. and Solomon, M.J. Nematic order in suspensions of colloidal rods by application of a centrifugal field. *Soft Matter*, 7:540–545, 2010.

[186] Liu, B., Besseling, T.H., Hermes, M., Demirörs, A.F., Imhof, A., and van Blaaderen, A. Switching plastic crystals of colloidal rods with electric fields. *Nat. Commun.*, 5:3092, 2014.

[187] Cannell, M.B., Mcmorland, A., and Soeller, C. Image Enhancement by Deconvolution. In J.B. Pawley, editor, *Handbook of Biological Confocal Microscopy*, chapter 25, pages 488–500. Springer Science+Business Media, New York, third edition, 2006.

[188] Besag, J., York, J., and Mollié, A. Bayesian image restoration, with two applications in spatial statistics. *Ann. Inst. Statist. Math.*, 43(1):1–59, 1991.

[189] Al-Awadhi, F., Jennison, C., and Hurn, M. Statistical image analysis for a confocal microscopy two-dimensional section of cartilage growth. *Appl. Statist.*, 53(1):31–49, 2004.

[190] Desmond, K.W., Young, P.J., Chen, D., and Weeks, E.R. Experimental study of forces between quasi-two-dimensional emul- sion droplets near jamming. pages 41–47.

[191] Shakarji, C. Least-squares fitting algorithms of the NIST algorithm testing system. *J. Res. Natl. Inst. Stand. Technol.*, 103(6):633, 1998.

[192] Ni, R., Belli, S., van Roij, R., and Dijkstra, M. Glassy Dynamics, Spinodal Fluctuations, and the Kinetic Limit of Nucleation in Suspensions of Colloidal Hard Rods. *Phys. Rev. Lett.*, 105(8):088302, 2010.

[193] Savin, T. and Doyle, P.S. Static and dynamic errors in particle tracking microrheology. *Biophys. J.*, 88(1):623–638, 2005.

[194] Dhont, J. *An Introduction to Dynamics of Colloids*. Elsevier, Amsterdam, 1996.

[195] Cheong, F. and Grier, D. Rotational and translational diffusion of copper oxide nanorods measured with holographic video microscopy. *Opt. Express*, 18(7):6555–6562, 2010.

[196] Brenner, H. Taylor Dispersion in Systems of Sedimenting Nonspherical Brownian Particles. *J. Colloid Interface Sci.*, 71(2):189—-208, 1979.

[197] Svedberg, T. and Pedersen, K. *The Ultracentrifuge*. Oxford Univ. Press, London, 1940.

[198] Tirado, M.M., Martinez, C.L., and de la Torre, J.G. Comparison of theories for the translational and rotational diffusion coefficients of rod-like macromolecules. Application to short DNA fragments. *J. Chem. Phys.*, 81(4):2047, 1984.

[199] Segur, J.B. and Oberstar, H.E. Viscosity of Glycerol and Its Aqueous Solutions. *Ind. Eng. Chem.*, 43(9):2117 – 2120, 1951.

[200] Peng, B., van der Wee, E., Imhof, A., and van Blaaderen, A. Synthesis of monodisperse, highly cross-linked, fluorescent PMMA particles by dispersion polymerization. *Langmuir*, 28:6776–6785, 2012.

[201] Ye, X., Zheng, C., Chen, J., Gao, Y., and Murray, C.B. Using binary surfactant mixtures to simultaneously improve the dimensional tunability and monodispersity in the seeded growth of gold nanorods. *Nano Lett.*, 13(2):765–71, 2013.

[202] Gorelikov, I. and Matsuura, N. Single-step coating of mesoporous silica on cetyltrimethyl ammonium bromide-capped nanoparticles. *Nano Lett.*, 8(1):369–73, 2008.

[203] Peng, B., Smallenburg, F., Imhof, A., Dijkstra, M., and van Blaaderen, A. Colloidal clusters by using emulsions and dumbbell-shaped particles: experiments and simulations. *Angew. Chem., Int. Ed.*, 52(26):6709–12, 2013.

[204] Kremer, J.R., Mastronarde, D.N., and McIntosh, J.R. Computer visualization of three-dimensional image data using IMOD. *J. Struct. Biol.*, 116(1):71–6, 1996.

[205] Mastronarde, D.N. Dual-axis tomography: an approach with alignment methods that preserve resolution. *J. Struct. Biol.*, 120(3):343–52, 1997.

[206] Grzelczak, M., Sánchez-Iglesias, A., Mezerji, H.H., Bals, S., Pérez-Juste, J., and Liz-Marzán, L.M. Steric hindrance induces crosslike self-assembly of gold nanodumbbells. *Nano Lett.*, 12(8):4380–4, 2012.

[207] Troppenz, T., Kuijk, A., Imhof, A., van Blaaderen, A., Dijkstra, M., and van Roij, R. Nematic ordering of polarizable colloidal rods in an external electric field: theory and experiment. *in preparation.*

[208] Colin, R., Yan, M., Chevry, L., Berret, J.F., and Abou, B. 3D rotational diffusion of micrometric wires using 2D video microscopy. *Europhys. Lett.*, 97:30008, 2012.

[209] Bolhuis, P. and Frenkel, D. Tracing the phase boundaries of hard spherocylinders. *J. Chem. Phys.*, 106(2):666 – 687, 1997.

[210] Ball, P. Material witness: Colloids get active. *Nat. Mater.*, 12(8):696, 2013.

[211] Bates, M.A. and Frenkel, D. Influence of polydispersity on the phase behavior of colloidal liquid crystals: A Monte Carlo simulation study. *J. Chem. Phys.*, 109(14):6193–6199, 1998.

[212] Koumakis, N., Schofield, A.B., and Petekidis, G. Effects of shear induced crystallization on the rheology and ageing of hard sphere glasses. *Soft Matter*, 4(10):2008 –2018, 2008.

[213] Duff, N. and Lacks, D. Shear-induced crystallization in jammed systems. *Phys. Rev. E*, 75(3):1–8, 2007.

[214] Larsen, A.E. and Grier, D.G. Melting of metastable crystallites in charge-stabilized colloidal suspensions. *Phys. Rev. Lett.*, 76(20):3862–3865, 1996.

[215] Vissers, T., Besseling, T.H., van Blaaderen, A., and Imhof, A. Sustained rotational instabilities and crystallization in driven suspensions of oppositely charged colloids. *submitted*, 2014.

[216] Palacci, J., Sacanna, S., Steinberg, A.P., Pine, D.J., and Chaikin, P.M. Living crystals of light-activated colloidal surfers. *Science*, 339(6122):936–40, 2013.

[217] Nahmad-Molinari, Y. and Ruiz-Suárez, J. Epitaxial Growth of Granular Single Crystals. *Phys. Rev. Lett.*, 89(26):264302, 2002.

[218] Cheng, X., Xu, X., Rice, S.A., Dinner, A.R., and Cohen, I. Assembly of vorticity-aligned hard-sphere colloidal strings in a simple shear flow. *Proc. Natl. Acad. Sci. U.S.A.*, 109(1):63–67, 2012.

[219] Yan, Y.D., Dhont, J.K.G., Smits, C., and Lekkerkerker, H.N.W. Oscillatory-shear-induced order in nonaqueous dispersions of charged colloidal spheres. *Phys. A Stat. Mech. its Appl.*, 202(1-2):68–80, 1994.

[220] Paulin, S.E., Ackerson, B.J., and Wolfe, M.S. Equilibrium and Shear Induced Nonequilibrium Phase Behavior of PMMA Microgel Spheres. *J. Colloid Interface Sci.*, 178(1):251–262, 1996.

[221] Haw, M.D., Poon, W.C.K., and Pusey, P.N. Direct observation of oscillatory-shear-induced order in colloidal suspensions. *Phys. Rev. E*, 57(6):6859, 1998.

[222] Cohen, I., Mason, T.G., and Weitz, D.A. Shear-Induced Configurations of Confined Colloidal Suspensions. *Phys. Rev. Lett.*, 93(4), 2004.

[223] Solomon, T. and Solomon, M.J. Stacking fault structure in shear-induced colloidal crystallization. *J. Chem. Phys.*, 124(13):134905, 2006.

[224] McMullan, J.M. and Wagner, N.J. Directed self-assembly of suspensions by large amplitude oscillatory shear flow. *J. Rheol.*, 53(3):575, 2009.

[225] Derks, D., Wu, Y.L., van Blaaderen, A., and Imhof, A. Dynamics of colloidal crystals in shear flow. *Soft Matter*, 5(5):1060, 2009.

[226] Delhommelle, J., Petravic, J., and Evans, D.J. Non-Newtonian behavior in simple fluids. *J. Chem. Phys.*, 120(13):6117–6123, 2004.

[227] Komatsugawa, H. and Nosé, S. Nonequilibrium molecular dynamics simulations of oscillatory sliding motion in a colloidal suspension system. *Phys. Rev. E*, 51(6):5944, 1995.

[228] Erpenbeck, J.J. Shear Viscosity of the Hard-Sphere Fluid via Nonequilibrium Molecular Dynamics. *Phys. Rev. Lett.*, 52(15):1333, 1984.

[229] Delhommelle, J., Petravic, J., and Evans, D.J. Reexamination of string phase and shear thickening in simple fluids. *Phys. Rev. E*, 68(3):031201, 2003.

[230] Delhommelle, J. Should 'lane formation' occur systematically in driven liquids and colloids? *Phys. Rev. E*, 71(1):1–10, 2005.

[231] D'Haene, P., Mewis, J., and Fuller, G.G. Scattering Dichroism Measurements of Flow-Induced Structure of a Shear Thickening Suspension. *J. Colloid Interface Sci.*, 156(2):350–358, 1993.

[232] Xue, W. and Grest, G.S. Shear-induced alignment of colloidal particles in the presence of a shear flow. *Phys. Rev. Lett.*, 64(4):419, 1990.

[233] Butler, S. and Harrowell, P. Shear induced ordering in simulations of colloidal suspensions: Oscillatory shear and computational artefacts. *J. Chem. Phys.*, 105(2):605, 1996.

[234] Cheng, X., McCoy, J.H., Israelachvili, J.N., and Cohen, I. Imaging the microscopic structure of shear thinning and thickening colloidal suspensions. *Science*, 333(6047):1276–9, 2011.

[235] Xu, X., Rice, S.A., and Dinner, A.R. Relation between ordering and shear thinning in colloidal suspensions. *Proc. Natl. Acad. Sci. U.S.A.*, 110(10):3771–3776, 2013.

[236] Besseling, T.H. *Shear induced hard sphere crystallization.* MSc thesis, Utrecht University, 2010.

[237] ten Wolde, P., Ruiz-Montero, M.J., and Frenkel, D. Numerical Evidence for bcc Ordering at the Surface of a Critical fcc Nucleus. *Phys. Rev. Lett.*, 75(14):2714, 1995.

[238] Wu, Y.L., Brand, J.H.J., van Gemert, J.L.A., Verkerk, J., Wisman, H., van Blaaderen, A., and Imhof, A. A new parallel plate shear cell for in situ real-space measurements of complex fluids under shear flow. *Rev. Sci. Instrum.*, 78(10):103902, 2007.

[239] Ermak, D. A computer simulation of charged particles in solution. I. Technique and equilibrium properties. *J. Chem. Phys.*, 62(10), 1975.

[240] Wu, Y.L., Derks, D., van Blaaderen, A., and Imhof, A. Melting and crystallization of colloidal hard-sphere suspensions under shear. *Proc. Natl. Acad. Sci. U.S.A.*, 106(26):10564–10569, 2009.

[241] Brady, J.F. Computer simulation of viscous suspensions. *Chem. Eng. Sci.*, 56(9):2921–2926, 2001.

[242] Steinhardt, P.J., Nelson, D.R., and Ronchetti, M. Bond-orientational order in liquids and glasses. *Phys. Rev. B*, 28(2):784–805, 1983.

[243] Alsayed, A.M., Islam, M.F., Zhang, J., Collings, P.J., and Yodh, A.G. Premelting at defects within bulk colloidal crystals. *Science*, 309(5738):1207–1210, 2005.

[244] Reinitzer, F. Beiträge zur Kenntnis des Cholesterins. *Monatsh. Chem.*, 9(1):421–441, 1888.

[245] Lehmann, O. Über fliessende Krystalle. *Z. Phys. Chem.*, 4:462472, 1889.

[246] Friedel, G. Mesomorphic States of Matter. *Ann. Phys.*, 18:273, 1922.

[247] Onsager, L. The effects of shape on the interaction of colloidal particles. *Ann. N. Y. Acad. Sci.*, 51:627, 1949.

[248] Frenkel, D., Lekkerkerker, H., and Stroobants, A. Thermodynamic stability of a smectic phase in a system of hard rods. *Nature*, 332:822–823, 1988.

[249] Dogic, Z. and Fraden, S. Smectic phase in a colloidal suspension of semiflexible virus particles. *Phys. Rev. Lett.*, 78(12):2417–2420, 1997.

[250] Grelet, E. Hexagonal Order in Crystalline and Columnar Phases of Hard Rods. *Phys. Rev. Lett.*, 100(16):1–4, 2008.

[251] Livolant, F. Ordered phases of DNA in vivo and in vitro. *Phys. A Stat. Mech. its Appl.*, 176:117–137, 1991.

[252] Buining, P.A. and Lekkerkerker, H.N.W. Isotropic-nematic phase separation of a dispersion of organophilic boehmite rods. *J. Phys. Chem.*, 97(44):11510–11516, 1993.

[253] Vroege, G.J., Thies-Weesie, D.M.E., Petukhov, A.V., Lemaire, B.J., and Davidson, P. Smectic Liquid-Crystalline Order in Suspensions of Highly Polydisperse Goethite Nanorods. *Adv. Mater.*, 18(19):2565–2568, 2006.

[254] Ozaki, M., Kratohvil, S., and Matijević, E. Formation of monodispersed spindle-type hematite particles. *J. Colloid Interface Sci.*, 102(1):146–151, 1984.

[255] Sacanna, S., Rossi, L., Wouterse, A., and Philipse, A.P. Observation of a shape-dependent density maximum in random packings and glasses of colloidal silica ellipsoids. *J. Phys. Condens. Matter*, 19(37):376108, 2007.

[256] Lekkerkerker, H.N.W. and Vroege, G.J. Liquid crystal phase transitions in suspensions of mineral colloids: new life from old roots. *Phil. Trans. R. Soc. A*, 371:20120263, 2013.

[257] Ho, C.C., Keller, A., Odell, J.A., and Ottewill, R.H. Preparation of monodisperse ellipsoidal polystyrene particles. *Colloid Polym. Sci.*, 271(5):469–479, 1993.

[258] Park, J.G., Forster, J.D., and Dufresne, E.R. High-yield synthesis of monodisperse dumbbell-shaped polymer nanoparticles. *J. Am. Chem. Soc.*, 132(17):5960–1, 2010.

[259] Forster, J.D., Park, J.G., Mittal, M., Noh, H., Schreck, C.F., O'Hern, C.S., Cao, H., Furst, E.M., and Dufresne, E.R. Assembly of optical-scale dumbbells into dense photonic crystals. *ACS Nano*, 5(8):6695–700, 2011.

[260] Ming, T., Kou, X., Chen, H., Wang, T., Tam, H.L., Cheah, K.W., Chen, J.Y., and Wang, J. Ordered gold nanostructure assemblies formed by droplet evaporation. *Angew. Chem., Int. Ed.*, 47(50):9685–90, 2008.

[261] Nobile, C., Carbone, L., Fiore, A., Cingolani, R., Manna, L., and Krahne, R. Self-assembly of highly fluorescent semiconductor nanorods into large scale smectic liquid crystal structures by coffee stain evaporation dynamics. *J. Phys. Condens. Matter*, 21(26):264013, 2009.

[262] Vroege, G.J. and Lekkerkerker, H.N.W. Phase transitions in lyotropic colloidal and polymer liquid crystals. *Reports Prog. Phys.*, 55:1241–1309, 1992.

[263] Glotzer, S.C. and Solomon, M.J. Anisotropy of building blocks and their assembly into complex structures. *Nat. Mater.*, 6(8):557–562, 2007.

[264] Dugyala, V., Daware, S., and Madivala, B. Shape anisotropic colloids: synthesis, packing behavior, evaporation driven assembly, and their application in emulsion stabilization. *Soft Matter*, 9:6711–6725, 2013.

[265] Maeda, H. and Maeda, Y. Direct observation of Brownian dynamics of hard colloidal nanorods. *Nano Lett.*, 7(11):3329–35, 2007.

[266] Maeda, H. and Maeda, Y. Spontaneous Formation of Stringlike Clusters and Smectic Sheets for Colloidal Rods Confined in Thin Wedgelike Gaps. *Langmuir*, 29(33):10529–10538, 2013.

[267] Marechal, M. and Dijkstra, M. Colloidal hard dumbbells under gravity: structure and crystallization. *Soft Matter*, 7(4):1397, 2011.

[268] Allen, M.P., Evans, G.T., Frenkel, D., and Mulder, B.M. Hard Convex Body Fluids. *Adv. Chem. Phys.*, 86:1–166, 1993.

[269] Eggen, E., Dijkstra, M., and van Roij, R. Effective shape and phase behavior of short charged rods. *Phys. Rev. E*, 79(4):041401, 2009.

[270] Stroobants, A., Lekkerkerker, H., and Odijk, T. Effect of electrostatic interaction on the liquid crystal phase transition in solutions of rodlike polyelectrolytes. *Macromolecules*, 2238(18):2232–2238, 1986.

[271] Kramer, E.M. and Herzfeld, J. Avoidance model for soft particles. II. Positional ordering of charged rods. *Phys. Rev. E*, 61:6872–6878, 2000.

[272] Bohle, A., Holyst, R., and Vilgis, T. Polydispersity and ordered phases in solutions of rodlike macromolecules. *Phys. Rev. Lett.*, 76(8):1396–1399, 1996.

[273] Piazza, R., Bellini, T., and Degiorgio, V. Equilibrium sedimentation profiles of screened charged colloids: A test of the hard-sphere equation of state. *Phys. Rev. Lett.*, 71(25):4267–4270, 1993.

[274] Royall, C.P., Roij, R.V., and van Blaaderen, A. Extended sedimentation profiles in charged colloids: the gravitational length, entropy, and electrostatics. *J. Phys. Condens. Matter*, 17(15):2315–2326, 2005.

[275] Piazza, R. Settled and unsettled issues in particle settling. *Rep. Prog. Phys.*, 77(5):056602, 2014.

[276] Dogic, Z., Philipse, A.P., Fraden, S., and Dhont, J.K.G. Concentration-dependent sedimentation of colloidal rods. *J. Chem. Phys.*, 113(18):8368, 2000.

[277] Baulin, V.A. and Khokhlov, A.R. Nematic ordering of rigid rods in a gravitational field. *Phys. Rev. E*, 60(3):2973–7, 1999.

[278] Savenko, S. and Dijkstra, M. Sedimentation and multiphase equilibria in suspensions of colloidal hard rods. *Phys. Rev. E*, 70(5):051401, 2004.

[279] Biben, T., Hansen, J.P., and Barrat, J.L. Density profiles of concentrated colloidal suspensions in sedimentation equilibrium. *J. Chem. Phys.*, 98(9):7330, 1993.

[280] van Roij, R. Defying gravity with entropy and electrostatics: sedimentation of charged colloids. *J. Phys. Condens. Matter*, 15:3569–3580, 2003.

[281] Kuijk, A. *Fluorescent colloidal silica rods - Synthesis and phase behavior*. Ph.D. thesis, Utrecht University, 2012.

[282] Beltran-Villegas, D.J., Schultz, B.A., Nguyen, N.H.P., Glotzer, S.C., and Larson, R.G. Phase behavior of Janus colloids determined by sedimentation equilibrium. *Soft Matter*, 2014.

[283] Al-Barwani, M. and Allen, M. Isotropic-nematic interface of soft spherocylinders. *Phys. Rev. E*, 62(5), 2000.

[284] Sage, D. OrientationJ, http://bigwww.epfl.ch/demo/orientation/, 2014.

[285] Rezakhaniha, R., Agianniotis, A., Schrauwen, J.T.C., Griffa, A., Sage, D., Bouten, C.V.C., van de Vosse, F.N., Unser, M., and Stergiopulos, N. Experimental investigation of collagen waviness and orientation in the arterial adventitia using confocal laser scanning microscopy. *Biomech. Model. Mechanobiol.*, 11(3-4):461–73, 2012.

[286] Duclos, G., Garcia, S., Yevick, H.G., and Silberzan, P. Perfect nematic order in confined monolayers of spindle-shaped cells. *Soft Matter*, 10(14):2346–53, 2014.

[287] Oppenheim, A.V., Schafer, R.W., and Buck, J.R. *Discrete-Time Signal Processing*. Prentice Hall, 1999.

[288] Datskos, P. and Sharma, J. Synthesis of Segmented Silica Rods by Regulation of the Growth Temperature. *Angew. Chem., Int. Ed.*, 53:451–454, 2014.

[289] Rowan, D.G. and Hansen, J.P. Salt-induced ordering in lamellar colloids. *Langmuir*, 18(11):2063–2068, 2002.

[290] Aoki, K.M., Yoneya, M., and Yokoyama, H. Entropy and heat capacity calculations of simulated crystal - hexatic smectic-B - smectic-A liquid-crystal phase transitions. *Phys. Rev. E*, 81(2):021701, 2010.

[291] van Roij, R., Bolhuis, P., Mulder, B., and Frenkel, D. Transverse interlayer order in lyotropic smectic liquid crystals. *Phys. Rev. E*, 52(2):1277–1281, 1995.

[292] van Duijneveldt, J.S. and Allen, M.P. Free energy barriers for interlayer diffusion in the smectic-A phase of hard spherocylinders. *Mol. Phys.*, 90(2):243–250, 1997.

[293] Dijkstra, M., van Roij, R., and Evans, R. Wetting and capillary nematization of a hard-rod fluid: A simulation study. *Phys. Rev. E*, 63(5):051703, 2001.

[294] Shundyak, K. *Interfacial phenomena in hard-rod fluids.* Ph.D. thesis, Utrecht University, 2004.

[295] Wolfsheimer, S., Tanase, C., Shundyak, K., van Roij, R., and Schilling, T. Isotropic-nematic interface in suspensions of hard rods: Mean-field properties and capillary waves. *Phys. Rev. E*, 73(6):061703, 2006.

[296] Odijk, T. and Lekkerkerker, H. Theory of the isotropic-liquid crystal phase separation for a solution of bidisperse rodlike macromolecules. *J. Phys. Chem.*, 89:2090–2096, 1985.

[297] Speranza, A. and Sollich, P. Simplified Onsager theory for isotropic-nematic phase equilibria of length polydisperse hard rods. *J. Chem. Phys.*, 117(11):5421, 2002.

[298] Wensink, H.H. and Vroege, G.J. Isotropic-nematic phase behavior of length-polydisperse hard rods. *J. Chem. Phys.*, 119(13):6868, 2003.

[299] van der Kooij, F.M., Kassapidou, K., and Lekkerkerker, H.N.W. Liquid crystal phase transitions in suspensions of polydisperse plate-like particles. *Nature*, 406(6798):868–71, 2000.

[300] van den Pol, E., Thies-Weesie, D.M.E., Petukhov, A.V., Vroege, G.J., and Kvashnina, K. Influence of polydispersity on the phase behavior of colloidal goethite. *J. Chem. Phys.*, 129(16):164715, 2008.

[301] Lekkerkerker, H.N.W., Coulon, P., Van Der Haegen, R., and Deblieck, R. On the isotropic-liquid crystal phase separation in a solution of rodlike particles of different lengths. *J. Chem. Phys.*, 80(7):3427, 1984.

[302] Mori, N., Fujioka, H., Semura, R., and Nakamura, K. Brownian dynamics simulations for suspension of ellipsoids in liquid crystalline phase under simple shear flows. *Rheol. Acta*, 42(1-2):102–109, 2003.

[303] Larson, R. Arrested tumbling in shearing flows of liquid-crystal polymers. *Macromolecules*, 23(1):3983–3992, 1990.

[304] Auernhammer, G., Brand, H., and Pleiner, H. Shear-induced instabilities in layered liquids. *Phys. Rev. E*, 66(6):1–14, 2002.

[305] Stewart, I.W. and Stewart, F. Shear flow in smectic-A liquid crystals. *J. Phys. Condens. Matter*, 21(46):465101, 2009.

[306] Leist, H., Maring, D., Thurn-Albrecht, T., and Wiesner, U. Double flip of orientation for a lamellar diblock copolymer under shear. *J. Chem. Phys.*, 110(17):8225, 1999.

[307] Panizza, P., Archambault, P., and Roux, D. Effects of shear on the smectic A phase of thermotropic liquid crystals. *J. Phys. II Fr.*, 5:303–311, 1995.

[308] Mottram, N., Sluckin, T., Elston, S., and Towler, M. Shear-induced melting of smectic-A liquid crystals. *Phys. Rev. E. Stat. Phys. Plasmas. Fluids. Relat. Interdiscip. Topics*, 62:5064–5080, 2000.

[309] Luckhurst, G., Saielli, G., and Sluckin, T. Shear-induced structural changes of a smectic-A phase: A computer simulation study. *Phys. Rev. E*, 65(4):041717, 2002.

[310] Cagnon, M. and Durand, G. Positional anchoring of smectic liquid crystals. *Phys. Rev. Lett.*, 70(18):2742–2745, 1993.

[311] Besseling, R., Weeks, E.R., Schofield, A.B., and Poon, W.C.K. Three-Dimensional Imaging of Colloidal Glasses under Steady Shear. *Phys. Rev. Lett.*, 99(2), 2007.

[312] Adrian, R.J. Twenty years of particle image velocimetry. *Exp. Fluids*, 39(2):159–169, 2005.

[313] Smith, P., Petekidis, G., Egelhaaf, S., and Poon, W. Yielding and crystallization of colloidal gels under oscillatory shear. *Phys. Rev. E*, 76(4):041402, 2007.

[314] Chaikin, P.M. and Lubensky, T.C. *Principles of Condensed Matter Physics.* Cambridge University Press, 1995.

[315] Russel, W.B., Saville, D.A., and Schowalter, W.R. *Colloidal Dispersions.* Cambridge University Press, 1999.

[316] Timmermans, J. Plastic crystals: a historical overview. *J. Phys. Chem. Solids*, 18(1):1–8, 1961.

[317] Sherwood, J.N. *The Plastically Crystalline State: Orientationally Disordered Crystals.* Wiley, 1979.

[318] Riley, E.K. and Liddell, C.M. Confinement-controlled self assembly of colloids with simultaneous isotropic and anisotropic cross-section. *Langmuir*, 26(14):11648–56, 2010.

[319] Mock, E.B. and Zukoski, C.F. Determination of static microstructure of dilute and concentrated suspensions of anisotropic particles by ultra-small-angle X-ray scattering. *Langmuir*, 23(17):8760–71, 2007.

[320] Wojciechowski, K.W., Frenkel, D., and Branka, A.C. Nonperiodic solid phase in a two-dimensional hard-dimer system. *Phys. Rev. Lett.*, 66(24):3168–3171, 1991.

[321] Ungar, G. Structure of rotator phases in n-alkanes. *J. Phys. Chem.*, 197(1):689–695, 1983.

[322] Vega, C. and Monson, P.A. Plastic crystal phases of hard dumbbells and hard spherocylinders. *J. Chem. Phys.*, 107(7):2696, 1997.

[323] Marechal, M. and Dijkstra, M. Stability of orientationally disordered crystal structures of colloidal hard dumbbells. *Phys. Rev. E*, 77(6):061405, 2008.

[324] Uhlenbeck, G.E. and Ornstein, L.S. On the theory of the Brownian motion. *Phys. Rev.*, 36:823–841, 1930.

[325] Imhof, A. Private communication. 2014.

[326] Weiss, J.A., Larsen, A.E., and Grier, D.G. Interactions, dynamics, and elasticity in charge-stabilized colloidal crystals. *J. Chem. Phys.*, 109(19):8659, 1998.

[327] Hsu, M.F., Dufresne, E.R., and Weitz, D.A. Charge stabilization in nonpolar solvents. *Langmuir*, 21(11):4881–7, 2005.

[328] Schweizer, K. Dynamical fluctuation effects in glassy colloidal suspensions. *Curr. Opin. Colloid Interface Sci.*, 12(6):297–306, 2007.

[329] Kramb, R.C., Zhang, R., Schweizer, K.S., and Zukoski, C.F. Glass Formation and Shear Elasticity in Dense Suspensions of Repulsive Anisotropic Particles. *Phys. Rev. Lett.*, 105(5):055702, 2010.

[330] Renner, C., Löwen, H., and Barrat, J. Orientational glass transition in a rotator model. *Phys. Rev. E*, 52(5):5091–5099, 1995.

[331] Leunissen, M.E. and van Blaaderen, A. Concentrating colloids with electric field gradients. II. Phase transitions and crystal buckling of long-ranged repulsive charged spheres in an electric bottle. *J. Chem. Phys.*, 128(16):164509, 2008.

[332] Kogan, M., Dibble, C.J., Rogers, R.E., and Solomon, M.J. Viscous solvent colloidal system for direct visualization of suspension structure, dynamics and rheology. *J. Colloid Interface Sci.*, 318(2):252–63, 2008.

[333] Lorenzi, L.D., Fermeglia, M., and Torriano, G. Density, refractive index, and kinematic viscosity of diesters and triesters. *J. Chem. Eng. Data*, 42:919–923, 1997.

[334] Wypych, G. *Handbook of plasticizers.* ChemTec Publishing, 2004.

[335] Lorenzi, L.D., Fermeglia, M., and Torriano, G. Density, kinematic viscosity, and refractive index for bis (2-ethylhexyl) adipate, tris (2-ethylhexyl) trimellitate, and diisononyl phthalate. *J. Chem. Eng. Data*, 43:183–186, 1998.

[336] Myroshnychenko, V., Rodríguez-Fernández, J., Pastoriza-Santos, I., Funston, A.M., Novo, C., Mulvaney, P., Liz-Marzán, L.M., and García de Abajo, F.J. Modelling the optical response of gold nanoparticles. *Chem. Soc. Rev.*, 37(9):1792–805, 2008.

[337] Wang, T., Zhuang, J., Lynch, J., Chen, O., Wang, Z., Wang, X., LaMontagne, D., Wu, H., Wang, Z., and Cao, Y.C. Self-assembled colloidal superparticles from nanorods. *Science*, 338(6105):358–63, 2012.

[338] Kang, K. and Dhont, J.K.G. Electric-field induced transitions in suspensions of charged colloidal rods. *Soft Matter*, 6(2):273, 2010.

[339] Ediger, M. Spatially heterogeneous dynamics in supercooled liquids. *Annu. Rev. Phys. Chem.*, pages 99–128, 2000.

[340] Götze, W. Recent tests of the mode-coupling theory for glassy dynamics. *J. Phys. Condens. Matter*, 11:1–45, 1999.

[341] Anderson, P.W. Through the Glass Lightly. *Science*, 267(5204):1615, 1995.

[342] Hunter, G.L. and Weeks, E.R. The physics of the colloidal glass transition. *Rep. Prog. Phys.*, 75(6):066501, 2012.

[343] Mattsson, J., Wyss, H.M., Fernandez-Nieves, A., Miyazaki, K., Hu, Z., Reichman, D.R., and Weitz, D.A. Soft colloids make strong glasses. *Nature*, 462(7269):83–6, 2009.

[344] Chen, K., Ellenbroek, W.G., Zhang, Z., Chen, D.T.N., Yunker, P.J., Henkes, S., Brito, C., Dauchot, O., van Saarloos, W., Liu, A.J., and Yodh, A.G. Low-Frequency Vibrations of Soft Colloidal Glasses. *Phys. Rev. Lett.*, 105(2):025501, 2010.

[345] Pham, K., Egelhaaf, S., Pusey, P., and Poon, W. Glasses in hard spheres with short-range attraction. *Phys. Rev. E*, 69(1):011503, 2004.

[346] van der Linden, M.N., El Masri, D., Dijkstra, M., and van Blaaderen, A. Expansion of charged colloids after centrifugation: formation and crystallisation of long-range repulsive glasses. *Soft Matter*, 9(48):11618, 2013.

[347] van der Linden, M. *Long-range repulsive charged colloids in and out of equilibrium.* Ph.D. thesis, Utrecht University, 2013.

[348] Michele, C.D., Schilling, R., and Sciortino, F. Dynamics of uniaxial hard ellipsoids. *Phys. Rev. Lett.*, 265702:2–5, 2007.

[349] Pfleiderer, P., Milinkovic, K., and Schilling, T. Glassy dynamics in monodisperse hard ellipsoids. *EPL*, 84(1):16003, 2008.

[350] de Michele, C., Schilling, R., and Sciortino, F. Simulation of the dynamics of hard ellipsoids. *Philos. Mag.*, 88(33-35):4117–4123, 2008.

[351] Zhang, R. and Schweizer, K. Theory of coupled translational-rotational glassy dynamics in dense fluids of uniaxial particles. *Phys. Rev. E*, 80(1):011502, 2009.

[352] Zheng, Z., Ni, R., Wang, F., Dijkstra, M., Wang, Y., and Han, Y. Structural signatures of dynamic heterogeneities in monolayers of colloidal ellipsoids. *Nat. Commun.*, 5:3829, 2014.

[353] Kang, K. and Dhont, J.K.G. Glass Transition in Suspensions of Charged Rods: Structural Arrest and Texture Dynamics. *Phys. Rev. Lett.*, 110(1):015901, 2013.

[354] Kang, K. Glass transition of repulsive charged rods (fd-viruses). *Soft Matter*, 2014.

[355] Bermejo, F.J., Jiménez-Ruiz, M., Criado, A., Cuello, G.J., Cabrillo, C., Trouw, F.R., Fernández-Perea, R., Löwen, H., and Fischer, H.E. Rotational freezing in plastic crystals: a model system for investigating the dynamics of the glass transition. *J. Phys. Condens. Matter*, 12:391–397, 2000.

[356] Rycroft, C.H. VORO++: a three-dimensional voronoi cell library in C++. *Chaos*, 19(4):041111, 2009.

[357] Rotunno, M., Bellini, T., Lansac, Y., and Glaser, M.a. Phase behavior of polarizable spherocylinders in external fields. *J. Chem. Phys.*, 121(11):5541–9, 2004.

[358] Venermo, J. and Sihvola, A. Dielectric polarizability of circular cylinder. *J. Electrostat.*, 63(2):101–117, 2005.

A

Electric Field Induced Dipole-Dipole Interactions

In this appendix, we estimate the electric-field induced dipole-dipole pair interaction potential as a function of field strength and rod-rod separation, which can also be found in the Supplementary Information of Ref. 186. The shape of our rods is nearly a spherocylinder with a length l (end to end) and a diameter d. To simplify the calculation, we make four assumptions:

1. a dipole is regarded as two point charges with a separation of $(l-d)$ at a distance $d/2$ from the two ends [357].
2. the dipole moment is only induced by the applied electric field, and not influenced by its neighbours or its surface charge (double layer)
3. the long axis of the rods has the same orientation as the field
4. the rods cannot overlap

The dielectric polarizability of a particle is dependent on its shape. However, they are not easily analytically solved except for some simple geometries such as spheres and ellipsoids [358]. A numerical approach is probably needed for other more complicated particle shapes such as for the spherocylinder shape of our rods. For simplification, we use an ellipsoidal approximation of our spherocylinder rods to estimate their dielectric polarizability. A numerical study has already shown that the polarizability of a circular cylinder differs less than 10% from that of an ellipsoid with the same volume and aspect ratio [358]. Therefore, we also expect that such an approximation is reasonable for our particles. Based on the following calculation results that the maximum interaction potential is at most on the order of k_BT, we think that the difference in shape does not change the results significantly.

The dipole moment p of a colloidal particle is the product of the polarizability α_e and the applied field E

$$p = \alpha_e E \tag{A.1}$$

The normalized polarizability is given as:

$$\alpha = \frac{\alpha_e}{\epsilon_s v_p} \tag{A.2}$$

with ϵ_s the dielectric constant of the solvent and v_p the particle volume. For a prolate ellipsoid, with three orthogonal semi axes of a_x, a_y, and a_z, with $a_y = a_z$, the polarizability in the a_x direction is given by [358]

$$\alpha_x = \frac{\epsilon_p - \epsilon_s}{\epsilon_s + (\epsilon_p - \epsilon_s)N_x} \tag{A.3}$$

$$N_x = \frac{1-e^2}{2e^3}\Big(\ln\frac{1+e}{1-e} - 2e\Big) \tag{A.4}$$

$$e = \sqrt{1-(a_y/a_x)^2} \tag{A.5}$$

Where ϵ_p is the dielectric constant of the particle, N_x is called the depolarization factor in the a_x direction, and e is the eccentricity of the ellipsoid. For the other depolarization factors N_y or N_z, interchange a_x, a_y, and a_z. We estimate the point charge q from the effective dipole moment p_{eff} by

$$q = \frac{p_{eff}}{l-d} \tag{A.6}$$

Next, we calculate the pair interaction energy of two aligned rods along the electric field separated by a distance r using Coulomb's law

$$U_{dip} = \frac{1}{4\pi\epsilon_0\epsilon_s}\sum_{i\neq j,\alpha,\beta}\frac{q_{i_\beta}q_{j_\alpha}}{r_{i_\beta} - r_{j_\alpha}}. \tag{A.7}$$

Equation (A.7) can be further expanded to formula (A.8), where θ is the angle between the center-to-center direction of the two rods and the electrical field.

$$U_{dip} = \frac{q^2}{4\pi\epsilon_s\epsilon_0}\Big(\frac{2}{r} - \frac{1}{\sqrt{r^2\sin^2\theta + (r\cos\theta-(l-d))^2}} - \frac{1}{\sqrt{r^2\sin^2\theta + (r\cos\theta+(l-d))^2}}\Big) \tag{A.8}$$

Using equation (A.8), we plot U_{dip} as a function of θ (0 - 2π) (see Fig. A.1) with four different center-to-center distances r. The curves indicate that U_{dip} is dependent on both θ, r and E_{rms}. For constant r, the maximum attractive potential occurs for $\theta = 0$ or $\theta = \pi$, which corresponds to a head-to-toe arrangement, and the maximum repulsive potential occurs for $\theta = \pi/2$ or $3\pi/2$, which corresponds to a side-by-side arrangement. These interactions are less than 1 k_BT if $r/l > 1.5$ for the head-to-toe structure and if $r/l > 1$ for rods in side-by-side structure, with l the end-to-end length of the rod (see Fig. A.2). For the highest fields used, $E_{rms} = 400$ V/mm, the maximum attractive U_{dip} is only around 1.26 k_BT for $r = 3$ μm (corresponding to $\phi \sim 0.02$) at θ equal to 0 or π. Furthermore, when ϕ is lower, then r is larger, for example, $r = 5.7$ μm for $\phi \sim 0.005$. In this case, the U_{dip} is two orders of magnitude lower than the thermal energy. Additionally, for the quantitative measurements in the high volume fraction range in Chapter 9 ($\phi \sim 0.02$), the field strength was always < 100 V/mm. These results suggest that the electric-field-induced dipole-dipole interactions are considerably less than 1 k_BT even at the highest field strengths used. Therefore, dipole-dipole interactions are negligible in the experiments described in Chapter 8 and Chapter 9.

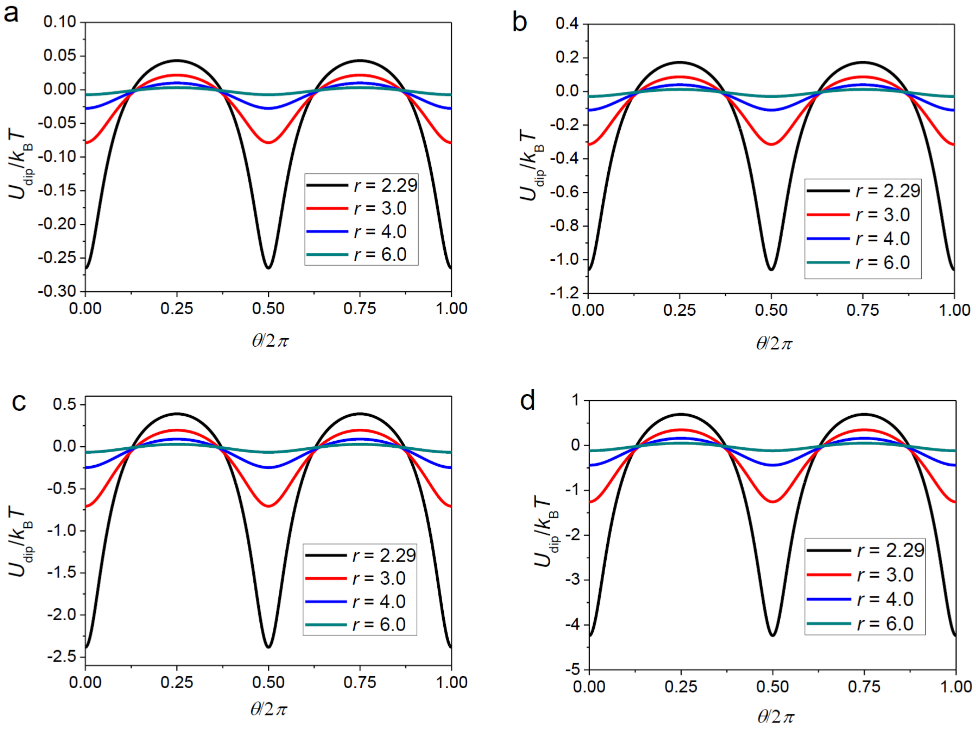

Figure A.1. The dipole-dipole interaction potential as a function of the angle between the center-to-center direction and the applied field. (a) $E_{rms} = 100$ V/mm. (b) $E_{rms} = 200$ V/mm. (c) $E_{rms} = 300$ V/mm. (d) $E_{rms} = 400$ V mm. The model parameters are: $l = 2.29$ μm, $d = 0.6$ μm, $\epsilon_{rod} = 4.5$ and $\epsilon_{CHC} = 7.4$.

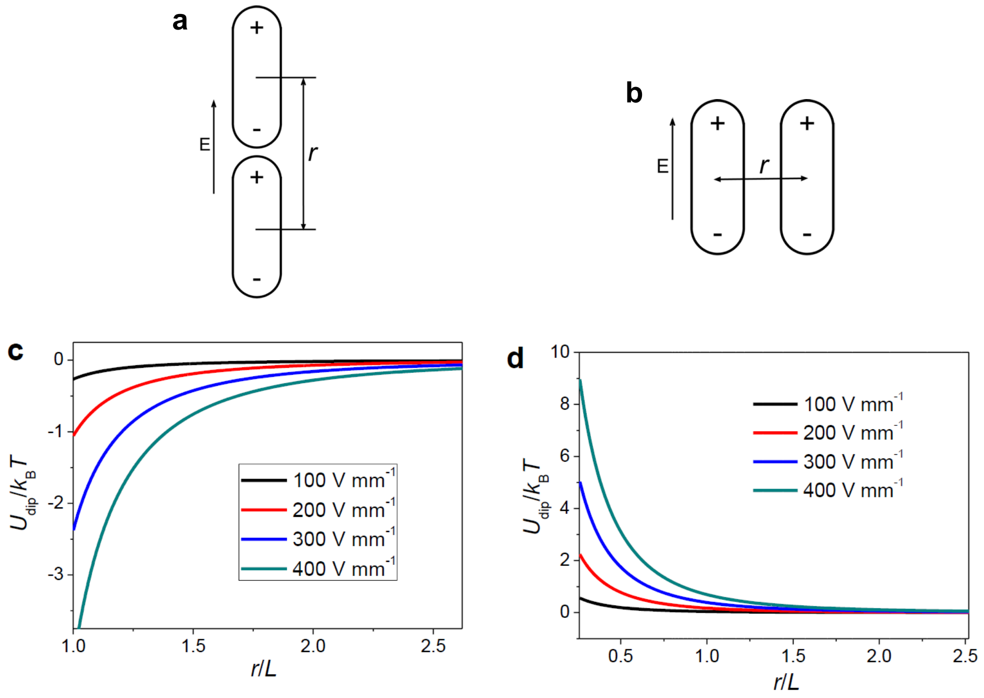

FIGURE A.2. The dipole-dipole interaction potential as a function of the rod-rod separation at a fixed center-to-center direction. (a,c) parallel to and (b,d) perpendicular to the applied electric field. The model parameters are: $l = 2.29$ μm, $d = 0.6$ μm, $\epsilon_{rod} = 4.5$ and $\epsilon_{CHC} = 7.4$.

B

Supporting Movies

Digital version only: please click on the movie titles for playback

B.1. OUT-OF-EQUILIBRIUM CRYSTALLIZATION IN HARD-SPHERE COLLOIDAL FLUIDS DRIVEN BY OSCILLATORY SHEAR

Confocal microscopy time-series are shown of oscillatory shear-induced crystallization of spherical particles with diameter $\sigma = 2.07$ μm and polydispersity $\delta = 3.0\,\%$. The particles were in a fluid phase in equilibrium with volume fraction $\phi = 0.49 \pm 0.01$. The images show a view of the velocity-vorticity plane and were acquired at the zero velocity plane. The shear was started at $t = 0$.

1. **Formation of a shear-induced oscillatory twinned fcc phase**
   An oscillatory twinned fcc phase was induced by applying oscillatory shear with Peclet number $Pe = 0.5$ and maximum strain amplitude $\gamma_{max} = 0.3$. The time-series were recorded with 2.4 fps and displayed with 10 fps. The field-of-view is 60×63 μm^2.

2. **Formation of a shear-induced sliding layer phase**
   A sliding layer phase was induced by applying oscillatory shear with Peclet number $Pe = 0.5$ and maximum strain amplitude $\gamma_{max} = 0.6$. The time-series were recorded with 2.4 fps and displayed with 10 fps. The field-of-view is 58×62 μm^2.

   Confocal microscopy time-series are shown of melting of the shear-induced crystalline phases due to cessation of the shear. The particles had a diameter $\sigma = 2.64$ μm and polydispersity $\delta = 2.5\,\%$. The images show a view of what was previously the velocity-vorticity plane and were acquired in the middle of the shear cell.

3. **Melting of an oscillatory twinned fcc phase after cessation of the shear**
   An oscillatory twinned fcc phase was induced by applying oscillatory shear with

Peclet number $Pe = 2.0$ and maximum strain amplitude $\gamma_{max} = 0.3$ for a duration of 150 τ_B. At $t = 0$ the shear was stopped. The volume fraction $\phi = 0.46 \pm 0.02$. The time-series were recorded with 0.6 fps and displayed with 10 fps. The field-of-view is 122 × 122 μm^2.

4. **Melting of a sliding layer phase after cessation of the shear**
   A sliding layer phase was induced by applying oscillatory shear with Peclet number $Pe = 1.0$ and maximum strain amplitude $\gamma_{max} = 0.6$ for a duration of 79 τ_B. At $t = 0$ the shear was stopped. The volume fraction $\phi = 0.47 \pm 0.02$. The time-series were recorded with 1.2 fps and displayed with 20 fps. The field-of-view is 122 × 122 μm^2.

B.2. RHEOLOGY AND REAL-SPACE ANALYSIS OF COLLOIDAL SILICA RODS UNDER SHEAR

Confocal microscopy times-series are shown of a suspension of rod-like particles under shear. The particles had an end-to-end length $l = 5.2$ μm (11 %), diameter $d = 0.67$ μm (8 %) and aspect ratio $l/d = 7.8$, dispersed in 85 wt% glycerol water (viscosity $\eta =$ 92 cP). The initial volume fraction of the suspension was $\phi = 0.25$. Steady shear was applied with a cone-plate rheometer with a transparent bottom plate that allowed for confocal microscopy imaging. The movies show a view of the velocity-vorticity plane. Images were shifted backwards with a magnitude equal to the average displacement, i.e. the movies show a view of the frame that moves with the average speed of the suspension. The field-of-view is 37 × 37 μm^2.

1. **Shear rate $\dot{\gamma} = 1$ s^{-1}**
   Images were recorded 20 μm above the bottom plate with 71 fps. The movie is displayed at 15 fps.
2. **Shear rate $\dot{\gamma} = 2$ s^{-1}**
   Images were recorded 4 μm above the bottom plate with 10 fps. The movie is displayed at 15 fps.
3. **Shear rate $\dot{\gamma} = 5$ s^{-1}**
   Images were recorded 4 μm above the bottom plate with 10 fps. The movie is displayed at 15 fps.

B.3. SWITCHING PLASTIC CRYSTALS OF COLLOIDAL RODS WITH ELECTRIC FIELDS

Confocal microscopy time-series are shown of long-range repulsive silica rods dispersed in de-ionized cyclohexylchloride (CHC). All time-series show a view of the *xy*-plane (perpendicular to gravity).

1. **Brownian motion of rods in a plastic crystal phase.**
   The movie shows the bcc(110) plane of a plastic crystal of colloidal rods. The rods have length $l = 2.36$ μm (6.3 %), diameter $d = 0.58$ μm (10.6 %) and aspect ratio

$l/d = 4.1$ (system R1). The movie was taken at 0.5 fps and displayed at 10 fps. The window size is 71.2 μm × 71.2 μm.

2. **Rotational trajectory of a single rod in a plastic crystal**
   The rotational trajectory is shown of a rod with length $l = 2.29$ μm (6.0 %), diameter $d = 0.60$ μmm (6.5 %) and aspect ratio $l/d = 3.8$ (system R2). The movie was taken in x-y-z-t mode at 69.1 fps and displayed in x-y-t mode at 15.4 fps. The window size is 24.9 μm × 17.8 μm.

3. **A plastic glass of rods**
   Brownian motion of rods R1 in a plastic glass phase is shown. The movie was taken at 1.22 fps and displayed at 6 fps. The window size is 59.5 μm × 59.5 μm.

4. **Slow switching of a plastic crystal**
   A slow electric field switch is shown between the ON-state (same orientation) and the OFF-state (random orientation). It shows a slow alignment of rods R2 in a (110) plane in a plastic BCC phase in response to an electric field. The field strength increases first to 59.6 V/mm and then decreases to zero in steps. The nematic order parameter increased and decreased correspondingly. The movie was taken at 1 fps and displayed at 20 fps. The window size is 68.0 μm × 68.0 μm.

5. **Fast switching of a plastic crystal**
   A fast electric field switch is shown between the ON-state (same orientation) and OFF-state (random orientation). This movie shows a fast on-off response of rods R2 in a BCC(110) plane of a plastic crystal phase by using an external field. The field was quickly switched on and off by pressing a button. The nematic order parameter quickly changed correspondingly. The movie was taken at 1 fps and displayed at 5 fps.

B.4. PLASTIC GLASS TO CRYSTAL TRANSITION IN A SYSTEM OF LONG-RANGE REPULSIVE RODS

Confocal microscopy time-series are shown of long-range repulsive silica rods dispersed in de-ionized cyclohexylchloride (CHC). The particles had an average length $l = 2.29$ μm (6.0 %), diameter $d = 0.60$ μmm (6.5 %) and aspect ratio $l/d = 3.8$ (system R2). Both time-series show a view of the xy-plane (perpendicular to gravity). Due to the high (effective) volume fraction, the particles failed to crystallize into a plastic crystal, but instead formed a 'plastic glass'.

1. **'Plastic glass' to crystal transition**
   An AC electric field (1 MHz, perpendicular to the field-of-view) was turned on slowly by hand (in ~ 5 s) to $E = 90$ V/mm. Crystalline regions slowly started to form. The movie was recorded with 2 fps and displayed with 8 fps. The total timespan of

the movie is 500 s. The field-of-view is 66 × 66 μm^2.

2. **Crystal to ‘plastic glass’ transition**
   After approximately 1 hour, the sample was completely crystalline, and the electric field (E = 90 V/mm) was turned off again. The crystal melted within minutes. The movie was recorded with 10 fps and displayed with 10 fps. The total timespan of the movie is 100 s. The field-of-view is 66 × 66 μm^2.

Summary

Colloidal particles are applied throughout industry, for example in paints, food, personal care products, ceramics and pharmaceutics. The characterization of the structure and dynamics of colloidal suspensions is therefore important for many industrial applications. Besides their industrial significance, colloids can also be used as a valuable model system to study fundamental questions in condensed matter physics. Because of their size, colloids are much slower than atoms or simple molecules, yet they can display the same equilibrium phase behavior. Furthermore, colloids are easily manipulated with external fields and they are large enough to be observed in real-space with an optical microscope. Phenomena such as crystallization, the glass transition and flow-induced behavior of spherical colloids have been extensively studied in 3D real-space over the last decades. However, despite the recent increase in synthesis methods that produce (shape) anisotropic colloids, quantitative 3D real-space studies of anisotropic colloids still remain scarce. In this thesis, we therefore investigated the self-assembly of not only colloidal spheres but also of suspensions of (shape anisotropic) colloidal rods. The colloidal spheres consisted of poly(methyl methacrylate) (PMMA), the rod-like particles consisted of silica and both particles were fluorescently labeled. In analogy with the spherical particles, we developed a new image processing method that allowed us to study the rod-like particles in 3D real-space on the single particle level using confocal microscopy. We manipulated and directed their self-assembly process by application of three external fields: shear, gravity, and electric fields.

This thesis is organized in two parts. In the first part, consisting of Chapters 2 - 4, we described the methodology that we developed to analyse the structure of colloidal suspensions in real-space. In the second part of this thesis, consisting of Chapters 5 - 9, we investigated the self-assembly of spherical and rod-like particles in external fields on the single particle level.

In **Chapter 2** we first described the general properties of the colloidal suspensions presented in this thesis and we described the imaging techniques that we applied to investigate their self-assembly. We used colloidal spheres, consisting of poly(methyl methacrylate) (PMMA) dispersed in a mixture of *cis*-decahydronaphthalene (*cis*-decalin) in cyclohexyl bromide (CHB) saturated with the salt tetrabutylammonium bromide (TBAB). We also used rod-like silica particles which were dispersed in either a mixture of glycerol and water, a mixture of dimethylsulfoxide (DMSO) and water or in pure (de-ionized) cyclohexylchloride (CHC). In this chapter, we also described the basics of

confocal microscopy imaging and the effect of the point spread function (PSF) on the imaging of rod-like particles.

In **Chapter 3** we presented two methods to calibrate axial distances in 3D confocal microscopy that are both accurate and easily implemented. Often, there is a refractive-index mismatch between the sample and the immersion fluid used for imaging, resulting in a distortion of axial distances. Using one of our calibration methods, we measured the axial scaling factors as a function of refractive-index mismatch for high-aperture confocal microscopy imaging. We found that our scaling factors are almost completely linearly dependent on refractive index and that they were in good agreement with theoretical predictions that take the full vectorial properties of light into account. There was however a strong deviation from the theoretical predictions using (high-angle) geometrical optics, which predict much lower scaling factors.

In **Chapter 4** we presented a new particle-fitting algorithm that can extract the positions and orientations of fluorescent rod-like particles from three dimensional confocal microscopy data stacks. The algorithm is tailored to work even when the fluorescent signals of the particles overlap considerably and a threshold method and subsequent clusters analysis alone do not suffice. We demonstrated that our algorithm correctly identified all five coordinates of uniaxial particles in both a concentrated disordered phase and a liquid-crystalline smectic-B phase. The algorithm also worked on confocal microscopy images of other uni-axial symmetric particles such as dumbbells and on 3D electron tomography reconstructions of gold nanorods. We also gave examples of position and orientation fitting from 2D images of concentrated 3D samples of silica rods and PMMA dumbbells. Lastly, we determined the accuracy of the algorithm using both simulated and experimental confocal microscopy data-stacks of diffusing silica rods in a dilute suspension.

We studied the oscillatory shear-induced crystallization in hard-sphere colloidal fluids in **Chapter 5**. We performed experiments on PMMA colloids and non-equilibrium Brownian Dynamics (NEBD) simulations. All samples in both experiments and simulation were *below* the coexistence density of hard-sphere freezing, so the shear induced crystals were out-of-equilibrium and melted after cessation of the shear. The physics was therefore fundamentally different from shear-induced crystallization in jammed or glassy systems. We investigated two distinct oscillatory shear-induced phases: an oscillatory twinned fcc phase and a sliding layer phase. For the twinned fcc phase, the crystallization seemed to proceed via a nucleation-and-growth type of mechanism. For the sliding layer phase, however, we found a much more continuous crystallization process. The simulation results (without hydrodynamic interactions and an enforced linear shear profile) were in strong agreement with the experiments, suggesting that hydrodynamic interactions did not strongly affect the shear-induced structures. We also presented preliminary experimental results on the melting of these phases, which occurred immediately after cessation of the shear.

In **Chapter 6** we investigated the phase behavior of fluorescent rod-like silica particles in a gravitational field. When left to sediment, these particles formed equilibrium liquid crystal phases, such as nematic and smectic phases. With confocal microscopy and our new particle fitting algorithm we determined all 3D positions and orientations of these particles, even in the most concentrated liquid crystal phases, for aspect ratios up to $l/d = 5.4$. We found a smectic-B phase with small regions of AAA-stacked crystalline layers. Additionally, we determined the complete equilibrium density profile of a sediment of coexisting isotropic and smectic-B phases in 3D real-space. At the isotropic - smectic-B interface, we found a difference between the inflection points of the density and the nematic order parameter, which agrees well with theoretical predictions. We also measured the 2D (projected) orientation distributions of both nematic and smectic phases of particles with aspect ratio $l/d > 7$. We compared our results to theory and simulations on both hard and soft spherocylinders and found a reasonable to good agreement. At the end of the chapter we also presented preliminary results on super-resolution imaging of a smectic phase.

The phase behaviour of the fluorescent silica rods under shear was investigated in **Chapter 7**. We used two different shear cell configurations that both allowed simultaneous confocal microscopy measurements to be made while the system was sheared. Steady shear flow was successfully applied to align rods with an aspect ratio $l/d = 6.0$, and create shear-aligned para-nematic and para-columnar liquid crystal phases. The application of oscillatory shear led to the formation of para-smectic-like domains in a sample that was previously in a shear-aligned para-nematic state. Rheological measurements on rod-like particles, with aspect ratio $l/d = 7.8$ and initial volume fraction $\phi \sim 0.3$, were characterized by pronounced shear thinning behaviour, a Newtonian regime and (the onset of) shear-thickening for increasing shear rate. However, we could not directly correlate the rheological measurements with the suspension microstructure. Although these experiments were only preliminary, they gave a strong indication that shear is a powerful external field to align colloidal liquid crystal phases over larger areas, which could for instance be applied in spin coating.

In the last two chapters of this thesis, we changed the interaction potential of the silica rods from hard to long-range repulsive by strongly lowering the salt concentration of the solvent. In **Chapter 8** we demonstrated by quantitative three-dimensional studies that these charged rod-like colloidal particles formed three-dimensional plastic crystals (or rotator phases) and plastic glasses if their repulsions extended significantly beyond their length. We also showed that these plastic phases could be reversibly switched to full crystals by an electric field. These new phases provide insight into the role of rotations in phase behaviour and could be useful for photonic applications.

In **Chapter 9**, we further investigated the plastic glass phase formed by the long-range repulsive silica rods. In this phase, particles lacked long-ranged positional order and translational motion was frozen-in, whereas rotational motion remained almost free. This phenomenon is a remarkable demonstration of the decoupling of the glass transitions associated with the positional and rotational degrees of freedom. Moreover, this glassy phase could completely crystallize into a stretched body-centered-cubic (bcc) lattice upon application of an AC electric field. Intriguingly, when the field was turned off, the crystal became unstable and the sample returned to the plastic glass phase. The ability to follow the 3D rotations of the particles quantitatively in real-space gives unprecedented possibilities to study this new type of glass transition and its connection to crystallization.

Samenvatting voor een breder publiek

In dit proefschrift staat onderzoek beschreven op het gebied van *colloïdale suspensies*. Dit zijn mengsels die bestaan uit kleine deeltjes van ongeveer een micrometer groot, die zich bevinden in een vloeistof. Hoewel de term 'colloïdale suspensie' (of kortweg 'colloïd') over het algemeen niet erg bekend is, zijn we er elke dag mee in aanraking. Vele voedselproducten zijn colloïden, zoals melk, mayonaise en boter, maar ook cosmetische producten zoals scheerschuim en gezichtscrème zijn voorbeelden van colloïden. Verder behoren bijvoorbeeld ook verf, boorvloeistof en klei tot de colloïden. Bovendien worden colloïden toegepast in moderne elektronica, zoals de elektronische inkt in e-readers. Het begrijpen van de eigenschappen van colloïden is daarom belangrijk voor een groot aantal sectoren in de industrie.

Hoewel de eigenschappen van de deeltjes in de vloeistof erg kunnen verschillen per colloïd, hebben ze een belangrijke overeenkomst: door continue botsingen met de moleculen in de vloeistof zijn de deeltjes voortdurend in beweging. De richting waarin de deeltjes zich bewegen is echter volledig willekeurig en verandert ook voortdurend. Deze willekeurige manier van beweging staat bekend als 'Brownse beweging', maar wordt ook wel 'dronkemansloop' genoemd. Echter, onder de juiste condities kunnen deze willekeurig bewegende deeltjes zich spontaan ordenen in regelmatige structuren. Dit heet *zelforganisatie*. Sommige colloïden kunnen zelfs vergelijkbare of dezelfde structuren vormen als atomen of moleculen. Hoewel de individuele deeltjes in een colloïdale suspensie niet te zien zijn met het blote oog, zijn ze wel een factor duizend groter dan atomen of eenvoudige moleculen. Ze kunnen daardoor direct worden bekeken met een optische microscoop, wat analyse van hun structuur tot in detail mogelijk maakt. Bovendien zijn de bewegingen van colloïdale deeltjes veel langzamer dan die van atomen, wat het mogelijk maakt om ze een lange tijd te volgen tijdens een experiment. Daarom worden colloïdale suspensies ook wel gezien als een *modelsysteem* voor onderzoek naar fundamentele vragen in de natuurkunde van zowel vloeistoffen als vaste stoffen.

In dit proefschrift hebben we colloïdale modelsystemen gebruikt om verschillende vormen van zelforganisatie te onderzoeken. Het is bekend dat de zelforganisatie sterk afhangt van de vorm van de deeltjes en van hun onderlinge interactie. Het meeste simpele en veelgebruikte modelsysteem bestaat daarom uit colloïdale bollen die, behalve dat ze niet indrukbaar zijn, geen onderlinge interactie hebben, zogenoemde 'harde bollen'. Als de bollen niet te veel verschillen in grootte en het systeem in thermodynamisch evenwicht is, zijn er maar twee toestanden mogelijk waarin het zich kan bevinden: een vloeistof bij lage dichtheid (die wanordelijk is) en een kristal bij hoge dichtheid (die volledig geordend is). In dit proefschrift hebben we echter ook een recent ontwikkeld modelsysteem gebruikt van harde *staafvormige* colloïden. Dit systeem kan een rijkdom aan nieuwe structuren vormen. Staafvormige colloïden kunnen namelijk structuren (of fasen) vormen die deels eigenschappen hebben van een vloeistof en deels die van een kristal. Dit worden daarom 'vloeibare kristallen' genoemd. Zo kunnen staafvormige deeltjes in een *nematische fase* verkeren, waarin de oriëntaties van de deeltjes geordend zijn, maar de posities nog steeds wanordelijk zijn. Bij hogere dichtheden, kunnen de deeltjes zich vervolgens ook positioneel ordenen door lagen te vormen. Men spreekt dan van een *smectische fase*. Afhankelijk van de orde binnen de lagen bestaat er een reeks aan verschillende smectische fasen. Voor nog hogere dichtheden, stapelen de lagen precies regelmatig op elkaar en is er sprake van een kristal. De bekendste toepassing van vloeibare kristallen (gemaakt van staafvormige moleculen) is overigens in LCD-schermen (Liquid Crystal Displays).

Behalve door de vorm van de deeltjes, kan de zelforganisatie ook sterk worden bepaald door invloeden van buitenaf. In dit proefschrift gebruiken we daarom in totaal drie verschillende *externe velden* om de zelforganisatie te sturen, te weten: zwaartekracht, een elektrisch veld en (vloeistof)stroming. Deze externe (kracht)velden hebben invloed op de positionele orde van de deeltjes. In het geval van de staafjes kunnen de externe velden ook gebruikt worden om de oriëntaties van de deeltjes te beïnvloeden.

Zowel de bollen als de staven hebben we een fluorescente kleurstof gegeven, zodat ze kunnen worden bestudeerd met behulp van *confocale microscopie*. In vergelijking met een normale microscoop heeft de confocale microscoop een hogere resolutie en is er de mogelijkheid om 3D beelden te maken van de deeltjes in de vloeistof. Met computeralgoritmes kunnen vervolgens de posities (en de oriëntaties) van de deeltjes worden bepaald op basis van de 3D beelden. Zo is het mogelijk om een *3D reconstructie* te maken van de structuur van het systeem en om lokale orde in detail te analyseren.

Dit proefschrift bestaat uit twee delen. In het eerste deel, bestaande uit Hoofdstukken 2 - 4, worden de methodes beschreven die we hebben ontwikkeld om de structuur van onze colloïdale modelsystemen te analyseren met behulp van confocale microscopie. In het tweede deel van deze thesis, bestaande uit Hoofdstukken 5 - 9, hebben we de zelforganisatie van colloïdale bollen en staven in externe velden onderzocht op het niveau van individuele deeltjes.

In **Hoofdstuk 2** beschreven we allereerst de algemene eigenschappen van de colloïdale suspensies die we hebben gebruikt. We maakten gebruik van colloïdale bollen, gemaakt van poly(methyl methacrylaat) (PMMA, ook wel bekend als plexiglas) in een mengsel van de organische oplosmiddelen. Voor het modelsysteem van staafvormige deeltjes gebruikten we een recent ontwikkelde synthese, waarmee je staafjes van silica (het belangrijkste bestanddeel van glas) kan maken. Voor de staven gebruikten we zowel organische als anorganische oplosmiddelen. In dit hoofdstuk beschreven we ook het gebruik van confocale microscopie om fluorescente colloïden te bestuderen.

In **Hoofdstuk 3** presenteerden we twee methoden om de afstanden in 3D confocale microscopie te ijken. Het licht dat gebruikt wordt om de colloïden af te beelden moet door verschillende materialen heen voordat het op een sensor valt en er een beeld van wordt gemaakt. Vaak is er een onderling verschil in hoe sterk deze materialen het licht afbuigen, wat resulteert in een vertekening van het beeld (denk aan de vertekening die je ziet bij een rietje in een glas water). Met behulp van onze ijk-methoden hebben we de grootte van de vertekening (of afwijking) gemeten voor verschillende materialen. Daardoor is het toch mogelijk om nauwkeurig de werkelijke afstanden en volumes te bepalen in de colloïdale suspensies.

We ontwikkelden ook een nieuw computer-algoritme om de posities en oriëntaties te bepalen van de staafvormige deeltjes aan de hand van 3D digitale beelden, beschreven in **Hoofdstuk 4**. Het algoritme was toegespitst om zelfs nog te werken als de fluorescente signalen van de deeltjes sterk overlappen en simpele methoden op basis van een drempelwaarde niet meer toereikend zijn. We hebben aangetoond dat we met behulp van het algoritme de coördinaten van alle staven konden bepalen, zowel in een geconcentreerde wanordelijke fase als in een smectische-B fase. We hebben ook de nauwkeurigheid van het algoritme bepaald aan de hand van gesimuleerde en experimentele beelden van de Brownse beweging van individuele staafjes.

Hoofdstukken 5 - 9 bevatten toepassingen van deze technieken. In **Hoofdstuk 5** hebben we de invloed van stroming op de structuur van een suspensie van colloïdale bollen bestudeerd. Dit hebben we gedaan met zowel experimenten als met computersimulaties. De evenwichtssituatie van de suspensies was die van een vloeistof maar door een trillende vloeistofstroom aan te leggen organiseerden de deeltjes zich toch in een geordende structuur die lijkt op een kristal. Omdat dit niet de evenwichtssituatie van het systeem was, verdween de geordende structuur vrijwel direct nadat de stroming werd uitgezet. Afhankelijk van de amplitude van de oscillatie werden er verschillende structuren gevormd. Voor twee van deze structuren hebben we het kristallisatie proces bestudeerd. We constateerden dat het voor de eerste heel continu verliep, terwijl de tweede veel minder continu was en erg leek op het kristallisatieproces dat zich normaal gesproken in de evenwichtssituatie afspeelt.

In **Hoofdstuk 6** hebben we de vloeibare kristalfasen bestudeerd, die de silica staven vormden onder invloed van zwaartekracht. Doordat de deeltjes zwaarder waren dan het oplosmiddel, vormde zich na verloop van tijd een geconcentreerd sediment op de bodem. Het was al bekend dat de deeltjes spontaan nematische en smectische fasen vormen in dit sediment. Maar met ons nieuw ontwikkelde algoritme konden we deze fase nu in detail bekijken en analyseren. Zo bleek dat er ook kleine gebieden waren waar de deeltjes een kristalfase hadden gevormd. Opvallend was, dat de lagen van deeltjes niet alternerend op elkaar waren gestapeld (in een ABC stapeling, zoals voorspeld door computersimulaties) maar precies bovenop elkaar waren gestapeld (dus in een AAA stapeling). Ook hebben we de overgang kunnen onderzoeken van een volledig wanordelijke fase en een smectische fase en hebben we een 3D reconstructie kunnen maken van zogenoemde ‘dwarsliggers’. Dit zijn individuele staafjes die dwars op de gemiddelde richting van het vloeibare kristal liggen, een fenomeen dat in de jaren 90 is voorspeld aan de hand van computersimulaties.

We onderzochten in **Hoofdstuk 7** de invloed van (vloeistof)stroming op de staafvormige deeltjes. Door gebruik te maken van een constante stroming konden we de staven uitlijnen in de richting van de stroom. Door een trillende stroming op te leggen konden we kleine smectische gebieden laten ontstaan. We hebben ook gemeten hoe de viscositeit (een maat voor hoe makkelijk iets stroomt, ook wel stroperigheid genoemd) verandert als functie van de kracht waarmee de stroming wordt opgelegd. Hieruit bleek dat de viscositeit eerst afneemt naarmate de kracht toeneemt. Dit gebeurt bijvoorbeeld ook als ketchup ook de fles wordt geknepen: hoe harder je knijpt, hoe makkelijker het stroomt. Vervolgens was er een regime waar de viscositeit constant was. Dit is meestal het geval bij vloeistoffen waar geen deeltjes in zitten, zoals bijvoorbeeld zuiver water. Uiteindelijk nam de viscositeit weer toe naarmate de kracht groter werd. Dit fenomeen is duidelijk te voelen als je door een mengsel van maizena en water roert: als je hard genoeg roert (en voldoende maizena gebruikt), kan de weerstand plotseling heel sterk toenemen. Het verklaren van de veranderingen in de viscositeit, aan de hand van de onderlinge structuur van de deeltjes, is een complex (en industrieel belangrijk) probleem. Hoewel de metingen in dit hoofdstuk daarvoor een eerste aanzet geven, is meer onderzoek nodig om dit volledig te verklaren.

In de laatste twee hoofdstukken van dit proefschrift hebben we de staven een sterk afstotende wisselwerking (of interactie) gegeven.

In **Hoofdstuk 8** hebben we aangetoond (met behulp van 3D reconstructies en analyses) dat de sterk afstotende staven een plastisch kristal kunnen vormen. In een plastisch kristal bevinden de staafjes zich in een regelmatig kristalrooster, maar doordat de onderlinge afstoting ze bewegingsruimte biedt, kunnen ze nog wel vrij roteren. Hierdoor zijn hun oriëntaties wanordelijk, zoals in een vloeistof. In een plastisch kristal zijn de posities dus weliswaar geordend maar de oriëntaties niet, wat precies omgekeerd is bij een nematische fase. Vandaar dat een plastisch kristal wordt beschouwd als een broertje van een vloeibaar kristal. Ook lieten we zien dat bij hogere dichtheden een ‘plastische glasfase’ werd gevormd. Hierbij zijn de deeltjes positioneel niet meer geordend, maar roteren nog wel. Door de hoge dichtheid gedraagt het materiaal zich toch als een vaste stof. We toonden aan dat beide plastische fasen konden worden omgezet in een 3D kristal met behulp van een extern elektrisch veld. Dit proces was omkeerbaar: wanneer het elektrisch veld werd uitgezet keerde het materiaal terug naar zijn oorspronkelijke fase. Dit effect kan van pas komen in bijvoorbeeld de ontwikkeling van kleurenbeeldschermen op basis van elektronische inkt.

In het laatste hoofdstuk van dit proefschrift, **Hoofdstuk 9**, hebben we de plastische glasfase verder onderzocht, waarbij we nadrukkelijk naar de 3D verplaatsingen en rotaties van de deeltjes hebben gekeken. Ook de transitie naar een volledig kristal, onder invloed van een extern elektrisch veld, hebben we stap voor stap geanalyseerd. Daaruit bleek dat er (subtiele) verschillen zijn in het heen- en terugschakelen van het materiaal.

De techniek die wij hebben ontwikkeld om de 3D rotaties van individuele deeltjes te volgen biedt een hoop nieuwe mogelijkheden voor onderzoek naar de glasovergang, een fenomeen dat ondanks decennia van onderzoek nog steeds niet goed wordt begrepen.

Dankwoord

Dit proefschrift is uiteraard niet alleen door mijzelf tot stand gekomen. Vandaar dat ik iedereen wil bedanken die hier de afgelopen jaren (op wat voor manier dan ook) aan heeft bijgedragen.

Ten eerste wil ik mijn promotor Alfons van Blaaderen bedanken voor de mogelijkheid om een promotieonderzoek te doen in een bijzonder inspirerende omgeving. Deze omgeving, gecombineerd met jouw enthousiasme en nieuwe ideeën, heeft geleid tot de vele verschillende projecten (en side-projecten) waar ik aan heb kunnen werken tijdens mijn promotie. Ook de state-of-the-art apparatuur (lees: SP8) kwam voor mij op precies het juiste moment. Daarnaast waardeer ik de uitvoerige wetenschappelijke gesprekken die we in de afgelopen vier jaar hebben gevoerd en de vrijheid die ik heb gehad om nieuwe richtingen in te slaan met mijn onderzoek.

Uiteraard wil ik ook mijn copromotor Arnout Imhof bedanken voor zijn begeleiding. Bedankt dat ik altijd kon binnenlopen voor vragen of advies. Met name de laatste periode van mijn promotie heb ik aardig beslag gelegd op je tijd maar bedankt dat je altijd in groot detail naar mijn werk hebt gekeken en hebt voorzien van commentaar.

Ook wil ik Marjolein Dijkstra en René van Roij bedanken voor de vele suggesties, discussies en samenwerkingen op het gebied van de 'harde (en zachte) staafjes'. Bedankt ook voor jullie steun in de aanloop naar en tijdens de conferentie in Lissabon. Ook bedankt aan de rest van de vaste staf, Patrick, Krassimir, Marijn, Marcel en Laura, voor jullie input en advies. Laura, bedankt voor alle wetenschappelijke discussies, inzichten in de Canadese samenleving en voor het corrigeren van mijn Engels!

Van mijn directe collega's wil ik allereerst een paar mensen in het bijzonder bedanken. Michiel, zonder jouw computercodes en analyse methoden zou dit proefschrift er heel anders hebben uitgezien. Na zo'n drie jaar gezamenlijk testen en verbeteren, is nu het algemeen beschikbaar stellen van de '3D rod fitting methode' in zicht! Bedankt voor je geduld en de tijd die je (tussendoor) steeds hebt weten vrij te maken. Ook bedankt voor je vele adviezen en onze gesprekken over shear, dynamica, glazen, fotografie, etc., gedurende zo'n vijf jaar inmiddels! Anke, sinds onze gezamenlijke shear-experimenten aan staafjes hebben deze deeltjes centraal gestaan als onderwerp van mijn project. De vele discussies en antwoorden over de staafjes-systemen hebben enorm veel bijgedragen aan mijn werk, heel erg bedankt daarvoor (mijn kopie van je thesis is inmiddels uit elkaar gevallen, dat zegt wel genoeg denk ik). Teun, het is vrijwel onmogelijk om cynisch of chagrijnig te zijn in jouw gezelschap! Met veel plezier denk ik terug aan onze partijtjes GO, oud-en-nieuw in Berlijn met 'the Hoff' en de skype-sessies over de 'swirls paper'. Anjan, thank you for your patient explanantions on anything related to colloids. I also enjoyed our conversations on everything outside academia and your great sense of humour! Ernest, wie had gedacht bij speciale relativiteitstheorie dat we jaren later samen achter een confocal in het AMC zouden zitten? Liquid Matter in Wenen was top met jou als lokale gids.

I would also like to thank all my other colleagues that I had the pleasure to work with over the last four years. I thank my roommates Marlous, Nina, Michiel, Matthieu, Rao, Djamel, Tian-Song and Wiebke for many conversations, related or unrelated to science, and for a great atmosphere (pushing the 'Little Miss Sunshine' minivan around the parking lot was memorable). Bo, Rao, Marlous, Tian-Song, Bing, Jissy, Djamel, Bas, Henriëtte and Zdenek, thank you for collaborating with me on various topics. Matthieu and Frank, thank you for your help with simulations and theory. Johan, thanks for the large amount of PMMA (I blame it on the shear-cell). Judith, Chris and Peter: thank you for your extensive help with my research. My thanks also goes out to all current and former SCM members: John, Simone, Guido, Nick, Wessel, Chanming, Da, Tonnishtha, Somil, Rik, Murphy, Berend, Vasileios, Fabian, Harini, Srivatssan, Thomas (from the ITF), Peter, Joost, Bart, Ahmet, Simone B, Ran, Carlos, Christina, Lin, Marion, Thea and Marjoke, although this list is probably not complete, for which I apologize. Furthermore, I would also like to thank the Biophysics group, especially Hans, Gerhard, Dave and Helene. I would also like to thank the people that I've met (or joined me) during graduate schools and conferences. Frank, Marlous, Jissy, Anke, Simone, Dima and Marco, the summerschool in Corsica was the best start of my PhD that I could have imagined. Luckily the harpoon made it safely back to its proud owner... I would also like to thank the '2011 Han-sur-Lesse crowd' for a great week (except for the 'local flu') and for the follow-up trip to Berlin. Jissy, Marjolein and Nick, the training course in Edinburgh was inspiring. Bo, Jissy, Djamel and Arnout: Sendai was quite an experience, I still have vivid memories of the encouter with the Emperor and Empress of Japan and of the beef tongue specialities. Special thanks to Daisuke Nagao for showing us around on- and off-campus.

It was a delight to supervise my students, Tim and Chris. Tim, je bleef me verrassen met nieuwe vragen en onverwachte experimentele resultaten, wat heeft geleid tot een waardevolle samenwerking met de theoretici en een recente publicatie. Chris, thank you for all the work that you performed: a significant part of both the synthesis and the analysis in Chapter 6 is based on your work. So thanks to both of you!

I also thank John Kelly for getting me out of the lab and onto the squash court on a regular basis. My time is running out to improve my game (so far I counted only one real win...). Ook bedankt aan Dries, Jildou, Esger en Brigitte voor de nodige afleiding!

There are several people from outside Utrecht that I would like to thank: Andrea Fortini en Matthias Schmidt for our collaboration on shear. I thank Michiel Hermes, Rut Besseling (not related), Job Thijssen and Niek Hijnen for support during my stay in Edinburgh. I thank Anand Yethiraj for useful discussion and collaboration. I also thank the program manager of M2i, Derk Bol, for his continued support and Mark Boerakker and Damien Reardon from DSM for their interest in my project. Another thanks goes out to Vincent Schoonderwoert and Hans van der Voort from SVI and Patrick van Wieringen and Henk den Hartog from Leica. And finally, Harry Linders, our conversations in the final stages of my PhD were a delight.

Aan mijn vrienden en familie: bedankt voor jullie steun, begrip en/of afleiding de afgelopen jaren!
Dennis, Thomas, Stephan, Beelen, Peter, Frank, Mark en Bart (en aanhang) bedankt voor de talloze avonden, weekenden en vakanties, voor de interesse in mijn werk (weer lekker promoveren morgen?) en voor het accepteren van uit de hand gelopen discussies over bijv. trillingen en piramides. Ook mijn huisgenoten op ‘de van mollem’, Stephan en Thomas, bedankt!

Ook wil ik graag Cor en Els bedanken voor hun continue betrokkenheid bij alles wat mij bezighoudt, en voor de fantastische en ontspannen sfeer tijdens etentjes, schouwburgbezoeken en weekenden samen met Jasper, Liedeke en Sanny, ook jullie bedankt!

Pap en mam, bedankt voor jullie onvoorwaardelijke steun en geloof in mij. Bedankt dat jullie mijn wetenschappelijke interesses altijd hebben aangemoedigd, en ik waardeer jullie geduld en vertrouwen enorm. Tijdens mijn promotietijd heeft jullie advies en positieve instelling me altijd weer weten te motiveren.

Joris en Cecile, heel erg bedankt voor jullie medeleven en betrokkenheid tijdens mijn gehele promotietijd. Jullie energie en opgewekte verhalen doen me altijd goed! Laten we snel weer een bezoek aan Londen plannen! Lieve Mira, ik weet dat je het maar moeilijk kon bevatten dat ik na een jaar onderzoek aan ‘bolletjes’, nog eens vrijwillig vier jaar verder ging. Toch waardeer ik je eigenwijze kijk op dingen en je humor heel erg, bedankt!

Lieve Sas, jij bent de enige die werkelijk alle ups en downs heeft meegemaakt van de laatste jaren. Geen enkel detail heb ik je bespaard en toch heb ik je nooit kunnen betrappen op het feit dat je niet zat te luisteren. Ik heb grote bewondering voor hoe je bent omgegaan met alles rondom de afronding van dit proefschrift. Ik ben onvoorstelbaar dankbaar voor je liefde en ik kan me geen beter vooruitzicht bedenken dan de verloren dagen zo snel mogelijk met je in te halen!

List of Publications

This thesis is partially based on the following publications:

- A. Kuijk, A. Imhof, M. H. W. Verkuijlen, **T. H. Besseling**, E. R. H. van Eck & A. van Blaaderen, Colloidal silica rods: material properties and fluorescent labeling, *Particle & Particle Systems Characterization* **31**, 706-713 (2014) - Chapter 2

- **T. H. Besseling**, J. Jose & A. van Blaaderen, Methods to calibrate and scale axial distance in confocal microscopy as a function of refractive index, *Journal of Microscopy*, accepted, arXiv:1404.3952v1 (2014) - Chapter 3

- **T. H. Besseling** / M. Hermes, A. Kuijk, B. de Nijs, T.-S. Deng, M. Dijkstra, A. Imhof & A. van Blaaderen, Determination of the positions and orientations of concentrated rod-like colloids from 3D microscopy data, *Journal of Physics: Condensed Matter*, accepted, arXiv:1406.4985v1 (2014) - Chapter 4

- **T. H. Besseling**, M. Hermes, A. Fortini, M. Dijkstra, A. Imhof & A. van Blaaderen, Oscillatory shear-induced 3D crystalline order in colloidal hard-sphere fluids, *Soft Matter* **8**, 6931-6939 (2012) - Chapter 5

- **T. H. Besseling**, M. Hermes, A. Fortini, M. Dijkstra, A. Imhof, & A. van Blaaderen, Out-of-equilibrium crystallization kinetics in colloidal hard-sphere fluids driven by oscillatory shear, *in preparation* - Chapter 5

- **T. H. Besseling**, A. Imhof & A. van Blaaderen, Real-space measurements of nematic and smectic phases of monodisperse colloidal silica rods, *submitted* (2014) - Chapter 6

- **T. H. Besseling**, C. Kennedy, A. Imhof & A. van Blaaderen, Experimental measurement of the equation of state of hard rods, *in preparation* - Chapter 6

- B. Liu, **T. H. Besseling**, M. Hermes, A. F. Demirörs, A. Imhof & A. van Blaaderen, Switching plastic crystals of colloidal rods with electric fields, *Nature Communications* **5**, 3092 (2014) - Chapter 8

- **T. H. Besseling**, B. Liu, M. Hermes, A. Imhof & A. van Blaaderen, Reversible martensitic plastic glass to crystal transition in a system of long-range repulsive rods, *in preparation* - Chapter 9

Other publications by the author:

- T. Vissers, **T. H. Besseling**, A. van Blaaderen & A. Imhof, Sustained rotational instabilities and crystalization in driven suspensions of oppositely charged colloids, *submitted* (2014)
- B. W. Kwaadgras, **T. H. Besseling**, T. J. Coopmans, A. Imhof, A. van Blaaderen, M. Dijkstra & R. van Roij. Orientation of a dielectric rod near a planar electrode, *Physical Chemistry Chemical Physics*, DOI: 10.1039/c4cp02799j (2014)
- B. Liu, **T. H. Besseling**, A. van Blaaderen & A. Imhof, Confinement induced crystal - plastic crystal transitions in rod-like particles with long-ranged repulsion, *submitted* (2014)

About the author

Thijs Besseling was born on March 26, 1984 in Fiesole, Italy. He attended secondary school at the Gymnasium Haganum in the Hague, from which he graduated in 2002. After graduation, he spend a year travelling in Thailand and Australia. In 2003, he started his studies at the Utrecht University, where he studied Chemistry for one year and obtained a BSc degree in Science and Innovation Management. He graduated from Utrecht University with a MSc degree in Physics (cum laude) in 2010. He performed his MSc research project in the Soft Condensed Matter group at Utrecht University, under the supervision of Prof. Alfons van Blaaderen and Prof. Marjolein Dijkstra. As a MSc student, he received the 1st Poster Prize in the Crystal & Structural Research Group during an NWO-CW Study Group Meeting in Veldhoven. In 2010, he continued to work in the same group as a PhD student, the results of which are described in this thesis. Parts of this thesis are published in international peer-reviewed journals. He received a European Soft Matter Infrastructure (ESMI) grant for a research project in the Soft Matter Physics group at the University of Edinburgh, which he performed in Jan. 2012. Oral presentations were given at various national and international conferences, including the 8th Liquid Matter Conference in Vienna, the 14th conference on the International Association of Colloid and Interface Scientists in Sendai (Japan), Physics@FOM in Veldhoven and the 9th Liquid Matter Conference in Lisbon. In 2011, he received a poster prize for 'Best innovative research value' during a conference of the Materials Innovation Institute (M2i) in Noordwijkerhout. Part of his research was highlighted in the Dutch newspaper 'de Volkskrant' on Jan. 25, 2014.